






# Engineering High-Dimensional Quantum States in Silicon Photonic Circuits

Submitted to the Graduate School of Physics in partial fulfillment of the requirements for the degree of

DOTTORE DI RICERCA IN FISICA
at the University of Pavia

DOCTEUR EN PHYSIQUE
at the Université Grenoble Alpes

*Author:*
Sara Congia

*Date:*
23 October 2026

*Supervisor:*
Prof. Matteo Galli
Dr. Ségolène Olivier

*Co-supervisor:*
Prof. Daniele Bajoni
Dr. Johan Rothman

# Engineering High-Dimensional Quantum States in Silicon Photonic Circuits

Sara Congia

## Abstract

Thanks to their low decoherence and compatibility with optical fiber infrastructures, quantum states of light are ideal carriers of quantum information and are expected to form the backbone of future quantum communication and information–processing networks. The ability to generate and manipulate photon pairs with a high degree of entanglement is key to scaling up the number of photonic qubits and quantum gates, enabling light–based secure quantum communication and efficient quantum computation. Achieving this goal requires a monolithic and stable integrated platform embedding all the necessary optical and electronic components on a single chip. Among the available photonic platforms, silicon photonics stands out thanks to its compatibility with complementary metal–oxide–semiconductor technology, crucial for large–scale fabrication, high reproducibility, and co–integration of photonic and electronic circuits on the same millimeter–scale devices.

In this thesis, I present the design, fabrication, and experimental characterization of silicon photonic integrated circuits developed for high–dimensional quantum information processing based on frequency–encoded photonic states. This three–year PhD research work, carried out half at the research center CEA-Leti in Grenoble and half at the Quantum Photonics Laboratory of the University of Pavia, focuses on two approaches to increase both the dimensionality and the programmability of frequency–bin quantum states: hyperentanglement and integrated quantum frequency processing.

First, I demonstrate an integrated source of photon pairs entangled simultaneously across two independent degrees of freedom, time and frequency, based on multiple high–brightness silicon microring resonators. I generate 16–dimensional bipartite quantum states and experimentally verify genuine hyperentanglement through quantum state tomography techniques and hyperentanglement witnesses. I then introduce and characterize a new generation of silicon hyperentangled sources with a higher level of on–chip integration, devices currently being fabricated in the CEA-Leti cleanroom. These devices incorporate photon–pair generation, routing, and spectral filtering, enabling the combination of frequency–bin and, potentially, time–bin entanglement with additional degrees of freedom such as path and polariza-

tion, with the aim of further increasing the quantum information capacity of single photons.

Finally, I present the first monolithic silicon quantum frequency processor, integrating a microring–resonator source of high–dimensional frequency–bin states, two phase modulators, and a programmable spectral phase shifter in between the two. This device enables coherent and reconfigurable transformations of frequency–encoded qubits and qudits. Its capabilities are showcased through the realisation of a post–selection–free tunable frequency beam splitter over two classical frequency modes, showing high fidelity and low leakage to neighboring modes, a key prerequisite for quantum information processing in the frequency domain. Furthermore, the processor is operated in the quantum regime to implement a frequency–domain quantum walk and to reconstruct, via quantum state tomography, the density matrix of a two–photon state generated on the same chip.

Overall, this work confirms the suitability of the silicon photonics platform for quantum information processing, proposing possible strategies to scale up the telecommunication–compatible frequency–bin encoding for the on–chip generation and manipulation of complex quantum states.

# Contents

**Introduction** **7**

**1 Integrated Silicon Photonics** **13**

1.1 The waveguide . . . . . 14

1.1.1 Theory of linear optical propagation in waveguides . . . . . 15

1.1.2 Theory of nonlinear optical phenomena in waveguides . . . . 18

1.2 Waveguide simulation . . . . . 30

1.3 The ring resonator . . . . . 34

1.3.1 Coupling formalism . . . . . 34

1.3.2 Resonance condition and transmission spectra . . . . . 35

1.3.3 Figures of merit . . . . . 37

1.3.4 Nonlinear Enhancement . . . . . 38

1.4 Ring resonator simulation . . . . . 39

1.4.1 Point coupler simulation . . . . . 40

1.4.2 Figures of merit calculations . . . . . 42

1.5 The directional couplers . . . . . 45

1.5.1 Directional coupling modeling . . . . . 46

1.6 The Mach–Zehnder interferometer . . . . . 49

1.6.1 The cascaded MZI filters . . . . . 50

1.7 In- and out-coupling devices . . . . . 52

1.7.1 Edge couplers . . . . . 53

1.7.2 Grating Couplers . . . . . 53

1.7.3 Dual-polarization Grating Couplers . . . . . 54

1.8 Active devices . . . . . 55

1.8.1 Thermal phase shifters . . . . . 55

1.8.2 Phase modulators in silicon . . . . . 56

1.9 Conclusions and further perspectives . . . . . 59

**2 Generation of hyperentangled photon pairs** **61**
2.1 Motivation and state of the art . . . . . 62
2.1.1 Time and frequency –*bin* hyperentanglement . . . . . 62
2.2 Experimental realisation . . . . . 64
2.2.1 Silicon source design and characterization . . . . . 64
2.2.2 Generation method . . . . . 70
2.2.3 Quantum state analysis . . . . . 71
2.3 Results and discussion . . . . . 77
2.3.1 Two-photon interference . . . . . 77
2.3.2 Quantum state tomography . . . . . 79
2.3.3 HE witness . . . . . 82
2.3.4 Discussion . . . . . 83
2.4 Conclusions and further perspectives . . . . . 85

**3 Integration of sources of hyperentangled photon pairs** **87**
3.1 Background and motivation . . . . . 88
3.2 State of the art . . . . . 89
3.2.1 Proposed source architectures . . . . . 91
3.3 Fabrication . . . . . 95
3.3.1 Process flow . . . . . 95
3.3.2 Layer definition . . . . . 98
3.4 Chip design . . . . . 100
3.4.1 Device simulations . . . . . 103
3.5 Wafer-scale optical characterizations . . . . . 110
3.5.1 Optical losses . . . . . 110
3.5.2 Ring resonators . . . . . 112
3.5.3 Optical couplers . . . . . 117
3.5.4 Cascaded MZI DEMUX . . . . . 117
3.6 Conclusions and further perspectives . . . . . 120

**4 A silicon quantum frequency processor** **123**
4.1 State of the art . . . . . 124
4.2 Design and characterization of the silicon chip . . . . . 126
4.2.1 Biphoton quantum frequency comb source . . . . . 128
4.2.2 p–n phase modulators . . . . . 134
4.2.3 Line-by-line waveshaper . . . . . 136
4.3 Experimental demonstrations in the classical and quantum domain . 144

4.3.1 Experimental setup . . . . . 144
4.3.2 The frequency beam splitter operation . . . . . 147
4.3.3 General single-qubit gates . . . . . 155
4.3.4 Quantum walk manipulation . . . . . 159
4.3.5 Bell-curve measurements and quantum state tomography . . 163
4.4 Conclusions and further perspectives . . . . . 165

**Conclusions** **166**

**A Supplementary device modeling and simulations** **170**
A.1 Si300nm WG simulations . . . . . 170
A.2 Si WG nonlinear parameter estimations . . . . . 171
A.3 List of ring resonator figures of merit . . . . . 172
A.4 Additional point coupler simulations . . . . . 175
A.5 TMM for structures based on ring resonators . . . . . 176

**B Supplementary experimental methods and characterizations** **180**
B.1 Layout and characterization of circuit test structures . . . . . 181
B.2 Additional characterization of the silicon phase modulators . . . . . 181
B.3 Source generation rate characterizations . . . . . 184
B.4 Integrated WS calibration technique . . . . . 184
B.5 Additional quantum frequency processor characterizations and simulations . . . . . 191

**List of Publications and Conferences** **194**

**Bibliography** **198**

# Introduction

*Quantum* technologies have emerged as one of the most promising strategies to potentially revolutionize future computation, communication, and sensing. The year 2025 has been proclaimed the International Year of Quantum Science and Technology, indicating the rapidly growing worldwide interest in this field. Today, quantum technologies are moving from fundamental research toward practical deployment. Fundamental and applied research activities have experienced a significant acceleration driven by private investors and government funding programs across the globe. According to McKinsey, the global quantum technology market is expected to reach up to $97 billion by 2035 [1]. Many countries have launched dedicated national quantum strategies and roadmaps for the coming years, including Italy [2] and France [3].

The present work is situated within this rapidly evolving scenario. In this manuscript, I describe the research projects I have carried out through a collaboration between the Quantum Photonics Laboratory of the University of Pavia and the French government–funded technological research center CEA–Leti in Grenoble. The work presented in this thesis focuses in particular on silicon integrated photonic circuits and their application to quantum technologies, with special emphasis on the generation, manipulation, and analysis of frequency–encoded quantum states of light. This introduction provides a broad overview of the scientific and technological context.

## Quantum integrated photonics

Quantum photonics is a leading technological frontier for the implementation of quantum information technologies, including computation [4] and quantum communication [5]. Photons are often considered the ideal medium for qubit encoding and manipulation, thanks to their low interaction with the environment, i.e. long

coherence times, support for high–speed and room–temperature operations, and compatibility with existing optical fiber networks.

Light offers a large variety of degrees of freedom (DoFs) to encode information [6], such as polarization, spatial (or path) modes, orbital angular momentum, time–bin and frequency modes. Each encoding presents specific advantages and limitations; however, across all of them, a common trend has emerged in recent years: the transition from early bulk–optical demonstrations toward more scalable implementations in *integrated* photonic platforms.

Photonic integrated circuits play a central role in enabling robust quantum photonic technologies [7, 8, 9, 10]. Beyond the reduction of weight, size, power consumption and cost, integration provides lower optical losses, enhanced phase and thermal stability, and improved reproducibility. These advantages directly translate into higher fidelity of the implemented quantum operations and, depending on the chosen DoF, may also produce a reduction in system complexity. As a result, quantum photonic integrated circuits (QPICs) are indeed often considered *the* way toward scalable quantum systems [11, 12, 13]. In particular, thanks to its compatibility with complementary–metal–oxide–semiconductor (CMOS) technology, *silicon* photonics is the leading platform for the development of low–cost and high–volume quantum photonic technologies [14, 15]. Moreover, it offers the possibility to generate, filter, (de–)multiplex, and modulate quantum states of light on chip, using ready–to–use components developed for the telecommunication industry.

## Frequency-bin quantum information processing

Among the available photonic DoFs, the *frequency* has recently attracted considerable attention, shifting the paradigm from being used primarily to multiplex information in telecommunication networks to exploiting the orthogonality of different colors to encode quantum information itself. Specifically, in its discrete-variable version [16, 17] extremely large Hilbert spaces can be realized by taking as quantum levels non-overlapping frequency intervals, i.e., the frequency-*bins* (FBs). They can all coexist within a single spatial mode, i.e. one optical fiber or waveguide, making frequency-bin encoding easier to transmit than alternatives based on, for example, path modes [18]. Moreover, FB quantum gates are known for their parallelizability, i.e. the extension of a quantum operation from one to multiple qubits without changing its implementation [19, 20], confirming the inherent compactness and resource efficiency of this encoding technique.

Last but not least, entangled photon pairs distributed across multiple FBs are easy to generate through spontaneous parametric down conversion or spontaneous four wave mixing (SFWM). More interestingly, by means of integrated optical cavities, at the narrow resonances the probability of generation of quantum states of light is enhanced [21], thus directly producing entangled photon pairs encoded in the FB DoF more efficiently.

In this manuscript, I present the development, fabrication and test of multiple circuits for FB states generation and manipulation, all based on the use of integrated silicon microring resonators. In particular, I explored different approaches to increase both the dimensionality and the programmability of SFWM-generated FB quantum states. The two strategies are briefly presented in the next two paragraphs, but dedicated introductory sections are reported at the beginning of each project's chapter.

## Hyperentanglement

The simultaneous entanglement of photons in multiple degrees of freedom, namely hyperentanglement (HE) [22], is considered a promising approach to increase the dimensionality of photonic quantum systems, a crucial requirement for the development of large–scale quantum technologies [23, 24]. Although frequency–bin entanglement is already intrinsically high–dimensional, encoding multiple qubits onto a single photon by adding further DoFs such as time–bin, path, or polarization can efficiently save quantum computing resources [25]. Moreover, hyperentanglement unlocks a range of unique capabilities, including the realisation of Bell–state analyzers using linear optics [26, 27], superdense coding [28, 29], and cluster–state quantum computation [30, 31, 32]. It can also be directly employed in quantum communication protocols, showing either higher robustness against decoherence in lossy channels compared to multi–photon quantum states with equal Hilbert space dimensionality [33], or enabling high–fidelity entanglement distillation [34].

While the generation of high–dimensional entanglement within a single DoF on photonic chips has already seen substantial progress [35], experimental demonstrations of HE sources in integrated platforms remain relatively limited (see the introduction of chapter 2 and chapter 3). In this thesis, I therefore explore hyperentanglement as a way to further extend the capabilities of frequency–bin–based quantum photonics. This is done both by experimentally demonstrating a source of time–frequency HE photon pairs based on multiple silicon microring resonators, and by designing additional integrated circuits combining FB entanglement with other

DoFs, such as path and polarization. These approaches aim to increase not only the dimensionality of the generated quantum states, but also the level of integration and on–chip programmability achievable within silicon photonic platforms.

### Quantum optical processors

Integrated optical processors are chips incorporating all the necessary functions to generate, process, and transmit information based on light. To date, the working principle of classical processors is based on shaping the amplitude and phase of the processed optical fields by using large interferometric networks [25, 36]. The same paradigm has been successfully transferred to the quantum domain. Path–encoding has emerged as the leader of this new landscape, thanks to easy–to–implement manipulation gates based on meshes of beam splitters and phase shifters, already capable of implementing arbitrary unitary transformations on high–dimensional quantum states [37, 38, 39].

On the other hand, frequency–bin processing has so far been mostly realized using bulk components, with performance limited by losses and stability issues, and would therefore greatly benefit from integration [16, 17]. An on–chip quantum frequency processor (QFP) would require *(i)* a source of frequency–encoded quantum states, *(ii)* a mechanism for implementing coherent, reconfigurable frequency mixing with high fidelity, and *(iii)* line–by–line spectral phase and amplitude control to implement arbitrary mode transformations.

Contrary to the path DoF, works demonstrating the co–integration of multiple necessary building blocks for frequency–domain processing remain limited. Nevertheless, QFPs have solid theoretical foundations [40] and relevant experimental demonstrations using hybrid bulk–integrated approaches have confirmed their potential (see the introduction of chapter 4). In this thesis, these concepts are pushed further by presenting the first integrated quantum frequency processor that combines a FB source, frequency mode mixing, and programmable single–mode phase control, all integrated on a monolithic silicon photonic chip, paving the way toward scalable frequency–based quantum information processing.

## Outline

Chapter 1 provides the theoretical background necessary for the development of silicon photonic devices, with particular attention to the practical aspects required for the efficient and accurate design of the components used across the various

projects. The remainder of the manuscript details these research projects, focusing on my specific contributions across each chapter.

In Chapter 2, the demonstration of an integrated HE source in the frequency– and time–bin DoFs is presented, with emphasis on the concept, the experimental implementation, and the analysis of the generated quantum state. In Chapter 3, the simulation, design, and preliminary linear optical characterization of other HE sources are presented. These devices feature a higher level of integration and are currently undergoing the final fabrication steps.

Chapter 4 is dedicated to the quantum frequency processor, a project to which I contributed across all its fundamental aspects. The simulation and design of the photonic building blocks are first presented, together with their linear optical and electrical characterizations. In the final part, key experimental demonstrations showing the system–level capabilities of the processor are reported, including the realisation of a post–selection–free frequency beam splitter and the quantum–state manipulation and analysis of on–chip–generated biphoton quantum frequency combs.

# Chapter 1

# Integrated Silicon Photonics

Photonic Integrated Circuits (PICs) have made significant progress since the late 1980*s* [41], when the concept of guiding light in silicon was first introduced. Since then, various material platforms have been studied, with the ultimate goal of enabling efficient generation, transport, processing, and detection of light within a single miniaturized circuit. Much of this development has been driven by the telecom and datacom industries, focusing respectively on light processing in the C–band (wavelength band across 1550 nm) and O–band (1310 nm). Historically, thanks to its transparency window accommodating both wavelength ranges and the possibility of integrating lasers, indium phosphide (InP) rapidly became the platform commercially utilized for advanced PICs [42]. However, emerging markets demand higher performance, a broader wavelength range of operation, and scalability. All these requirements are met by Silicon Photonics (SiPh), which combines lower losses, a broader transparency region, and higher integration density. Moreover, it leverages the robust processing infrastructure of the CMOS electronic industry, promising significantly cheaper PICs compared to other options, including InP–based microchips [43].

Silicon Photonics is a cutting–edge technology now entering the era of *large–scale integration*, possibly integrating up to $10^4$ components on a single chip [44]. Its market is expanding rapidly and is expected to reach USD 9.02 billion within five years, with a *compound annual growth rate* of 30.5% [45]. Major industrial players such as TSMC, GlobalFoundries, and STMicroelectronics have established their own silicon photonics programs, while research and innovation centers such as CEA-Leti and Imec have also set up pilot lines. Today, basic passive and active devices (waveguides, splitters, couplers, modulators, thermal shifters, etc.) are manufactured in

these centers with well–established performance, and they are available in device libraries, namely Process Design Kits (PDKs), making them accessible to external customers [46, 43]. The road ahead is rich with opportunities, motivated also by ongoing research across numerous potential applications, from traditional high–speed communication to optoelectronics, LIDAR, nonlinear optics, and quantum photonics [47].

In this chapter, I describe some of the basic SiPh components and the associated design optimization process, covering the theoretical concepts and the simulation steps required to match the target performance. The list presented here does not aim to include all the devices that can be realized on this platform, which would be much broader. It contains instead the building blocks embedded in the quantum photonics circuits described in detail in later chapters. In particular, the focus is on waveguides, microring resonators, directional couplers, Mach–Zehnder interferometers, and phase modulators, designed for the Silicon–On–Insulator (SOI) platforms employed in the presented research work: the SOI 200mm Si220nm (CEA–Leti [48]) and the SOI 300mm Si300nm (CEA–Leti [49] and STMicroelectronics [50]).

## 1.1 The waveguide

The core concept behind integrated photonics is guiding light waves from one point to another through planar circuits. The fundamental physical structure is the so-called waveguide (WG), a nanometric-scale dielectric channel in which light propagates along predefined paths.

By exploiting both vertical ($y$-axis) and horizontal ($x$-axis) confinement, one can create "*optical wires*" whenever the refractive index of the wire is higher than that of the surroundings ($n_1 > n_2$). The electromagnetic field is then confined in the medium with the higher refractive index, namely the *core*, thanks to the phenomenon of total internal reflection (TIR) [51], which occurs at the interface with the lower-index medium, i.e., the *cladding*. The shape of the waveguide cross–section affects the distribution of the fields, the so-called optical *mode*, and consequently the properties of the propagating light, as explained in the next paragraph. Waveguides are typically designed as simple rectangular (*strip*) geometries or "T"-shaped (*rib*) geometries. For the latter, two etching levels are applied, producing a WG head on top, with typical dimensions around 0.4–1.0 $\mu$m, and a much larger bottom region (around 3–4 $\mu$m), usually called the *slab* region. Thanks to this lower part, the fields interact less with the $Si/SiO_2$ interface, experiencing lower scattering losses compared with strip waveguides. Although this is usually considered a significant

advantage, strip WGs allow the design of more compact circuits and are therefore preferred for high-density integration.

The situation becomes even more complex for components such as silicon modulators, in which doped-silicon regions are involved, and the WG cross–section can differ from the two geometries presented here [52]. As a matter of fact, an accurate study of the modes supported by the WG and their properties is necessary to achieve the target performance, usually carried out through numerical simulations, as more specifically reported in the dedicated section (1.2).

As previously mentioned, the description focuses on CMOS–compatible SOI

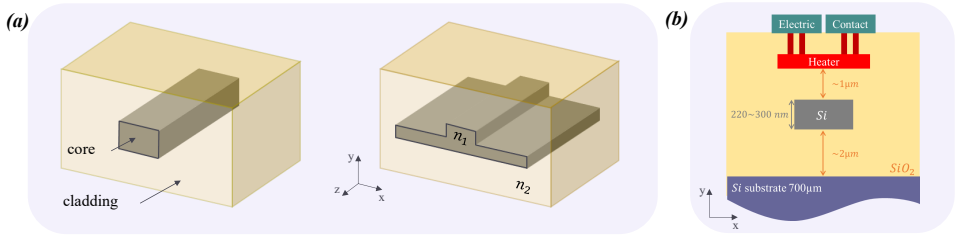



*Figure 1.1:* ***SOI waveguides.*** *(a) Strip and rib waveguide geometries. The light propagates along the z-axis, confined in the core material by TIR if $n_1 > n_2$. (b) Cross–section scheme for tunable passive silicon photonic components.*

waveguides and devices, since this is the platform used to integrate the circuits presented in this work. Light is confined within a thin *silicon* core medium, surrounded by silicon dioxide (*silica*), as depicted in Figure 1.1. This configuration provides a high refractive index contrast (around 40% at 1550 nm) and thus tight confinement, allowing the integration of small device cross–sections and high integration density [53]. In particular, two main standards are used in the industry, differing in the thickness of the silicon slab: 300 nm and 220 nm. In this chapter, the simulation results obtained for both Si slab thicknesses are reported. A more detailed treatment of the fabrication of these SOI–based circuits can be found in the chapter dedicated to the integration of novel circuits for quantum photonics applications, namely chapter 3.

### 1.1.1 Theory of linear optical propagation in waveguides

Light propagates in the dielectric medium along the length of the WG ($z$–axis in Figure 1.1) in what are commonly called *optical modes*. They describe the distribution of the electric and magnetic fields ($\boldsymbol{E}$, $\boldsymbol{H}$) in the cross–section plane $(x, y)$, propagating along the $z$–axis without changing shape.

If we assume that the two dielectric media are homogeneous, isotropic, and non–absorbing, the distribution of the refractive index along the vertical profile $n(x, y)$ is a real value. Under these hypotheses, following the treatment reported in detail in [51], the discrete solutions of the Maxwell equations have the form:

$$\begin{aligned} \boldsymbol{E} &= \mathscr{E}(x, y, \omega) \, \exp\left[i \, (\beta z - \omega t \,)\right] \,, \\ \boldsymbol{H} &= \mathscr{H}(x, y, \omega) \, \exp\left[i \, (\beta z - \omega t)\right] \,, \end{aligned} \tag{1.1}$$

while the Maxwell equations reduce to:

$$\nabla^2 \mathscr{E} + \left[ \left( \frac{\omega}{c} \right)^2 \, n^2(x, y) - \beta^2 \right] \, \mathscr{E} = 0 \,. \tag{1.2}$$

This can be seen as an eigenvalue problem, where the complex amplitudes of the electric field $\mathscr{E}(x, y, \omega)$ are the *eigenfunctions* and $\beta^2$ are the *eigenvalues*, i.e., the propagation constant associated with the given mode, *squared*. For each angular frequency $\omega$ at which the field oscillates there are, in general, an infinite number of eigenvalues for a given index profile. However, only a discrete set of propagation constants $\beta(\omega)$ corresponds to confined modes. If the set includes only *one* mode, they are called *single–mode* WGs[1]; otherwise, we generally speak about *multi–mode* WGs.

From the propagation constant of the supported modes, other fundamental quantities commonly used to describe light propagation in structured media can be derived. By expanding $\beta$ in a Taylor series, each term of the expansion can be rewritten by defining the following quantities: the effective index $n_{eff}(\omega)$, the group index $n_g$, and the dispersion $D$ (usually measured in ps/nm/km), namely

$$n_{eff} \stackrel{\text{def}}{=} \frac{\beta c}{\omega} \,, \tag{1.3}$$

$$n_g \stackrel{\text{def}}{=} \frac{\delta \beta}{\delta \omega} \cdot c = n_{eff} + \omega \, \frac{\delta n_{eff}}{\delta \omega} \,, \tag{1.4}$$

$$\mathcal{D} \stackrel{\text{def}}{=} \frac{\delta^2 \beta}{\delta \omega \, \delta \lambda} = -\frac{\lambda}{c} \cdot \frac{\delta^2 n_{eff}}{\delta \lambda^2} \,. \tag{1.5}$$

A given nanostructured material can be classified as exhibiting either *normal dispersion*, when $\mathcal{D} < 0$, or *anomalous dispersion*, when $\mathcal{D} > 0$. It is also worth mentioning the group velocity dispersion (GVD), which is sometimes defined instead of $\mathcal{D}$: $\beta_2 \stackrel{\text{def}}{=} \frac{\delta^2 \beta}{\delta \omega^2} = -\mathcal{D} \, \frac{\lambda^2}{2 \pi \, c}$.

[1] In SiPh circuits, SM WGs support only the fundamental TE mode *and* the fundamental TM mode, i.e., the two lowest-order transverse modes, namely $TE_{00}$ and $TM_{00}$.

All the reported quantities depend on the wavelength and on the refractive index distribution of the analyzed cross–section; therefore, their values can be tuned through careful WG geometry engineering. An example of this process is reported in section 1.2.

The supported waveguide modes have intrinsic orthogonality properties, which give rise to two different types of modes: transverse electric (TE), with components $E_y$, $H_x$, and $H_z$, or transverse magnetic (TM), whose non-zero fields are $H_y$, $E_x$, and $E_z$ [51]. Since TE modes usually have a higher effective index than the corresponding TM mode of the same order [53], they are more strongly confined in the core medium. As a consequence, they are less localized in the cladding and along the sidewalls of the WG, where roughness contributes to light leakage. For this reason, designers mainly choose TE modes to transfer and manipulate light on-chip, thanks to their lower propagation losses.

It is worth introducing at this point the definition of *propagation losses* in optical integrated circuits. The power transmitted at the end of a WG with length $L$ is equal to:

$$\mathcal{P}(L) = \mathcal{P}(0)e^{-\tilde{\alpha}L}\,, \tag{1.6}$$

in which $\tilde{\alpha}$ is the power attenuation coefficient, expressed in $\mathrm{m}^{-1}$. Usually, the value of losses of a photonic component (as well as for optical fibers, etc.) is given in dB/cm. One can easily convert between the two using the dB definition[2]: $\tilde{\alpha}\,[cm^{-1}] = \ln(10)/10\,\alpha\,[dB\,cm^{-1}] = 0.23\,\alpha\,[dB\,cm^{-1}]$.

In Figure 1.2 two examples of fundamental TE *modes* can be visualized, i.e.,

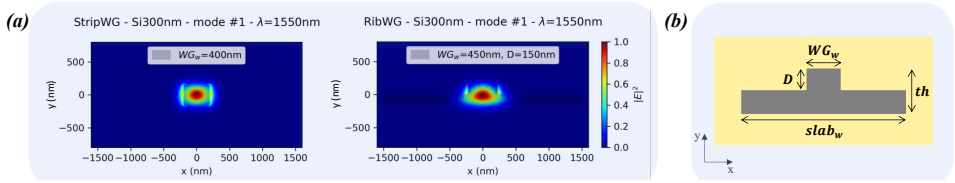



*Figure 1.2:* ***SOI waveguides.*** *(a) Example of the $TE_{00}$ mode in the two standard SM WGs of the CEA-Leti SOI platform of thickness $th = 300\,nm$ at wavelength $1550\,nm$. In particular, the parameters are: for the strip geometry $WG_w = 400\,nm$; for the rib geometry $WG_w = 450\,nm$, partial etching depth $D = 150\,nm$, $slab_w = 3\,\mu m$. (b) General scheme of the WG, with all the geometrical parameters defined. These labels will be used in section 1.2 to refer to the parameters used to optimize the WG performance.*

[2] Given the power at the end of a line of length $L$, $\mathcal{P}$, and the reference power $\mathcal{P}_0$, both measured in *linear* scale (usually mW), the power level can be expressed in decibels as: $10\,\log_{10}(\mathcal{P}/\mathcal{P}_0)\,[dB]$.

the distribution of the magnitude of the electric field in the case of the two typical SM waveguides of the Si300 nm platform (respectively with waveguide width $WG_w$ of 400 nm for the strip and 450 nm for the rib).

The quantum photonic circuits presented in this work are all based on the generation, propagation, and manipulation of light in the $TE_{00}$ mode. Therefore, in the following section 1.2, the analysis carried out to properly design the silicon photonic components for operation in the fundamental transverse electric mode is reported.

### 1.1.2 Theory of nonlinear optical phenomena in waveguides

In semiconductor waveguides, an external optical field interacts with the electrons of the material, generating nonlinear optical phenomena that couple electromagnetic fields with different amplitudes and frequencies. Assuming the (*linear*) isotropy of the material and an instantaneous dielectric response, the input electric field $E(t)$ induces a polarization of the form [54]:

$$P(t) = \epsilon_0 \left( \chi^{(1)} E(t) + \chi^{(2)} E^2(t) + \chi^{(3)} E^3(t) + ... \right) , \tag{1.7}$$

where $\chi^{(i)}$ are the $i$-th order susceptibilities, complex tensors of rank $(i+1)$. Their role is briefly examined in the following lines, focusing mostly on the material under consideration here: silicon.

The first-order susceptibility $\boldsymbol{\chi^{(1)}}$ is related to single-photon–induced dipole excitations, arising from the interaction between the photon and the bound and free electrons of the material. In particular, its real part is connected to the refractive index of the medium, while its imaginary part is related to optical gain and losses.

Nonlinear phenomena are thus expressed by the higher-order susceptibilities, describing the exchange of energy among different *frequencies*, i.e., electromagnetic fields at different frequencies. Both second- and third-order processes, respectively arising from susceptibilities of rank $i = 3$ and $i = 4$, can be divided into two groups. In *parametric* processes, such as harmonic generation (*second* and *third*) and Four-Wave Mixing, the energy transfer occurs only between waves, with no energy exchange with the material itself. These processes can be described by the *real* part of the corresponding susceptibility term. In the case of processes such as Stimulated Raman Scattering and Two-Photon Absorption, the conservation of energy is fulfilled by the whole system, therefore also involving the material. These are called *non-parametric* processes and are described by the *imaginary* part of the corresponding susceptibility tensor.

Crystal symmetry and properties influence the entries of the susceptibility tensors

and may limit the variety of allowed phenomena [55]. In centrosymmetric crystals such as Si, the second-order susceptibility term $\boldsymbol{\chi^{(2)}}$ is absent. Therefore, the interest in silicon as a nonlinear medium arises from the variety of third-order effects described by its $\boldsymbol{\chi^{(3)}}$, which are discussed later.

Moreover, all optical WGs, and thus also the Si-based ones, offer important advantages with respect to their bulk counterparts:

- The light *confinement* enhances the field strength inside the nonlinear WG,
- The propagation is not affected by *diffraction* effects; therefore, the light–matter interaction can be maintained efficiently over centimeters, or even more,
- The WG *geometry* can be adapted to optimize the efficiency and the bandwidth of the desired nonlinear effect.

In the following paragraph, I focus on third-order nonlinear phenomena in silicon WGs. There are a multitude of processes, all described in various reviews [56, 57, 58] and textbooks [54, 55]. Therefore, the description here is limited to presenting the basic concepts behind nonlinear optical processes, in order to define the key quantities that are usually optimized when designing efficient silicon-based nonlinear WGs. Particular attention is given to Four-Wave Mixing (FWM), Two-Photon Absorption (TPA), and Free Carrier Dispersion (FCD), as they are directly employed/experienced in the research works presented in this thesis.

### Third-order processes in silicon waveguides

Silicon-based integrated waveguides exhibit strong nonlinearities that can be used to generate and process optical signals. Even if other materials, such as AlGaAs and other III−V semiconductors, show much higher nonlinear coefficients [59], the CMOS compatibility of silicon photonics motivates the use of third-order nonlinear phenomena on this platform. The polarization $\boldsymbol{P}$ induced by an electric field $\boldsymbol{E}$ is:

$$P_i^{(3)} = \epsilon_0 \sum_{jkl} \chi_{ijkl}^{(3)} E_j E_k E_l \,, \tag{1.8}$$

where I have re-written the third term of Equation 1.7 hiding the *time* dependence and making explicit the tensor nature of the equation. The indices *i, j, k, l* representing the components along a generic axis, can assume the value 1, 2 or 3,

indicating the component respectively along axis $x$, $y$ and $z$. By including the induced polarizations in the wave equation given above (Equation 1.2), the perturbed fields travelling inside the WG can be written as:

$$\begin{aligned} \boldsymbol{E}(\boldsymbol{r},\omega) &\simeq \mathscr{E}(x,y,\omega)\,\mathscr{E}(z,\omega)\,, \\ \boldsymbol{H}(\boldsymbol{r},\omega) &\simeq \mathscr{H}(x,y,\omega)\,\mathscr{H}(z,\omega)\,. \end{aligned} \tag{1.9}$$

It holds under the assumptions that the waveguide modes $\mathscr{E}(x,y,\omega)$ are not affected (slowly varying envelope approximation), and that the induced polarization is regarded as a *small perturbation* producing a modulation in the propagation direction $\mathscr{E}(z,\omega)$ [60].

The polarization induced by the $\chi^{(3)}$ terms, as reported in Equation 1.8, involves four fields. Let's start the description from the simplest case, the third-order nonlinear effects induced by a *monochromatic* beam, i.e. the nonlinear contribution to the polarization at the same frequency as that of the incident field. Given a material with susceptibility $\chi^{(3)}$ to which a beam $E(t)$ is applied, the term of polarization in Equation 1.8 becomes $P^{(3)}(t) = \epsilon_0 \chi^{(3)}\, E(t)^3$. The two possible effects caused by three identical fields are the third harmonic generation (THG) and the Kerr effect.

In the former process, destroying three photons at frequency $\omega$, one photon at $3\omega$ is created. The feasibility of the process is limited by momentum conservation, and thus by the chromatic dispersion of the nanostructured WG, similarly to what will be outlined in further detail for the FWM process in section 1.1.2.

The latter describes how the real part of the refractive index $n$ of the material changes by applying an external electric field with intensity $I$. In particular, the equations governing the Kerr effect are:

$$\Delta n = n_2\, I\,, \quad n_2 = \frac{3\, Re(\chi^{(3)}_{eff})}{4\,\epsilon_0\, c\, n^2} \tag{1.10}$$

The index change induces phase effects, affecting the propagation of the optical beam. As a consequence, self-phase modulation (SPM) and cross-phase modulation (XPM) arise. In the expression of the *Kerr coefficient* $n_2$, we have introduced an *effective* susceptibility $\chi^{(3)}_{eff}$, due to the anisotropic optical nonlinearity of silicon. In particular, it depends on the independent terms of the susceptibility tensor [61], and reduces to $\chi^{(3)}_{eff} = \chi^{(3)}_{1111}$. In silicon, the values reported in the literature for the Kerr coefficient vary greatly, as pointed out in the review [62]. The value usually taken as reference at telecommunication wavelength is the one measured in bulk silicon, close to $4.5 \pm 1.5 \cdot 10^{-14}\, cm^2/W$ [63, 64].

When multiple optical frequencies copropagate inside an SOI waveguide simultaneously, i.e. the implied fields have different frequencies, the situation becomes more complicated. This is the case of FWM, a four–photon elastic scattering process originating from the third–order nonlinearity. Here, we take into account some approximations to simplify its theoretical description, following [65, 66]; a more complete treatment can be found in [60, 56]. Specifically:

- The case of degenerate FWM between fields with the same polarization is considered, so only three waves are involved: the *pump*, the *idler* (higher energy) and the *signal* (lower energy). These must satisfy the energy conservation law $2\,\omega_P = \omega_I + \omega_S$;
- Phonon contributions are neglected and only the electronic part of the third-order susceptibility is considered (Eq. 99 of [60]);
- Only a continuous-wave (CW) pump is considered, with limited power (on the order of a few $mW$), as is typically the case in practical silicon photonic experiments. Consequently, in intrinsic Si WGs, free-carrier and TPA effects are marginal (see the next paragraph for a more detailed description) and are neglected in the following equations;
- The pump is assumed to be much more intense than the generated beams, therefore SPM and XPM induced by the idler and the signal are neglected. The *undepleted pump* approximation [67] is adopted, i.e. the number of pump photons remains effectively constant along propagation.

As a result, the complex amplitudes of the three electric fields along the propagation direction $z$ can be written as [60]:

$$\begin{aligned}
\frac{d\mathscr{E}_P(z)}{dz} &= -\alpha_P/2\,\mathscr{E}_P(z) + i\,\gamma_P\,\mathscr{P}_P\,\mathscr{E}_P(z)\,,\\
\frac{d\mathscr{E}_S(z)}{dz} &= -\alpha_S/2\,\mathscr{E}_S(z) + 2i\,\gamma_{SP}\,\mathscr{P}_P\,\mathscr{E}_S(z) + i\,\gamma_{SPIP}\,\mathscr{E}_P^2\,\mathscr{E}_I^\star(z)e^{-i\Delta\beta z}\,,\\
\frac{d\mathscr{E}_I(z)}{dz} &= -\alpha_I/2\,\mathscr{E}_I(z) + 2i\,\gamma_{IP}\,\mathscr{P}_P\,\mathscr{E}_I(z) + i\,\gamma_{IPSP}\,\mathscr{E}_P^2\,\mathscr{E}_S^\star(z)e^{-i\Delta\beta z}\,.
\end{aligned} \tag{1.11}$$

The following quantities have been defined: $\mathscr{P}_P = |\mathscr{E}_P(z)|^2$, which is proportional to the pump power in the WG [56][3], while $\mathscr{E}_j(z)$ is the complex mode amplitude at

[3] The total optical power carried by the perturbed field at frequency $\omega_P$, i.e. the pump while the nonlinear interaction is occurring, is $\mathcal{P}_P = \mathcal{P}_{P0}\,\mathscr{P}_P(z,\omega_P)$, where $\mathcal{P}_{P0}$ is the power of the unperturbed electromagnetic pump field, i.e. in the absence of nonlinear interactions.

position $z$ and frequency $\omega_j$, according to the definition in Equation 1.9. Notice that, in the last term, the term is $\mathscr{E}_P^2$, meaning the square of the pump field amplitude, i.e. the pump phase explicitly enters this term. $\gamma_{ijkl}$ is the *nonlinear parameter*, which quantifies the strength of the interaction among the fields involved in the process (see next paragraph for a more detailed definition). The phase mismatch $\Delta\beta = \beta_S + \beta_I - 2\beta_P$ has also been introduced.

In the group of equations 1.11, looking at the elements in the right-hand side, one can recognize, from left to right: the contribution of optical losses, the contribution of XPM and SPM due to the more intense pump field, and finally the FWM term. In the next paragraph, I will focus on the FWM term and the related fundamental nonlinear properties specifically for the here considered SOI WGs.

### Four Wave Mixing

The $4th$ term in Equation 1.11 describes the degenerate Four Wave Mixing effect. It is responsible for a contribution to the signal and idler fields coming respectively from the pump–idler and pump–signal energy exchanges. The SPM and XPM contributions are now neglected in order to focus on a more detailed description of the FWM properties.

**Nonlinear parameter in FWM process** The rigorous definition of the third-order nonlinear parameter, specifically for the FWM process, is reported here. From the study of the effect of dispersion on the optical pulses circulating in the WG, the following general expression is derived [58]:

$$\gamma_{ijkl} = \frac{3\,\omega_i\,\sqrt{n_{g,i}\,n_{g,j}\,n_{g,k}\,n_{g,l}}}{4\,\epsilon_0\,A_0\,c^2}\,\Gamma_{ijkl}\,, \tag{1.12}$$

where $A_0$ is the WG cross–section, $n_{g,i(jorkorl)}$ is the group index of the modes participating in the nonlinear process $(i,j,k,l)$, and $\Gamma_{ijkl}$ is the *effective* nonlinear susceptibility, i.e. the weighted integral of the $\boldsymbol{\chi^{(3)}}$ tensor over the four modes.

A simplified expression for these quantities can be obtained by considering the following three conditions: the degenerate FWM case, idler and signal generated in the same mode in which the pump light propagates, and idler and signal wavelengths

*close* to the pump one $\lambda_P$. The result is reported below:

$$\gamma_{IPSP} = \gamma_{SPIP} \stackrel{\text{def}}{=} \gamma^{(SOI)} = \frac{3\,\omega_P\, n_{g,P}^2}{4\,\epsilon_0\, A_0\, c^2}\,\Gamma^{(SOI)}\,, \tag{1.13}$$

$$\Gamma^{(SOI)} = \frac{A_0 \int_{core} \mathscr{E}^{\star}(x,y)\,\boldsymbol{\chi^{(3)}}\,\mathscr{E}(x,y)\,\mathscr{E}^{\star}(x,y)\,\mathscr{E}(x,y)\,dx\,dy}{\left(\int n^2(x,y)\,|\mathscr{E}(x,y)|^2\,dx\,dy\right)^2}\,. \tag{1.14}$$

The effective susceptibility can thus be calculated for the pump mode only, since $\omega_P \simeq \omega_I \simeq \omega_S$ and $\mathscr{E}(x,y,\omega_P) \simeq \mathscr{E}(x,y,\omega_I) \simeq \mathscr{E}(x,y,\omega_S)$ have been assumed. The numerator represents the nonlinear overlap, i.e. the integral of the optical mode over the nonlinear medium cross–section (only the WG *core* region). The contribution of the surrounding $SiO_2$ can be neglected, since its third-order nonlinearity is much smaller ($\sim 10^{-3}$ lower).

It should be noted that the resulting nonlinear coefficient strongly depends on the considered pump frequency and on the WG geometry, via the integral over $A_0$ and, above all, through the group index of the propagating pump mode $n_{g,P}$. In the more general case, the overlap integral between the different propagating modes must be considered.

It is also worth mentioning that in the literature [60, 57] another definition is often reported, directly coming from the more standardized fiber optics field [68, 67]:

$$\gamma^{(F)} = \frac{2\pi\, n_2}{\lambda\, A_{eff}}\,, \quad A_{eff}^{(F)} = \frac{\left(\int |\mathscr{E}(x,y)|^2\,dx\,dy\right)^2}{\int_{core} |\mathscr{E}(x,y)|^4\,dx\,dy}\,. \tag{1.15}$$

Here, the *effective mode area* ($[m^2]$) is defined from the electric field distribution at the WG cross–section.

Comparing equations 1.14 and 1.15, describing the nonlinear parameters for SOI and optical fibers, respectively, reveals a key conceptual difference. The SOI expression reduces to the well–known fiber expression only if the group index is close to unity, an assumption that typically holds for the weak dispersion of optical fibers. In practice, the strong dispersion of silicon WGs, caused by the high optical confinement in high–index contrast nanostructures, is essentially neglected in the fiber formulation. Due to its compact form and its dependence solely on the cross–section and the modal electric field distribution, the nonlinear coefficient $\gamma^{(F)}$ is frequently adopted in the literature for silicon waveguides, even though the definition of $\gamma^{(SOI)}$ is physically more accurate given that $n_g/n$, i.e. the ratio of the mode group index to the refractive index of the material, is significantly larger than unity. A detailed

quantitative comparison between these two formulations is provided in Appendix section A.2.

In this work, the expression introduced for the fiber optics case will be adopted. Beyond aligning with standard literature conventions and enabling direct comparison with published works, this choice is justified by a pragmatic consideration: any theoretical definition of the nonlinear parameter serves as a simplified model parameter rather than an exact, deterministic predictor of real–world nonlinear efficiency. In experimental implementations, such as SFWM–based sources of photon pairs, the overall performance is governed by several practical factors, including linear propagation losses, two–photon absorption, free–carrier absorption, dispersion engineering, and fiber–to–chip coupling efficiency. Consequently, a highly refined theoretical estimation of $\gamma$ alone does not directly yield an exact prediction of the measured nonlinear response. I will thus adopt the simplified formulation. In the following, the notation will be simplified to $\gamma$ and $A_{\text{eff}}$ and will refer to the fiber optics case. Since $\gamma \propto \frac{1}{A_{\text{eff}}}$, a smaller effective area directly corresponds to stronger light confinement and enhanced nonlinear interaction strength. This renders $A_{\text{eff}}$ a convenient and robust figure of merit for comparing different WG cross–sections and spatial modes in terms of their capacity to enhance nonlinear phenomena such as FWM.

**Efficiency of the FWM process** The treatment reported above refers to the stimulated FWM case, where a signal wave is injected together with the pump and an idler is generated. The symmetric situation can also occur, without any difference in the derivation. Under the undepleted-pump and small-signal approximations, and in the limit of negligible loss, the degenerate FWM conversion efficiency can be written as

$$\eta_{FWM} \overset{\text{def}}{=} \frac{\mathcal{P}_I(L)}{\mathcal{P}_S(0)} = \left(\gamma\, \mathcal{P}_P(0)\, L e^{-\tilde{\alpha} L}\right)^2 \operatorname{sinc}^2\left(\frac{\Delta\beta\, L}{2}\right), \tag{1.16}$$

where $\mathcal{P}_P(0) = \mathcal{P}_{P0}\, \mathcal{P}_P(0)$ and $\mathcal{P}_S(0) = \mathcal{P}_{S0}\, \mathcal{P}_S(0)$ are the pump power ($P$) and the signal power ($S$) at $z = 0$ (cf. footnote 3), $\gamma$ is the nonlinear coefficient, $L$ is the physical waveguide length, $\Delta\beta$ is the phase mismatch above defined, and $\tilde{\alpha}$ represents the propagation loss of the interacting waves, assumed equal for all three interacting wavelengths.

Clearly, the efficiency is maximized when $\Delta\beta = 0$ (*perfect phase matching* condition), i.e. $2\,\omega_P\, n_{eff}(\omega_P) - \omega_S\, n_{eff}(\omega_S) - \omega_I\, n_{eff}(\omega_I) = 0$ in the approxima-

tion in which the SPM and XPM contributions are neglected (the nonlinear phase-mismatch term is negligible for typical pump powers $< 100\,\mathrm{mW}$ [69]).

For symmetric detuning around the pump $\Delta\omega = \omega_S - \omega_P = \omega_P - \omega_I$, expanding the phase mismatch parameter as a Taylor series yields $\Delta\beta \simeq \beta_2\,\Delta\omega^2$ (stopping at second order). From this, the approximated expression for the *bandwidth* of the FWM process is usually derived as:

$$BW \simeq \sqrt{\frac{\Delta\beta_{max}}{\beta_2}} = \sqrt{\frac{4\pi}{|\beta_2|\cdot L}} \propto \sqrt{\frac{1}{|\mathcal{D}|\cdot L}}\,. \tag{1.17}$$

Longer devices yield a narrower bandwidth, while engineering the waveguide dispersion to approach $\beta_2 \simeq 0$ at the pump wavelength enables broadband FWM.

In the limit of perfect phase matching, the generated idler power increases quadratically with the pump power and linearly with the signal power:

$$\mathcal{P}_I(L)_{FWM} = \mathcal{P}_S(0)\big(\gamma\,\mathcal{P}_P(0)\,L\big)^2\,. \tag{1.18}$$

***Spontaneous* FWM process** As can be seen from Equation 1.11, the FWM process is *stimulated* by the presence of a signal beam. However, even in the absence of a signal field, one pair of signal and idler photons can be generated spontaneously from two photons of the pump, i.e. stimulated by random vacuum fluctuations. This process is called *spontaneous* FWM (SFWM) and is the basis for the generation of correlated photon pairs in silicon waveguides.

The theoretical description of SFWM is more complex than that of stimulated FWM and goes beyond the scope of this thesis manuscript (see [70, 71, 72]). In the stimulated case, the generation of a fixed idler frequency occurs, determined univocally by the signal and pump frequencies. In the spontaneous case, instead, the generation of a broadband spectrum of signal and idler photon pairs is possible, provided that they satisfy the energy conservation law $2\omega_P = \omega_S + \omega_I$ and the phase–matching condition. Given the bandwidth $\mathcal{T}^{-1}$ of the process, which depends on the material dispersion and on the filtering applied to the total SFWM spectrum, and in the limit of perfect phase matching, the role of the signal seed field is played by $\hbar\omega_P/\mathcal{T}$. Thus, again under the undepleted–pump approximation and assuming low conversion efficiency (i.e. the probability of generating more than one photon pair is negligible), the average power of the generated idler and signal photons is

$$\mathcal{P}_{I,S}(L)_{SFWM} = \frac{\hbar\omega_P}{\mathcal{T}}\big(\gamma\,\mathcal{P}_P(0)\,L\big)^2\,. \tag{1.19}$$

### Two Photon Absorption

Among the third-order nonlinear interactions, it is worth looking more closely at one non-parametric process: TPA. Given (in the general case) a polychromatic beam with frequencies such that $\hbar\omega_1 + \hbar\omega_2 > E_g$, where $E_g \simeq 1.12\,\text{eV}$ is the energy band gap in Si, the simultaneous absorption of two photons may occur, assisted by phonons. It produces an electron–hole pair (*free carriers*) across the valence and conduction bands of the semiconductor. Of course, the process can also be *degenerate*; thus, two photons from the same pump laser at frequency $\omega_P$ are absorbed; from now on, this case is considered for simplicity.

The density of electron–hole pairs, $N$, evolves in the presence of a time-varying optical intensity $I(t)$ as described by the following equation [73]:

$$\frac{dN(t)}{dt} = \frac{\beta_{TPA}}{2\,\hbar\omega_P}\, I^2(t) - \frac{N(t)}{\tau_{FC}}\,. \tag{1.20}$$

$\beta_{TPA}$ is the so-called TPA coefficient, and it is directly linked to the imaginary part of the (*effective*) third-order susceptibility tensor via:

$$\beta_{TPA} = \frac{3\,\omega_P\,\mathcal{I}(\chi^{(3)}_{eff})}{2\,\epsilon_0\,c^2\,n^2}\,. \tag{1.21}$$

Its measured value, reported in the literature for wavelengths around 1550 nm, ranges from 0.4 to 0.9 cm/GW [74, 64], relatively small compared to III−V semiconductors.

By looking at Equation 1.20, we can identify a first term on the right–hand side. Because the excitation process is nearly instantaneous (10 fs [60]), this term describes the generation of free carriers as directly proportional to the square of the injected optical beam intensity. The second term is responsible for the *slower* decrease in the number of electron–hole pairs due to their recombination. This process is characterized by the FC lifetime $\tau_{FC}$, which is of the order of 100 ns in bulk silicon, but is considered shorter in nanostructured WGs. In practice, the Si–$SiO_2$ interfaces are populated by interface defect states, giving rise to surface recombination. Values ranging between 10 and 200 ns are reported in the litterature [74, 75], confirmed also by measurements performed within this research work (see Figure 1.3).

The produced charges are responsible for other processes: free–carrier absorption (FCA) and free-carrier dispersion (FCD, often called plasma dispersion PD).

In addition, since silicon is an indirect band–gap semiconductor, the process is phonon–assisted, thus heat is produced, which changes the refractive index through the thermo-optic effect (TOE). These effects are of fundamental importance in the field of phase and intensity modulation in silicon WGs; they are therefore briefly described in the next paragraphs.

FCD and the TOE have been largely used as the physical mechanisms to modify the optical properties of photonic components. For resonant devices, such as photonic crystals, microdisks, or microrings, the two effects respectively produce a blue and a red shift in the resonance wavelength, characterized by different time scales. Of particular interest is the regime of optical bistability [76, 77, 78], which enables switching [79, 80, 81], logic-gate [82] and memory [83, 84] operations. For other applications, such as the generation of light through parametric nonlinear effects in which high power is employed, optical bistability represents in most cases a detrimental effect. As a matter of fact, the change in the refractive index modifies the resonance condition and introduces deformation of the resonance shape itself [85].

**Free Carrier Absorption**

Electrons in the conduction band, which may be present due to two-photon absorption or due to doping of the silicon WG, have access to a continuum of energy states. As a result, they contribute to the absorption of light over a broad frequency spectrum, thus in the presence of other nonlinear phenomena such as FWM, the pump, idler, and signal components would all be affected. Therefore, FCA often introduces undesired losses in photonic WGs.

As an example, the effect of TPA–induced FCA in a silicon WG under a pump–probe experiment is reported here. A CW probe laser is transmitted through a 1 cm WG; in the same WG, a short bright optical pulse is also injected, at a wavelength around 1550 nm but far enough from the CW wavelength to ensure off-chip separation of the CW and pulsed lasers. The CW power measured with a high-speed photodiode is reported in Figure 1.3, featuring a clear dip corresponding to the time instant at which the pulse copropagates inside the WG. This dip is due to the presence of free carriers in the WG, generated by TPA of the pump photons. Because they are out of equilibrium, these free carriers immediately start recombining; thus, the reference transmitted power is recovered after the typical exponential decay. The FC lifetime is extracted through the exponential fit (pink line) as $\tau_{FC} = 11.1 \pm 0.3$ ns.

Finally, once the electrons relax to the bottom of the conduction band, additional heat is generated, which changes the refractive index through the TOE (see section 1.1.2).

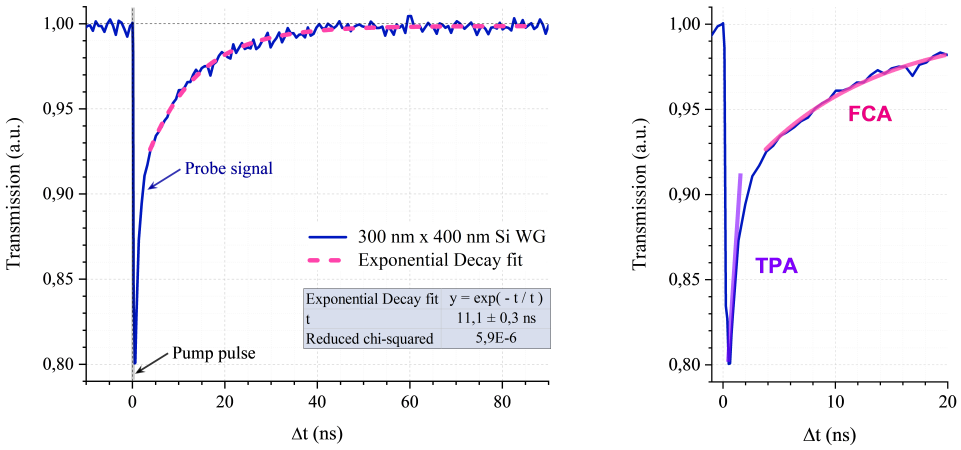



*Figure 1.3:* ***TPA–induced FCA.*** *Experimental characterization of TPA–induced FCA obtained through a pump–probe experiment, pumping with a femtosecond laser (*10 *MHz repetition rate at* 1560 *nm) and probing with a continuous–wave laser at* 1550 *nm. The sample under test is a* 1 *cm-long straight waveguide with a strip cross–section of* $300 \times 400$ $nm^2$*. The x-axis shows the time delay between the arrival of the pump pulse at the waveguide input and the measured CW probe transmission at the output. The dip in transmitted power is caused by free carriers generated via two–photon absorption of the pump photons. The pink solid line represents an exponential fit to the power recovery, from which the free–carrier lifetime is extracted.*

### Free Carrier Dispersion

As stated before, a change in free-carrier concentration produces both a change in the material refractive index and in the absorption coefficient. In particular, the free-carrier dispersion effect arises because the present free carriers interact with the travelling electromagnetic waves, effectively producing an oscillation of the free carriers themselves that follows the optical wave and, at the same time, affects the wave propagation [60].

This effect, known since the first studies on integrated photonics thanks to the work of R. A. Soref and B. R. Bennett in 1987 [86, 87], produces a change in both the real and the imaginary parts of the refractive index, which depend on the local density of electrons and holes. In Ref. [87], they report the empirical expressions of the variation of the absorption coefficient $\tilde{\alpha}$ and of the real part of the refractive index $n$ in silicon, due to injection or depletion of charges. At the wavelength of

interest $\lambda = 1550\,\text{nm}$, the equations are:

$$\begin{aligned} \Delta\tilde{\alpha}(N_e, N_h) &= 8.5 \cdot 10^{-18}\, N_e \,+\, 6.0 \cdot 10^{-18}\, N_h \\ \Delta n(N_e, N_h) &= -8.8 \cdot 10^{-22}\, N_e \,-\, 8.5 \cdot 10^{-18}\, N_h^{0.8}\,, \end{aligned} \tag{1.22}$$

where $N_e$ and $N_h$ are the concentrations of electrons and holes in the considered region in $\text{cm}^{-3}$; notice that here $\Delta\tilde{\alpha}$ is in $\text{cm}^{-1}$. Therefore, the presence of FCs produces a decrease in the refractive index (*blue*-shift) and is always associated with amplitude modulation (increase of the absorption coefficient), both proportional to the density of free carriers.

This effect can be further enhanced and engineered by applying voltages across doped Si regions, thus obtaining a variation of charge concentration inside the region where the voltage-driven current flows. Furthermore, since the FCD is caused by the interplay between the electromagnetic wave and the charges, in an integrated structure the magnitude of the effect is governed by the overlap between the optical mode and the profile of the charge variation. In a WG, the propagation loss and the effective index become [88]:

$$\begin{aligned} \alpha_{WG}(V) &= \tilde{\alpha}_{WG} + \Delta\alpha_{WG}(N_e, N_h) + \Delta\alpha_{WG}(V) \\ n_{eff}(V) &= n_{eff} + \Delta n_{eff}(N_e, N_h) + \Delta n_{eff}(V)\,, \end{aligned} \tag{1.23}$$

where $\tilde{\alpha}_{WG}$ ($\text{cm}^{-1}$) and $n_{eff}$ are the respective quantities in the intrinsic WG, i.e., in the absence of applied voltage and charges.

Finally, FCD is the method of choice in Si to produce conventional silicon optical modulators and variable optical attenuators (VOAs) [89]. Electrical carrier injection/depletion is employed in integrated p-n/p-i-n junctions [90, 91] for high-speed optical signal processing, but also in less common applications [92]. More details on those devices are reported in subsection 1.8.2. FCD generated through photo-excitation has also been reported in other photonic structures, such as photonic crystals [81], microdisks [93], and microring resonators [94, 79].

#### Thermo-Optic Effect

The thermo-optic effect finds its origin in the displacements of the atomic nuclei in the presence of thermal energy stored in the crystal. The polarization that arises from it produces an overall increase in the refractive index of the medium, governed

by the thermo-optic coefficient.

Silicon has a large thermo-optic coefficient, which allows tuning its optical response by inducing a local change in the temperature $T$. At 1550 nm it is around three times higher than the one measured in those materials where it has been historically exploited, precisely $\frac{dn}{dT} = 1.86 \cdot 10^{-4}\,\mathrm{K}^{-1}$ [95].

This TOE is the one used in classical CMOS-compatible phase shifters, the *heaters*. More details on those components are reported in subsection 1.8.1.

## 1.2 Waveguide simulation

A good photonic design always begins with WG simulations. As noted earlier, the supported optical modes propagate without changing shape along the optical wire, with associated parameters such as effective index, group velocity ($v_g = c/n_g$), dispersion, and propagation loss. Depending on the application and the role of a given component within the photonic circuit, one parameter may be more critical than the others, so a *single* cross–section choice is not always feasible. Moreover, in some applications multiple wavelengths and/or modes can be accommodated within the same WG, such as in intermodal SFWM [96], where the cross–section must be engineered to support higher-order modes. In this work, the fundamental mode at telecommunication wavelength is chosen to propagate the pump and the generated photons throughout the circuits. Therefore, all the following simulations will be focused on this mode and wavelength range.

A fixed parameter is the Si slab thickness, determined by the SOI wafer used in fabrication: Si300nm and Si220nm in this work. An eigenmode solver is used to extract the mode field distribution and its properties in the studied WG cross–section. I used the Finite–Difference Eigenmode (FDE) method implemented in the Lumerical MODE software [97], solving Maxwell's equations in the frequency domain on a meshed WG cross–section, providing a solution for a single optical frequency. Examples of the obtained electric field distribution for the $TE_{00}$ mode of strip and rib Si300nm WGs are shown in Figure 1.2. In addition, integrated frequency sweeps enable the calculation of group velocity and dispersion.

Regarding the rib geometry, the thickness ($th$) and partial etching depth ($D$, Figure 1.2) are fixed by the technology process: $D = 110\,\mathrm{nm}$ for Si220nm and $D = 150\,\mathrm{nm}$ for Si300nm. The slab width is set to $slab_w = 3\,\mu\mathrm{m}$, which is compatible with both the platforms presented here. Therefore, the WG geometry optimization presented below focuses on varying the waveguide width $WG_w$.

The effective indices at our operating wavelength $\lambda = 1550$ nm have been extracted for both rib and strip WGs, for the two slab thicknesses mentioned above, and are reported in Figure 1.4.

As pointed out in section 1.1.2, the effective area $A_{eff}$ is widely exploited in

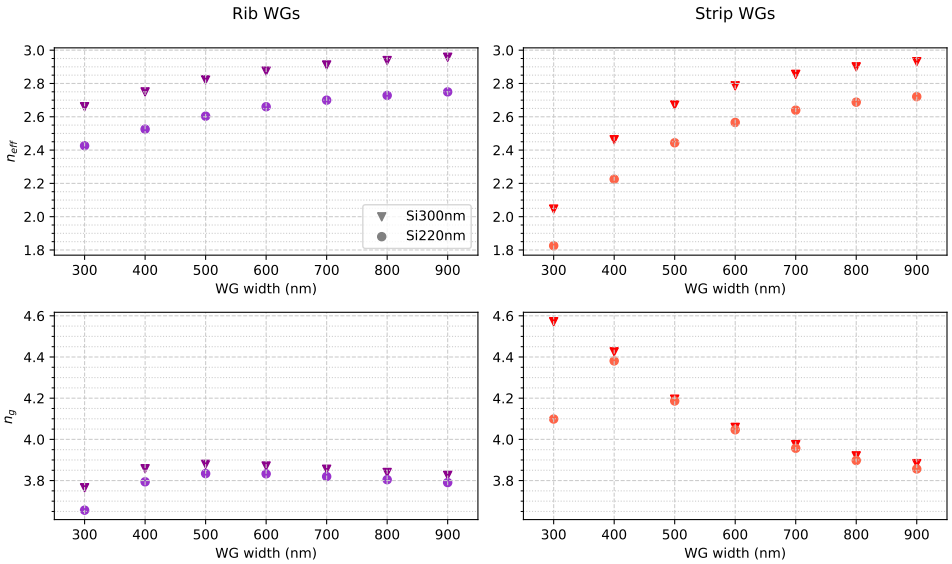



*Figure 1.4:* ***SOI WG FDE simulation at*** $\lambda = 1550$ ***nm.*** *Extracted effective index and group index of the* $TE_{00}$ *mode of strip and rib WG, as a function of* $WG_w$.

both fiber and integrated photonics studies as a metric for nonlinear performance. Its values are reported in Figure 1.5. In the lower panel, the resulting $\gamma$ is shown, calculated from Equation 1.15. As discussed above, the estimations for the coefficient $n_2$ in silicon vary greatly. Considering the value of $4.5 \cdot 10^{-14}\, cm^2/W$ [63, 64] measured in bulk silicon, together with the more recent of $6 \cdot 10^{-14}\, cm^2/W$, coming from studies on nonlinear effects in SOI WGs (in particular SM Si220nm WG, with $WG_w = 500$nm) [98], the value used here is $n_2 = (4.5 \pm 1.5) \cdot 10^{-14}\, cm^2/W$, following Ref. [57]. Therefore, in the plot the points correspond to the central value of $n_2$, while the shaded region behind indicates the uncertainty in the $\gamma$ value, coming from the error of $n_2$.

The effective index and the group index are also used to calculate the dispersion of the WG; an example is reported in Figure 1.6 (for the platform Si300nm, see Appendix A, Figure A.1). As pointed out in section 1.1.2, dispersion influences

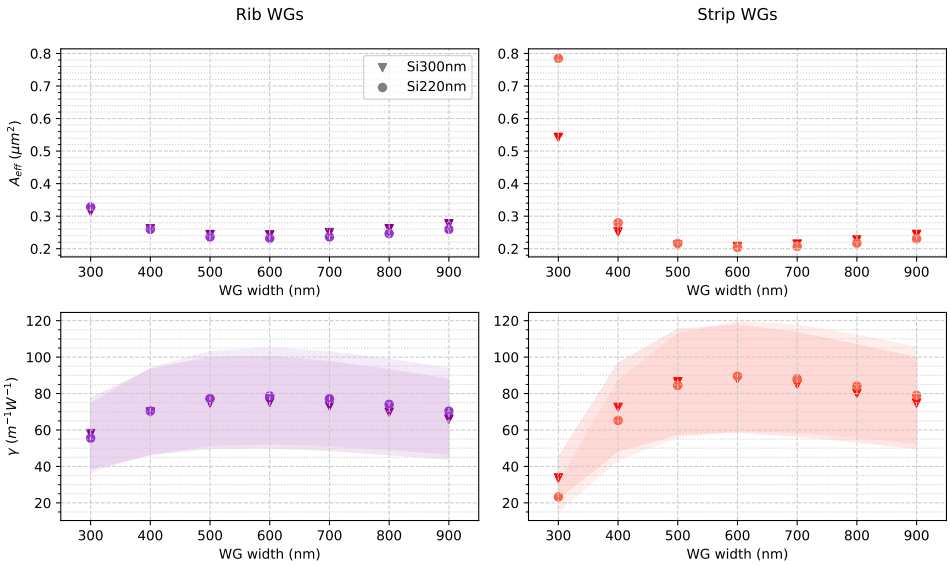



*Figure 1.5:* ***Calculated effective area and nonlinear parameter at*** $\lambda = 1550\,$***nm.*** *The reported values are calculated using Equation 1.15, here reported for the fundamental* $TE_{00}$ *mode of strip and rib WG, as a function of* $WG_w$*.*

the efficiency of nonlinear processes such as FWM. Ideally $\mathcal{D}$ should be as close as possible to zero in order to prevent phase mismatch between the wavelengths involved in the generation process. Moreover, the smaller the dispersion, the larger the bandwidth; thus idler and signal can be generated farther away from the pump.

The value of the dispersion at 1550 nm of the $220 \times 600\,\mathrm{nm}^2$ WG is very close to zero, confirming that among the standard cross-sections that can be considered, it is the most suitable for the FWM process. All the indices of this WG geometry are summarized in Table 1.1.

| Indices for strip WG $220 \times 600\,\mathrm{nm}^2$ at 1.55 $\mu$m | |
|---|---|
| $n_{eff}$ | 2.56 |
| $n_g$ | 4.05 |
| $\mathcal{D}$ (ps/nm/km) | 83 |
| $A_{eff}$ ($\mu$m$^2$) | 0.20 |
| $\gamma$ (m$^{-1}$W$^{-1}$) | 90±30 |

*Table 1.1: WG simulations: indices of the fundamental mode of our Si waveguide* 220×600 *nm, extracted from Figure 1.6.*

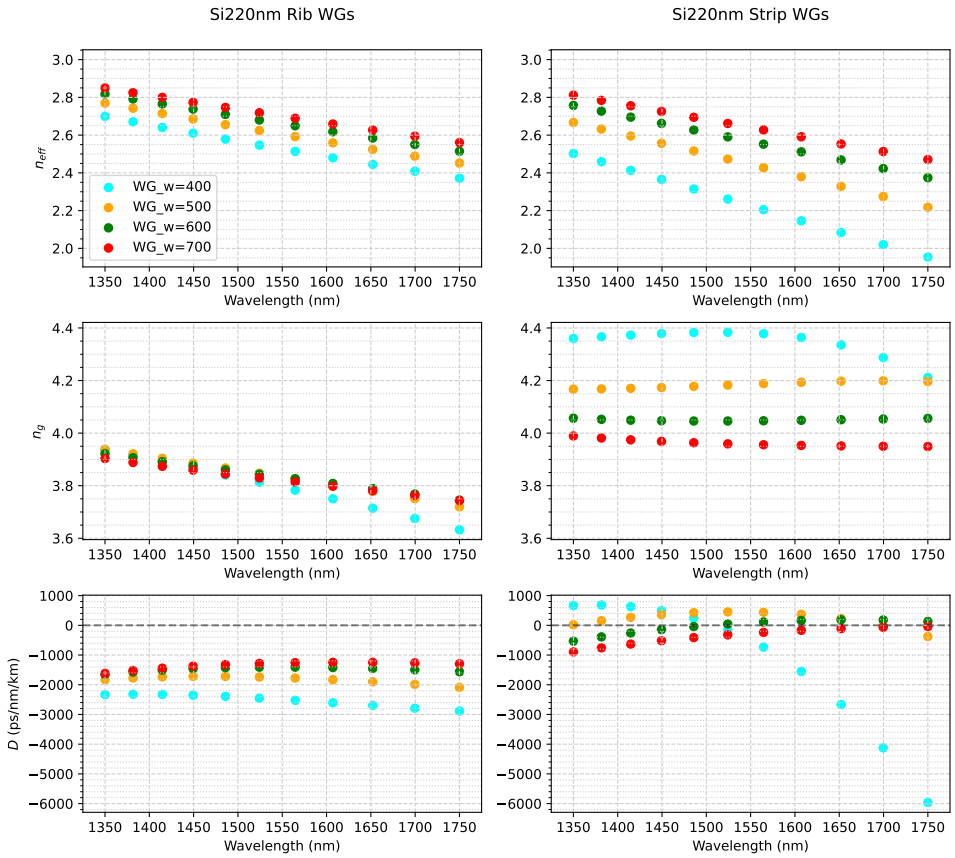



*Figure 1.6:* ***WG dispersion simulations.*** *Extracted WG indices as a function of the wavelength for the fundamental $TE_{00}$ mode of strip and rib WG for the platform Si220nm, as a function of $WG_w$.*

Finally, more sophisticated WG geometries can in principle be considered to obtain higher mode confinement (higher $\gamma$) and/or engineered dispersion for a large variety of applications. For example, the etching depth and the sidewall angle could be optimized [69], or more sophisticated sub-wavelength structures could be explored [99]. However, all these solutions are more subject to fabrication variability and/or are not suitable for large-scale production using CMOS-compatible techniques.

## 1.3 The ring resonator

Microring resonators (MRRs) are compact, wavelength-selective devices that play a central role in silicon photonics. They are employed as filters [100, 101], multiplexers/demultiplexers [102], modulators [91], and, thanks to their resonant field buildup, as platforms for enhancing nonlinear interactions [103]. Their small footprint and high quality factor ($Q$) make them indispensable in integrated photonic circuits. In this work, ring resonators are used both as filters and as nonlinear enhancement cavities for FWM.

### 1.3.1 Coupling formalism

The fundamental building block of a ring resonator is the coupler, where two side waveguides exchange power through evanescent interaction. The coupling structures are many: point couplers, directional couplers (two parallel straight WGs, see section 1.5), pulley couplers (arc of a circular WG), or even Mach–Zehnder interferometers, which offer a certain level of tunability by acting on the phase shifter in one of the two arms (see section 1.6). As a matter of fact, the amount of light exchanged at the coupler is crucial to match the required performances for any application.

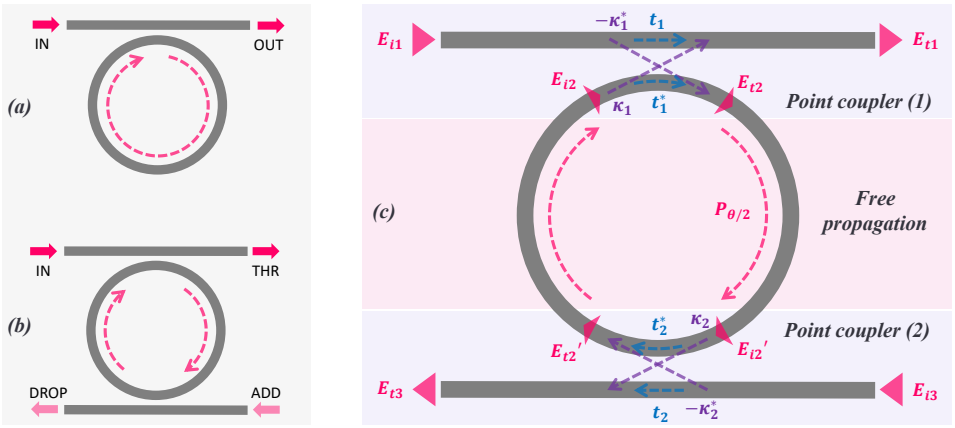



*Figure 1.7:* ***MRR configurations.*** *(a) All-pass and (b) add–drop rings. (c) Description of the field propagation directions and interplay.*

As the simplest and common coupler type, I now consider the point coupler, depicted in Figure 1.7, where the interaction region is assumed to occur only at the

point of minimum distance, i.e., the gap. The input and output fields are related by a unitary matrix, i.e., the coupler *transfer matrix*:

$$\begin{pmatrix} E_{t1} \\ E_{t2} \end{pmatrix} = \begin{pmatrix} t & \kappa \\ -\kappa^* & t^* \end{pmatrix} \begin{pmatrix} E_{i1} \\ E_{i2} \end{pmatrix} \tag{1.24}$$

where $t_i$ and $\kappa_i$ are the bar- and cross-coupling coefficients of the $i$-th coupler, which are real numbers and satisfy $|t_i|^2 + |\kappa_i|^2 = 1$ in the lossless case. Any other coupler geometry featuring the same $t_i$ and $\kappa_i$ will behave as in Equation 1.24. This formalism is the starting point for modeling both all–pass (AP, single bus) and add–drop (AD, double bus) configurations. As a matter of fact, by cascading the transfer matrices of the couplers and the free propagation regions, i.e. semi-circumference for the AD and full circle for the AP, the transmission spectra of the two configurations can be derived, but also more complex structures such as coupled MRRs. In Appendix A (section A.5) a particular structure comprising a pair of identical AD rings with connected drop ports is considered.

### 1.3.2 Resonance condition and transmission spectra

The ring itself is a closed waveguide loop of round-trip length $L_{rt}$. A resonance occurs whenever the optical phase shift per round trip equals an integer multiple of $2\pi$:

$$m\,\lambda_m = n_{eff}\,L_{rt}\,, \qquad m \in \mathbb{Z}\,. \tag{1.25}$$

This condition defines a discrete set of resonant wavelengths $\lambda_m$.

**All–pass (AP).** In the AP geometry, the ring couples to a single bus waveguide. Therefore, an additional constraint for the fields circulating inside the ring is: $E_{i2} = E_{t2} \cdot P_{\theta/2}^2$, where $P_{\theta/2} = e^{i\,\theta(\omega)/2 - \tilde{\alpha}/2\,L_{rt}/2}$ accounts for the accumulated half round-trip phase in the free propagation region (depicted in Figure 1.7), with $\theta(\omega) = n_{eff}(\omega)\frac{\omega}{c} \cdot L_{rt}$. The power transmitted at the out port of Figure 1.7 (a) is:

$$T_{\mathrm{AP}}(\omega) \;=\; \frac{t^2 + a^2 - 2at\cos\big(\theta(\omega)\big)}{1 + a^2t^2 - 2at\cos\big(\theta(\omega)\big)}\,, \tag{1.26}$$

where $a = e^{-\tilde{\alpha}L_{rt}/2}$ accounts for round-trip loss. On resonance, i.e., $\theta(\omega_m) = 2\pi m$, this simplifies to

$$T_{\mathrm{AP}}(\omega_m) \;=\; \frac{(a-t)^2}{(1-at)^2}\,. \tag{1.27}$$

The *critical coupling* condition for the AP geometry is therefore reached when the on-resonance transmission vanishes, i.e., when

$$a = t \qquad \text{(AP critical coupling)}. \tag{1.28}$$

Physically, this means that the intrinsic round-trip loss ($a$) equals the coupling leakage ($t$), so that the directly transmitted field destructively interferes with the field leaking back from the ring, producing a deep transmission null at resonance. This condition simultaneously maximizes the intracavity energy (useful for nonlinear enhancement) and the extinction ratio (useful for filtering).

**Add–drop (AD).** For the AD geometry with two couplers (first coupler characterized in general by $t_1, \kappa_1$ and the second by $t_2, \kappa_2$), the power transmitted from the input (IN) to the through (THR) port of Figure 1.7 (b) is:

$$T_{IN\to THR}(\omega) \;=\; \frac{t_1^2 + a^2 t_2^2 - 2a t_1 t_2 \cos\big(\theta(\omega)\big)}{1 + a^2 t_1^2 t_2^2 - 2a t_1 t_2 \cos\big(\theta(\omega)\big)}\,. \tag{1.29}$$

Similarly, the power transferred from the input to the drop (DROP) port is

$$T_{IN\to DROP}(\omega) \;=\; \frac{\kappa_1^2 \kappa_2^2 a}{1 + a^2 t_1^2 t_2^2 - 2a t_1 t_2 \cos\big(\theta(\omega)\big)}\,, \tag{1.30}$$

which follows from the squared modulus of the corresponding field transfer expression. The *add–drop critical coupling* condition that yields zero through-port transmission (i.e., maximum transfer to the drop port) is therefore

$$a\, t_2 = t_1 \qquad \text{(AD critical coupling)}. \tag{1.31}$$

As a matter of fact, the AD configuration can be treated exactly as the AP one with an additional channel for losses, the second coupler. In the common symmetric limit ($t_1 \simeq t_2$), this condition holds only in the limit where the coupling rates are much higher than the intrinsic losses, i.e., $a \simeq 1$. This ensures efficient dropping of the resonant channel.

In practice, satisfying the critical coupling condition requires accurate knowledge of both the waveguide propagation loss and the point–coupler cross–coupling coefficient ( or coefficients, for the asymmetric AD). Neither can be predicted *a priori* with sufficient accuracy: the former depends on fabrication–specific losses

that are only known after measurement, while the latter is typically affected by a non-negligible mismatch between simulated and fabricated values. For this reason, a Design of Experiments varying the point–coupler gap is always included in the mask, to ensure that the critical coupling condition is reached in at least one of the fabricated devices. See chapter 3 for a practical example of this procedure.

### 1.3.3 Figures of merit

Several figures of merit (FoMs) characterize the performance of a ring resonator. Here I summarize the main FoMs, which will be mentioned multiple times throughout the following design and experimental chapters. For the specific AP and symmetric-AD configurations, all the listed formulas can be further simplified, and simple relationships with the ring and point coupler geometry can be established. All of them are summarized in the Appendix A (section A.3).

**Free Spectral Range (FSR).**

$$\Delta\lambda_{\mathrm{FSR}} = \frac{\lambda^2}{n_g L_{rt}}\,. \tag{1.32}$$

It quantifies the spacing between adjacent resonances. A small FSR enables dense wavelength multiplexing but risks channel crosstalk, while a large FSR provides spectral isolation.

**Quality Factor ($Q$).**

$$Q = \frac{\lambda_m}{\delta\lambda}\,, \tag{1.33}$$

where $\delta\lambda$ is the FWHM linewidth. $Q$ measures spectral selectivity: higher $Q$ means narrower resonances, smaller losses experienced on resonance, longer photon lifetime, and stronger energy storage.

The total $Q$ (or *loaded*) can be decomposed into intrinsic ($Q_i$, or *unloaded*) and coupling ($Q_c$) contributions:

$$Q = \frac{2\pi\, n_g\, L_{rt}}{\lambda\,(\sum_{c=1}^{w}\kappa_c^2 + \tilde{\alpha}L_{rt})} = \left(\frac{1}{Q_i} + \sum_{c=1}^{w}\frac{1}{Q_c}\right)^{-1}\,, \tag{1.34}$$

where $w$ is the number of couplers, $\kappa_c$ the cross-coupling coefficient of the $c$-th coupler, and $\tilde{\alpha}$ the linear propagation loss coefficient.

**Finesse ($\mathcal{F}$).**

$$\mathcal{F} = \frac{\Delta\lambda_{\text{FSR}}}{\delta\lambda}\,. \tag{1.35}$$

The finesse expresses how many distinct resonant cycles can be resolved within the FSR. It is crucial for applications requiring precise wavelength discrimination.

**Visibility ($\mathcal{V}$).**

$$\mathcal{V} = 1 - \frac{T(\theta = 2\pi)}{T(\theta = \pi)}\,, \tag{1.36}$$

which is maximum (equal to 1) when the device is in critical coupling (Eq. 1.28 and 1.31). A high $\mathcal{V}$ is essential for high-performance filtering, switching, and logic operations.

**Field Enhancement (FE).** The intracavity field enhancement factor is calculated as the ratio between the field traveling inside the ring and the input one $FE = \left|\frac{E_{t1}}{E_{i2}}\right|$. It is approximately $\propto \sqrt{Q}$ and is directly relevant for nonlinear optics: it measures the amplification of the interaction between the optical mode and the hosting WG medium.

Furthermore, it can be shown (see [66]) that in the critical coupling condition, FE is directly measurable from the resonance shape, as it can be written as: $FE_{@\lambda_m} = \sqrt{\mathcal{F}/\pi}$. This relation is very useful because it allows estimating the nonlinear enhancement of a MRR just by looking at its transmission spectrum.

### 1.3.4 Nonlinear Enhancement

Inside the ring, nonlinear processes can be largely amplified near resonance frequencies due to constructive interference of the electromagnetic field. The circulating intracavity power is increased by a factor $FE(\omega)^2$ compared to the input. If we assume that the pump and the signal frequencies are each centered on one ring resonance, the stimulated FWM efficiency (cf. Eq. 1.16) becomes [104]:

$$\eta_{FWM}^{\text{MRR}} \;=\; \left(\gamma\,\mathcal{P}_P(0)\,L_{rt}\right)^2 FE(\omega_P)^4\,FE(\omega_S)^2\,FE(\omega_I)^2\,. \tag{1.37}$$

By assuming that the three fields are close enough in wavelength to experience similar enhancement, and furthermore that we are at the center of critically coupled ($c.c.$) resonances, the efficiency simplifies to:

$$\eta_{FWM}^{\text{MRR@c.c.}} \;\simeq\; \left(\gamma\,\mathcal{P}_P(0)\,L_{rt}\right)^2 FE(\omega_P)^8 \;=\; \left(\gamma\,\mathcal{P}_P(0)\,L_{rt}\right)^2 \left(\frac{Q\cdot c}{\pi\nu n_g\,L_{rt}}\right)^4\,. \tag{1.38}$$

This makes MRRs ideal candidates for integrated nonlinear photonics: compared with the simple WG case in Equation 1.16, the process is enhanced by the *eighth* power of the field enhancement.

A similar enhancement also applies to SFWM, where:

$$\mathcal{P}_{I,S\ SFWM}^{\text{MRR@c.c.}} \simeq \left(\gamma\, \mathcal{P}_P(0)\, L_{rt}\right)^2 \left(\frac{Q \cdot c}{\pi \nu n_g\, L_{rt}}\right)^3 \frac{\hbar\omega c}{2 n_g\, L_{rt}}\,. \tag{1.39}$$

which is the average generated power at the signal and idler frequencies coupled to the bus WG, as the coupling is already considered in the $Q$ factor and in the c.c. condition assumed here.

As mentioned previously, SFWM is widely used in silicon MRRs to generate correlated photon pairs for quantum information applications [103, 105]. Being in the single photon-pair regime, the generation rate is more relevant than the generated power. The generation rate $R$ (in pairs per second) can be estimated from the average generated power as $R = \mathcal{P}_{SFWM}^{\text{MRR@c.c.}}/\hbar\omega$.

## 1.4 Ring resonator simulation

As presented in the previous sections, the MRR target performances, measured in terms of the above-listed FoMs, highly depend on the target application. In particular, here I will focus on depicting the optimization needed for a device meant to operate as an efficient nonlinear source. The discussion will be limited to the simplest geometry: a circular microring coupled to the bus WG through point couplers, but as mentioned previously other configurations may be employed.

In the analytical formulation, these FoMs depend essentially on three parameters:

- the resonator length $L_{rt} = 2\pi R$, where $R$ is the radius, which fixes the FSR once the waveguide cross–section (hence $n_{eff}$ and $n_g$) is defined;
- the propagation losses, determined mainly by the quality of the fabrication steps and on the geometry of the materials stack;
- the coupling strength between the bus WG and the ring, expressed by the cross-coupling coefficient $\kappa$.

The first two parameters have been analyzed and derived through simulations in the waveguide design section; I therefore focus here on the modeling of the coupling region.

### 1.4.1 Point coupler simulation

The point coupler between the straight bus and the curved ring waveguide plays a central role in defining the overall performance of the resonator. In practice, the coupling efficiency depends not only on the nominal gap between the two waveguides, but also on the curvature radius of the ring and the modal overlap along the coupling region. For this reason, the effective coupling cannot be estimated analytically with sufficient accuracy, and numerical simulations are required.

Using the commercial software *Lumerical*, the geometry of the point coupler is reproduced (see the schematic in Figure 1.8), and the coupling is modeled by injecting light in the desired mode (here $TE_{00}$) from the input port (IN) and recording the transmitted power in the through port (THR) with the Finite-Difference Time-Domain (FDTD) solver [106]. Thanks to a 2D monitor we have recorded an example of how the amplitude of the electric field propagates through the photonic structure, shown in the right panel.

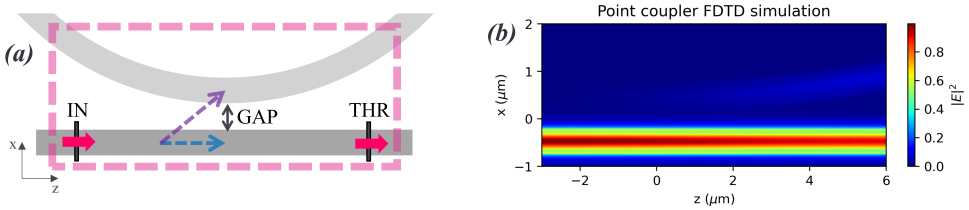



*Figure 1.8:* ***Point coupler simulation.*** *(a) Simulation setup: the input light is injected from the left (IN) and collected at the output of the straight WG (THR). (b) Example of simulated electric field amplitude propagation in the point coupler structure is reported. Precisely, it corresponds to a cross–power of 5% and a bar–power of about 95%.*

In a lossless coupler, the transmission function of the through port is related to the field transmission coefficient $t$ by $T_{THR} = |t|^2$. From the same simulation, the squared cross-coupling coefficient $\kappa^2$ can be extracted from the power transferred to the coupled port, imposing the condition $|t|^2 + |\kappa|^2 = 1$. This quantity depends on the WG cross–section (the more confined the mode, the smaller the cross coupling), on the ring resonator radius $R$ (a larger radius means a larger effective coupling

length), and of course on the gap (the smaller the distance, the larger the coupling). Moreover, $\kappa^2$ can be directly compared with the ring losses $1 - a^2$ (rectangles) to evaluate the critical coupling condition. A typical cross coefficient versus gap obtained from the simulations is shown in Figure 1.9.

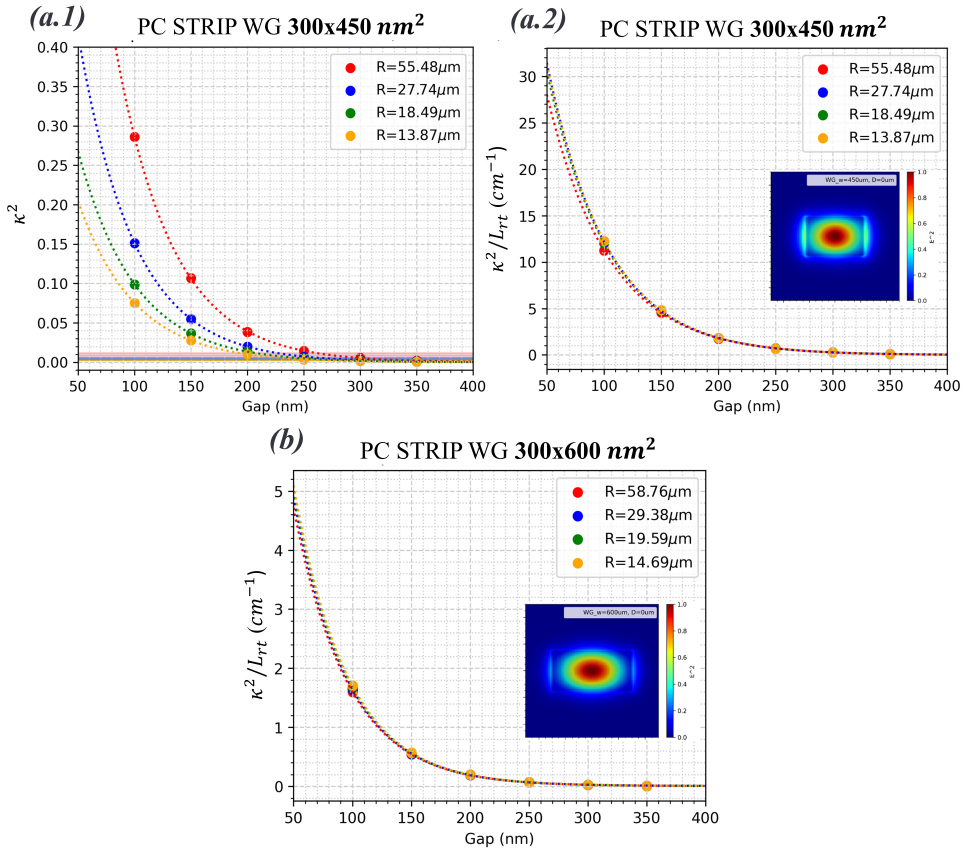



*Figure 1.9:* ***Point coupler simulation results.*** *Cross-coupling and cross coupling per length for different R, gaps, and cross-sections. The points represent the simulated data ($\lambda = 1550\,nm$), and the dotted lines represent exponential decay fits. The colors red, blue, green, and yellow correspond respectively to FSRs of 200, 400, 600, and 800 GHz. In (a), the standard SM Si300nm strip WG $300 \times 450\,\mathrm{nm}^2$ has been considered. The colored rectangles at the bottom of the curves in (a.1) represent the amount of losses experienced per $L_{rt}$ $1 - a^2$ (corresponding to the range 1–1.5 dB/cm). In (b), the coupling per length for a different WG geometry, $300 \times 600\,\mathrm{nm}^2$, is reported to underline the impact of the cross–section. In the insets, the mode profile of the two WGs considered is shown.*

The radii have been chosen in order to have an FSR compatible with the DWDM grid (multiples of 100 GHz). The WG cross-sections considered here are the standard

SM Si300nm strip WG, whose cross–section is $300 \times 450\,\mathrm{nm}^2$, and the $300 \times 600\,\mathrm{nm}^2$ one. The latter is more suitable for nonlinear optics applications (see the dedicated analysis in subsection 3.4.1).

For design purposes, it is useful to introduce the coupling per length: $\kappa^2/L_{rt}$. As simulations with the different radii give very similar results, mostly for larger gaps, the simulation time can be highly reduced. In particular, it is possible to perform the FDTD simulation for different gaps for a single radius, extract the coupling per length, and then apply the results to a wide range of radii. This holds if the cross–section of the WGs involved is the same, since the cross–section highly influences the coupling strength, as one can notice by comparing the y-axis of the plots in panels (a.2) and (b).

### 1.4.2 Figures of merit calculations

All the FoMs of the resonator can be derived from the analytical expressions summarized in the Appendix A (A.3). They link the electromagnetic simulations of the coupler, i.e., the values of $\kappa^2$, to the final device performance, for both AP and AD configurations. As a matter of fact, usually the design starts from a given set of desired device performances, and the geometrical parameters (the gap and radius) are finally set by means of electromagnetic simulations. In Figure 1.10, I report visibility, quality factor, and field enhancement, which are the fundamental quantities to refer to when looking for light generation through nonlinear processes. I thus report in Figure 1.10 an example of FoM calculation for strip WG of cross–section $300 \times 600\,\mathrm{nm}^2$. The 2D maps report the values obtained for both the AP and the symmetric AD configurations, as a function of the propagation loss and the cross-coupling per unit length defined above.

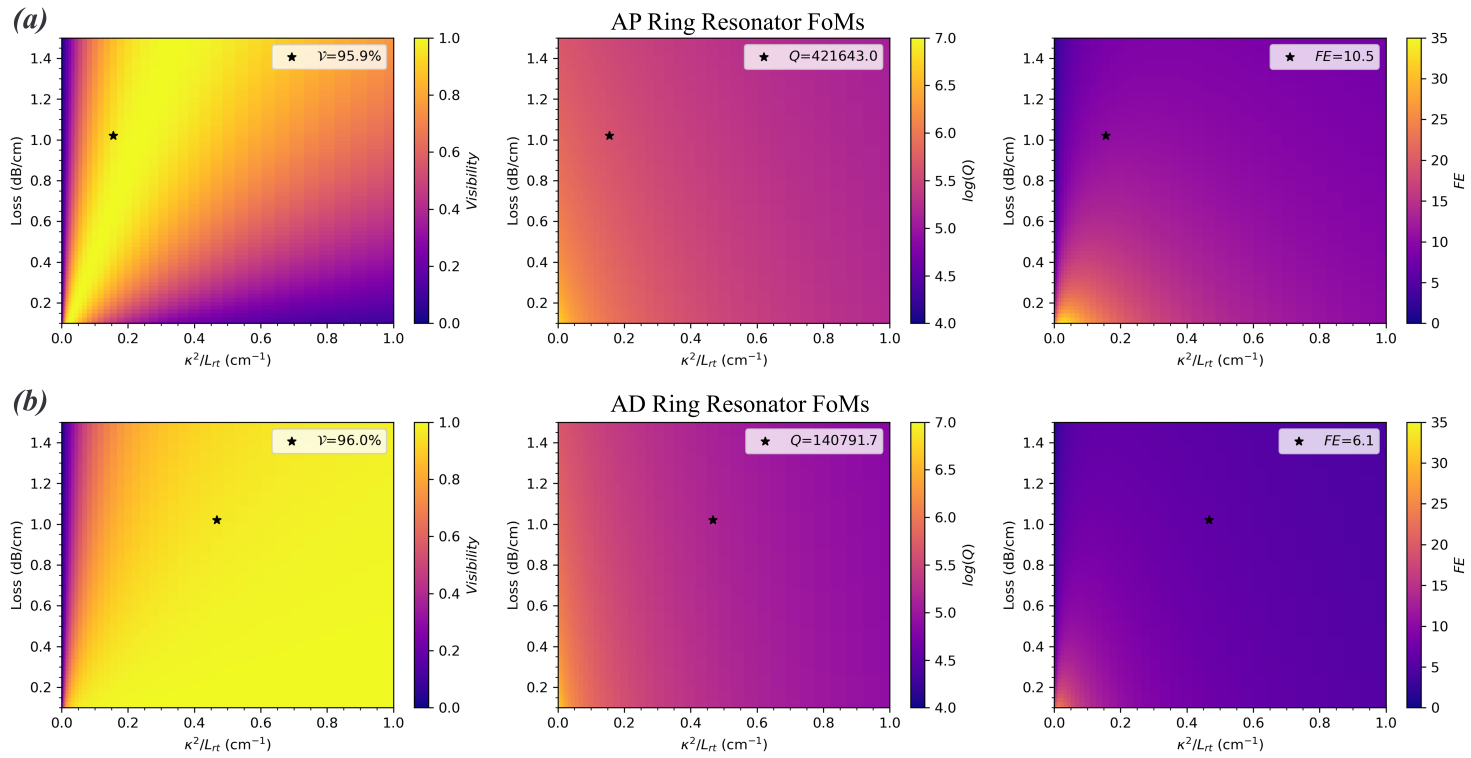



*Figure 1.10:* ***MRRs FoMs calculations****. Visibility, Q-factor and field enhancement are reported versus cross-coupling per unit length at* $\lambda = 1550\,nm$ *and cross–section* $300 \times 600\,nm^2$ *(*$n_g = 4.06$*). In (a) the MRR configuration is AP, while in (b) it is symmetric AD. The black star coordinates correspond to a typical FoM target search discussed in the text (expected loss of* $1\,dB/cm$ *and a high visibility above* $95\%$*).*

As is clear from the AP and AD treatments, a different behavior of these resonance-related FoMs is expected. For the former configuration, the critical coupling condition occurs only when Equation 1.28 is fulfilled; therefore, a precise $\kappa^2$ exists for each loss value at which the visibility is maximized. In the symmetric AD case, it occurs whenever the intrinsic losses are negligible with respect to the fraction of light lost by coupling with the bus WG; therefore, for sufficiently high $\kappa^2$ the visibility always approaches unity. As regards the Q-factor, the values for the AD case are slightly lower. In the right panel we report the field enhancement, which reaches maximum values of about 33 and 24 for the AP and AD configurations, respectively. Notice that $FE$ is a fundamental quantity for the nonlinear enhancement, thus for the case in which the MRR is used as a source of photon pairs (see subsection 1.3.4). Therefore, one may be tempted to obtain the efficiency and the generation rate directly from this value. Even though the equations are formally correct, the measurable values are unfortunately much more complex to obtain *a priori*. As already mentioned in the discussion on the nonlinear parameters in section 1.1.2, the overall performance is governed by several practical factors, which are not directly taken into account either in the FDTD simulations or in the analytical formulas used here to obtain the FoMs. Therefore, this analysis can certainly drive the design, but is not expected to quantitatively match the measured value when nonlinear processes are involved.

Keeping the discussion on the linear properties of the resonators, for the values of $Q$, $FE$, and $\mathcal{V}$ to be close to the calculated ones, it is fundamental that the coupling coefficient and propagation losses are identical in the ideal and fabricated device. However, as mentioned previously regarding the critical coupling condition, the actual values of the cross-coupling coefficients and losses inside the bend WG of the resonators are not known precisely, unless experimental data from previously fabricated devices are available. Therefore, the target performance is expected to be matched by one of the fabricated devices, but only within a parameter tuning range, which in the case of the MRR involves the gap. See chapter 3 for an example of this approach, in which simulated performance is matched to, and subsequently confirmed by, the characterization of the fabricated device.

Another relevant aspect is the relationship between $Q$, $FE$, and $\mathcal{V}$, explicitly reported later in the manuscript in the plots dedicated to specific source design, such as Figure 3.10. Here I report a specific case study to underline this aspect, indicated by the black stars in the plots. For the given cross–section, the typical propagation loss is about 1 dB/cm. Targeting a visibility $\mathcal{V} > 95\%$ (i.e., operation very close to

critical coupling, as required for both filtering and efficient SFWM pair generation), the AP configuration requires a cross-coupling per unit length of about $0.15\,\mathrm{cm}^{-1}$. This corresponds to a quality factor $Q \simeq 420000$ and a field enhancement $FE \simeq 10$.

For the AD configuration, instead, achieving the same visibility requires a much stronger coupling per length, i.e., $\kappa^2 L_{rt} \simeq 0.47\,\mathrm{cm}^{-1}$. This results in a quality factor about three times smaller and a field enhancement reduced to $FE \simeq 6$. Even more importantly, electromagnetic simulations of this cross–section (see Figure 1.9 (c)) show that such high coupling would correspond to an extremely narrow gap of about 70 nm. While it is possible in principle to fabricate sub-100 nm features in silicon photonics even with our CMOS-compatible deep-UV immersion photolithography [49, 107], this is not advisable for large-scale devices due to process variability and reproducibility issues. Instead, one should respect the so-called *critical dimensions*, defined by the PDK design rules to ensure robust fabrication, namely a minimum silicon critical dimension $CD^{Si}_{min} \simeq 60\,\mathrm{nm}$ and a minimum oxide gap $CD^{SiO_2}_{min} \simeq 100\,\mathrm{nm}$ for the Si300 nm platforms employed in this work.

Therefore, given the target performance ($\mathcal{V} > 95\%$), the cross-section, and the associated propagation loss, the resonator can be reliably designed only in the AP configuration. Alternatively, one could consider a smaller waveguide width (e.g., $300 \times 450\,\mathrm{nm}^2$; see Figure 1.9(b)) to achieve near-unity visibility in the AD configuration. Other waveguide geometry choices may also be made depending on the target performance, such as the one presented in subsection 3.4.1. The case study reported here highlights how the simulation techniques briefly introduced above must be jointly exploited to design a practical and reproducible device, always keeping in mind its target performance and application. A more complete and detailed simulation-to-layout workflow can be found in [108].

## 1.5 The directional couplers

The directional coupler (DC) is the integrated photonic counterpart of the beam splitter. The energy of the optical signal carried by one WG is coupled to a second one, and the strength of the coupling can be continuously tuned by changing the design parameters. Similarly to the point coupler already described, the physical mechanism is the evanescent coupling of the optical mode from the carrying WG to an adjacent WG, separated from the first one by a $SiO_2$ gap. This time, the coupling region is not limited to a point, but it extends over a certain coupling length $L_c$, in which the gap is kept constant. It is a two-input, two-output optical

element, as shown in Figure 1.11 (a). The input light is injected from one of the two WGs (IN) and collected from the two output ports (CROSS, BAR). The amount of power collected from each output port is usually expressed through the cross- and bar-coefficients, defined as $C = {}^{P_{CROSS}}/_{P_{IN}}$ and $B = {}^{P_{BAR}}/_{P_{IN}}$, respectively. In a lossless DC, they satisfy $C + B = 1$.

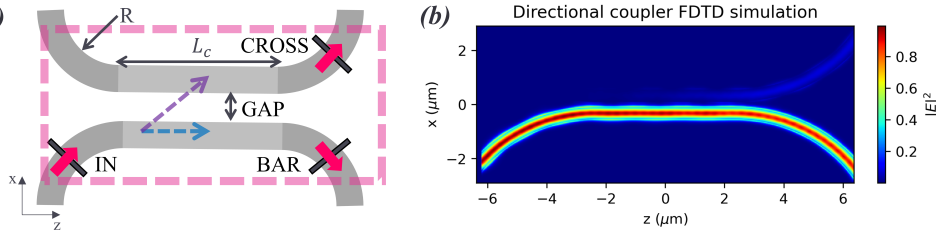



*Figure 1.11:* ***Directional coupler simulation.*** *(a) Simulation setup: the input mode ($TE_{00}$) is injected from the bottom left WG (IN) and collected from the two output ports (CROSS, BAR). (b) Example of simulated electric field amplitude propagation in the DC structure, corresponding to a cross-coefficient of 4% and a bar-coefficient of about 96%.*

Here the simple geometry reported in Figure 1.11 is used: two SM WGs sharing the same cross–section, $L_c$ is a linear segment, and the inputs and outputs are 90° bends with a certain radius $R$. More complex geometries can be considered, which try to solve different DC-related issues. For example, to increase the operating bandwidth, i.e., the wavelength range in which the DC operates at the target splitting ratio, either bent waveguides [109] or straight WGs with width asymmetry along the coupling length [110] can be introduced. Furthermore, to reduce the loss and the amount of back-reflected light (which is in general always undesired), the 90° bends used as transition between uncoupled and coupled WGs can be replaced by adiabatic bends.

### 1.5.1 Directional coupling modeling

The coupling mechanism in a directional coupler (DC) is often described in terms of *supermodes* [89], i.e., the optical modes supported by the coupled waveguides. In the simplest case, only two supermodes are supported: the symmetric (*even*, +) and antisymmetric (*odd*, −) combinations of the fundamental modes of the individual waveguides. Their effective indices differ slightly, denoted here as $n_{eff}^{+}$ and $n_{eff}^{-}$, respectively. The power transferred from the input port to the cross port after a

coupling length $L_c$ is given by:

$$P_C(L_c) = P_{IN}\,\sin^2\left(\frac{\pi\,L_c\,\Delta n^{\pm}}{\lambda}\right), \tag{1.40}$$

where $\Delta n^{\pm}$ is the absolute difference between the two supermode effective indices. Its behavior depends on the WG cross–section, gap, and wavelength.

As an example, the single-mode Si300nm strip WG is considered. The dependence of $\Delta n^{\pm}$ on both wavelength and gap is shown in Figure 1.12 (left), obtained from FDE simulations, as in the case previously reported for the single WG. Although the difference is small, its variation with wavelength, which arises from the considered material dispersion and mode confinement, demonstrates the intrinsically narrowband nature of standard DCs [51].

By extracting $\Delta n^{\pm}$ at $\lambda = 1550\,\text{nm}$, the normalized cross-coupled power as a function of the coupling length $L_c$ is calculated (central panel), according to Equation 1.40. As expected, larger gaps result in weaker coupling, which in turn requires longer coupling lengths to achieve the same power transfer. The effect is periodic, reflecting the fact that light oscillates back and forth between the two waveguides. Consequently, for a given target splitting ratio, there are multiple possible choices of $L_c$. However, as explicitly shown in the right panel, there is one important difference: the longer the coupler, the narrower its spectral bandwidth. This is because the accumulated phase mismatch between the supermodes increases with length, reducing tolerance to wavelength detuning. Therefore, in practice, shorter couplers are often preferred when broadband operation is required.

The previous analysis is based on the supermode theory, which provides a good first-order estimate of the coupling behavior. However, in practical cases, the coupling starts (and ends) outside the $L_c$ region. Therefore, full electromagnetic simulations using the FDTD method must be performed to evaluate the contribution of the transition regions between uncoupled and coupled waveguides. The simulations show that $L_c^{FDTD} < L_c^{MODE}$, and this is in general a non-negligible correction. Indeed, in Figure 1.13 the transmittivity obtained through full 3D FDTD simulations of one of the DCs previously shown in the right panel of Figure 1.12 is reported. In particular, using the simulation setup described in Figure 1.11 (a), the transmittivity at the cross and bar ports is directly obtained for different coupling lengths. By interpolating the simulation points with a polynomial fit, the estimated $L_C$ for the target 50:50 splitting ratio is obtained, which is $\sim 2\,\mu$m shorter than expected

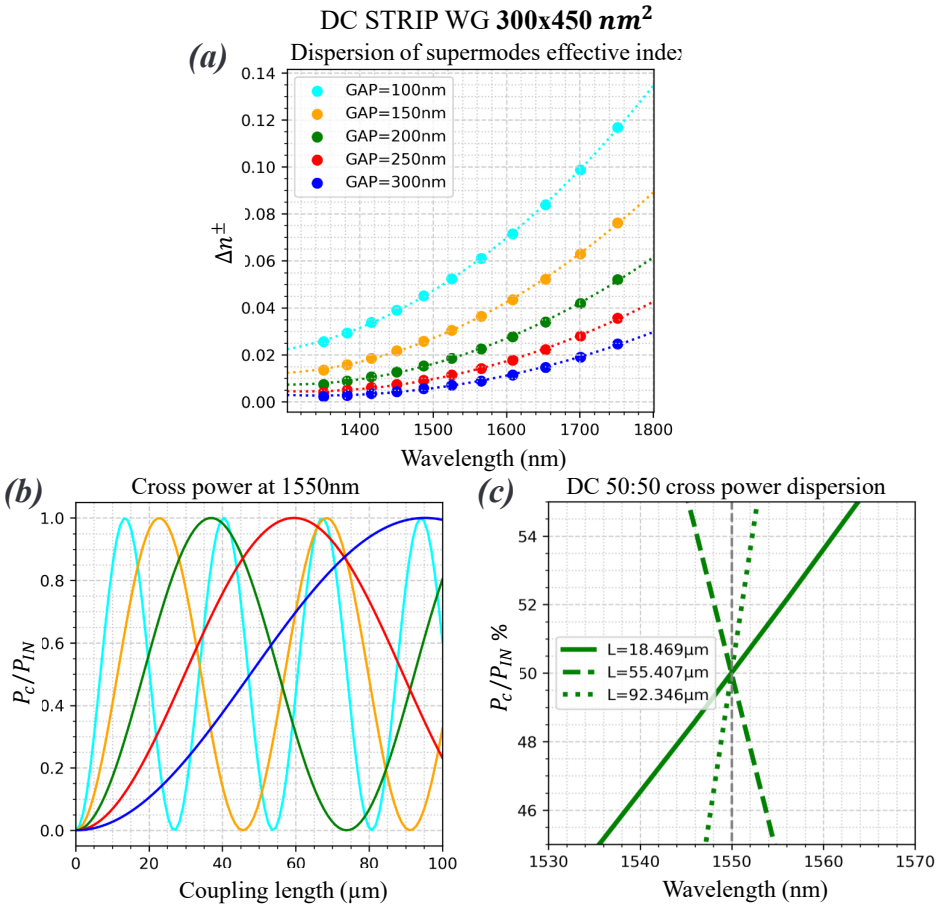



*Figure 1.12:* ***DC simulations results using the supermode method.*** *Left panel:* $\Delta n^{\pm}$ *as a function of the wavelength and the gap for SM Si300nm WG. Central panel: normalized cross-coupled power as a function of the coupling length and the gap at* $\lambda = 1550\,nm$. *Right panel: comparison of the spectral dependence of the cross-coupled power for a 50:50 DC with GAP=200 nm for three different coupling lengths* $L$.

from the previous analysis ($\sim 16.1$ obtained from FDTD and $\sim 18.5$ obtained with the FDE simulations and the following analytical calculations). Therefore, the contribution of the 90° bends of radius $R = 10\,\mu$m is not negligible, confirming the importance of performing full FDTD simulations also in the DC case after a first estimate of the expected parameter range through the analytical method.

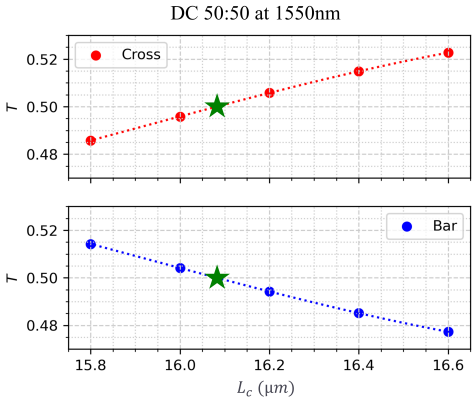



*Figure 1.13:* ***DC simulations results using FDTD.*** *FDTD simulation of a 50:50 DC, of standard geometry as in Figure 1.11 (a), with $R = 10\,\mu m$ and gap=200 nm, varying the coupling length. The considered WG cross–section is 300×450 $nm^2$.*

## 1.6 The Mach–Zehnder interferometer

The Mach–Zehnder interferometer (MZI) is a fundamental building block in integrated photonics, widely used for modulation, switching, filtering, and sensing applications. It consists of two DCs connected by two waveguide arms, as shown in Figure 1.14 (a). Light is injected (in general) into the two left WGs and combined

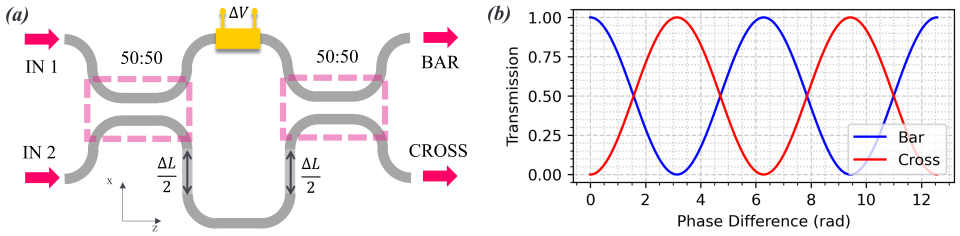



*Figure 1.14:* ***Mach–Zehnder interferometer.*** *(a) Light injected (in general) into the two input WGs is combined in the first 50:50 DC; a phase difference between the paths is then introduced and, finally, the light is recombined in the second 50:50 DC. (b) The transmission at the two output WGs is reported as a function of the overall phase difference between the two paths, while injecting light only in the IN 1 port, according to Equation 1.41.*

by two consecutive 50:50 DCs separated by a dephasing region. The phase difference acquired by the two branches determines the interference condition at the second coupler and thus the power splitting at the two output ports (CROSS and BAR). The behavior can be modeled by introducing the transfer matrix of the component, i.e., the product of the coupling matrices (Equation 1.24, $U_C$) and the propagation

matrix ($U_{FP}$):

$$\begin{aligned}\begin{pmatrix} E_{BAR} \\ E_{CROSS} \end{pmatrix} &= U_{C\,2} \cdot U_{FP} \cdot U_{C\,1} \begin{pmatrix} E_{IN\,1} \\ E_{IN\,2} \end{pmatrix} \\ &= \begin{pmatrix} t_2 & \kappa_2 \\ -\kappa_2^* & t_2^* \end{pmatrix} \cdot \begin{pmatrix} e^{i\phi_1} & 0 \\ 0 & e^{i\phi_2} \end{pmatrix} \cdot \begin{pmatrix} t_1 & \kappa_1 \\ -\kappa_1^* & t_1^* \end{pmatrix} \cdot \begin{pmatrix} E_{IN\,1} \\ E_{IN\,2} \end{pmatrix}\end{aligned} \tag{1.41}$$

where $\phi_1$ and $\phi_2$ are the phases accumulated in the two arms.

In the simple case where light is injected only into the first input port ($E_{IN\,1} = E_{IN}$, $E_{IN\,2} = 0$), and considering two identical lossless 50:50 DCs ($|t_1|^2 = |t_2|^2 = |\kappa_1|^2 = |\kappa_2|^2 = 0.5$), the power transmission at the two output ports takes the form of a simple sinusoidal function of the overall phase difference $\Delta\phi = \phi_1 - \phi_2$, reported in Figure 1.14 (b).

The phase difference between the two paths can be introduced in different ways: either by changing the effective index $n_{eff}$ experienced by the optical mode in one of the paths, for example by exploiting the TOE using thermal phase shifters (yellow element in the upper arm of the schematic), or by introducing a path imbalance $\Delta L$, thus $\phi_2 = \frac{2\pi n_{eff}\,\Delta L}{\lambda}$ (lower arm). In the first case, a tunable coupler can be realized, while in the second case the splitting ratio between the output ports is fixed for a given wavelength.

Other methods can also be used to introduce and/or tune the phase difference between the paths, such as exploiting the free-carrier dispersion effect through the integration of p-n or p-i-n junctions.

### 1.6.1 The cascaded MZI filters

An MZI with asymmetric arm length (here called *aMZI*) can operate as a periodic optical filter, playing a central role in Coarse Wavelength Division Multiplexing (CWDM). By exploiting the wavelength dependence of $\Delta\phi$, a periodic transmission spectrum is obtained, whose free spectral range (FSR) is given by

$$\Delta\lambda_{FSR}^{MZI} = \frac{\lambda^2}{n_g\,\Delta L}. \tag{1.42}$$

The transmission spectrum can be further engineered by cascading several aMZIs and properly adjusting the coupling ratios of the DCs and the arm length differences. These devices, usually referred to as *cascaded MZI filters*, are widely used in silicon photonics because of their broadband operation, low insertion loss, and the

possibility of achieving flat channel responses.

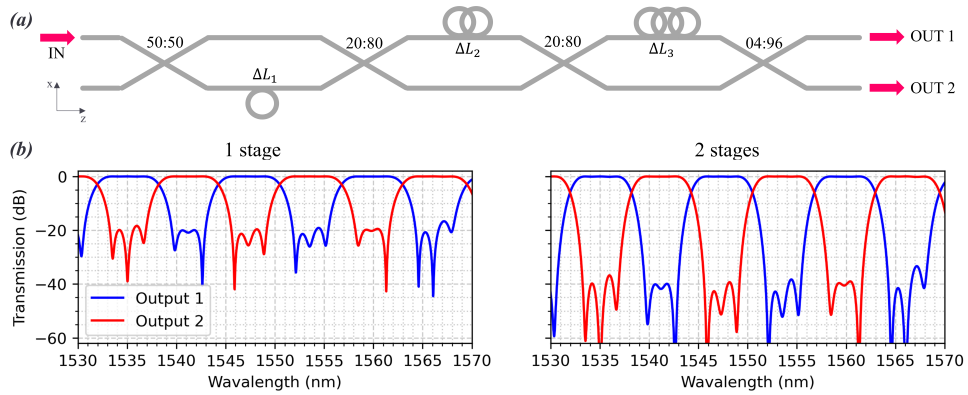



*Figure 1.15:* ***Flat-band cascaded MZI filter.*** *(a) Scheme of the design: light is injected at the IN and routed to two separate output WGs (OUT 1 and OUT 2) depending on the wavelength. (b) Theoretical spectra of the two collected channels, featuring an FSR of* 1600 *GHz. The spectra are obtained neglecting the WG and DC chromatic dispersion. The two plots specifically report the cases of a single stage and a double stage, the latter obtained by cascading two identical stages represented in (a).*

Here a possible configuration allowing a flat-band demultiplexer is introduced, corresponding to the model used to design the devices integrated and characterized in the framework of this research work. Following [109, 111, 112], the MZIs are arranged as reported in Figure 1.15 (a). It is composed of three aMZIs (thus four DCs in total), with bar transmission coefficients of 50%, 20%, 20% and 4%. The

| $\Delta L_1$ | $\Delta L_2$ | $\Delta L_3$ | $\Delta L_{FSR}$ |
|---|---|---|---|
| $\lambda^2/n_g\,\lambda_{FSR}$ | $2\cdot\Delta L_1$ | $2\cdot\Delta L_1+{}^{\Delta L_{FSR}}/_2$ | $\lambda/n_{eff}$ |

*Table 1.2:* ***Flat-band cascaded MZI filter model.*** *Arm length imbalance of the one-stage 3-aMZI flat-band cascaded MZI filter employed in this work.*

arm-length imbalances are given in Table 1.2, where $\lambda$ is the central wavelength of the filter, and $n_g$ and $n_{eff}$ are the group and effective indices of the waveguide mode. This filter routes periodic rectangular spectral channels into two separate WGs, according to the desired FSR $\lambda_{FSR}$, typically ranging from a few to several nanometers.

Using the transfer matrix method (i.e., multiplying the matrices of the individual MZIs written as in Equation 1.41), the theoretical filter spectrum can be

calculated. In Figure 1.15(b), the transmission spectra of the two channels are reported for a single 3-MZI stage (left), and for a double-stage configuration, i.e., where an identical stage is cascaded at each output (right). In the latter case, only one output WG per branch is collected.

The reported single-stage cascaded MZI filter provides periodic channel separation with a crosstalk level of about 20 dB (calculated as the amount of light collected in one channel at the center of the band of the other one). By increasing the number of stages, the crosstalk is further reduced, as already observed in the double-stage configuration reported here (about 20 dB of improvement), and the passband becomes flatter. The drawbacks of cascading multiple stages are, as expected, increased insertion loss, but also the narrowing of the spectral channels, together with a larger footprint and higher fabrication sensitivity.

Some experimental results on such integrated filters will be reported later in Chapter 3 (Figure 3.19).

## 1.7 In- and out-coupling devices

Coupling light from a fiber to a SiPh chip is challenging due to the large mode mismatch between the two systems. A standard SMF-28 fiber features a mode field diameter of 10 $\mu$m at telecommunication wavelengths, while typical silicon WGs have cross-sections of only a few hundred nanometers. Efficient coupling structures are therefore required to adapt the fiber mode to the waveguide mode. This problem is usually addressed using either *edge couplers*, where light is coupled in and out through the chip facet, or *grating couplers*, where light is coupled vertically at the chip surface. Both the coupling methods are schematically represented in Figure 1.16.

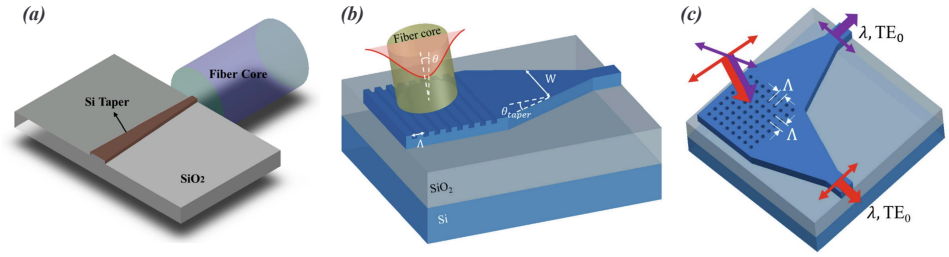



*Figure 1.16:* ***In- and out-couplers.*** *(a) Edge coupler; image adapted from [113]. (b) Single-polarization grating coupler; image adapted from [114]. (c) Dual-polarization grating coupler; image adapted from [114].*

Both approaches have advantages and drawbacks. In this thesis, edge couplers are used to couple light in and from the chip exploited in chapter 2. The cicruits I have personally designed, presented in chapter 3 and chapter 4, employ instead grating couplers, mainly because of their more robust fiber–chip alignment, which is particularly convenient when multiple input and output fibers must be coupled to the chip [114]. Specifically, both single-polarization (Figure 1.16 (b)) and dual-polarization (Figure 1.16 (c)) GCs have been used in the different projects reported in this manuscript and are described in more detail below. As these devices are taken directly from the foundries' PDKs, no design or simulation work on them has been personally carried out within the framework of this thesis.

### 1.7.1 Edge couplers

Edge couplers are known for achieving higher coupling efficiency, broader bandwidth, and polarization insensitivity compared to their GC counterparts. They consist of a tapered WG in which the WG width is varied adiabatically along the propagation direction. In the simplest case the variation is linear, although exponential profiles have also been shown to provide ultra-low-loss performance [113].

Depending on the integrated platform and on the desired input/output fiber, the taper can be designed either to reduce the WG width, so that the optical mode becomes mostly guided in the cladding and its diameter increases, or to enlarge the WG width when smaller mode field diameters are required (for example when lensed fibers are used or when the WG mode is already relatively large). The first configuration is typically used in SOI platforms.

More complex structures may also be implemented, such as tapers incorporating sub-wavelength regions, side-by-side multiple tapered WGs, or combinations of these approaches [113]. Nowadays, most foundries also provide material stacks incorporating additional lower-index guiding layers placed above the WG. For example, both the STMicroelectronics and IMEC SiPh platforms include upper silicon nitride tapers together with efficient Si-to-SiN evanescent transitions, allowing higher-performance edge coupling [115, 116].

### 1.7.2 Grating Couplers

Grating couplers are periodic structures diffracting light between free space and a single WG (input and output GC). They allow coupling at almost any point of the chip surface, provided that the radiative area is not covered by metal layers;

typically, a region of about $100 \times 50\,\mu m^2$ is reserved for this purpose.

Compared with edge couplers, their coupling efficiency depends strongly on wavelength and on the injected polarization. The spectrum of standard SOI GCs is typically Gaussian-like, with a 1-dB bandwidth of about 40–50 nm, and they usually couple the TE polarization more efficiently. Major advantages are their compact footprint, compatibility with wafer-scale testing, and higher tolerance to fiber–chip misalignment, which overall supports low-cost mass production. Moreover, their use has become highly standardized, and a fiber tilt angle of about 8° in glass (approximately 11° in air) has become the common SOI standard.

SOI GCs provided in foundries' PDKs typically exhibit losses below 3 dB, although significant effort has been devoted to further improving their efficiency. Partial etching, focusing geometries [117], and grating-period apodization are widely used strategies. The incorporation of sub-wavelength structures in standard SOI dual-etch platforms has enabled state-of-the-art insertion losses down to about 1.5 dB per coupler, although such small features often require electron-beam lithography. To increase the compatibility of these designs with high-volume production, efforts have been made to implement similar structures using standard immersion photolithography in CMOS-compatible SiPh processes, showing experimental results around 1.8 dB [118]. The coupling efficiency can also be enhanced through heterogeneous integration of additional materials assisting the diffraction process, such as aluminum or gold mirrors on the backside of the chip [119, 120], or through the integration of other materials such as PolySi [121].

### 1.7.3 Dual-polarization Grating Couplers

Dual-polarization grating couplers (2DGCs), also known as polarization-splitting GCs, couple orthogonal polarization components from a single-mode optical fiber into two planar waveguides [122]. They are essentially designed as two orthogonally arranged 1D gratings, as the ones previously introduced, each coupling light into the target polarization (typically TE) of its corresponding WG, resulting in a periodic array of holes.

Considering an input 2DGC for simplicity, a standard SMF-28 fiber carrying light with an arbitrary (generally elliptical) polarization state is placed at the appropriate coupling angle (for SOI, the same standard tilt used for single-polarization GCs). The optical power transmitted to the two WGs depends on the input polarization state, while the excited mode in each WG remains fixed. An important figure of merit of such structures is the polarization-dependent loss (PDL), defined so that

the sum of the transmitted powers in the two WGs remains as constant as possible when the input polarization state changes. Typical coupling losses are below 5 dB [123], although many studies have focused on improving the coupling efficiency.

Similarly to single-polarization GCs, focusing geometries [124] and backside mirrors have significantly improved performance [125]. In particular, record insertion losses of about 1.8 dB have been experimentally demonstrated in Ref. [120]. In addition, photonic-crystal-based designs have driven further developments, mainly through optimization of hole dimensions, shapes, and grating pitch [126, 127].

Among the proposed geometries, crossed ellipses acting as grating scattering elements have emerged as particularly promising. This geometry is used in the CEA-Leti PDK 2DGC and is therefore also employed in this work. A SEM image of such a 2DGC is reported in subsection 3.5.3.

## 1.8 Active devices

In the previous sections, the fundamental passive components of integrated photonics were presented. However, to build a complete photonic circuit, active devices are often required. In silicon photonics, the most common active components are modulators and photodetectors, which enable the manipulation and detection of optical signals, respectively. They require additional fabrication steps to build a more complex cross–section including electrical contacts, doped silicon regions, and possibly heterogeneous integration, such as with germanium as reported in Figure 1.17. It is worth noting that heaters are sometimes also labeled as "active" devices, as they can control the optical phase through an external electrical signal. However, in this manuscript, "active" components refer only to devices in which doping or heterogeneous integration is present, while "passive" refers to devices and/or circuits where only intrinsic silicon and heaters are present, together with the corresponding electrical contacts.

The active devices employed in the circuits developed within the framework of this research work are briefly introduced in the following paragraphs. Only their working principle is described, as simulations and designs were not performed personally.

### 1.8.1 Thermal phase shifters

The working principle of thermal phase shifters, or *heaters*, is the thermo-optic effect, described in section 1.1.2. A heater is an integrated metal bar (purple layer

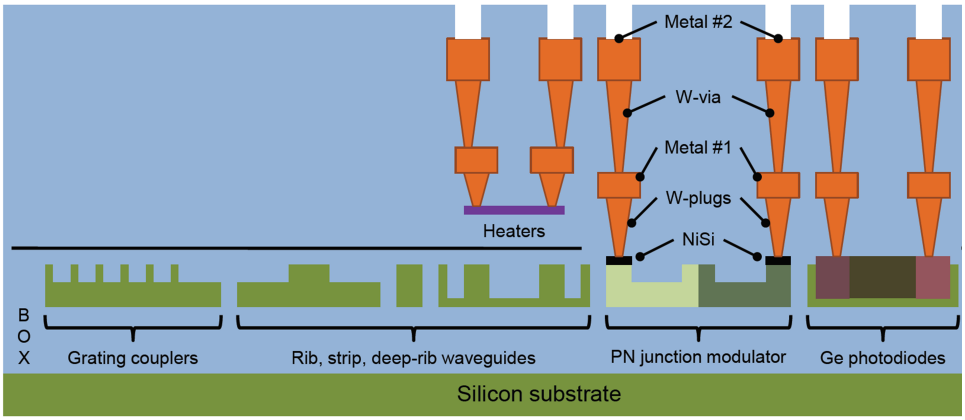



*Figure 1.17:* ***SiPh complete layer stack****. In particular, it represents CEA-Leti's silicon photonic platform for monolithic integration of passive and active chip components. Image adapted from [128].*

in Figure 1.17), connected to two electrical contacts exposed at the chip surface, where a potential difference is applied. The heater acts as a resistor: the electrical power dissipated as current flows is $P_{th} = V \cdot I$ (Joule effect), producing a local increase in the temperature. If the metal slab is close enough to the silicon WG to transfer part of the generated heat, the effective index experienced by the optical mode is locally tuned (TOE), thus acting as a phase-shifter.

The conducting material (often titanium nitride) is deposited and patterned on top of the Si WG, previously encapsulated with a suitable $SiO_2$ layer to avoid optical absorption. The thickness of the oxide layer is a trade-off between optical loss and thermal efficiency, together with compatibility with the other stack layers. Therefore, it is defined by the foundries' process flow.

The heater modulation speed is limited to 10–100 kHz, corresponding to the typical timescale of heat dissipation. Therefore, heaters are usually employed for calibration and slow feedback control of the circuit. For high-speed applications, p-n and p-i-n modulators are preferred, which can reach tens of GHz.

### 1.8.2 Phase modulators in silicon

In optical communication systems, modulation (i.e., a change in the optical field phase and/or amplitude due to an external stimulus) is a key functionality. The modulation mechanism relies on a refractive index change of the material, which produces a phase shift of the optical field traveling through it. If the index change follows a sine-wave function, typically with frequencies ranging from DC to 100 GHz,

the resulting phase modulation generates equispaced sidebands [51], separated by the modulation frequency. Their amplitude depends on the modulation index, which is proportional to the strength of the index change. This effect can be used for various applications, such as frequency comb generation [129], and quantum state manipulation [130, 131].

Silicon modulators are usually realized by exploiting the free-carrier dispersion effect (see section 1.1.2), by establishing a current flow in integrated p-n or p-i-n junctions, thus injecting or depleting carriers in the WG [91]. Their fabrication is CMOS-compatible, typically achieved through ion implantation, with multiple implantation steps (p++, p+, n+, n++) followed by rapid thermal annealing. Another possibility is the heterogeneous integration of materials featuring Pockels or Kerr effects [132], such as lithium niobate [133, 134]. However, this approach is not CMOS compatible, thus here silicon-only-based modulators have been used.

P–n junctions require highly doped p– and n–type regions in the WG, which cause strong free–carrier–induced propagation losses. To mitigate this, multiple doped regions are typically implemented, with decreasing doping levels toward the WG center, where the optical mode is mostly confined. These modulators operate through a *carrier depletion* mechanism: by applying a reverse bias across the diode, a depletion region is produced, whose width increases with the applied (negative) voltage, i.e. the reverse bias (see Figure 1.18(b)). By modulating the bias voltage around this initial operating point, the electric field generated across the waveguide is modulated, and so is the effective refractive index of the guided mode.

In p–i–n diodes, the guided optical mode is mostly confined in the central intrinsic Si region of the WG. Doped regions are placed on the sides of the WG (see Figure 1.18(a)), sufficiently far to ensure low loss at zero bias. Carrier injection into the i–region is then the index-tuning mechanism, controlled by applying a modulated electrical signal across the junction [89].

Both diode structures can be integrated into various devices, from single-waveguide phase shifters to Mach–Zehnder interferometers (MZIs) and microring resonators. In particular, MZIs are widely used as amplitude modulators, converting phase modulation into intensity modulation through interference. It is worth noting that foundries develop their own doping profiles for each modulator geometry, which may vary with the operating wavelength and the desired performance.

Important metrics guiding the optimization of modulator design and fabrication are the modulation speed, insertion loss, footprint, and phase–shifting efficiency.

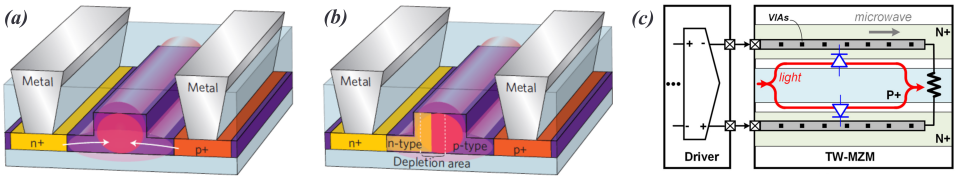



*Figure 1.18:* ***Silicon modulators.*** *(a) Schematic of a typical p–i–n modulator, with doping profile and electrical contacts shown. (b) Schematic of a typical PN modulator, showing at the center the depletion region created under reverse bias. (c) Schematic of a traveling-wave electrode on an amplitude modulator based on a push–pull MZI. Images (a) and (b) adapted from [91], and (c) from [135].*

The latter is often expressed through the $V_\pi L_{mod}$ product, i.e., the voltage required to obtain a $\pi$ phase shift ($V_\pi$, often called the half-wave voltage) multiplied by the modulator length ($L_{mod}$) [136, 132]. Ideally, this product should be as low as possible in order to reduce both the driving voltage and the device footprint.

### Electrodes

In Si phase modulators, the electrical signal is usually applied through coplanar waveguide electrodes: the electrical and optical signals propagate in the same direction and, if the phase velocity of the RF signal matches the optical group signal, the modulation is efficient [51]. The electrodes are placed on top of the WG, separated by an oxide layer to avoid optical absorption. Their design is crucial to achieve high–speed and low RF–power operation, as it must ensure good phase–velocity matching and mode overlap between the RF field induced at the junction and the optical mode, while minimizing losses and dispersion.

Several electrode topologies exist, each with its own advantages and drawbacks. Here the focus is on the traveling-wave (TW) type, as it is the one employed in this work. For a comparison among different configurations, see [52]. As an example, Figure 1.18(c) shows a typical geometry of an MZI push–pull modulator: the electrodes are placed on the sides of the two WGs, featuring mirrored p-n junctions. The high-frequency signal is injected at one end and propagates in the same direction as the optical wave. The transmission line is terminated with a resistor matched to the electrode wave impedance (usually designed to be 50 Ω), in order to prevent reflections of the RF signal [137, 52]. Modulators excited through TW transmission lines can reach lengths of a few millimeters, but long phase shifters also introduce loss and velocity mismatch, thus limiting their electro-optical bandwidth [138].

More advanced schemes are widely employed for high–speed operation; in partic-

ular, the two MZI arms may be independently controlled with two signals. Three– or five–electrode geometries are therefore often introduced: the Signal–Ground-Signal (SGS) and the Ground–Signal–Ground–Signal–Ground (GSGSG) configurations [139, 138, 140].

## 1.9 Conclusions and further perspectives

In this chapter, the foundational framework for designing and modeling integrated silicon photonic devices on SOI platforms was presented, focusing specifically on the core components that constitute the quantum photonic circuits designed and exploited in the subsequent chapters. The silicon photonics platform stands out as a highly promising route for scalable, reconfigurable quantum photonics. Leveraging mature, fully CMOS–compatible manufacturing techniques, it offers a complete toolkit of both passive and active components: from high–confinement waveguides and resonant cavities to high–speed phase modulators and thermal phase shifters.

While monolithic SOI technology serves as the primary benchmark for this work due to its commercial availability and high fabrication yield, looking toward further perspectives, additional silicon–based architectures can be envisioned. Currently, the development of hybrid and heterogeneous integration platforms is driven by the need to overcome the intrinsic physical limitations of pure silicon, such as two–photon absorption at high optical powers and free–carrier–induced propagation losses in active modulators. A major industrial trend involves co–integrating silicon with silicon nitride ($Si_3N_4$). Low-loss SiN waveguides offer a five–times lower thermo–optic coefficient, thus significantly reducing temperature–induced wavelength shifts, while providing high optical power handling due to the absence of TPA. Multi–layer platforms combining the tight footprint integration of Si waveguides with SiN devices are currently commercially available, as exemplified by 300 mm foundry processes such as STMicroelectronics' PIC100 platform [141]. Furthermore, heterogeneous integration of thin-film lithium niobate (TFLN) onto silicon-based optical circuits emerges as a game-changing strategy for electro-optic modulation [142]. Thanks to its Pockels effect, lithium–niobate–on–silicon modulators enable ultra fast, gigahertz–bandwidth operation with negligible absorption losses, effectively bypassing the efficiency–vs–loss trade-off of traditional carrier–depletion p–n junctions. Commercially available options are already reaching the market, such as Ligentec MPW runs dedicated to SiN co-integrated with TFLN [143, 144]. Incorporating this material platform into future quantum photonic silicon circuits will combine the photon-pair generation of SFWM silicon sources with

ultra-high bandwidth and low modulation loss.

Regardless of whether these architectures rely purely on SOI or incorporate hybrid materials, a central takeaway of this first chapter is that realizing high-performance photonic circuits requires careful physical design. Accurate simulation workflow combining FDTD and FDE methods is essential to guarantee reliable circuit execution. Moreover, as demonstrated across this chapter, every building block demands a tailored optimization approach based on a deep understanding of competing trade-offs.For instance, choosing between strip and rib geometries, as well as between 220 nm and 300 nm silicon film thicknesses, highly depends on the target application, requiring a balance between optical field confinement, sidewall scattering losses, and group velocity dispersion. Similarly, tunability highlights the classic trade-off between compact, lossless thermo-optic tuning and ultra-fast, gigahertz-bandwidth carrier-depletion $p$-$n$ junctions.

By systematically presenting the physical concepts and modeling strategies for these fundamental building blocks, this chapter presents the necessary theoretical and engineering tools for the subsequent chapters, where these components are combined to realize integrated sources of hyperentangled photon pairs and monolithic quantum frequency processors.

# Chapter 2

# Generation of hyperentangled photon pairs

This chapter bridges the theoretical framework of nonlinear integrated optics introduced in Chapter 1 with the practical realisation of a hyperentangled-state source based on a silicon photonic chip. In particular, I first review the state of the art, underlining those research works reporting integration of HE sources, with a specific focus on the simultaneous entanglement on the two degrees of freedom here used: time–bin (TB) and frequency–bin (FB).

The main part of the chapter is based on the results published in [145], representing, to the best of my knowledge, the first demonstration of a silicon integrated source of photon pairs hyperentangled in those two DoFs. First, I introduce the SiPh source itself, presenting its design together with the optical setup used for the photon–pair generation. After having characterized its generation rate and brightness, I then introduce the analysis setups and methods developed in the framework of this research work to verify the effective generation of the target 16–dimensional HE state.

Finally, I present the experimental results demonstrating the presence of entanglement in the individual DoF through quantum state tomography performed independently in the two subspaces, while the hyperentangled nature of the generated state is confirmed through the measurement of an HE witness.

## 2.1 Motivation and state of the art

To date, most experimental demonstrations of HE rely on photon pairs generated by spontaneous parametric down–conversion (SPDC) in nonlinear crystals [24]. These typically exploit polarization, momentum, or time–energy entanglement [146, 147, 148, 149] in different combinations, reaching Hilbert-space dimensions equivalent to multiple qubits, in particular up to five and ten qubits, respectively, in Refs. [150, 151]. Such bulk systems, however, lack scalability and are difficult to integrate into larger quantum photonic circuits.

The move toward integrated HE sources began with periodically poled lithium niobate (PPLN) waveguides. Early demonstrations reported hyperentanglement in spatial–mode and polarization DoFs [152], but also in frequency and polarization, enabled by an SPDC waveguide incorporated into a fiber-based Sagnac interferometer [153]. However, silicon photonics has emerged as a leading platform for integrated quantum photonics due to its compatibility with CMOS fabrication and the numerous demonstrations of on–chip generation and manipulation of quantum states of light. Entangled photon pairs naturally encoded in the time–energy DoF are often generated through SFWM in silicon WGs and MRRs [35, 154], but demonstrations of HE state generation on SiPh chips are, to the best of my knowledge, still limited.

Previous demonstrations include HE states entangled in time–polarization DoFs using silicon MRRs [155], and in the frequency–time–bin DoFs on the Hydex platform [32]. More recently, a hyperentangled source in the energy–time and frequency–bin spaces was reported by Gianini L. *et al.* [156], to which I also partially contributed within the framework of a collaboration between the Laboratory of Quantum Photonics of the University of Pavia and the Laboratory of Integrated Silicon Photonics of CEA–Leti, as part of the HYPERSPACE European Project [157].

### 2.1.1 Time and frequency –*bin* hyperentanglement

Frequency and time DoFs are particularly appealing for encoding information in photonic quantum carriers. In particular, their discretized versions, i.e. *time–bin* and *frequency–bin* encoding, are compatible with both free-space and fiber-optic links, as evidenced by the widespread use of telecommunication infrastructures that already exploit time–division and frequency–division multiplexing. Moreover, they naturally support high–dimensional state spaces, in contrast to, for example, the polarization DoF, which is intrinsically binary.

Photonic temporal modes can be easily generated using fast modulators and

are suitable for long–distance transmission through optical fibers [158], free space [159], and even in ground–satellite applications [160]. Recent demonstrations have reported multidimensional entanglement distribution [161, 162], confirming their suitability for high–dimensional information encoding. Furthermore, TB states are highly compatible with integrated photonic platforms [162, 163], whose intrinsic phase stability removes the need for active stabilization typical of fiber–based interferometer setups [164]. In particular, a recent demonstration of post–selection–free TB qubit entanglement certification and QKD protocol implementation using a fully integrated receiver [163] overcomes the manipulation limitations arising from the traditional Franson–like analysis scheme in a stable and compact fully–packaged photonic device.

On the other hand, FB–encoded quantum states are naturally generated through SFWM in MRRs [130, 165, 166], spanning high-dimensional Hilbert spaces [16]. Recently, they have also been employed in long–distance entanglement–based QKD experiments [167, 168, 169], demonstrating high resilience. In particular, in Ref. [167] the authors report a real–time phase compensation technique to enhance the stability of quantum state transmission over long distances when subjected to environmental thermal fluctuations, thus further improving the scalability and robustness of this encoding method.

Although time and frequency are often regarded as correlated and dependent variables, they can be jointly exploited to encode quantum information. In particular, they can be treated as two *distinct* DoFs if the frequency-bin spacing $f$ and the time-bin duration $t_w$ satisfy the condition $f \cdot t_w \gg 1$, i.e. if the temporal extents of the different frequency-bin wavepackets do not overlap.

Prior to the demonstration reported here, the on–chip generation of HE states in this particular combination of DoFs had been realized only once, in the pioneering work of Ref. [32]. That work presents a high–refractive–index glass source consisting of a single high–brightness ring resonator with an FSR of 200 GHz, which required the use of non–commercial electro–optic modulators (EOMs) to efficiently perform quantum state analysis in the FB basis.

The silicon integrated source of HE photon pairs over discrete *time–frequency* modes used in this work is composed of two high–finesse silicon microring resonators. The use of multiple resonators allows one to achieve high brightness and, at the same time, a small frequency–bin spacing [170, 165, 166], which are key requirements for efficient electro–optic manipulation using standard phase modulators and high–rate transmission over lossy links. This approach circumvents the limitation of using a single large resonator, where a small frequency–bin spacing is obtained

at the cost of a reduced photon-pair generation rate [170].

## 2.2 Experimental realisation

In the following, I first illustrate the device used, reporting both its linear characterization and its nonlinear operation in the photon-pair generation regime. I then describe the experimental setup built around the sample to generate and fully analyze the HE state. Finally, I present the experimental results, including the quantum state tomography of the reduced density matrices in the TB and FB subspaces and the measurement of the HE witness.

### 2.2.1 Silicon source design and characterization

The design and fabrication of the silicon chip were carried out within a previous collaboration between the Quantum Photonics Laboratory of the University of Pavia and the research center CEA–Leti. The device was fabricated on a 200 mm SOI wafer using the CMOS–compatible silicon photonics pilot line [48].

The source is composed of two nominally identical MRRs (R1 and R2), side-coupled to a single bus WG, as shown in Figure 2.2(b). They are designed to operate in the fundamental TE mode at the telecommunication wavelength of 1550 nm. The WG is implemented in strip geometry, with a cross–section of $220 \times 600\,\mathrm{nm}^2$. The ring radius is set to $22\,\mu$m, corresponding to an FSR of $\sim 524\,$GHz, and the bus-ring gap is 150 nm. Light is coupled into and out of the chip through on-chip inverse tapers and off-chip lensed fibers, selected experimentally to minimize coupling losses. This configuration, which was the only pre–existing element of the setup prior to this work, yields a coupling loss of approximately 3.5 dB per facet. Further details regarding the sample, its component figures of merit, and its fabrication process are reported in Refs. [66, 165, 166].

Heaters are integrated on top of the rings to allow resonance alignment and tuning, yielding the desired frequency-comb output used for the generation of HE photon pairs through SFWM. The resulting spectrum after heater calibration is reported in Figure 2.1 for the wavelength ranges of interest: from left to right, the idler, pump, and signal resonances, spaced by $f = 18.25\,$GHz. I personally calibrated the resonance positions by iteratively adjusting the power dissipated across the individual heaters while monitoring the continuous-wave (CW) laser transmission spectra on an oscilloscope. Once the target spacing $f$ was achieved, the heater settings were saved, and no further optimization was required throughout

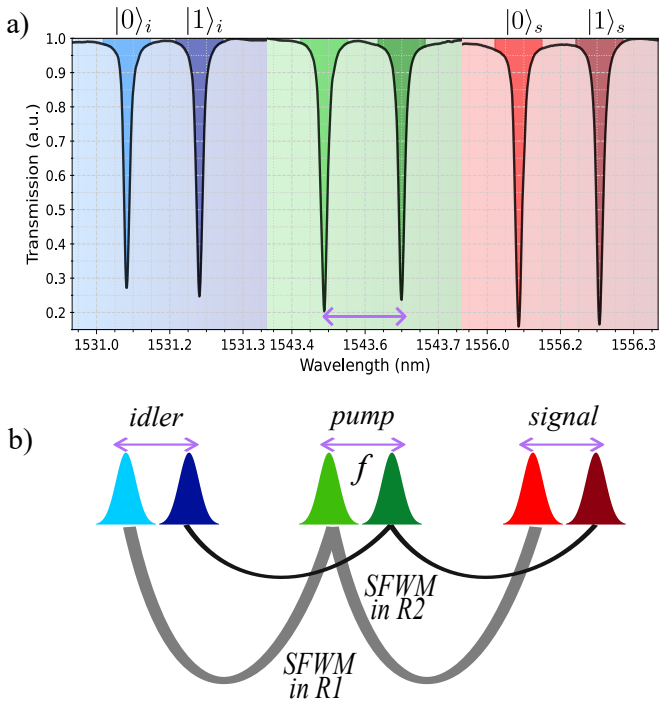



*Figure 2.1:* ***Linear characterization of the SiPh source and generation scheme.*** *(a) Transmission spectrum of the device in the wavelength range of interest. In particular, it shows the resonances exploited in this work, with $|0,1\rangle_{i,s}$ labeling the resonances at which photons are generated, according to the state notation in Equation 2.3; from left to right: idler (R1 and R2), pump (R1 and R2), and signal (R1 and R2) resonances, spaced by $f = 18.25\,GHz$. (b) Photon-pair generation scheme illustrating the relationship between energy-matched bin triplets belonging to the same microring.*

the entire setup construction or final experimental execution. The spacing $f$ is chosen to achieve efficient frequency-bin mixing in the analysis stage with commercial EOMs, typically operating at frequencies up to 70 GHz at modulation voltages $V_{\mathrm{pp}} \leq 20\,\mathrm{V}$, while maintaining near–zero spectral crosstalk between the frequency modes. Given measured resonance quality factors in the range $Q \sim (100\text{–}120) \times 10^3$, the ratio between the mode spacing and the mode full width at half maximum is $f/\mathrm{FWHM} = f \cdot Q/\nu \approx 100 \gg 1$, indicating that the spacing could in principle be further reduced. In this work, the lower limit for $f$ is set by the frequency–resolving detection stage, which relies on narrowband filters featuring a FWHM $\sim 12\,\mathrm{GHz}$ (detailed in the following section), thus requiring $f > 12\,\mathrm{GHz}$ to enable independent coincidence analysis between photons originating from different frequency bins.

### Generation of photon pairs setup

To characterize the nonlinear response of the silicon MRRs, the generation rate was first measured as a function of the pump power using the setup depicted in Figure 2.2(a). The results for R1 are reported in Figure 2.3, while the rate for R2 is not reported, as it is very similar to that of the first ring. The experimental setup used is described in the following.

Light emitted from a continuous-wave butterfly laser diode at a wavelength

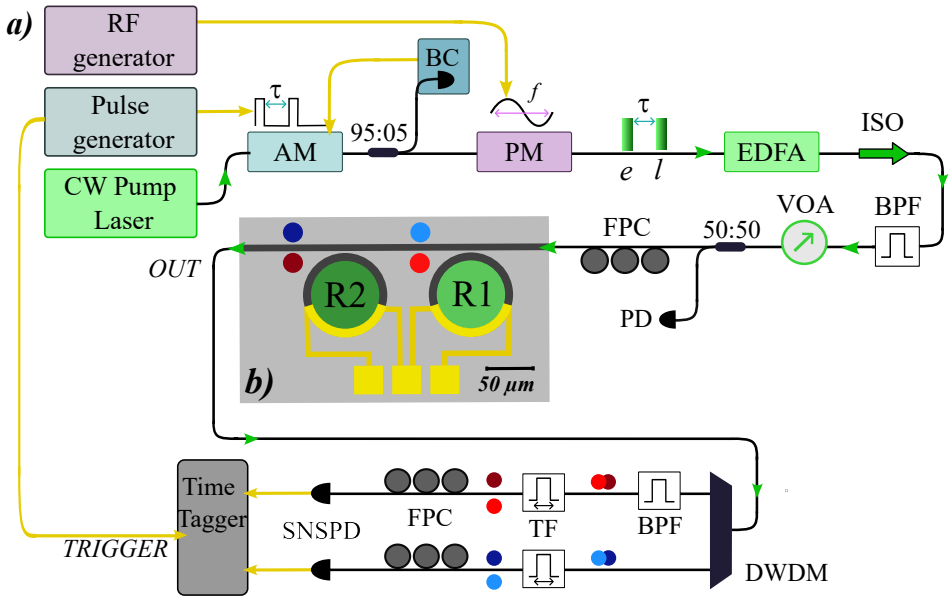



*Figure 2.2:* ***Source generation rate characterization.*** *(a) Setup used for the measurement of the source generation rate. $\tau$ is the pulse delay, applied by the pulse generator to the amplitude modulator (AM); $f$ is the frequency of the RF signal applied by the RF generator to the phase modulator (PM). BC: bias controller, EDFA: Erbium-doped fiber amplifier, ISO: fiber isolator, BPF: free-space band-pass filter within a fiber-to-fiber U-bench, VOA: variable optical attenuator, FPC: fiber polarization controller, TF: tunable filter, SNSPD: superconducting nanowire single-photon detector. (b) Schematic of the chip containing the two rings R1 and R2.*

of 1543.656 nm is amplitude modulated (AM) to carve a train of two rectangular pulses, with a relative delay $\tau = 13$ ns and a duration of $t_w = 2$ ns. The repetition rate of the experiment was set to 50 MHz. To increase the reproducibility of the generated pulses, the AM is locked to its minimum using a bias controller (BC). The coherence between the two pulses, which define the early ($e$) and late ($l$) TB modes, is ensured by the large coherence time of the laser (Santec, TSL–710), which

is much longer than the delay between the pulses: $t_{coh} \sim 1\,\text{ms} \gg \tau$.

The choice of the pulse duration and delay represents a trade–off between the repetition rate of the experiment and the indistinguishability between the joint signal–idler photon wavepackets of the two TB modes. For the former, the limitation lies in the requirement that the pulse duration be shorter than the timescale of other relevant processes occurring in the silicon WG. In particular, at the present optical power levels, the dominant process is the generation of free carriers through two-photon absorption inside the cavity, imposing the condition $t_w \ll \tau_{FC}$. Regarding the time delay between the two pulses, the main constraint is again imposed by the free-carrier dynamics. In this case, the photon pairs emitted in the early and late pulses may not be perfectly indistinguishable, as free carriers generated by the first pulse may not fully recombine before the arrival of the second pulse. This results in different losses and a slight shift in the resonance wavelength experienced by the two pulses. Given these constraints, the delay is set to satisfy $\tau > \tau_{FC}$. The estimated free–carrier lifetime is $\tau_{\text{FC}} \sim 10$ ns, obtained from independent measurements conducted on long WGs with the same cross–section as our sources, employing a methodology and experimental procedure similar to those presented in Figure 1.3.

The modulated pulses are then sent to an electro–optic phase modulator (PM) driven by a sinusoidal signal of amplitude around $V_{pp} = 9\,\text{V}$ at a frequency equal to the chosen FB spacing $f$. This results in the generation of an electro-optic comb composed of several coherent sidebands equally spaced in frequency by $f$ [51].

The modulated pump is then amplified by an Erbium-doped fiber amplifier (EDFA) and filtered by a band-pass filter (BPF) to suppress amplified spontaneous emission (ASE) noise and undesired electro-optic comb lines. In practice, the filter selects only the two central comb lines, one for each pump resonance, thus allowing simultaneous pumping of the two resonators and generation of entangled photon pairs through SFWM in the corresponding sets of idler and signal resonances, as depicted in Figure 2.1. The pump power is controlled by a variable optical attenuator (VOA), monitored through a 3 dB tap, and then coupled to the chip after polarization adjustment using a fiber polarization controller (FPC).

The light exiting the chip is filtered using a DWDM, providing an isolation of approximately 80 dB between non-adjacent ITU channels. The idler photons are separated from the signal and pump photons, which are collected in the same fiber. A free-space BPF (3 dB bandwidth of 5 nm centered at 1555 nm) is then used to eliminate the pump photons, providing an extinction ratio of up to 90 dB. Finally, the frequency bins of interest, corresponding to the idler and signal wavelengths associated with R1 for the generation-rate measurement reported here, are selec-

ted using tunable filters (TFs) based on fiber Bragg gratings (3 dB bandwidth of 12.5 GHz). Frequency-resolved detection is then performed using two superconducting nanowire single-photon detectors (SNSPDs). The electrical signals from the SNSPDs are sent to a time-to-digital converter (Qtag, Time Tagger) for coincidence analysis, together with the trigger from the pulse generator.

**Brightness estimation**

The brightness of the source is extracted from the internal generation rate $\mathcal{R}$, reported in Figure 2.3, i.e., the coincidence counts at the SNSPDs corrected for the total losses from generation to detection. Specifically, by fitting the experimental data (points in the graphs) with a quadratic function of the pump power (solid lines in the graphs), the brightness is commonly defined as the quadratic coefficient. At high power ($> 150\,\mu$W) the rate deviates from the quadratic behavior expected for SFWM generation in Equation 1.19, due to two-photon absorption (TPA) and free-carrier absorption (FCA) in the silicon WG.

In the CW regime, the brightness of the source was previously measured to be $27 \pm 1\,\mathrm{MHz\,mW^{-2}}$ in an earlier experiment. The result, reproduced from Ref. [167], is shown in Figure 2.3(a). In the HE demonstration presented here, the same sample and the same set of resonances were used. However, since the additional time-bin encoding requires pulsed pumping, the pump must operate in the pulsed regime rather than in CW. Therefore, the generation rate $\mathcal{R}$ was measured by operating the chip under the same pulsed conditions used in the experiment, as described in the previous paragraph. The obtained internal generation rate and coincidence-to-accidental ratio (CAR) are reported in Figure 2.3(b) and (c). The latter is defined as:

$$\frac{C_c - C_a}{C_a}\,, \tag{2.1}$$

where $C_c$ and $C_a$ are, respectively, the detection events associated to coincidences under the coicidence peak and accidental events, associated to coincidences delayed by multiples of the repetition period. Both quantities are integrated within equal duration time windows. The quantity $C_c - C_a$ are the coincidence events of proper photon pairs.

From the quadratic fit obtained in the pulsed regime (Figure 2.3 (b)), and considering the average pump power corresponding to the train of pulses, the extracted brightness is $24 \pm 2\,\mathrm{MHz\,mW^{-2}}$, which is compatible within two stand-

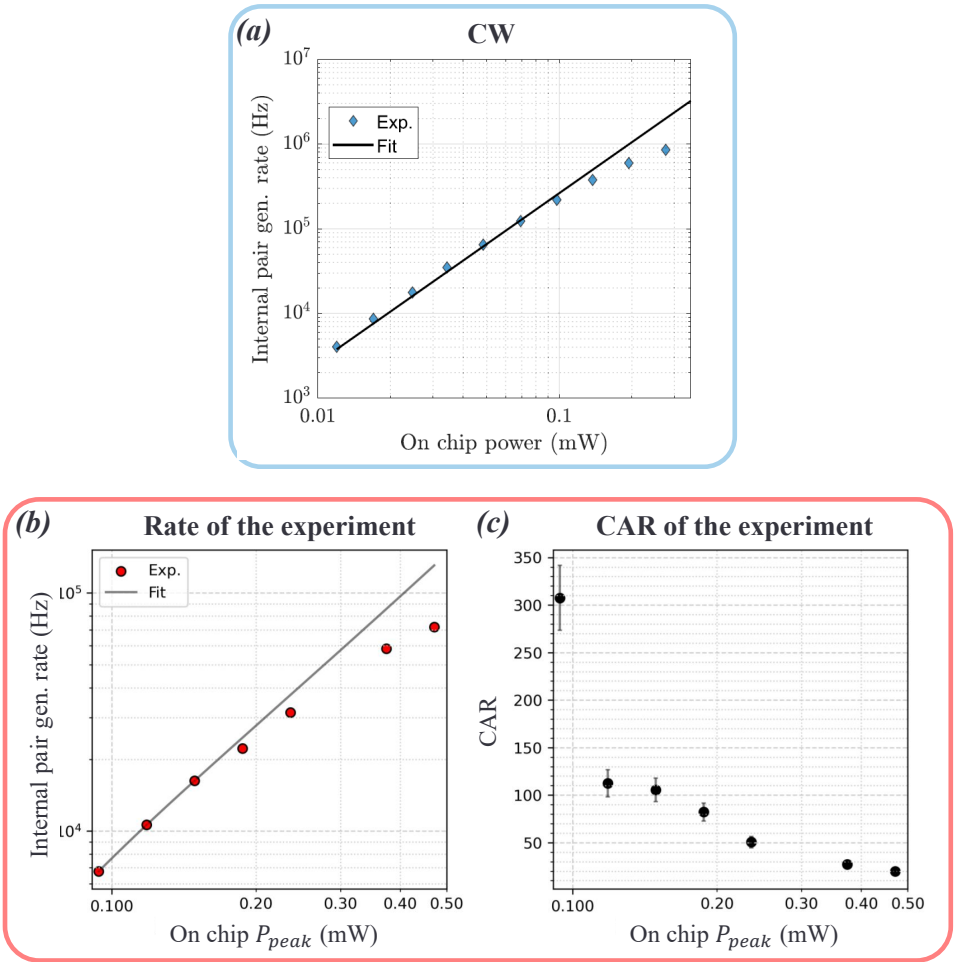



*Figure 2.3:* ***Internal generation rate of one ring resonator as a function of the pump power coupled into the chip.*** *(a) Generation rate in the CW regime (image reproduced from [167]). (b), (c) Generation rate $\mathcal{R}$ and CAR measured in the here reported experiment, using a train of 2 ns-long pulse pairs separated by 13 ns and repeated at 50 MHz. The solid lines in (a) and (b) correspond to quadratic fits of the data, yielding brightness values of $27 \pm 1$ and $24 \pm 2$ MHz mW$^{-2}$, respectively. Error bars are calculated assuming Poissonian statistics for the coincidence counts.*

ard deviations (STDs) with the CW value. Given the average resonance linewidth $FWHM \simeq 15\,\text{pm}$, the measured spectral brightness of the source is $B \simeq 1.5 \cdot 10^7\,\text{Hz}\,\text{mW}^{-2}\,\text{GHz}^{-1}$. This value is comparable to state-of-the-art silicon MRRs, as clearly summarized in the table 1 of Ref.[20].

### 2.2.2 Generation method

The HE biphoton state is created by combining techniques traditionally used for single-DoF entanglement. Specifically, time-bin entanglement is generated by pumping the source with two coherent pulses, while frequency-bin entanglement is obtained by simultaneously exciting two nominally identical MRRs. The complete setup used for the generation and analysis of the HE state is reported in Figure 2.5.

The pump preparation stage is identical to the one described in section 2.2.1. The on-chip pump peak power used in the experiment is $P_{peak} = 350\,\mu$W, selected for the HE state generation demonstration. This pumping power corresponds to an out-of-chip photon-pair rate of HE photons of $\mathcal{R}_{out} = 4.7 \pm 0.1\,$kHz and a coincidence-to-accidental ratio of $CAR \simeq 30$.

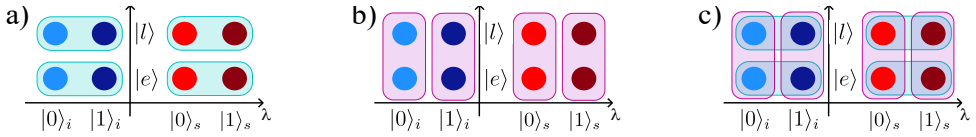



*Figure 2.4:* ***Schematic representation of the biphoton HE state.*** *The four modes are defined as $|0\rangle$ and $|1\rangle$ for the frequency-bin and $|e\rangle$ and $|l\rangle$ for the time-bin DoF, respectively. (a) TB entanglement, (b) FB entanglement, (c) HE state.*

In the pump preparation stage (section 2.2.1), the source is driven by two coherent optical pulses. If these pulses are identical and no distinguishability is introduced between them (as discussed previously with respect to both free-carrier effects and pulse shaping), they have equal probability of triggering photon-pair generation inside the resonators. When, in addition, the generation probability per pulse is kept sufficiently low, multi-pair emission is negligible. Under these conditions, the generated state in the time domain is a TB-entangled biphoton state of the form [171]:

$$|\Phi^+_{TB}\rangle = \frac{1}{\sqrt{2}} \left( |e\rangle_s |e\rangle_i + |l\rangle_s |l\rangle_i \right) , \tag{2.2}$$

where $|e(l)\rangle_{s(i)}$ denote the photon states associated with the signal (idler) photon generated in the early (late) pulse. The more general TB state that may be generated with this scheme can be written as $\propto |ee\rangle + e^{i\phi} |ll\rangle$, where $\phi$ is a relative phase between the two components. In this case, this phase is zero owing to the long coherence time of the CW laser pump, i.e. the carrier, from which the pulses are carved, which guarantees their mutual phase coherence.

The double-ring configuration, together with the generation of two coherent side-

bands at the frequencies of the pump resonances by the off-chip PM, allows each pump pulse to generate a frequency-bin-encoded Bell state:

$$|\Phi^+_{FB}\rangle = \frac{1}{\sqrt{2}} \left(|0\rangle_s |0\rangle_i + |1\rangle_s |1\rangle_i\right) , \tag{2.3}$$

where $|0\rangle_{s(i)}$ and $|1\rangle_{s(i)}$ denote the photon states associated with the signal (idler) FB generated by R1 and R2, respectively. This requires equal generation probabilities in R1 and R2, while keeping the overall pair–generation probability low enough to avoid simultaneous population of both FB modes. In practice, this is achieved by adjusting the intensities of the two electro–optic comb lines used to pump the rings (i.e., the power of the driving RF signal), balancing the generation rates while maintaining a per-pulse generation probability on the order of $10^{-4}$/pulse. Similarly to the TB case, the relative phase between the two components is set to zero. This time, this is ensured by the phase coherence of the employed RF driver (Anapico, APMS20G), offering relative phase stability between different channels of 3 mrad.

With these parameters, the time-bandwidth product is $f \cdot t_w \simeq 36 \gg 1$, which ensures that TB and FB can be treated as independent DoFs. Under these conditions, a genuine two-photon HE state in two DoFs is generated, expressed as the product of the two Bell states:

$$|\Phi^+_{HE}\rangle = |\Phi^+_{TB}\rangle \otimes |\Phi^+_{FB}\rangle = \frac{1}{2} \left(|ee\rangle + |ll\rangle\right)_{TB} \otimes \left(|00\rangle + |11\rangle\right)_{FB} . \tag{2.4}$$

Each of the two photons can occupy a total of four possible modes, as schematically depicted in Figure 2.4. Therefore, the system finally spans a 16-dimensional Hilbert space.

### 2.2.3 Quantum state analysis

To verify the effective generation of the target HE state, the signal-idler photon pairs and the pump are collected by a lensed fiber at the output of the chip and sent to either the time analyzer or the frequency analyzer, respectively denoted as *T-a* and *F-a*, as shown in Figure 2.5(b) and (c). These analyzers allow the implementation

of projective measurements in the three Pauli bases $X, Y, Z$, written as

$$\begin{aligned} Z &= \{|0\rangle, |1\rangle\} , \\ X &= \left\{ \frac{1}{\sqrt{2}}(|0\rangle + |1\rangle), \frac{1}{\sqrt{2}}(|0\rangle - |1\rangle) \right\} , \\ Y &= \left\{ \frac{1}{\sqrt{2}}(|0\rangle + i\,|1\rangle), \frac{1}{\sqrt{2}}(|0\rangle - i\,|1\rangle) \right\} , \end{aligned} \tag{2.5}$$

where $(|0\rangle, |1\rangle)$ label the logical states of either the TB or FB encoding for each DoF. A complete set of measurements is therefore performed to reconstruct the density matrix in both subspaces [172].

In the following, I describe how the projectors are realized, starting from the analyzers' setups and finally reporting the data analysis method used.

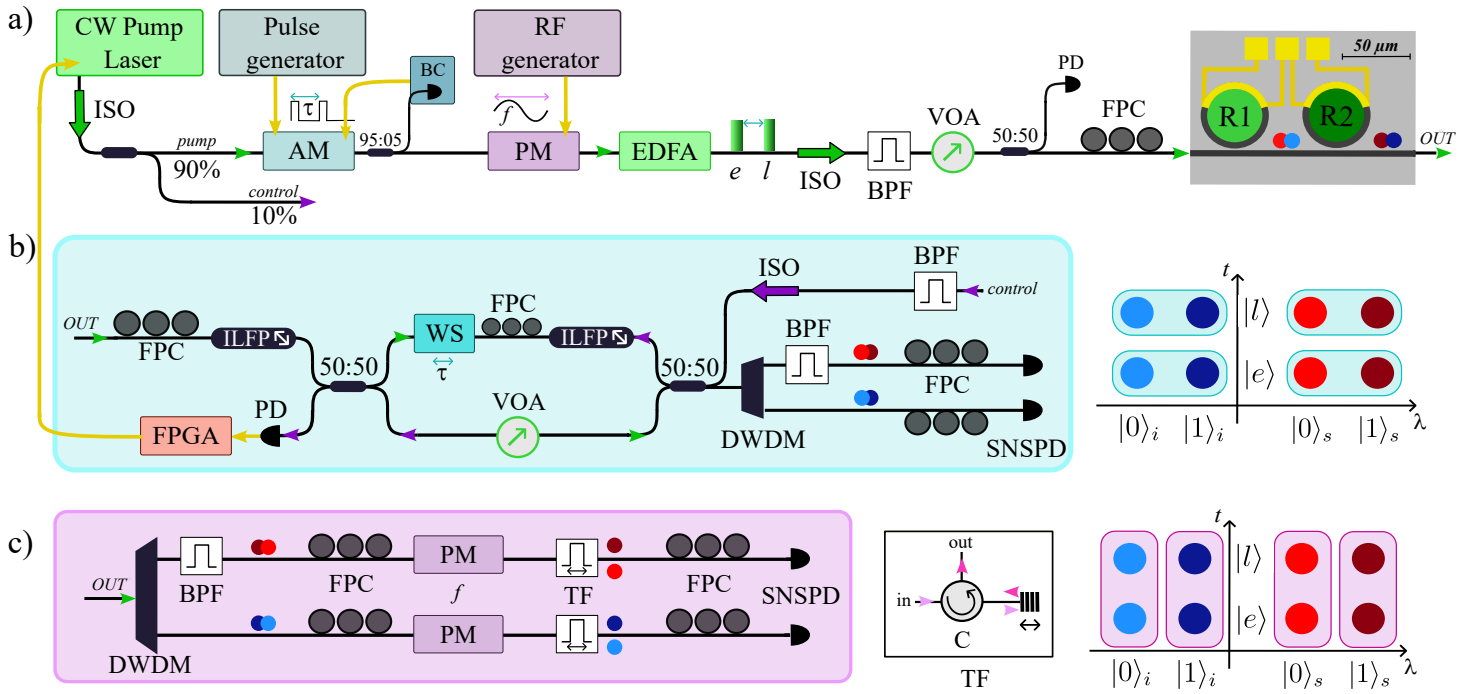



*Figure 2.5:* ***HE state generation and analysis setup.*** *The sketch is divided into the three parts of the setup: (a) generation stage, (b) time analyzer, and (c) frequency analyzer. The direction of the pump laser and of the generated photons is indicated by the green arrows. The purple arrow indicates the direction of the CW control beam. FPGA: Field-Programmable Gate Array, ILFP: in-line fiber polarizer, C: circulator. The other acronyms are reported in the caption of Figure 2.2*

**Time-analyzer**

The time-analyzer stage is based on a fiber unbalanced Mach–Zehnder interferometer [173]. The interferometer is constructed from two $2 \times 2$ 50:50 beam splitters, and its long and short arms introduce a temporal delay exactly equal to the time-bin separation $\tau$. This configuration enables the analysis of quantum states in the time domain, as will be discussed in detail in the following paragraph. In this section, the setup is instead described, emphasizing the practical measurement-based procedure implemented to calibrate it.

To guarantee stable operation, the MZI is actively stabilized. A small portion of the CW pump light, after ASE removal and passage through an optical isolator, is injected into one of the interferometer ports in the counter-propagating direction with respect to the pulsed pump and the generated photons. At the opposite side of the interferometer, a photodiode detects this control beam, and a Field Programmable Gate Array (FPGA) closes the active feedback loop. The FPGA feedback signal controls the wavelength of the butterfly laser, which is thus finely adjusted to maintain the relative phase of the interferometer constant. Locking the interferometer at the relative phase of the pump $\theta^p$ ensures stable interference at the pump wavelength. At the same time, stabilization of the interference of the generated idler and signal photons $\theta^{i(s)}$ is guaranteed by the phase-matching condition of the SFWM process itself [174].

The use of a single MZI for analyzing both signal and idler photons usually introduces a limitation, since it does not allow independent control of the phases $\theta^s$ and $\theta^i$. Here, this issue is overcome by introducing a programmable waveshaper in the long arm, which allows independent control of the amplitude and phase of the signal and idler photons. This innovation greatly simplifies TB quantum-state analysis, eliminating the need for two separate MZIs, both of which would require stabilization to a common reference in order to perform the biphoton projectors necessary for state analysis.

Another critical practical aspect is polarization control of the photons entering the MZI: any polarization drift leads to reduced interference visibility. To address this issue, polarization-maintaining (PM1550) fibers were used whenever possible, and the polarization was adjusted in the sections where a transition from SMF-28 to PM1550 fibers was unavoidable. This was achieved using a FPC and an in-line fiber polarizer (ILFP), ensuring that the output polarization was correctly aligned. This solution was implemented in particular after the lensed fiber and after the WS, both of which are SMF-28-based fiber components.

The WS, together with the ILFP and the FPC, introduces approximately 3 dB of additional loss in the long arm, which is compensated by inserting an attenuator in the short arm. This balancing ensures high indistinguishability between the two optical paths, thus maximizing the visibility of both classical and quantum interference.

After recombination at the output of the interferometer, the photons are demultiplexed: a dense wavelength-division multiplexer (DWDM, Opneti CH58, 80 GHz channel bandwidth) separates the idler from the signal and the pump. In the signal branch, the pump is further suppressed by a notch filter (BPF, Semrock). Finally, the photon pairs are directed to the detection apparatus, consisting of a pair of SNSPDs, each preceded by a FPC to account for their polarization dependence.

**Time-bin quantum state analysis**

The above-described time-analyzer setup realizes a typical Franson-like interferometer [173, 175]. The unbalanced MZI introduces a delay $\tau$ between its two arms, equal to the separation between the early and late time bins. Single-photon detectors, together with the time tagger, register coincidence events, producing the characteristic three-peak histogram in arrival time. These three peaks map directly to the time-bin projectors as follows.

Detection at the early time $\Delta t = 0$ corresponds to pairs generated in the *early* pulse with both photons taking the short (S) arms (SS events); this yields the projector $|ee\rangle\langle ee|$. Detection at the late time $\Delta t = 2\tau$ corresponds to pairs generated in the *late* pulse with both photons taking the long (L) arms (LL events), i.e. $|ll\rangle\langle ll|$. Coincidences in these two lateral peaks therefore provide the diagonal elements of the TB density matrix, corresponding to the $Z$-basis projectors.

The central peak at $\Delta t = \tau$ originates from two processes: pairs generated in the early pulse that both traverse the long arms, and pairs generated in the late pulse that both traverse the short arms. These two processes are indistinguishable at the detectors, thus their probability amplitudes interfere; therefore, coincidences in the central peak implement projectors in the superposition bases (the $X$ and $Y$ bases) of the TB qubit. By controlling the relative phase between the early and late contributions (via the WS in the long arm), different superposition projectors can be implemented. For example, choosing the relative phase $\varphi = \pi$ projects onto the $X$ basis, while $\varphi = \pm\frac{\pi}{2}$ implements the $Y$ basis.

Operationally, TB projectors are realized by post-selecting coincidence events in the three time windows ($\Delta t = 0$, $\Delta t = \tau$, $\Delta t = 2\tau$) and by scanning the WS phase

at the idler and signal frequencies. Importantly, signal and idler photons, regardless of the frequency bin in which they are generated, are processed identically by the WS and the MZI interferometer and are detected according to their arrival time only, without resolving their frequency. As a result, the measurement projects the state in the time domain while effectively tracing out the frequency DoF.

**Frequency-analyzer**

The frequency-analyzer stage is designed to characterize the frequency-bin states of the generated photons. The light collected at the chip output first passes through a DWDM filter, which provides about 80 dB isolation between non-adjacent ITU channels. This allows the idler photons to be separated from the signal and pump photons, which remain in the same fiber. To further suppress residual pump light, a free-space band-pass filter (BPF, Semrock, 5 nm 3 dB bandwidth centered at 1555 nm) is used, achieving up to 90 dB extinction at the signal wavelength.

The core of the frequency-bin analysis consists of two PMs, one acting on the signal and one on the idler photons. They are driven by an RF signal coherent with the input pump. The amplitude of the modulating RF signal is chosen to maximize the power transfer from the carrier to the first-order sideband. However, higher-order sidebands are unavoidably generated by the PMs, leading to scattering into unwanted frequency modes and additional losses. To isolate the desired modes, narrowband tunable passband filters (TFs) based on 12.5 GHz-wide fiber Bragg gratings are placed after the modulators. In particular, the photons are directed to a Bragg grating whose reflection band is tuned by straining the fiber and are finally collected through a circulator (C), as schematically illustrated in the inset of Figure 2.5(c). These filters allow precise selection of the frequency modes, completing the state analysis in the FB subspace. Finally, the photons are directed to superconducting nanowire single-photon detectors (SNSPDs), and detection events are recorded using time-tagging electronics, enabling measurement of coincidence counts between signal and idler photons.

**Frequency-bin quantum state analysis**

The FB projective measurements are implemented through the *F-a* described above. In particular, projectors in the $X_{s(i)}$ and $Y_{s(i)}$ bases require coherent mixing of the $|0\rangle_{s(i)}$ and $|1\rangle_{s(i)}$ frequency-bin states [166]. This is achieved by activating the RF signal that drives the signal (idler) PM and adjusting the RF power to equalize the

intensities of the sidebands involved in the mixing. In this way, coherent interference between $|0\rangle_{s(i)}$ and $|1\rangle_{s(i)}$ is obtained with high visibility. The specific superposition projector is then selected by tuning the RF phase: setting $\phi = 0$ implements the $X_{s(i)}$ basis projector, while $\phi = \pm\frac{\pi}{2}$ realizes the $Y_{s(i)}$ projector. Conversely, the $Z_{s(i)}$ basis projectors are realized by switching off the RF signal, so that no mixing occurs.

As pointed out in the $T$-$a$ description, the procedure here can also be regarded as independent of the other DoF. Since the PMs and TFs are insensitive to photon arrival time, the analysis is performed purely in the frequency domain, effectively tracing out the time DoF. By contrast, the SNSPDs and the time tagger resolve photon arrival times and therefore distinguish between early and late time-bin photons. The trace over the TB DoF is thus performed, for each signal-idler frequency-bin combination, by summing all events over s, i.e. both photons are detected at $\Delta t_{s(i)} = 0$ (pairs generated in the $e$-pulse), $\Delta t_{s(i)} = \tau$ (pairs generated in the $l$-pulse), or with a relative delay of $\tau$.

## 2.3 Results and discussion

To demonstrate the generation of the 16-dimensional target state $|\Phi^+_{HE}\rangle$, I first verified entanglement in the TB and FB DoFs separately and then measured an HE witness. The former is performed by means of quantum state tomography and by extracting the $S$-parameter to verify the violation of the Clauser-Horne-Shimony-Holt (CHSH) inequality [176] in each DoF. The HE witness is necessary to rule out the possibility that the target state, although exhibiting entanglement in each DoF, could be written as a mixture of two or more non-HE states [177]. In addition, two-photon interference fringes were measured in both DoFs, which are required for the calibration of the two-qubit projectors implemented for the entanglement and witness measurements, as explained in the following section.

All the results reported here are published in the peer-reviewed article Ref. [145].

### 2.3.1 Two-photon interference

The signal and idler photons are jointly measured in a superposition basis using either the $F$-$a$ or the $T$-$a$, namely $1/\sqrt{2}(|0\rangle + e^{i\Phi}|1\rangle)$, while the phase $\Phi$ is swept. This results in two-photon interference fringes of the form $\propto 1 + V\cos(\Phi)$. The visibility

$$V = \frac{C_{max} - C_{min}}{C_{max} + C_{min}} \tag{2.6}$$

quantifies the coherence between the two components of the superposition: a value above $1/\sqrt{2}$ is sufficient to violate the CHSH inequality, thus demonstrating entanglement.

In practice, the theoretical phase $\Phi$ defining the measurement basis differs from the experimentally applied phase $\phi$, due to phase offsets introduced by the optical elements of the analyzer. The two are related by $\Phi = \phi - \phi_0$, where $\phi$ is the phase detuning applied experimentally and $\phi_0$ represents the calibration offset determined from the interference measurement. Therefore, the two-photon interference curves are reconstructed prior to the QST and HE witness analyses in order to calibrate the projectors.

### Time-bin interference

The phase $\phi$ is scanned by applying a relative phase shift between the idler and signal wavelengths using the WS in the long arm of the *T-a*. Coincidence counts in the above-defined time windows are recorded. The result is reported in Figure 2.6. The coincidence counts in the central peak (red points) show a visibility of $V_{TB} = (93.2 \pm 1.2)\%$, thus confirming high coherence between the early and late contributions of the TB state.

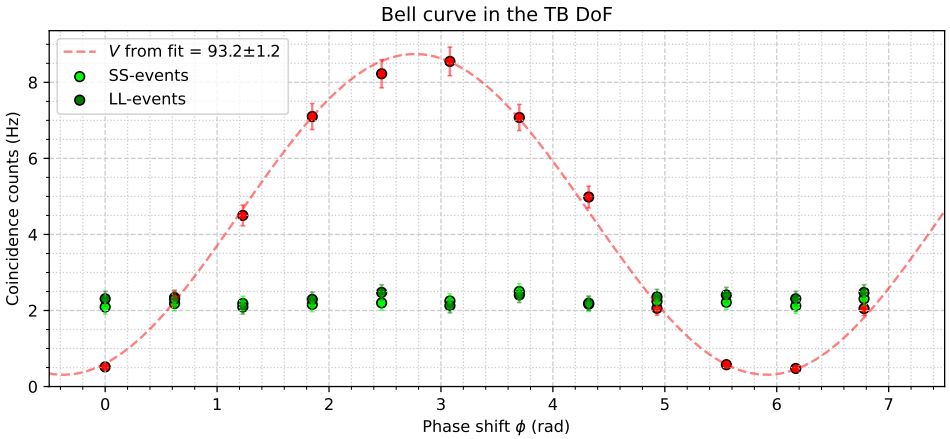



*Figure 2.6:* ***TB two-photon interference.*** *Coincidence counts in the central peak of the time histogram as a function of the phase $\phi$ introduced by the WS in the long arm of the MZI are shown (red points), together with their sinusoidal fit (dashed red line). Coincidence counts in the lateral peaks, corresponding to SS and LL events (green points), are also reported. Error bars are calculated assuming Poissonian statistics for the coincidence counts. Each measurement is integrated for 120 seconds; the reported values are expressed in Hz.*

The counts obtained in the lateral peaks (in green) are also reported in the plot to demonstrate that the sine–like behavior originates from genuine two-photon interference, excluding the possibility that the observed modulation arises from phase-dependent losses in the interferometer. As expected, the peaks corresponding to SS and LL events remain constant over the entire phase sweep, further demonstrating the correct operation of the interferometer stabilization method.

A final remark concerns the phase acquired by the two different FB modes while propagating through the setup before recombination in the MZI. The two modes accumulate slightly different phases, resulting in two distinct Franson interference curves that are shifted with respect to each other. When the frequency DoF is traced out, this phase offset would strongly reduce the measured visibility. To compensate for this effect, a preliminary calibration measurement was performed to determine the relative phase shift, which was then corrected by applying an additional phase offset to one of the two frequency-bin pairs using the WS filter. The result shown above is obtained after applying this calibration.

#### Frequency-bin interference

The phase $\phi$ is scanned by changing the relative phase between the two RF signals driving the idler and signal PM. In this case, the coincidence counts can be recorded either in the first or the second pair of frequency modes, since they correspond respectively to projector $|+\rangle\langle+|$ or $|-\rangle\langle-|$, thus the two curves will differ of only by a $\pi$ phase shift. The result is reported in Figure 2.7, showing a visibility of $V_{FB} = (83.1 \pm 1.4)\%$.

The phase corresponding to the maximum of the curve ($\phi_0$) is recorded and used for the calibration of the projectors employed later.

### 2.3.2 Quantum state tomography

A complete set of two-qubit tomographic projectors is implemented in each DoF, and the corresponding coincidence counts are recorded. In particular, $2^4 = 16$ measurements are performed in each DoF to unambiguously determine the density matrix $\rho_r$. It is then reconstructed using a maximum-likelihood estimation algorithm [166]. Several figures of merit are then obtained: the fidelity with respect to the target density matrix $\rho_t = |\Phi^+\rangle\langle\Phi^+|$, the purity, and the $S$-parameter; they are defined

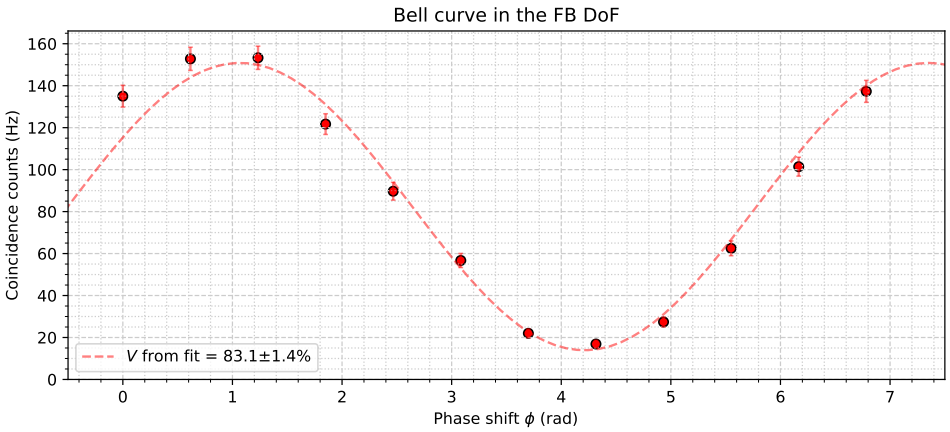



*Figure 2.7:* ***FB two photon interference.*** *Sum of the coincidence counts recorded in the SS-events and LL-events time window (red points). The phase shift $\phi$ reported in the x-axis is introduced in the RF signal by the driver. The dashed red line is a sinusoidal fit of the data. The error bars are calculated assuming Poissonian statistics for the coincidence counts. Each measurement is integrated for 10 seconds, here the values are reported in $Hz$.*

as follows:

$$\begin{aligned} F &= \mathrm{Tr}\sqrt{\sqrt{\rho_t}\rho_r\sqrt{\rho_t}}\,, \\ P &= \mathrm{Tr}(\rho_r^2)\,, \\ S &= \langle\psi|A_0\otimes(B_0+B_1)+A_1\otimes(B_0-B_1)|\psi\rangle\,. \end{aligned} \tag{2.7}$$

The first quantifies the distance between the target state and the reconstructed one, the second quantifies the mixedness of the state, while the last is used to verify the violation of the CHSH inequality, thus demonstrating entanglement.

$A_0$, $A_1$, $B_0$ and $B_1$ are local observables defined for two general qubits (A, B) [176]. In this case, the target state is the maximally entangled Bell state $\Phi^+$; therefore, to achieve the maximum CHSH violation the optimal settings are employed:

$$\begin{aligned} A_0 &= \sigma_Z\,, \\ A_1 &= \sigma_X\,, \\ B_0 &= \frac{1}{\sqrt{2}}(\sigma_Z+\sigma_X)\,, \\ B_1 &= \frac{1}{\sqrt{2}}(\sigma_Z-\sigma_X)\,, \end{aligned} \tag{2.8}$$

where $\sigma_{X,Y,Z}$ are the Pauli matrices. The maximum value achievable by a separable state is $S = 2$, while in the presence of quantum correlations the limit becomes $S = 2\sqrt{2} \simeq 2.828$.

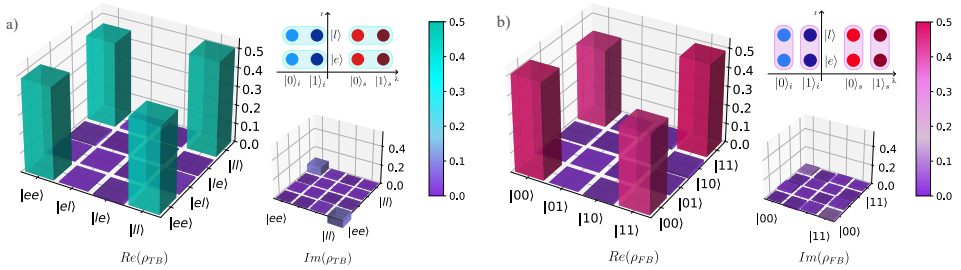



*Figure 2.8:* ***TB and FB reconstructed density matrices.*** *(a) Reconstructed reduced density matrix (real and imaginary parts) of the HE state in the TB subspace, while tracing out the FB DoF. (b) Same as (a), but referred to the FB subspace, while tracing out the TB DoF. The associated fidelity, purity, and S-parameter are reported in Table 2.1.*

The results of the QST in the TB and FB DoFs are reported in Figure 2.8, as the left and right matrices, respectively. The corresponding values of the figures of merit listed above are reported in Table 2.1. The errors are obtained from Monte Carlo simulations by generating multiple instances of the dataset and calculating all the FoMs for each of them. The simulated datasets are generated assuming that the measured coincidence counts follow a Poissonian distribution with a mean value equal to the measured coincidence rate. From the mean and the STD, the experimental value and the associated uncertainty of each FoM are extracted.

| **DoF** | Fidelity (%) | Purity (%) | $S$-parameter |
|---|---|---|---|
| **FB** | $90.6 \pm 1.1$ | $83.7 \pm 1.3$ | $2.55 \pm 0.02$ |
| **TB** | $94.9 \pm 0.6$ | $92.1 \pm 0.6$ | $2.669 \pm 0.013$ |

*Table 2.1:* ***Figures of merit of the reconstructed density matrices.*** *Values of the fidelity, purity, and S-parameter extracted from the reduced density matrix in each DoF. The errors are estimated assuming Poissonian statistics for the coincidence counts.*

The high values of fidelity and purity confirm the successful generation of the target Bell state in both DoFs. Furthermore, the presence of entanglement is confirmed by exceeding the bound of $S = 2$ by more than 27 STDs in both subspaces. The slightly lower values obtained in the FB subspace can be attributed to the reduced indistinguishability between the two frequency modes, as discussed later.

### 2.3.3 HE witness

Following Refs. [178, 179, 177], various witness operators can be defined for a generic connected two-particle graph state, differing in the number of measurements required and, consequently, in their robustness against noise. To preserve the clarity and efficiency of the quantum state analysis methods developed here, the following operator was chosen as the HE witness:

$$W = (N-1) - \sum_{k=1}^{N} S_k \,, \tag{2.9}$$

where $N = 2 \cdot d$, $d$ is the number of DoFs, and $S_k$ are the *stabilizers* of the HE state, which in our specific case are

$$S_1 = \sigma_{X\,s}^{TB}\,\sigma_{X\,i}^{TB} \quad S_2 = \sigma_{Z\,s}^{TB}\,\sigma_{Z\,i}^{TB} \quad S_3 = \sigma_{X\,s}^{FB}\,\sigma_{X\,i}^{FB} \quad S_4 = \sigma_{Z\,s}^{FB}\,\sigma_{Z\,i}^{FB} \tag{2.10}$$

The Pauli matrices $\sigma_{X_j,Z_j}^{TB(FB)}$ act on the $j = \{s, i\}$ photon in the TB (FB) subspace. Crucially, they are all two-qubit operators defined within a single subspace; therefore, they can be measured using the two separate time and frequency analyzers implemented in the experiment.

The defined witness $W$ confirms the presence of HE whenever $\langle W \rangle < 0$. Experimentally, a value of $-0.60 \pm 0.01$ was measured, as reported in Table 2.2, which is lower than the bound for non-HE states ($\langle W \rangle \geq 0$) by 60 standard deviations.

| $\langle S_1 \rangle$ | $\langle S_2 \rangle$ | $\langle S_3 \rangle$ | $\langle S_4 \rangle$ |
|---|---|---|---|
| $0.905 \pm 0.005$ | $0.981 \pm 0.004$ | $0.720 \pm 0.007$ | $0.994 \pm 0.001$ |
| $\langle W \rangle = -0.600 \pm 0.010$ | | | |

*Table 2.2:* ***Measured values of stabilizers and witness.*** *The values of the four stabilizers $S_k$ defined in Equation 2.10 are reported, together with the value of the witness $W$ defined in Equation 2.9. The errors are estimated assuming Poissonian statistics for the coincidence counts.*

Therefore, it can be concluded that the generated state is indeed hyperentangled in the TB and FB DoFs.

### 2.3.4 Discussion

Here the reported above experimental results are discussed, comparing the different achieved results, mostly in terms of visibility of the two-photon interference, purity of the reconstructed state and indistinguishability of the generated photons. Finally, a comparison between the measured and the ideal HE witness is also reported.

**Purity in the FB subspace** The maximum achievable purity and fidelity of a frequency-encoded density matrix are limited by the indistinguishability of the photons populating the frequency modes, as derived in Ref. [166]. This is further confirmed by the independently measured two-photon interference visibility. For a two-dimensional bipartite system, the visibility obtained in a Bell test coincides with the photon indistinguishability. A visibility of $(83.1 \pm 1.4)\%$ was measured, which also sets the limit for the obtainable purity of the FB marginal state, measured to be $(83.7 \pm 1.3)\%$.

The imperfect indistinguishability in the frequency-bin DoF is mainly attributed to the different lineshapes of the resonances encoding the logical states $|0\rangle$ and $|1\rangle$, which exhibit slightly different quality factors and extinction ratios. These differences originate from fabrication inhomogeneities between the two rings and from the stochastic sidewall roughness of the waveguides, which leads to different amounts of backscattering in the two resonators.

**Purity in the TB subspace** The measured purity of the state in the TB subspace is $(92.1 \pm 0.6)\%$, consistent with the two-photon interference visibility of $(93.2 \pm 1.2)\%$. The deviation from unit purity is most likely due to thermal and free-carrier relaxation occurring between the two consecutive pump pulses. As a result, the resonance wavelength and the amount of free-carrier absorption slightly differ between the early and late pulses, introducing distinguishability in the joint temporal emission of photon pairs. This effect can be mitigated by increasing the time separation between the pump pulses, although at the cost of a reduced generation rate in the experiment.

**CHSH and purity** The observed large violation of the CHSH inequality is consistent with the measured purity of the state. This can be demonstrated by considering a simple noise model that accounts for the non-unit purity: a white depolarizing noise channel. The ideal density matrix $\rho_t$, either in the time or frequency domain,

is thus replaced by a Werner density matrix [180] described by:

$$\rho_w(\eta) = \eta\rho_t + (1-\eta)\frac{\mathbb{I}_4}{4}\,, \tag{2.11}$$

where $\eta$ is the mixing parameter. The purity and the $S$-parameter of this non-ideal state can be written as:

$$P_w(\eta) = \mathrm{Tr}[\rho_w^2] = \frac{1+3\eta^2}{4} \quad ; \quad S_w(\eta) = 2\sqrt{2}\,\eta\,. \tag{2.12}$$

For example, in the FB subspace a purity of $P_{FB} = 83.7 \pm 1.3\%$ was measured, corresponding to a CHSH parameter of $S_w(\eta) = 2.5 \pm 0.02$, which is consistent within a 2-STD range with the measured value $S = 2.55 \pm 0.02$. Therefore, it can be concluded that the lower value of the CHSH parameter compared to the theoretical maximum bound is due to the non-unit purity of the state, and is consistent with the other presented results.

**HE witness value** Despite the lower robustness to noise of the chosen metric compared to other HE witnesses [177], the violation of the non-HE limit ($W = 0$) is observed by 60 standard deviations. This confirms that the amount of noise present, both during the generation and the analysis stages, is negligible.

The deviation from the maximally hyperentangled value $W = -1$ is mainly due to the imperfect indistinguishability between photon pairs generated in the two sources, which can be equivalently described as the action of a depolarizing noise channel, as previously discussed. The same considerations applied to the purity-limited CHSH parameter also extend to other entanglement metrics, such as the single-DoF entanglement witnesses. Using the same notation, the witness for each DoF $n = (\mathrm{TB}, \mathrm{FB})$ is defined as:

$$W^n_{DoF} = \mathbb{I}_2 - \sigma^n_{Z\,i}\sigma^n_{Z\,s} - \sigma^n_{X\,i}\sigma^n_{X\,s}\,. \tag{2.13}$$

The non-entangled limit is again $W^n_{DoF} \geq 0$, while the maximally entangled state yields $W^n_{DoF} = -1$.

Since the chosen HE witness $W$ is a linear combination of the single-DoF witnesses, the imperfect indistinguishability that limits the purity in each DoF also explains the deviation between the experimental value and the ideal case.

## 2.4 Conclusions and further perspectives

In this chapter, I reported the first demonstration of hyperentangled state generation from multiple integrated SFWM sources. The setup presented here, built around a previously designed and fabricated silicon photonic chip featuring a pair of high-brightness MRRs, enables both the characterization of the source performance and the implementation of two-qubit projectors in the employed time– and frequency–*bin* encodings. I presented the methods and experimental results used to derive the figures of merit required to certify the generation of a genuine hyperentangled state. In particular, a high level of entanglement and purity was measured in the two marginal states, together with fidelities exceeding 90% with respect to the maximally entangled Bell states, confirming the presence of bipartite entanglement in both DoFs. Moreover, by employing hyperentanglement witnesses, I demonstrated the presence of hyperentanglement. The experimental results were further analyzed in the discussion section, where two-photon interference metrics were quantitatively compared with those derived from QST, showing good agreement with the theoretical expectations.

Although the complete quantum state tomography of the target HE state goes beyond the scope of the present study, the setup introduced here would in principle permit its realisation by serially connecting the time– and frequency–analyzers. In the present implementation, the main limitation arises from the insertion losses of the analyzers, which would require relatively long integration times for each of the $16^2$ four-qubit projectors ($\sim$ 10 minutes per setting). However, considering that the number of required measurements can be significantly reduced using recently developed tomographic techniques [181], the presented method could enable complete hyperentangled–state tomography without suffering from long–term instabilities, such as chip–fiber misalignment.

The presented experimental configuration also allows one to scale up the dimensionality in the FB DoF without significantly increasing the complexity of the setup. This would require coherently pumping multiple microring resonators simultaneously and increasing the number of sidebands generated by the input and output phase modulators, as previously reported in Refs. [165, 166]. In the time domain, higher–dimensional states can be generated by increasing the number of time bins. Their analysis would require cascaded interferometers with delay lines of increasing length, which would in general need to be stabilized. A solution has already been demonstrated in Ref. [162], where these interferometers have all been integrated, thus removing the need for active stabilization and confirming that the

extension of the time dimension represents a concrete continuation of the present work. This method, however, comes at the cost of a reduced repetition rate and a decreased generation rate. Therefore, strategies to mitigate the reduction in photon counts will be necessary, such as further integration of the optical components or the adoption of post–selection–free schemes as in Ref. [163], where the efficiency of the analysis setup is improved.

The presented method for the generation and analysis of FB and TB HE states is compatible with *other* DoFs, such as polarization or spatial modes. In particular, the next chapter explores a new generation of silicon photonic circuits aimed at advancing this research direction. The integration of polarization– or path–encoded sources, while keeping the existing architecture presented here for simultaneous TB and FB entangled state generation, would enable the generation of hyperentangled states in three DoFs, further enlarging the accessible Hilbert space.

# Chapter 3

# Integration of sources of hyperentangled photon pairs

In this chapter, I present the next generation of silicon quantum photonic sources, which exhibit a higher level of integration compared to the device presented in the previous chapter. In particular, I report novel designs of hyperentangled sources that introduce on–chip routing and manipulation stages for idler and signal photons, while exploiting additional degrees of freedom such as polarization and position (usually referred to as *path* in integrated circuits).

After introducing the proposed sources and reviewing the related state of the art, I describe the SOI photonic platform used to realize the desired circuits. In particular, the presented chip stack corresponds to the technology employed for the fabrication of tunable SiPh devices on the 300 mm Si300 nm pilot line of CEA-Leti (Grenoble). I thus present the design of the full chip, supported by the numerical simulations which guided the choice of the final geometrical parameters.

Finally, I report the results of the morphological and optical characterization performed at the wafer scale, carried out during my research stay at CEA–Leti. They validate the fabrication process and confirm the expected performance of the fabricated devices. At the current stage, only passive components have been fabricated and tested at wafer scale, enabling an assessment of the routing and filtering functionalities of the circuits, together with the figures of merit of the microring resonator sources through their spectral features.

## 3.1 Background and motivation

The scalability of quantum photonic technologies strongly depends on the ability to integrate not only efficient sources of entangled photons, but also the circuitry required for their routing, filtering, and manipulation. In fact, the fidelity of quantum algorithms and gates is highly influenced by optical losses, as well as by phase and thermal stability, all greatly improvable by means of integrated photonic platforms. The performance of current integrated devices is, however, generally not sufficient to demonstrate fundamental breakthroughs in the field, such as computational operations in the fault–tolerant regime [182, 8], for which photon loss still remains the primary limitation [183]. For this reason, further engineering efforts are required, with the purpose of developing ultra–low–loss integrated building blocks which can be assembled into larger architectures. In particular, complex integrated circuits for scaling toward multidimensional programmable quantum states exhibiting rich entanglement structures are currently being developed, with the final goal of accomplishing several record quantum information processing tasks [**2023_Lee_4qubit**, 184, 185, 8].

Silicon and silicon nitride have emerged as the leading material platforms for quantum photonic circuits, combining the advantages of large–scale CMOS fabrication, high optical confinement, strong third-order nonlinearity, and mature design libraries, all necessary requirements for addressing the scalability challenge. These unique properties have already enabled the realisation of compact sources of entangled photon pairs with on–chip high–dimensional manipulation [37, 186, 187], as well as integrated multi–photon quantum information processing [188, 189, 190]. The long–term vision is that of a *"quantum lab–on–a–chip"*, where the generation, manipulation, and detection of quantum states are all performed within a single integrated device [191, 186]. For a more comprehensive overview of quantum demonstrations based on integrated photonic circuits, refer to the review articles in Refs. [14, 25, 192].

A significant milestone in this direction has been achieved by PsiQuantum, which demonstrated a fully integrated silicon nitride platform featuring SFWM–resonator–based photon–pair sources, electro–optic phase shifters, and superconducting nanowire single–photon detectors [186]. This work represents a major experimental breakthrough for photonic hardware, showcasing state–of–the–art losses for most of the integrated components and opening the way to feasible large–scale quantum photonic integration.

Within this broad and fast–evolving context, the work presented in this chapter

introduces novel designs aimed at achieving a higher degree of integration compared to the results discussed in chapter 2, while also enhancing the dimensionality and complexity of the generated entangled states. In particular, the final goal is to obtain CMOS–compatible efficient on–chip generation of high–dimensional quantum states, leveraging the unique capability of hyperentanglement and including processing and filtering stages to minimize optical losses. These devices are intended for future quantum communication and quantum information–processing experimental demonstrations.

## 3.2 State of the art

The combination of single or multiple silicon sources, together with engineered photonic circuits, can enable the generation of different types of biphoton states, including path [37, 193], polarization [194] (see Figure 3.1(a)), [195], time–bin [162], and frequency–bin [130, 165] entanglement. A more general introduction to off–chip demonstrations has already been reported in Sections 2.1 and 2.1.1, while a more complete survey of chip–based multi–dimensional and multi–photon entangled states can be found in the review paper Ref. [35].

Here, I briefly review the state of the art of integrated HE sources that are more closely related to the designs presented later in this chapter, which combine in integrated platforms frequency–bin with path *or* polarization, and eventually time–bin, in different combinations. Some of those remarkable devices are also summarized in Figure 3.1.

Chip–based demonstrations of entangled states combining frequency or energy–time and polarization have already been reported in the literature. In particular, AlGaAs–based devices capable of directly generating hybrid polarization–frequency entangled biphoton states without post–manipulation were demonstrated in Ref. [198], with the further possible perspective of shifting the paradigm to hyperentanglement by modifying the semiconductor stack, similarly to what was previously proposed in Ref. [199]. Other relevant works are reported in Ref. [155] (see Figure 3.1 (b)), [153], where energy–time entanglement is generated on chip (consisting of a silicon MRR and a periodically poled lithium niobate (PPLN) waveguide, respectively), while the polarization DoF is entangled off chip by means of a fiber loop including a polarization beam splitter, thus resulting in proper energy–time–polarization HE.

More recently, a proposal for a fully integrated source of polarization and frequency–bin HE photon pairs was put forward in Ref. [196], also reported in Figure 3.1 (c).

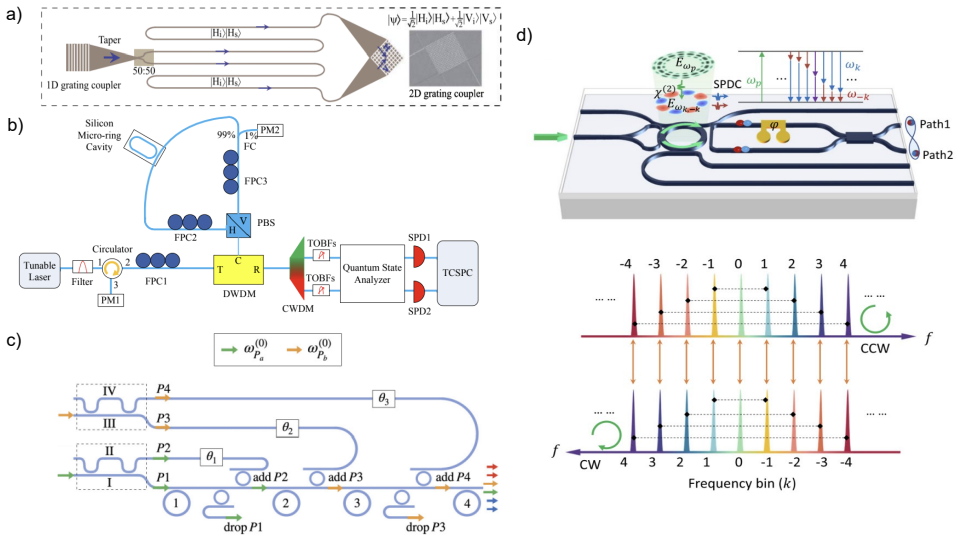



*Figure 3.1:* ***Chip–based entangled and hyperentangled state generation.*** *(a) Generation of polarization–entangled photon pairs on a SiPh chip based on path–to–polarization conversion through a 2DGC (source [194]). (b) Energy–time and polarization hyperentanglement generation exploiting a SiPh MRR (source [155]). (c) Theoretical work on a chip–based frequency–bin polarization HE source (source [196]). (d) Energy–time and path entanglement generation on a chip (source [197]).*

The authors propose generating photon pairs in an arrangement of multiple ring resonators, excited simultaneously by an engineered pump laser beam composed of multiple frequency lines and prepared in a coherent superposition of horizontal ($H$) and vertical ($V$) polarization modes. Importantly, the ring resonators are also specifically designed to selectively couple to different spectral and polarization components of the pump. The strategy proposed in this research work (see subsection 3.2.1) simplifies this scheme by removing the need for both pump and WG polarization engineering, directly obtaining frequency–bin and polarization HE states by injecting single–polarization (TE) laser light and converting the path DoF of the generated photon pairs (generated and propagating along the chip in the fundamental TE mode) into the polarization DoF with the two–dimensional grating coupler (2DGC).

Concerning frequency or energy–time and path hyperentanglement on chip, fewer integrated circuits have been dedicated to the generation of such HE states. A remarkable architecture toward path–frequency HE is reported in Ref. [197], reported also in Figure 3.1 (d). Two parallel frequency combs, generated through a single MRR exploiting CW and CCW circulating modes, are used to generate

photon pairs in two distinct path modes; a complete certification of HE is, however, not covered in the article.

Finally, other remarkable on–chip proposals and experimental demonstrations of other DoF combinations are also reported in the literature, such as path–polarization [200, 201]. More recently, on–chip HE distribution and entanglement purification based on polarization–spatial HE states were shown in the preprint Ref. [202], demonstrating how this field is constantly evolving and how the development of novel integrated sources of hyperentangled photon pairs is crucial for the advancement of quantum photonic technologies.

### 3.2.1 Proposed source architectures

The designs proposed here are SFWM–based sources of HE photon pairs. They again exploit time–bin and frequency–bin DoFs while additionally introducing polarization or path encoding, together with integrated routing and filtering functionalities. The sources comprise MRRs for photon–pair generation, MZIs for both pump-laser routing and path–encoded state analysis, cascaded–MZI filters for idler and signal separation, and couplers for light injection and extraction. Most of the components have been simulated and designed within the framework of this research work, following the methods reported in chapter 1, with the exception of the couplers (GC and 2DGC), which were taken from the Si300 nm PDK provided by CEA–Leti.

The proposed circuits are schematized in Figure 3.2. They can be divided into two categories, depending on the type of encoding: frequency–bin and polarization (FB–Po), and frequency–bin and path (FB–Pa). Polarization encoding is enabled through a path–to–polarization on–chip conversion implemented using 2DGCs, which are standard components available in foundry PDKs. This approach allows transmission through a single optical fiber rather than two, while remaining fully compatible with silicon photonics platforms. Although the path DoF requires dual independent fibers at the output of the chip (one per path, i.e., one per logical state), it is particularly appealing as it is the most straightforward to manipulate on–chip. Indeed, while manipulating polarization on–chip requires complex polarization rotators or splitters, not included in this design, a simple MZI with internal and external phase shifters directly performs arbitrary single–qubit rotations on path–encoded qubits. Integrating one MZI on the signal arm and another on the idler arm allows full projective measurements (and quantum state tomography) to

be performed entirely on–chip before detection.

These two types of circuits, illustrated in Figure 3.2(a,b) and Figure 3.2(c), respectively, are also compatible with an additional degree of freedom: time–bin. This can be achieved under the time–bandwidth constraint, as mentioned in the previous chapter. Such three–DoF HE state generation would constitute, to the best of my knowledge, the first demonstration through integrated sources.

In addition, some circuits further incorporate on-chip routing and filtering functionalities, as shown in Figure 3.2(b), thus contributing to the attempt to fully integrate all the necessary manipulation steps on chip. For all circuits, two versions are included: one with all–pass ring resonators, to reach high generation rates at critical coupling, and another with add–drop rings of lower Q-factor, compatible with high–repetition-rate short–pulse pumping. Moreover, the AD scheme also offers simpler operation, since the integrated sources are only two instead of four, as explained in more detail in the description of the working principle of these sources below.

The generation scheme is common to all circuits. A laser pump is coupled into the chip through a GC and split into two arms by a tunable MZI. Each arm feeds a pair of MRRs, where photon pairs are generated through SFWM. In the present design, two nominally identical MRRs are integrated per arm. Consequently, FB entanglement requires a pumping scheme analogous to that implemented in subsection 2.2.2, in which two coherent pumps simultaneously excite the two resonators, as schematically illustrated in Figure 3.3(a). The pump laser light is coupled to the fundamental TE modes of the integrated MRRs, generating idler–signal photon pairs again in the fundamental TE mode of the WGs.

In the AD version of the circuits, only two physical MRRs are present instead of four; however, an equivalent configuration is achieved by exciting orthogonal resonant modes associated with the two pump paths. Following the method reported in [197, 195], clockwise (CW) and counter–clockwise (CCW) modes are exploited to generate photon pairs in two distinct path modes. This approach removes the possibility of partial distinguishability between photons generated in the two paths, which may arise in the AP scheme due to fabrication imperfections. Moreover, since only two rings are required, the AD version is simpler to operate. In a practical scenario, residual effects, such as backscattering and coupling asymmetries, can still introduce minor distinguishability between the two generation processes.

Consider first the circuits designed for FB–Po encoding. The corresponding working principle is illustrated in Figure 3.3. After photon–pair generation in the

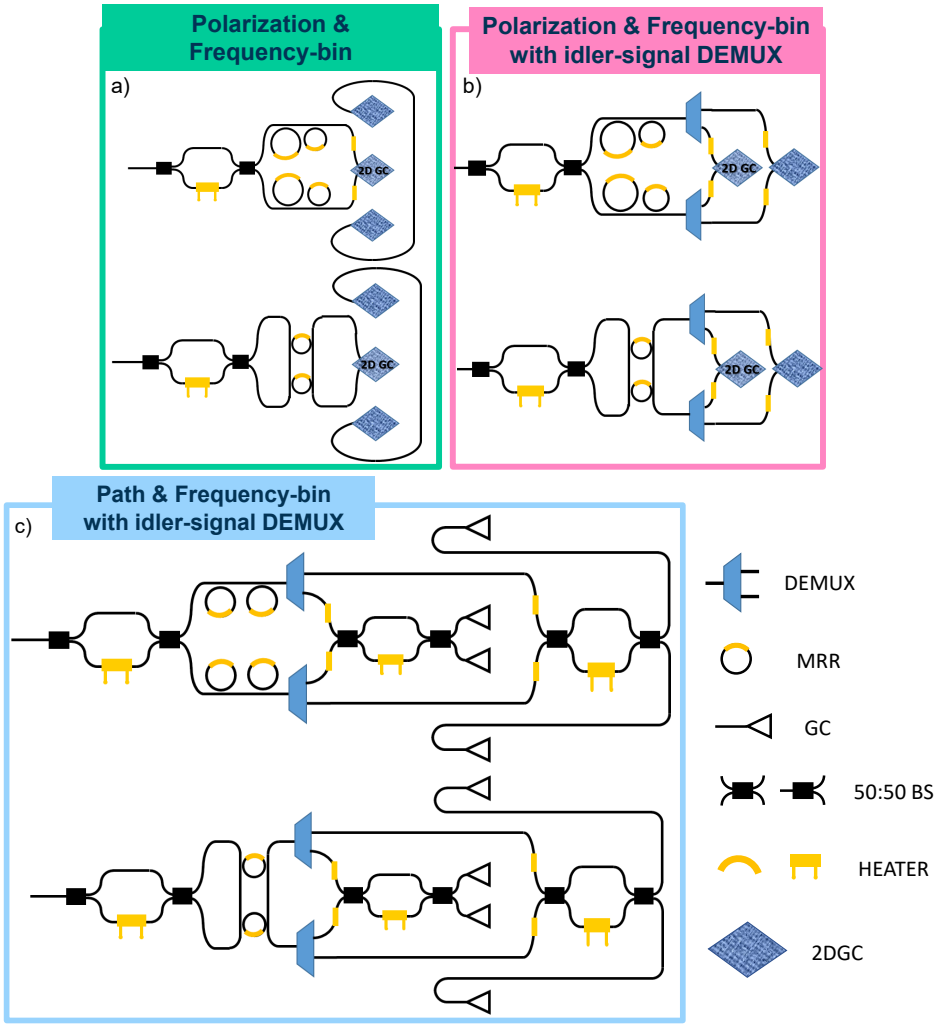



*Figure 3.2:* ***Overview of the integrated hyperentangled photon–pair sources.*** *The circuits here schematized have been integrated on a mask dedicated to 300 mm Si300 nm platform. (a,b) FB–Po, (c) FB–Pa. (b) and (c) illustrate versions with on-chip idler and signal separation. The used symbols are listed in the legend.*

ring 0 and ring 1 resonant modes (defining the frequency-bin encoding) and in both propagation paths (*UP* and *DOWN*), the photons are converted into two orthogonal polarization modes at the output fiber by means of a 2DGC. In the absence of interference between coherent fields originating from the two paths, the 2DGC maps photon pairs generated in the *up* and *down* paths onto the diagonal ($|D\rangle$) and anti–diagonal ($|A\rangle$) polarization states of the output SMF–28 fiber. State analysis

is then performed off chip. In the circuit version including on-chip idler and signal separation, cascaded MZI filters (defined in subsection 1.6.1) are employed, and the two photons are routed to separate 2DGCs for collection with a fiber array. The

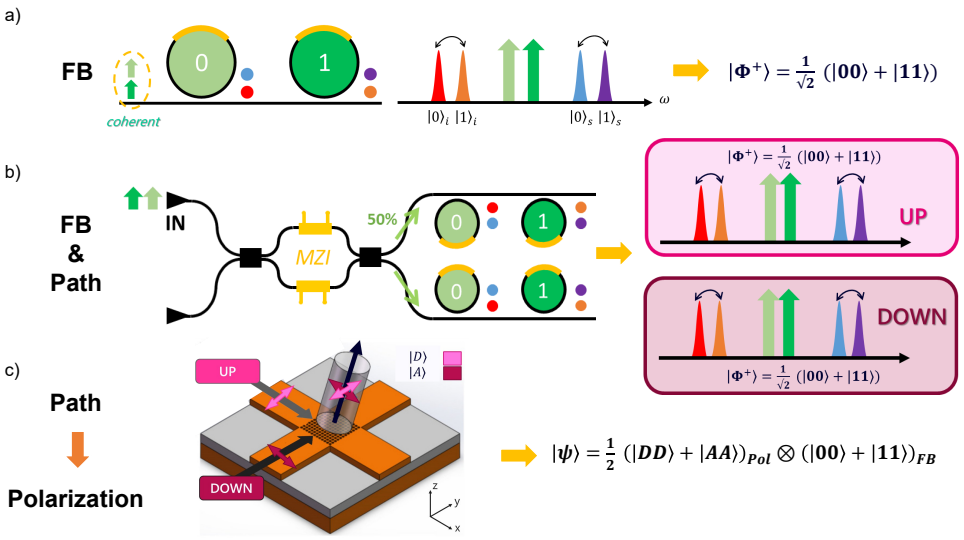



*Figure 3.3:* ***Operating principle of the FB–Po source.*** *(a) photon–pair generation, (b) path routing, (c) path–to–polarization conversion.*

second class of circuits, shown in Figure 3.2(c,d), is designed to generate HE states in the FB–Pa DoFs. In this case, after generation in the MRRs, the photons are routed through cascaded MZI filters to separate idler and signal photons on chip. Each photon is then directed to an on-chip analysis stage implemented by an MZI. Finally, the photons are coupled out of the chip through standard GCs and collected using a fiber array. In this case, PM1550 fiber can be used, since the polarization twisting induced by the birefringent fiber does not affect the quantum state, as polarization is not involved here.

All the designed components are compatible with the standard process flow of CEA-Leti, which consists of a series of well–established lithography, etching, deposition, annealing, and polishing steps used to realize low–loss tunable devices. The proposed HE sources use thermally tunable MZIs and MRRs, thus offering a high degree of reconfigurability and scalability.

## 3.3 Fabrication

The devices are fabricated in the 300 mm SiPh pilot line at CEA-Leti, which enables the realisation of fully etched and partially etched silicon components, such as strip and rib WGs, but also heaters for optical tuning, routed to the chip surface via metal layers for electrical control. The complete chip cross–section is shown in Figure 3.4. In this section, I describe the fabrication methodology by first detailing the overall process flow, followed by a systematic definition of each specific layer, required to integrate our tunable quantum photonic sources onto the silicon substrate.

### 3.3.1 Process flow

The fabrication process flow includes two WG–definition levels (WG and PROT-MOD), one heater level, and two metal layers with their corresponding via layers, i.e. the thin pillars connecting metal layers integrated at different stack levels (see Figure 3.6). Each layer corresponds to a quartz–chrome photomask used to physically transfer the patterns onto the wafer surface. The mask design, often referred to as the *mask layout*, is performed using the software Cadence Virtuoso [203] through its scripting language (SKILL).

Once the chip layout is completed, i.e. once the geometry of the entire chip

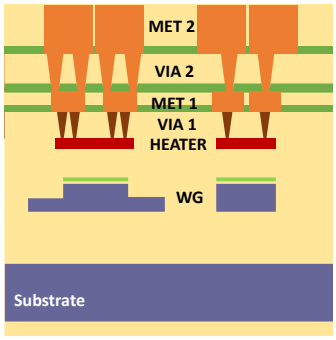



*Figure 3.4:* ***cross–section of the chips.*** *Final cross–section of the Si300 nm-thick 300 mm platform for tunable silicon photonic devices of CEA-Leti.*

surface is defined for all the fabrication layers in the stack (see the design and simulations paragraph 3.4), a GDSII file is generated by the software. This file contains all the information necessary to produce the physical masks used during the photolithography steps. From now on, I will simply refer to it as the *GDS* file or *layout*,

as commonly done in the integrated circuits field.

The fabrication of typical SiPh circuits starts with a batch of 300 mm SOI

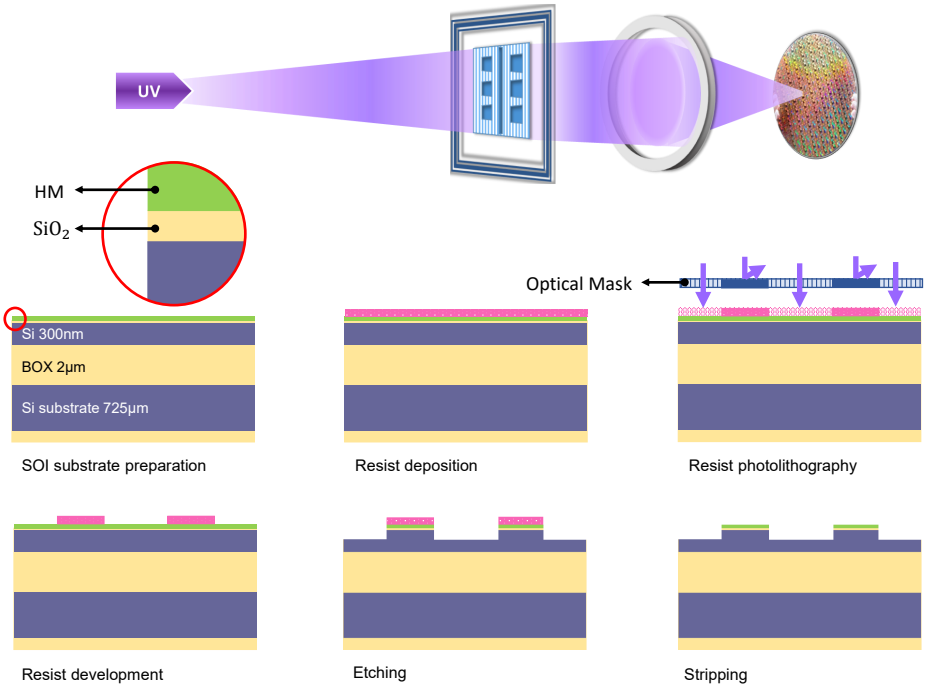



*Figure 3.5:* ***Schematic of the photolithography process.*** *After preparation of the SOI substrate (20 nm-thick $SiO_2$ and 90 nm-thick $Si_3N_4$ layer deposition), a photoresist (or resist, shown in pink) is deposited on the surface. The patterns defined on the photomask are projected onto the resist and subsequently developed, such that the regions exposed to UV light are removed (positive-resist mechanism). The pattern is then transferred to the underlying layers by etching the surfaces not protected by the resist. Finally, the remaining resist is stripped, leaving only the patterned material on the wafer.*

wafers. The wafers used here consist of the following three-layer stack: a crystalline silicon substrate (approximately 700 $\mu$m thick, bottom), a 2 $\mu$m-thick buried oxide (BOX) layer made of silica, and a 300 nm-thick crystalline silicon top layer dedicated to optical guiding (top). The wafer is prepared for fabrication by first depositing a 20 nm-thick $SiO_2$ layer, followed by a 90 nm-thick $Si_3N_4$ layer deposited through Plasma Enhanced Chemical Vapor Deposition (PECVD). The latter serves as an etching stopper, i.e. a hard mask (HM), as explained more clearly later.

Once the photomasks are ready, the pattern transfer onto the wafer surface is achieved through a sequence of photolithography, etching, and stripping steps. The masks are composed of glass and chromium, which respectively transmit and block

the incident deep-UV light at a wavelength of 193 nm. As schematically shown in Figure 3.5, the patterns defined on the mask are projected onto the photoresist through an optical reduction system, shrinking the original chromium–glass mask area (approximately $15 \times 15$ cm$^2$) onto individual dies of $26 \times 33$ mm$^2$. This projection is repeated multiple times across the wafer, resulting in several identical replicas of the same photonic circuits. Each replica is referred to as a *die*; finally, a total of 51 dies are fabricated on a single 300 mm wafer.

To improve resolution [204, 205], immersion lithography is employed for the WG and PROTMOD layers. In this process, a thin layer of water is introduced between the final lens and the wafer surface to increase the numerical aperture of the optical system. After light exposure, the resist is developed to remove the exposed regions (positive-tone resist), thereby exposing the wafer surface to the subsequent etching step. The etching technique and the resist composition vary depending on the materials, their thicknesses, and their specific role. For example, in the processes defining the WG sidewalls, it is critical to maintain vertical profiles, low roughness, and minimal critical dimensions. Therefore, a high-resolution chemically amplified trilayer resist is used [206], and the etching is performed using an Inductively Coupled Plasma (ICP) machine, which provides high etch rates while maintaining high selectivity and low-damage processing.

After etching, the remaining resist is stripped, leaving only the patterned material on the wafer. This sequence of lithography, etching, and stripping is repeated for each layer in the fabrication flow. It is accompanied by multiple dielectric and metal deposition steps, chemical mechanical polishing (CMP), and annealing processes. CMP is responsible for flattening the surface and reducing it to the target material thickness, while annealing consists of thermal and pressure treatments performed to densify the deposited material and reduce defects, often in the presence of specific gases in the chamber.

The complete fabrication flow is summarized in Figure 3.6, each panel describing a series of steps and accompanied by a brief description. Here, only the main process steps are reported to provide an overview of the fabrication and of the role of each designed layer. A more detailed description of the individual fabrication steps is beyond the scope of this manuscript, as a standard silicon photonics process was employed and no process modules were personally developed.

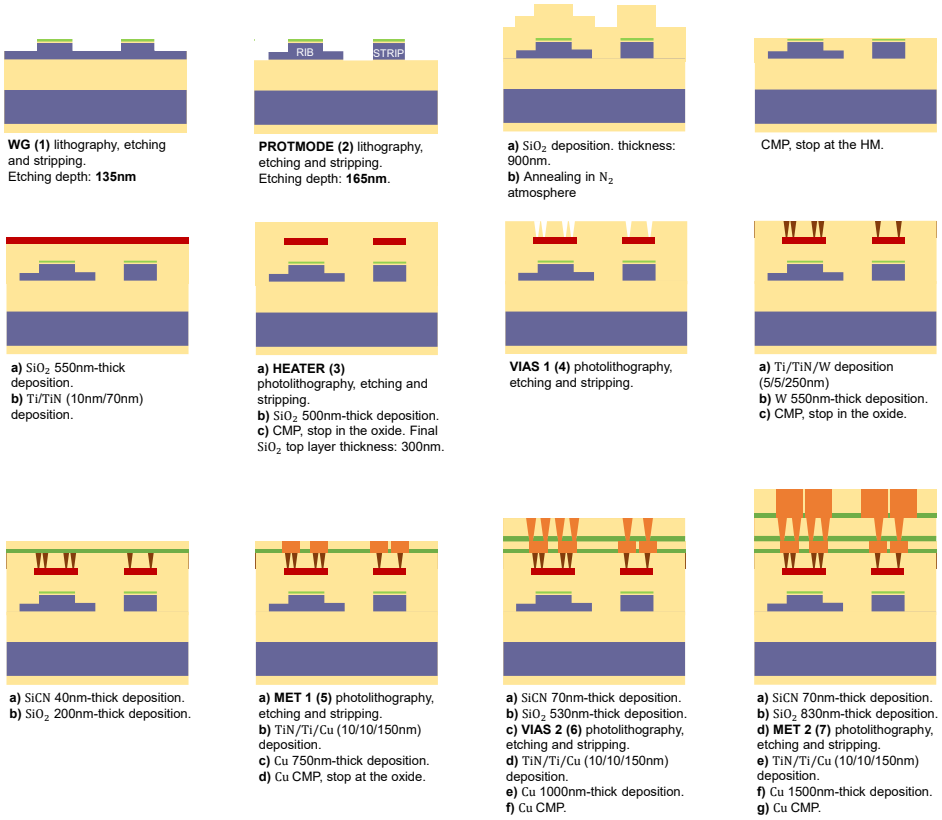



*Figure 3.6:* ***Schematic representation of the fabrication process flow.*** *Each panel describes a series of steps, with a brief description of the role of each layer.*

### 3.3.2 Layer definition

Here, I summarize the individual layers used in the fabrication process and their specific roles in the realisation of the designed photonic circuits, following the sequence of the process flow.

1. **WG**: This first layer defines the waveguides, including both the top part of mid-rib and strip waveguides. As above mentioned, the lithography is performed using immersion lithography, and the 300 nm silicon layer is etched to a depth of 150 nm. The HM is kept on top of the waveguides to protect them during subsequent processing.

2. **PROTMOD**: It defines a second immersion lithography step followed by an additional 165 nm etch, reaching the BOX layer below the silicon slab.

The mask protects the top of the mid-rib waveguides while exposing the strip waveguides, which are already protected by the remaining hard mask. After this step, the waveguides are encapsulated by successive silica deposition and planarization steps. Importantly, a high-temperature annealing process (up to 800°C) in 100% $N_2$ atmosphere is performed after the deposition of the upper cladding silica layer to reduce the hydrogen content and consequently the optical losses. In the next paragraphs, I will report some optical characterization I personally carried out *before* and *after* this step.

3. **HEATER**: It defines the geometry of the metallic Ti/TiN thin film used for thermal phase shifters. The metal, previously deposited over the entire wafer, is selectively etched, leaving the heater structures on top of the waveguides. Another layer of $SiO_2$ is deposited to cover the 80 nm–thick Ti/TiN.

4. **VIA 1**: This layer defines the first level of vias, opened in the $SiO_2$ above the heater and filled, using a typical Damascene process. After the deposition of a thin Ti/TiN barrier-layer and a tungsten-seed layer, the vias are filled with W and finally CMP is employed to remove the excess, reaching the $SiO_2$ level. After this step, an HM and an oxide layer are deposited again (40nm-thick SiCN and 200 nm-thick $SiO_2$ by using silane $SiH_4$ as precursor), which serves for the subsequent Damascene process.

5. **METAL 1**: This layer defines the first metal interconnection level: the oxide is etched till the HM and Cu is deposited to fill entirely the obtained holes. After CMP, the first metal level is completed, and the exposed metallic parts, i.e. PADs, can be already contacted using external probes for electrically contacting the underneath phase shifters.

6. **VIA 2**: A second Damascene process is fully performed, defining the second level of Cu vias, used to connect the first metal layer to a higher-level metallization.

7. **METAL 2**: This final Cu layer defines the higher-level metallization, used mostly for routing or pad definition.

The photomasks used for silicon patterning underwent Optical Proximity Correction (OPC) to ensure accurate pattern transfer at the sub-micrometer scale [207, 208]. The platform therefore supports the fabrication of tunable SiPh devices, i.e. *passive devices with heaters* according to the previously adopted definition (without the inclusion of doped regions).

Between the various fabrication steps, standard metrology procedures, such as measurements of layer thickness and surface roughness, are performed by specialized cleanroom operators to verify process uniformity and correctness in dedicated regions of the wafer. To directly assess the fabrication outcome on the devices presented in this work, I personally carried out optical microscope inspections inside the cleanroom. Representative results of these measurements are reported in the following (section 3.5).

## 3.4 Chip design

Within the fabrication platform described in the previous section, a silicon chip of area 100 $mm^2$ has been designed, including all the circuits mentioned above together with single-component test structures. The complete GDS layout of the chip is shown in Figure 3.7. Both test structures and fully functional circuits are replicated several times across the chip, while varying selected physical parameters of the components in order to compensate for fabrication imperfections. This approach follows a standard methodology in the field known as Design of Experiments (DoE), since performance metrics such as coupling coefficients, resonance wavelengths, extinction ratios, and insertion losses may slightly vary with respect to simulations. In this way, after fabrication it is possible to identify and select the best-performing devices by first characterizing the integrated test structures before proceeding to measurements on the complete circuits. The parameters varied across the replicas include the MRR source gaps, in order to ensure high generation rates, as discussed more extensively in the paragraphs dedicated to the component design.

Two main test structures have been integrated and, as will be reported later, characterized to assess the performance of the circuits: one dedicated to microring resonators and one to directional couplers. The layout of both is reported in the Appendix (see Figure B.1). The MRR test structure includes both add-drop and all-pass configurations, with different coupling gaps and waveguide widths, allowing the coupling coefficients and, consequently, the quality factors to be tuned. The DC test structure includes multiple directional couplers with varying coupling lengths, enabling the identification of the target coupling coefficient required to achieve optimal demultiplexing performance, according to the theoretical model reported in subsection 1.6.1. In the following paragraphs, the expected and measured spectral responses, together with the main extracted figures of merit of these components, are presented.

Once the components with the best performance have been identified and the

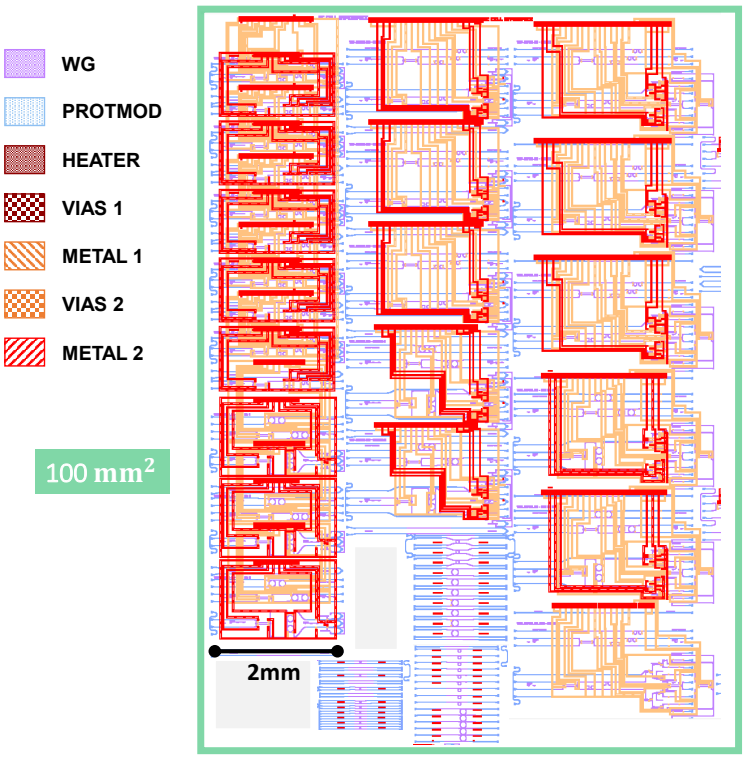



*Figure 3.7:* ***Complete GDS layout of the designed chip.*** *The layout includes multiple test structures and complete circuits, which are replicated several times across the chip with varying physical parameters. The test structures include MRRs and DCs, while the complete circuits include the FB–Pa and FB–Po sources, with and without idler and signal routing toward distinct out couplers.*

fabrication is completed, the corresponding circuit units will be diced and packaged. The electrical contacts are all arranged on one side of the unit, sufficiently far from the optical inputs and outputs to allow wire bonding, whose number ranges from 10 to 22 depending on the circuit complexity. The packaging will provide more stable and reliable heater control, necessary for the final quantum demonstrations. These units also include additional test structures useful for the final quantum demonstrations, such as alignment and reference circuits integrating fewer components for calibration purposes.

We report an example of a complete circuit unit and the resulting GDS layout in Figure 3.8. Different colors correspond to the layers used during the fabrication process, described in the previous section. The overall unit includes multiple

test structures as well as complete quantum photonic circuits (either the FB–Po or the FB–Pa circuit). In this way, once the best-performing circuit is selected, the entire unit is cut from the wafer, such that both the necessary test and calibration structures and the fully functional circuit are present on the same monolithic chip. The above-described design is based on geometrical parameters defined

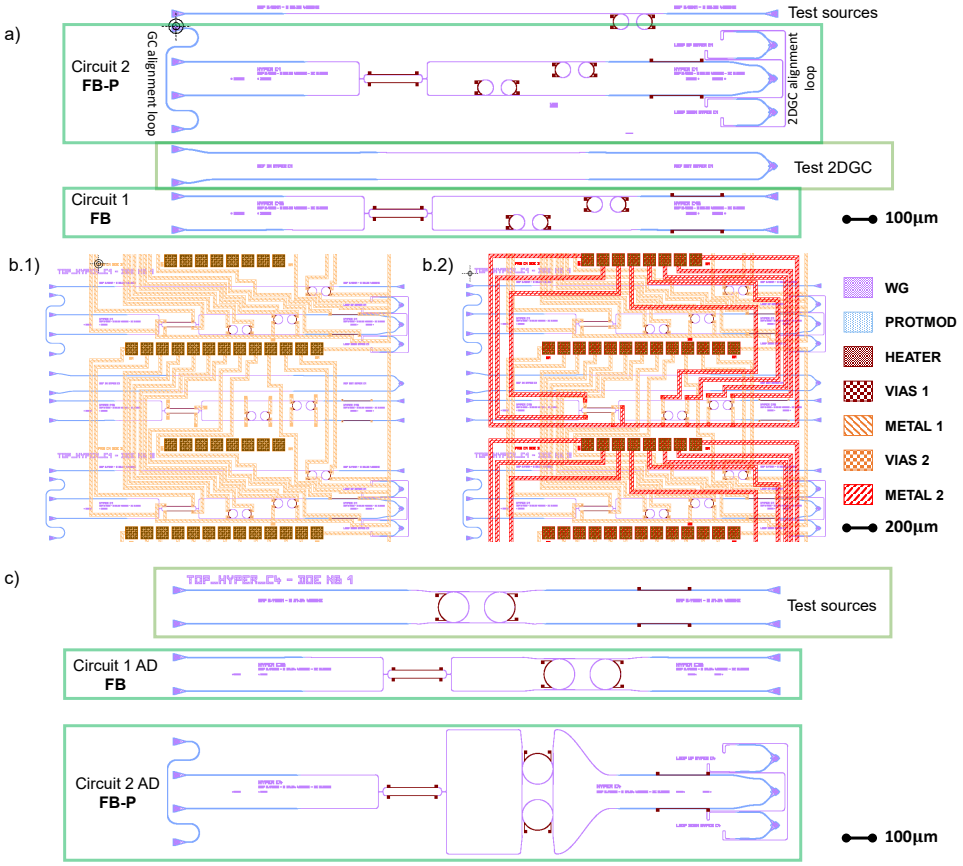



*Figure 3.8:* ***Examples of GDS layouts of the dicing units****. The unit includes multiple circuits, test structures, and alignment loops. (a) Zoom-in of a single DoE cell for the FB–Pa and FB–Po circuits, which also incorporates source test structures and two-dimensional grating coupler test structures. (b) Arrangement of multiple circuit cells across the chip. (c) Zoom-in of a single DoE cell for the FB–Pa and FB–Po circuits employing AD microring resonators. For clarity, the METAL 1 and METAL 2 layers are not shown in panels (a) and (c), while they are visible in panels (b.1) and (b.2), respectively.*

through a combination of numerical simulations and analytical models, as described in chapter 1. Here, I present the main simulation results used to define the layout

of the components and to predict their performance.

### 3.4.1 Device simulations

The simulations were performed following the methods described previously, using a combination of FDTD and FDE solvers [106, 97], as well as custom scripts for analytical calculations implemented in Python.

#### Waveguide simulations

The waveguide geometry was optimized to achieve single-mode operation at the target wavelength of 1550 nm, while also maximizing the effective nonlinearity for efficient SFWM. Here, I report the effective index, group index, and dispersion obtained for the fundamental TE mode of both rib and strip WGs for the Si300nm-thick platform used. The designs implement both geometries, according to the specific role of the corresponding component in the circuit. For example, standard SM rib WGs (core width of 450 nm and slab width of 3.05 $\mu$m) are used for long propagation sections, due to their expected lower losses ($\sim 0.8\,\mathrm{dB\,cm^{-1}}$), while standard single-mode strip WGs (WG width of 400 nm) are used for the DCs and MZIs to avoid mode mixing at the bends while keeping them compact. Their simulated properties are summarized in Table 3.1. For the MRR-based sources, to increase the effective nonlinearity, the WG width was engineered to minimize the effective area and the dispersion $\mathcal{D}$ at the target wavelength of 1550 nm.

In Figure 3.9, the dispersion properties for different waveguide widths are shown for the fundamental TE mode. As expected, the strip WGs show dispersion closer to zero also for the Si300nm platform compared to the rib ones; therefore, they have been selected for the sources. As already reported in Figure 1.5, the effective area of their modes reaches a minimum at 600 nm, which was therefore chosen as the nominal width for the source cross section. The corresponding properties are summarized in Table 3.1.

As previously mentioned, the width of the WG may vary if the required coupling coefficient between the bus and ring WGs (*cross* coefficient) cannot be achieved within the target gap range, which is limited by the fabrication process section 1.4. This is the case for the AD-type sources, where higher coupling coefficients are required for high-visibility resonance response. Thus, the width of the WG is reduced to 550 nm to accommodate the higher coupling requirements while keeping the gap

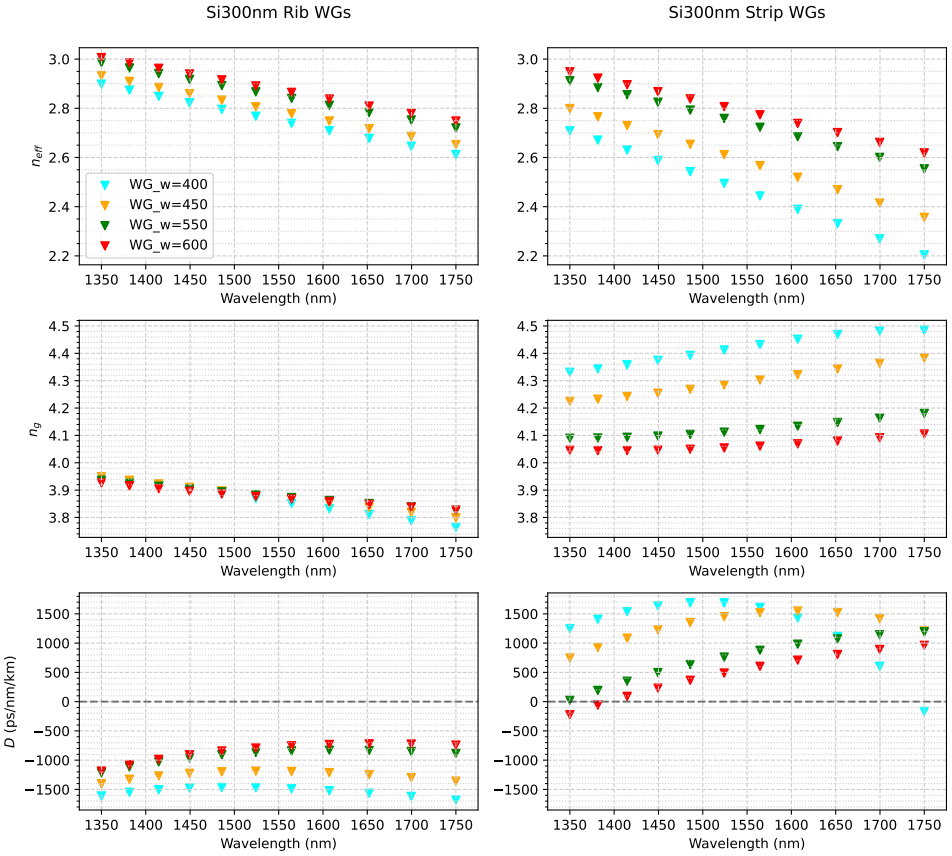



*Figure 3.9:* ***Simulated WG properties for the Si300nm platform.*** *Fundamental $TE_{00}$ mode effective index, group index, and dispersion as a function of wavelength for both strip and rib WGs. The $WG_w$ values reported here correspond to those used in the circuit design.*

| | $300 \times 600\,\mathrm{nm}^2$ | $300 \times 550\,\mathrm{nm}^2$ | $300 \times 400\,\mathrm{nm}^2$ |
|---|---|---|---|
| $n_{eff}$ | 2.79 | 2.74 | 2.46 |
| $n_g$ | 4.06 | 4.12 | 4.42 |
| $\mathcal{D}$ (ps/nm/km) | 580 | 825 | 1610 |
| $A_{eff}$ ($\mu$m$^2$) | 0.21 | 0.22 | 0.26 |

*Table 3.1:* ***WG simulations summary.*** *Indices at 1.55 $\mu$m of the fundamental mode of the Si WG cross-sections employed for circuit routing and sources, extracted from Figure 3.9 and Figure 1.6.*

in the constraints given by the lithography. The simulated properties of this cross–section are also reported in the table, showing a slightly higher effective area and

dispersion.

## MRR design and simulations

Once the WG geometry is defined, the MRR radius and point coupler geometry are optimized. Specifically, the FSR is set to 400 GHz and 200 GHz for the AD and AP versions of the circuits, respectively, to ensure subsequent wavelength separation (pump, idler, and signal wavelengths) by means of standard DWDM filters (centered at the ITU channels, spaced by 100 GHz). The relationship between the gap and the resulting cross coefficient $\kappa^2$ has been established by means of FDTD simulations, following the methods reported in chapter 1. In particular, the gap versus $\kappa^2$ for the WG cross–section $300 \times 600\,\mathrm{nm}^2$ is already reported in Figure 1.9, and similar simulations have been performed for the $300 \times 550\,\mathrm{nm}^2$ cross–section.

For the AP sources, the target point coupler should allow achieving the critical coupling condition, which strongly depends on the propagation losses experienced inside the ring cavity. Therefore, the FoMs of the MRRs were calculated for different $\kappa^2$ and different propagation losses, as reported in Figure 3.10. The ring radius considered is $29.38\,\mu$m, which corresponds to the target FSR. The cross coefficients obtained from the FDTD simulations are shown as vertical lines, and the corresponding gap values are reported in the legend.

Having chosen a WG cross–section different from the standard one, the losses will differ from the typical value of the PDK-like WGs (around $\sim 1.4\,\mathrm{dB\,cm^{-1}}$). Therefore, a broad range of $0.8 \sim 2.0\,\mathrm{dB\,cm^{-1}}$ is reported in the plot. Nevertheless, since the mode is more confined inside the WG core in our larger-width geometry, a slightly lower value of the losses is expected, although no quantitative estimation can be realistically performed. Therefore, taking into account the uncertainty in the effective cross coefficient and propagation losses, a DoE has been performed on the MRR gap to ensure operation close to the critical coupling condition in at least one of the integrated circuit versions. In particular, the same AP circuits have been replicated including three nominal gaps: 0.16, 0.18, and 0.2 $\mu$m, all comprised between the grey and purple dashed vertical lines in Figure 3.10, i.e. in the region where all curves show maximum visibility (critical coupling). The expected Q-factors in the covered cross-coefficient range are $150000 \sim 410000$, represented by the x-coordinates of the grey and purple triangles in the plots.

Similar calculations were performed for the $57.94\,\mu$m-radius AD sources, which are reported in the Appendix A, Figure A.3. As pointed out in the paragraph dedicated

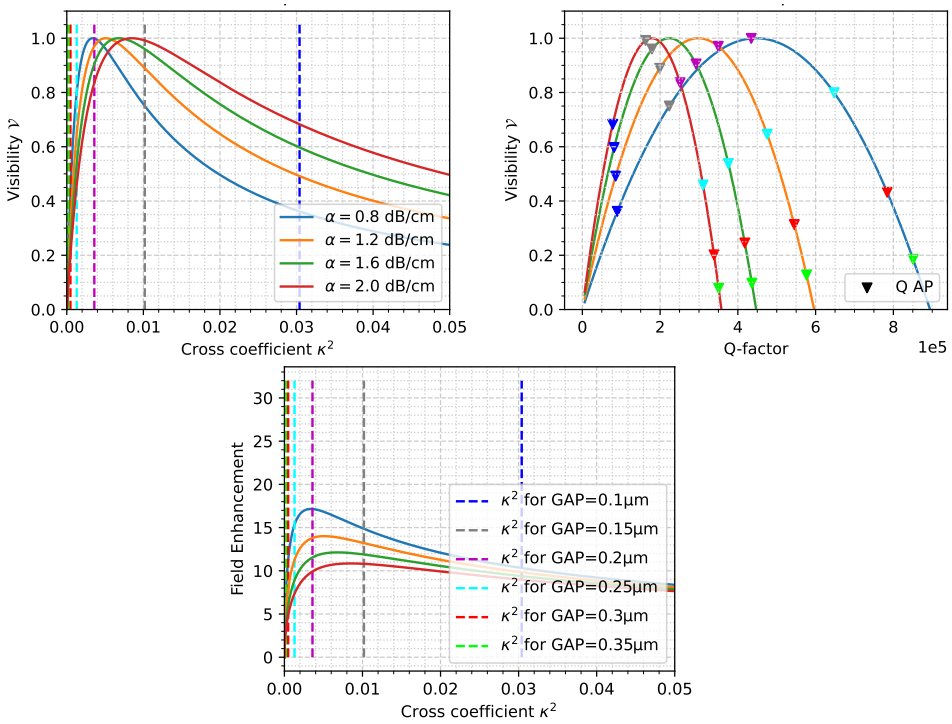



*Figure 3.10:* ***AP MRR FoMs.*** *Figures of merit of the AP MRRs (*$300 \times 600\,nm^2$ *cross–section) with radius* $29.38\,\mu m$*, shown as a function of the cross coefficient and propagation loss. The vertical dashed lines represent the expected cross coefficients corresponding to different gaps, simulated using FDTD, while the triangles of the same color represent the corresponding expected visibility (y-coordinate) and Q-factors (x-coordinate).*

to the theoretical treatment of MRRs, an symmetric AD resonators always operates in the under-coupling regime, and the visibility approaches asymptotically unity at the cost of a vanishing Q-factor. Therefore, for the AD case we target a reasonable value of the Q-factor, corresponding to a visibility $\mathcal{V} > 98\%$. The chosen DoE gaps are 0.125 and 0.135 $\mu$m, which correspond to target Q-factors of $45000 \sim 50000$.

## DCs and MZIs design and simulations

The MZI structures included in the circuits play three main roles: MZIs for pump routing (distributing the injected input beam between the two pairs of sources), MZIs for path-state analysis, and MZI-based cascaded DEMUX structures for idler and signal separation. In the first two cases, the MZIs include two 50:50 DCs; they are symmetrical (no path difference is introduced), and two heaters are integrated

in the MZI arms (*push-pull* configuration). In this way, the splitting ratio between the *up* and *down* arms at the output can be tuned by acting on the phase shifters, as described in Equation 1.41. The layout of the integrated 50:50 DC, shown in Figure 3.12(b), consists of the following simple geometry: two parallel straight single-mode strip WGs with a constant gap between them, connected to the non-interacting routing WGs by means of two 90° bends with radius $R_{DC} = 5\,\mu$m. This choice was made to maintain compactness while minimizing design-related errors. The same geometry is also used for the other target splitting ratios. All the coupling simulations are reported in Figure 3.11.

The cascaded MZI filters are instead composed of three unbalanced MZIs, whose arm length differences $\Delta L_i$ ($i = 1, 2, 3$) depend on the WG cross–section (i.e., the group and effective indices) and on the DEMUX single-channel FSR $\Delta_{FSR}$. The three propagation regions are separated by a total of four DCs, whose splitting ratios (from input to output) are 50:50, 20:80, 20:80, and 04:96, according to the model reported in subsection 1.6.1. The filters have been integrated in a double-stage configuration to reduce crosstalk, as predicted by the simulations. This configuration allows the light to be routed into two output WGs, depending on its wavelength. The layout of a DEMUX is reported in Figure 3.12(c), where the routing of the different spectral components, represented by the blue and red arrows, is also shown. The WGs not used for input and output collection are terminated with inverse tapers to prevent back-reflections.

Starting with the DC simulations, the method used is the same as the one described in section 1.5, employing a 3D FDTD solver. Here, the coupling coefficient $\kappa^2$ is calculated for a fixed gap, chosen to be $0.2\,\mu$m. This value is well above the minimum gap critical dimension of the fabrication process and is therefore considered a safe choice for relatively long parallel straight waveguides. The transmittivity $T$ of the *bar* and *cross* states is therefore varied by choosing $L_{coup}$. According to the simulations reported in Figure 3.11, the coupling lengths integrated for the target splitting ratios are summarized in Table 3.2. Overall, the small WG cross–section chosen allows for very compact designs, with all the target splitting ratios achievable with DCs shorter than $20\,\mu$m ($< 10\,\mu$m of coupling length plus $10\,\mu$m from the two bends).

The integrated DEMUX FSR was set to 1600 and 3200 GHz in different circuit versions. An example of spectral response of such cascaded MZI-based DEMUX, is shown in Figure 1.15, considering the pure theoretical model, i.e. ideal DCs and in the absence of chromatic dispersion. Their role inside the circuits is schematically

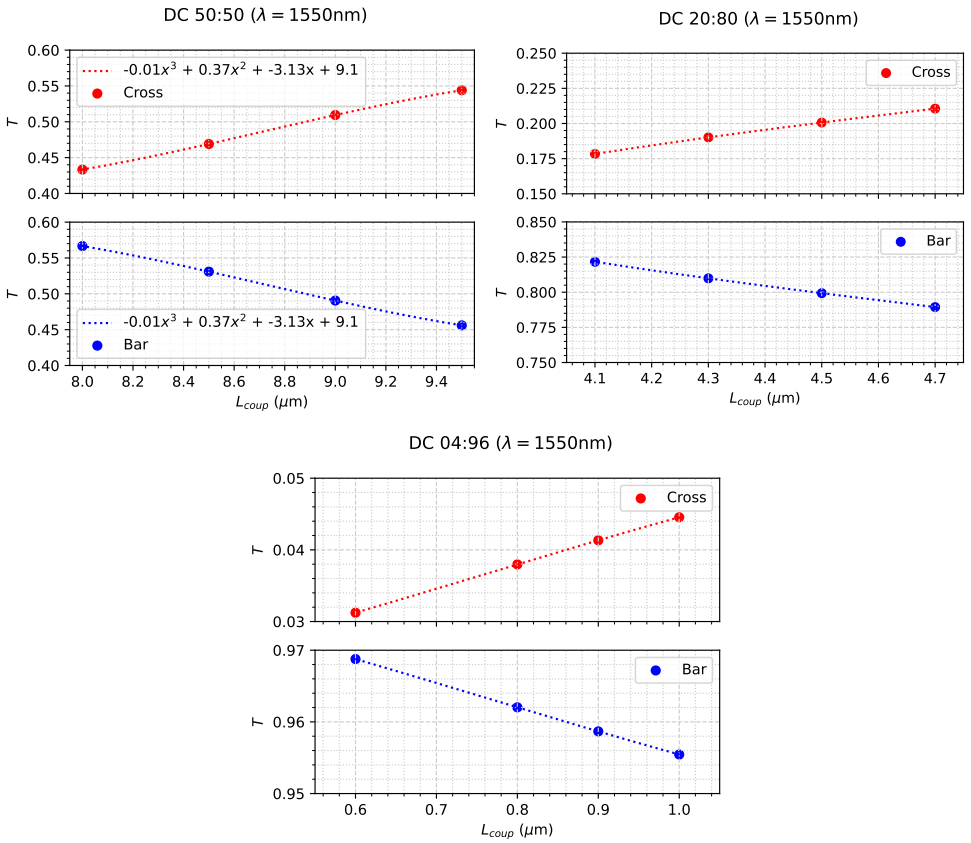



*Figure 3.11:* ***DCs simulations.*** *Cross (red) and bar (blue) coefficients extracted from the 3D FDTD simulations for different $L_{coup}$, with a fixed gap of 0.2 μm, for 50:50, 20:80, and 04:96. The WGs used are standard single-mode strip waveguides, while the DC geometry is reported in Figure 3.12 (b). Simulations have been performed using a 3D FDTD solver, following the method described in section 1.5.*

| DC splitting ratios: | 50:50 | 20:80 | 4:96 |
|---|---|---|---|
| $L_{coup}$ (μm) | 8.85 | 4.5 | 0.86 |

*Table 3.2:* ***DC simulations summary.*** *Length of the DCs integrated in the circuit. Specifically, the coupling length $L_{coup}$ required to achieve the target splitting ratio for a fixed gap of 0.2 μm is shown. The values are extracted from the simulations shown in Figure 3.11.*

depicted in Figure 3.12 (a). The two filter output channels will be used for idler and signal routing, while the pump will be allocated in between the two channels, similarly to what was done in Ref.[156]. It will produce an initial decrease of the

pump intensity (about $5 \sim 10$ dB depending on the filter type as predicted by the simulations), but further pump filtering off-chip will be required for photon counting. Thanks to their typical rectangular channel spectrum, we expect to collect one/three idler and signal 400GHz/200GHz source resonances per channel for the 1600GHz-DEMUX. For the 3200GHz-DEMUX, we expect to collect three/five resonances per channel, respectively.

Given the target FSRs and the WG simulated properties, the required path imbalance $\Delta L_i$ of the MZI arms can be calculated following the equations in Table 1.2. The obtained lengths for the two integrated DEMUX versions are summarized in Table 3.3.

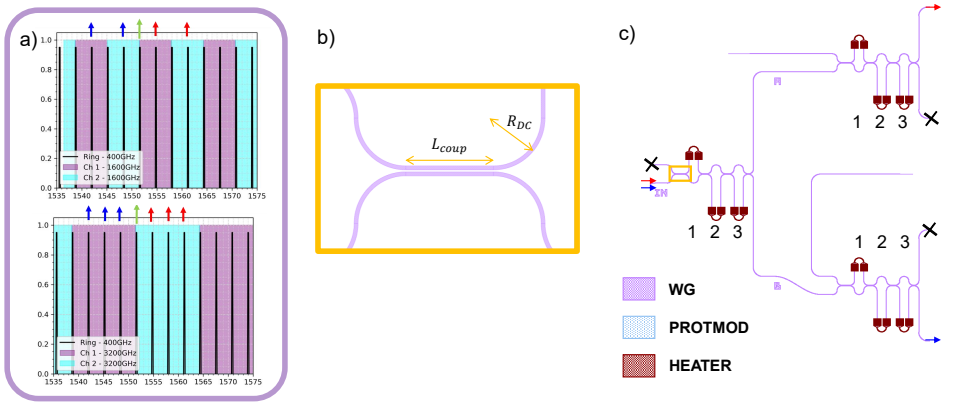



*Figure 3.12:* ***Cascaded MZI design.*** *(a) Schematic representation of the DEMUX and MRR source FSR relationship. The example shows the position (black) of the 400GHz MRR comb with respect to the 1600 and 3200 GHz DEMUX channels (ch 1 and ch 2). (b) Zoom of the GDS layout of the integrated 50:50 DC. (c) GDS layout of the integrated cascaded MZI filter, with the routing of the different spectral components represented by the blue and red arrows.*

| DEMUX FSR (GHz) | $\Delta L_1$ ($\mu$m) | $\Delta L_2$ ($\mu$m) | $\Delta L_3$ ($\mu$m) |
|---|---|---|---|
| 1600 | 42.353 | 84.706 | 85.021 |
| 3200 | 21.177 | 42.353 | 42.668 |

*Table 3.3:* ***Cascaded MZI design parameters.*** *Unbalancement between the arms of the three MZIs composing the single stage of the integrated cascaded MZI filter. The values are calculated following the model reported in Table 1.2.*

## 3.5 Wafer-scale optical characterizations

In this paragraph, I report the morphological characterizations I personally carried out inside the clean room and the optical characterizations performed in the Laboratory of Silicon Photonic Integration during my stay at CEA-Leti. In particular, I acquired Scanning Electron Microscope (SEM) images inside the clean room in Grenoble to verify the quality of the fabricated waveguides, i.e., on a wafer after the WG and PROTMOD etching steps. The optical measurements were performed after the necessary subsequent encapsulation step. To evaluate the uniformity of the fabrication, they were carried out at wafer scale, i.e., on multiple dies across the 300 mm wafer.

The setup used is a standard fiber-to-fiber transmission bench, where light from a tunable laser source is coupled into and out of the chip through GCs using a fiber array of polarization-maintaining fibers at the input and a single SMF28 fiber at the output, both mounted on high-precision stages. The measurement station used, i.e., the prober, is semi-automated: the wafer is loaded and aligned by the operator, while the movement from die to die and the spectral measurements are automated through Python programs, which I optimized to efficiently characterize the optical components of this work. The output light is collected by the fiber and measured by a photodiode for spectral analysis. The results reported here were analyzed using custom Python codes.

### 3.5.1 Optical losses

To evaluate the optical losses of the fabricated waveguides, I personally carried out optical transmission measurements both before and after the high-temperature annealing step. Precisely, the step under consideration is the annealing performed after the deposition of the upper silica cladding layer, with the goal of verifying its effectiveness. The structures used for this characterization consist of a standard set of spiral WGs with different lengths. From the slope of the linear fit of the measured insertion losses as a function of the WG length, the propagation losses are extracted and expressed as loss per unit length (dB $cm^{-1}$).

From the SEM image shown in Figure 3.13, it can be observed that the fabricated waveguides exhibit smooth sidewalls and well-defined geometries, which are crucial for minimizing scattering losses. On top of the waveguide, the $SiO_2$ layer and the HM are clearly visible. Notably, the roughness of the HM is significantly higher than that of the underlying Si slab surface, indicating that the etching pro-

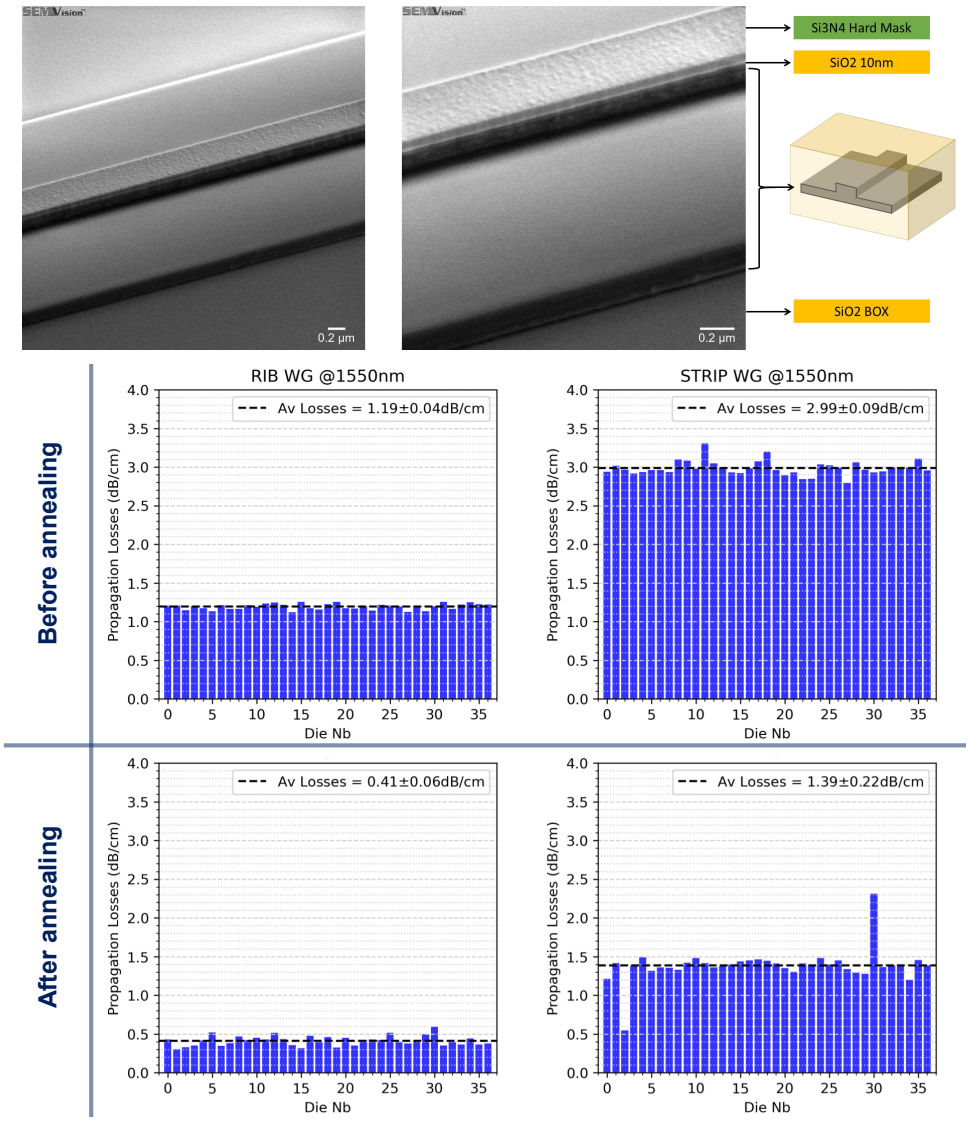



*Figure 3.13:* ***WG morphological and optical characterization.*** *Top panel: two SEM measurements of SM standard rib WGs are reported, with the different layers highlighted, as recognisable in the sidewalls of the WG. Bottom panel: propagation losses extracted from SM standard rib and strip WGs at 1550nm, before and after annealing.*

cesses associated with the WG and PROTMOD levels are, as intended, optimized to preserve a smooth and homogeneous silicon surface, while being less critical for the other integrated materials.

Once encapsulation was completed, two wafers were removed from the clean

room for optical characterization: one with and one without the cladding annealing step. As shown in Figure 3.13, the annealing process leads to a significant improvement in the optical losses of the waveguides. In particular, the propagation loss is reduced from approximately $1.19 \pm 0.04\,\mathrm{dB\,cm^{-1}}$ to $0.41 \pm 0.06\,\mathrm{dB\,cm^{-1}}$ for the rib geometry, while a similar improvement is observed for the strip geometry. In addition, I also extracted the standard single-polarization GC insertion loss, not reported in the image for brevity, which is also reduced, decreasing from $3.06 \pm 0.08\,\mathrm{dB}$ to $2.61 \pm 0.11\,\mathrm{dB}$.

These results confirm the effectiveness of the annealing step in reducing the hydrogen content in the silica cladding, which is known to introduce absorption losses at telecom wavelengths due to overtone vibrations of Si–H and O–H bonds [53]. The measured losses after annealing are homogeneous across the wafer and consistent with typical values reported for silicon photonic waveguides fabricated using comparable processes, indicating a successful fabrication outcome.

### 3.5.2 Ring resonators

After having assessed that the annealing step performed after the waveguide encapsulation is effectively improving the overall quality of the integrated components as expected, the optical tests on the individual circuit components were performed on the annealed wafer using the optical setup described above. An example of the recorded spectrum is reported in Figure 3.14.

Starting from the resonance positions, the FSR of the MRR can be extracted, thus providing a direct verification of the accuracy of the performed simulations. Following its definition in subsection 1.3.3, the FSR depends on the $n_g$ of the ring waveguide, which can thus be extracted by considering the nominal radius. The results are reported in Figure 3.15, showing an excellent agreement between the experimental and simulated values of $n_g$ for both the AP and AD chosen cross-sections.

Although the WG simulations have been experimentally validated, the more critical figures of merit of the resonances, namely the Q-factor and the visibility, still need to be extracted. As shown in the zoom of the spectrum in Figure 3.14, the main resonance characteristics are obtained through a Lorentzian fit. From this procedure, the FWHM, central resonance wavelength, and resonance depth are extracted, allowing both Q-factor and visibility calculation.

In Figure 3.16 I report, as an example, the values extracted across the full spectrum for the AD sources. The target Q-factor of approximately $5 \times 10^4$ is achieved

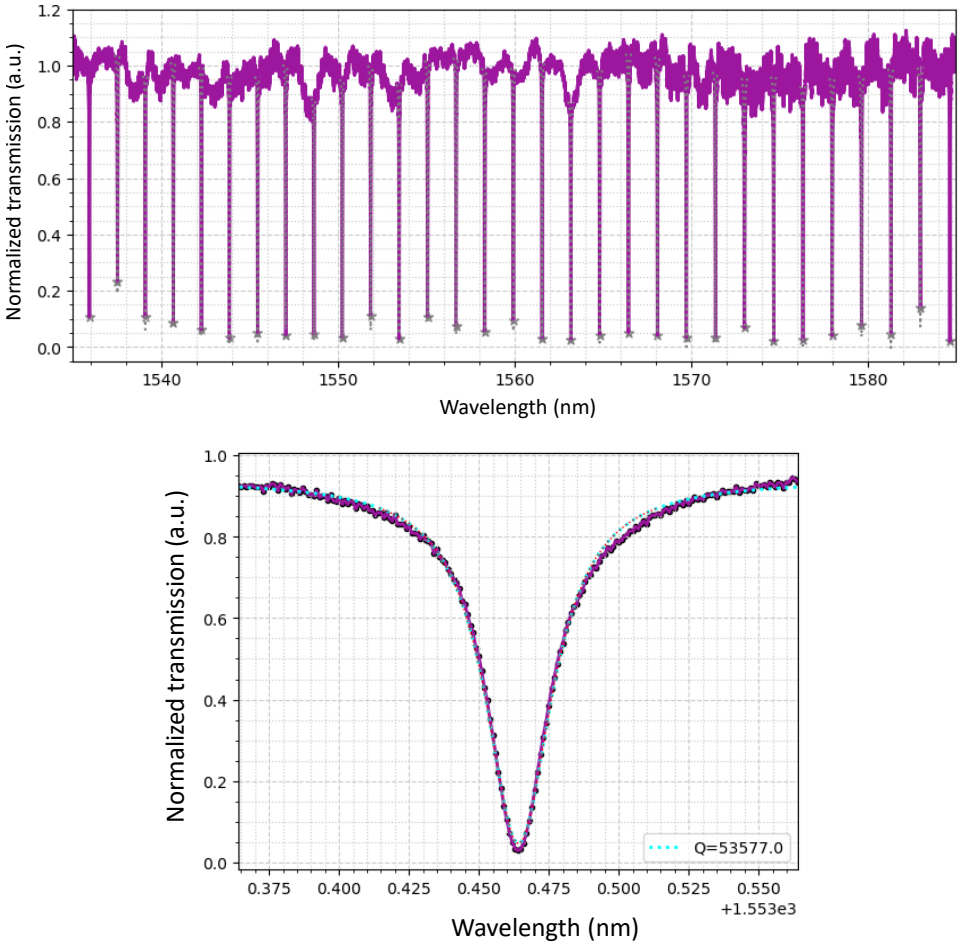



*Figure 3.14:* ***Typical MRR spectrum.*** *The presented data refer to an AD MRR with gap 0.15µm . The spectrum has been normalized with respect to the GC response. On the bottom, a zoom on one of the resonances is reported, showing the experimental data as both the purple solid line and black points. The Lorentzian fit is shown with the light-blue dotted line, and the extracted Q-factor is reported in the legend.*

for both gaps integrated in the fully functional circuits, namely 0.125 and 0.135 $\mu$m. These structures therefore represent good candidates for future quantum demonstrations.

For the AP sources, a similar analysis was performed. However, due to the much higher target Q-factor ($> 2 \cdot 10^5$), the resonances are likely to undergo bistability due to two-photon absorption-induced free-carrier dispersion and resonance splitting, caused by backscattering induced by sidewall roughness [209]. Together with

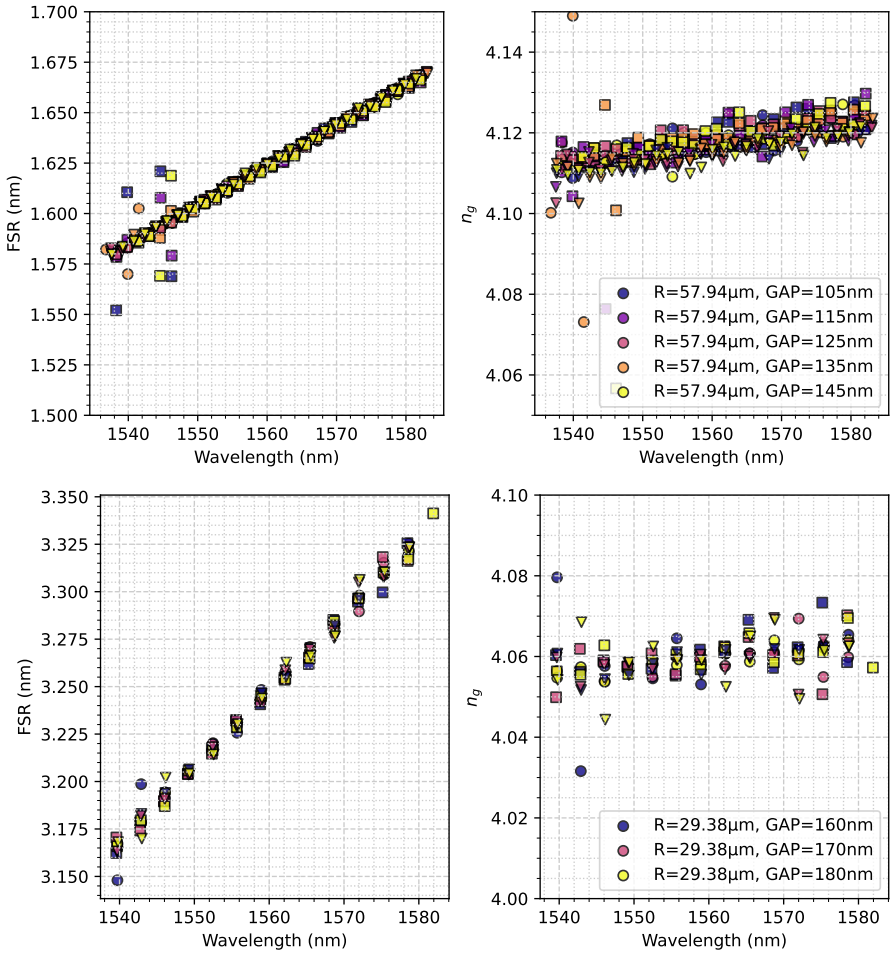



*Figure 3.15:* ***Ring resonance position analysis.*** *Extracted FSR and $n_g$ of the WGs from the MRR test structures. Different markers represent data taken from different dies (three are reported here). Top panel: AD MRR test structures. Bottom panel: AP MRR test structures.*

the smaller spacing between resonances (200 GHz instead of 400 GHz FSR), this prevented the acquisition of a statistically relevant dataset across the full spectrum for each die, as in the AD case.

Moreover, such high-Q resonances require careful measurements, since optical bistability in silicon may arise even at relatively low optical power in the presence of high intra-cavity enhancement. A rigorous analysis of the resonance FoMs in the presence of splitting would require a more advanced fitting model that includes the

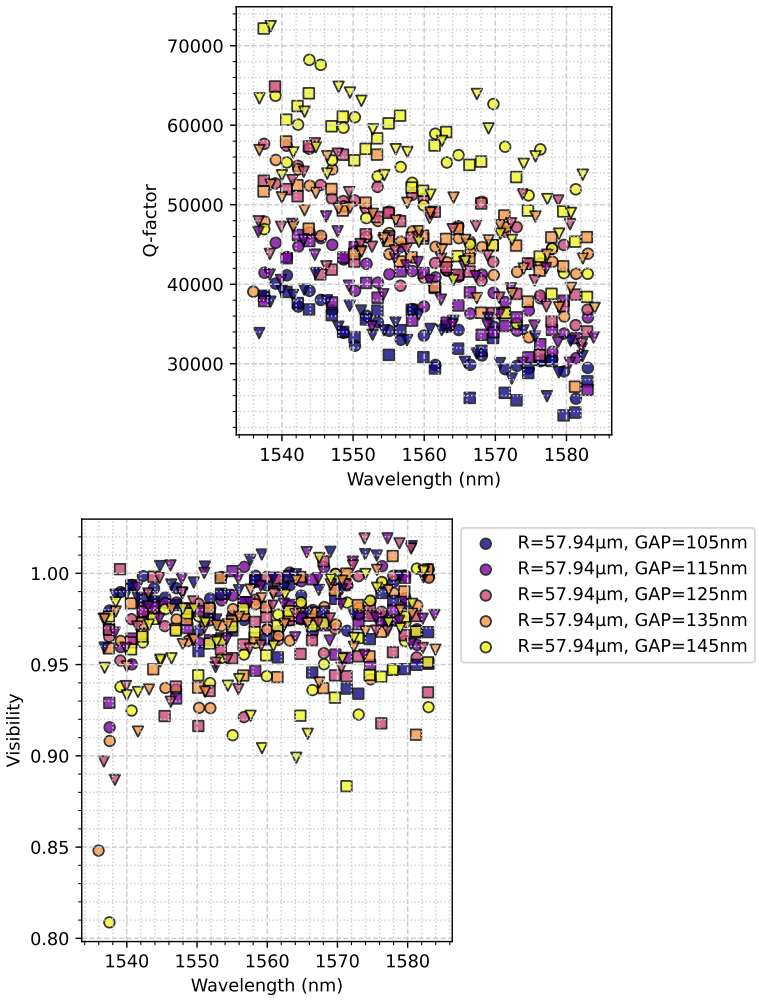



*Figure 3.16:* ***AD rings FoMs.*** *Extracted Q-factor and visibility for the AD MRR test structures; different markers correspond to data taken from different dies (three shown here).*

interaction between the injected CW mode and the CCW modes induced by backscattering, as demonstrated, for example, in Ref. [209]. Such an analysis is beyond the scope of this preliminary search for the best DoE elements.

For this reason, I report as an example a typical resonance measured from the AP test structures corresponding to gaps of 0.16 and 0.18 $\mu$m, together with their Lorentzian fit. Such clean single-peak resonances are found only a few times within the recorded spectral range ($2 \sim 4$ occurrences) across the 10 measured dies. Con-

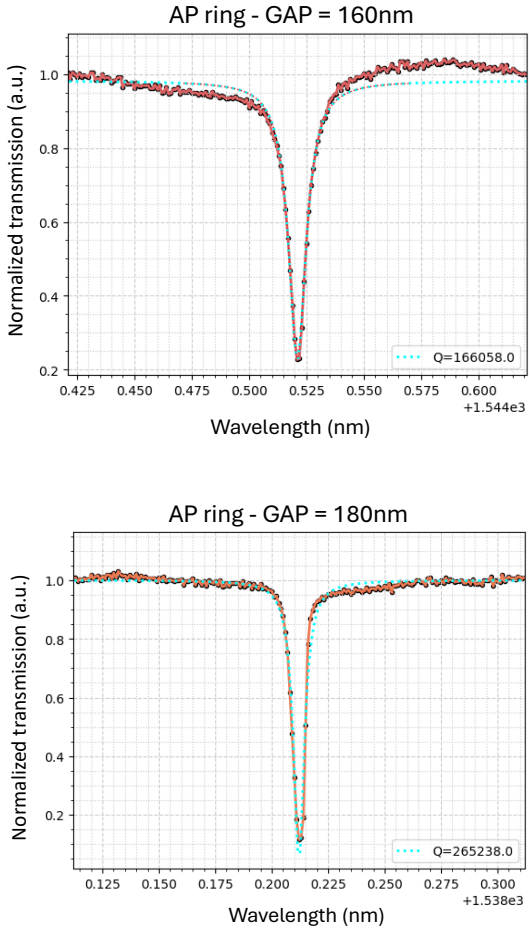



*Figure 3.17:* ***Typical AP ring resonance spectrum.*** *Example of a single resonance obtained from the spectrum of two distinct AP MRR test structures (respectively GAP 0.16 and 0.18 $\mu$m), measured on the same die. Colored solid lines and black points represent the experimental data, while the light-blue dotted curve represents the Lorentzian fit.*

sidering all the selected resonances across the dies, the extracted Q-factors range from $1.4 \cdot 10^5$ to $1.8 \cdot 10^5$ and from $2.0 \cdot 10^5$ to $2.8 \cdot 10^5$ for the two gaps, respectively.

For the AP circuit with gap 0.2 $\mu$m, even injecting lower pump power was not sufficient to recover a clean resonance shape. Therefore, the observed non-Lorentzian spectral features can most likely be attributed to interference between the CW and CCW modes rather than to bistability induced by free-carrier dispersion.

I can therefore conclude that the integrated AP ring resonators are potentially

capable of producing photon pairs with high generation rates, thanks to measured Q-factors exceeding 200000. However, resonances not showing splitting must be carefully selected across the spectrum. As a consequence, finding a triplet of energy-matched, non-split resonances may be relatively rare, and a high degree of tunability in the photon filtering stage will likely be required for off-chip pump removal and idler-signal separation. Consequently, the circuit version incorporating the idler-signal DEMUX may further limit the available resonances. As a matter of fact, it introduces discrete transmission bands whose spacing is fixed by design, thus efficient photon extraction from non-split resonances may be limited by this constraint. For this reason, the AP MRRs appear to be more suitable for the simpler circuit configuration incorporating only the photon-pair source.

### 3.5.3 Optical couplers

The input and output couplers utilized within the circuits presented here are of two types: standard single polarization (TE, 1D) GCs and their dual polarization version, 2DGCs. These components have been taken from the 300 mm SiPh PDK of CEA-Leti; therefore, I limit the treatment here to reporting the wafer-scale characterization of both types of couplers (Figure 3.18), in order to verify their proper operation and the insertion losses.

The insertion losses of the couplers are, respectively, $2.5 \pm 0.1$ dB and $3.6 \pm 0.1$ dB, with 3dB bandwidth of about $68 \pm 2$ nm and $51 \pm 3$ nm for the 1D GC and 2DGC, respectively. As these are well-established components in the Si300nm platform, the overall performance is very close to the nominal losses reported in the PDK, confirming the good outcome of the fabrication process. However, there is a shift in the central wavelength of about 20nm, probably due to a general offset between the fabricated and the simulated effective and group indices of the waveguides. We will find similar shifts in the following characterizations, confirming this hypothesis.

### 3.5.4 Cascaded MZI DEMUX

As already mentioned, the cascaded MZI DEMUX is introduced here as an idler–signal routing element. I report in Figure 3.19 the measured spectral response for both integrated filter versions (1600 and 3200 GHz FSR), in order to evaluate the outcome of the design and fabrication process.

As discussed in the simulation paragraph, to ensure good filtering performance of the cascaded MZI filters with the target channel spacing, both the DCs included in the structure and the MZI arm unbalances must correspond as closely as possible

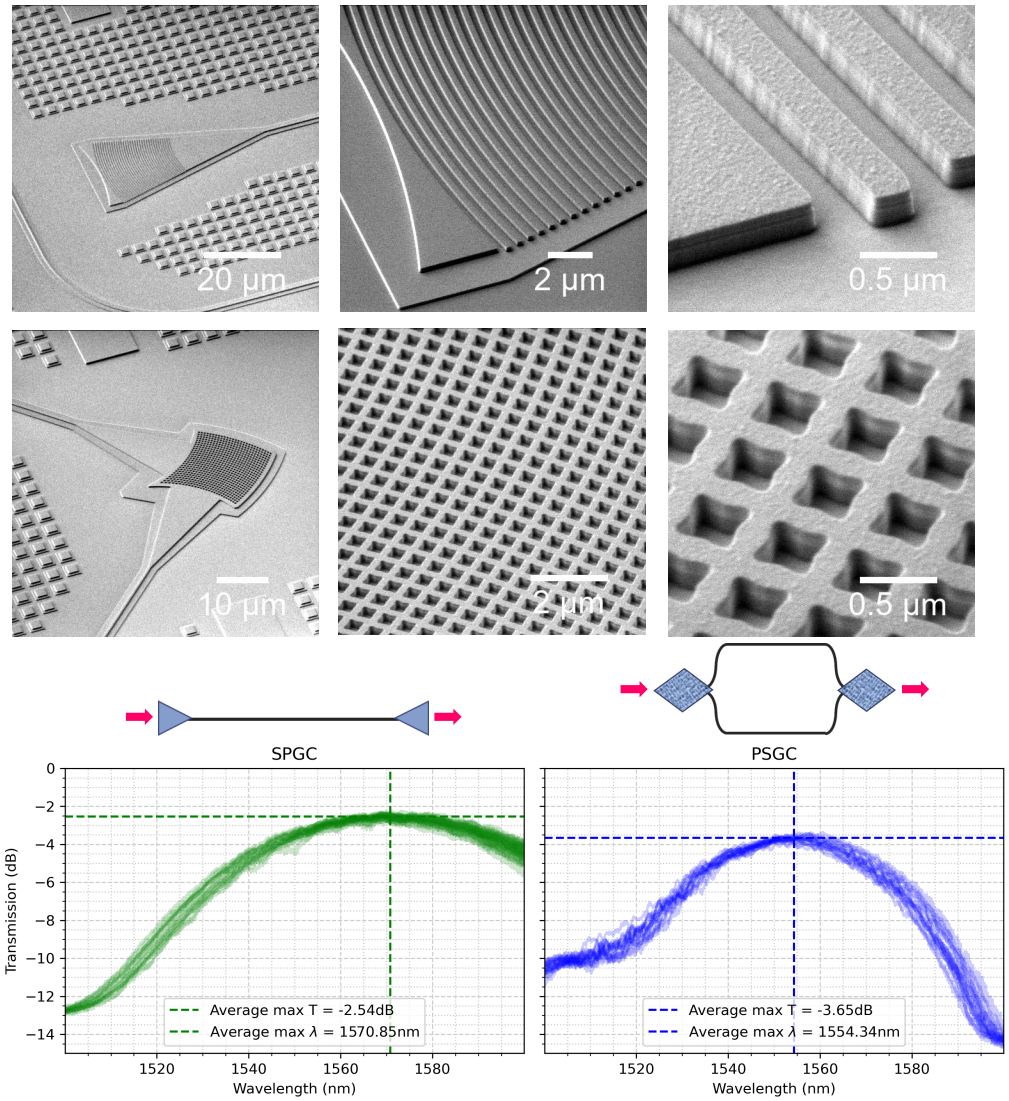



*Figure 3.18:* ***GCs morphological and optical characterizations.*** *Top panel: SEM image of the single polarization GC and of the dual polarization GC. Bottom panel: wafer scale characterization of the reference test structure, schematically depicted above each plot. The reported spectra have been taken on 17 dies.*

to the simulated values. Compared to the simulated spectra reported in subsection 1.6.1, some differences may arise due to the presence of chromatic dispersion, which is not implemented in the scattering-matrix-based model.

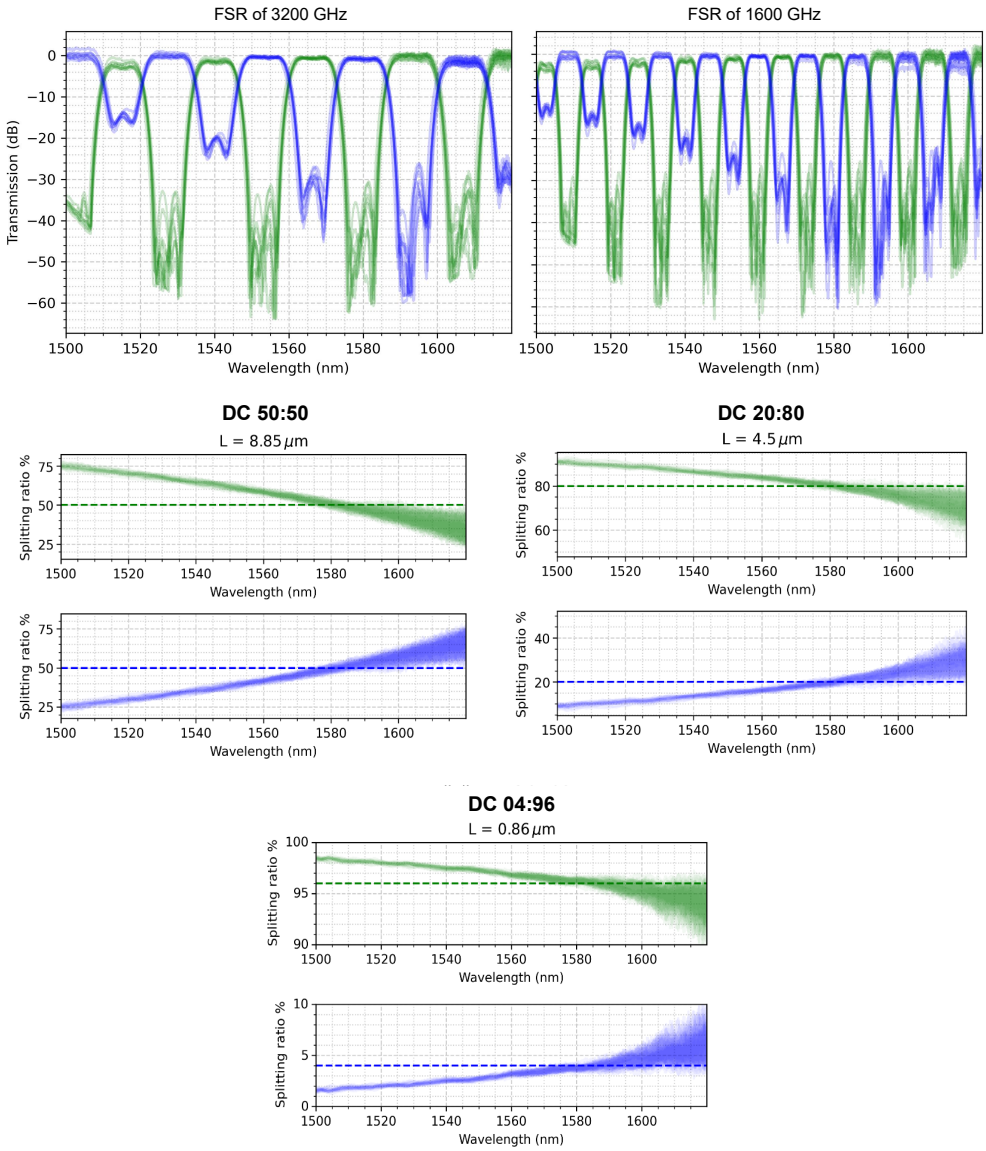



*Figure 3.19:* ***Wafer-scale characterization of the cascaded MZIs and their DCs.*** *Top panel: Cascaded Mach–Zehnder interferometer spectra, for the two integrated FSR (3200 and 1600 GHz). Lower panel: Directional coupler spectra measured through the dedicated test structures (see Figure B.1 for more details), for the three coupling lengths and corresponding expected splitting ratio integrated within the cascaded filters, respectively* 8.85 $\mu m$ *for 50:50,* 4.5 $\mu m$ *for 20:80 and* 0.86 $\mu m$ *for 04:96. All the reported spectra have been normalized to reference straight WGs in order to remove the grating coupler response. Measurements were taken on 10 dies across the 300 mm wafer to evaluate the uniformity of the fabrication process.*

Therefore, I first assessed the performance of the individual DCs through the integrated dedicated test structures, whose performance was evaluated over the wavelength range of interest. From the DC spectra, the coupling coefficients are derived, showing good agreement with the target values. The desired splitting ratios are indeed obtained, although not exactly at 1550 nm; a small wavelength shift is observed, similarly to what was found in the GC spectra reported above, which may be attributed to fabrication imperfections.

Nevertheless, the overall DEMUX response is very close to the simulated one. The measured FSRs are respectively $25.6 \pm 0.1$ nm and $12.8 \pm 0.1$ nm (corresponding to 3200 and 1600 GHz), with 3 dB bandwidths of about 10 nm and 5 nm, respectively, and a central-channel insertion loss below 1 dB. The single-channel extinction ratios exceed 15 dB over a bandwidth of 100 nm around 1550 nm. The global envelope of the DEMUX crosstalk strongly depends on the coupling coefficients of the DCs, as expected from simulations and from the literature [112]. As a matter of fact, the central-channel crosstalk reaches its minimum value of about $-30$ dB around 1580 nm, exactly where the three DCs reach their target splitting ratios. This wavelength shift is consistent with the one observed in the GC characterization, confirming a general offset most likely due to fabrication imperfections.

To compensate for this shift in future fabrication runs, the coupling coefficients of the DCs should therefore be slightly adjusted in order to further improve the crosstalk performance at the target wavelength of 1550 nm. In particular, from the measured spectra of the multiple DCs integrated in the test structures, whose results are reported in the Appendix (Figure B.2), it can be observed that the DCs integrated inside the DEMUX are slightly overcoupled. Therefore, in the next generation of integrated filters the DC coupling lengths will be slightly reduced to compensate for this effect.

## 3.6 Conclusions and further perspectives

In this chapter, I presented the design, fabrication, and preliminary characterization of a new generation of silicon photonic sources for the generation of hyperentangled photon pairs. The proposed architectures extend the capabilities of the integrated source discussed in the previous chapter by introducing additional degrees of freedom, routing, filtering, and analysis stages directly on chip. In particular, two classes of circuits were proposed, combining frequency–bin (and optionally time–bin) encoding with either polarization or path degrees of freedom. Building on the lessons learned from the simpler chip design presented in chapter 2, these

architectures integrate multiple MRRs for efficient photon–pair generation in the frequency–bin degree of freedom while directly addressing previous off–chip bottlenecks by integrating pump routing, state analysis, and signal/idler photon filtering onto a single monolithic substrate.

The layer stack composing the CEA–Leti 300 mm Si300 nm pilot line for tunable silicon photonic devices was described, highlighting the main technological steps involved in fabrication. All components were designed to match target performances, evaluated through a combination of analytical models and numerical simulations. To ensure a robust design and enable component–level testing, specific derisking strategies were implemented, including Design of Experiments parameter sweeps to mitigate fabrication tolerances and standalone test structures integrated alongside full circuits. Finally, heaters were incorporated where active phase control and resonance alignment are strictly required, such as on the MRRs and reconfigurable interferometric stages.

Morphological inspection through SEM imaging on target key components and preliminary wafer-scale optical characterization were performed, confirming the high quality of the fabricated waveguides and devices, which exhibit smooth sidewalls and well–defined geometries. Optical measurements further demonstrated the effectiveness of the fabrication process. In particular, an important result concerns the propagation losses, which were significantly reduced after the high–temperature annealing step, reaching values below $0.41\,\mathrm{dB\,cm^{-1}}$ for rib waveguides. This is crucial for efficient photon-pair generation via SFWM, as the pair generation rate scales inversely with waveguide loss. Under the simplified hypothesis largely discussed in subsection 1.3.4, an approximate scaling rule is given by $R \propto \mathrm{IE}^3 \propto Q^3 \propto \frac{1}{\alpha^3}$, where $IE = FE^2$ is the intesity enhancement experience within the cavity.

However, efficiently generating target hyperentangled states requires not only low waveguide losses, but also careful MRR design. The spectral characterization of microring resonators at wafer scale confirmed the accuracy of the design. From the measured free spectral ranges, waveguide group indices were retrieved at 1550 nm, showing excellent agreement with simulated values. For add–drop resonators, measured Q–factors of approximately $5 \times 10^4$ matched target design values, confirming their suitability for pair generation with moderate cavity enhancement. For all–pass resonators, much higher Q factors exceeding $2 \times 10^5$ were observed for selected resonances, although backscattering–induced splitting requires careful selection of the frequency modes involved in SFWM.

The wafer–scale recorded spectra of the cascaded MZI demultiplexers are very close to the simulated behavior. A small wavelength shift of the optimal operating

point was observed, consistent with the grating coupler characterization, identifying the DC splitting ratios as the most critical parameter affecting filter crosstalk and central wavelength. By leveraging the dedicated DC test structures included on this mask, optimized coupling lengths can be identified in a second fabrication run to realize higher performance demultiplexers. Overall, these results validate the design methodology and confirm the successful fabrication of the integrated photonic components required for the proposed hyperentangled photon sources.

Future work will focus on a more detailed characterization of the photon–pair generation rates of the microring resonator test structures, as spectral measurements alone do not allow for an unambiguous identification of the most efficient photon–pair sources. In particular, coincidence measurements will be required to quantitatively compare different resonator configurations. For circuits incorporating the polarization degree of freedom, additional characterization will be carried out to assess the performance of the path–to–polarization conversion stage (the 2DGC), including polarization selectivity and extinction ratio.

At the time of writing, the fabrication of the complete circuits is ongoing. Specifically, the integrated heaters and the first level of metallization are complete, while the second metal layer is currently in progress. Once fabrication is completed, the most promising circuit units will be diced and packaged, providing robust and stable tunable devices for subsequent quantum optical measurements. These experiments will aim to demonstrate the on–chip generation of hyperentangled photon pairs, ultimately validating the full functionality of the proposed integrated quantum photonic platform.

# Chapter 4

# A silicon quantum frequency processor

In this chapter, I present the experimental realisation of a monolithically integrated quantum frequency processor (QFP), representing, to the best of my knowledge, the first on–chip implementation of the theoretical framework proposed by J. M. Lukens and coworkers [40] on a silicon photonics platform. The chapter begins with an overview of the state of the art in the field, emphasizing recent experimental realisations and integration efforts documented in the literature.

I then detail the design of the circuit, fabricated using a 300 mm silicon–on–insulator pilot line by STMicroelectronics. A clear distinction is drawn between standard process design kit building blocks, such as the carrier–depletion p–n phase modulators, and components personally designed for this architecture, namely the 15 GHz microring resonator biphoton comb source and the novel line–by–line waveshaper (WS). For these custom elements, target quantitative specifications are explicitly defined and subsequently compared with experimental results. For standard PDK elements, dedicated characterizations are presented to validate their performance in the context of our circuit operations.

Finally, I report the key experimental demonstrations carried out with this chip: i) a tunable classical frequency beam splitter, ii) a single–qubit arbitrary rotation, iii) frequency quantum walks of high–dimensional frequency–bin states, and iv) quantum state tomography of two–qubit frequency–bin entangled states. Taken together, these demonstrations show the coherent processing of classical and quantum frequency modes on chip. The results presented in this chapter are published in Ref.

[210].

## 4.1 State of the art

Thanks to its intrinsic high dimensionality, massive parallelization on a single spatial mode, and compatibility with standard telecommunication infrastructures, frequency–bin encoding has the potential to address the scalability challenge of QKD systems [211, 16]. However, despite these advantages, the practical use of frequency–bin states has long been hindered by the difficulty of manipulating them coherently [212]. In particular, implementing arbitrary operations in the frequency basis requires precise mixing between discrete spectral modes, which cannot be achieved using passive linear optical elements, in contrast to the path or polarization basis.

Early approaches relied on nonlinear optical processes [213, 214] to achieve mode mixing, but these methods typically suffered from low efficiency and limited reconfigurability. The introduction of *frequency processors* then revolutionized this field in both the quantum and classical domains [215]. J. M. Lukens and coworkers first proposed this concept in 2016 [40], demonstrating that arbitrary linear-optical transformations on frequency modes can be achieved using a combination of table-top telecommunication components, such as electro–optic modulators and waveshapers. The EOMs are respectively responsible for realizing cross-coupling between frequency modes, while the WSs provide single-mode phase shifts.

More precisely, the proposed QFP architecture consists of, in this order, an input EOM, a WS, and an output EOM, as reported in Figure 4.1(a). It serves as a building block for realizing general unitary transformations in the frequency domain, similarly to the two-mode MZI commonly used for path encoding [211]. This approach has been experimentally validated by several demonstrations reporting high–fidelity frequency beam splitters and tritters [216] (see Figure 4.1(b)), arbitrary rotations [217] (see Figure 4.1(c)), and controlled-NOT gates [219] acting on frequency-bin qubits. Unitary gates have also been implemented on multiple qubits in parallel [220, 20], exploiting the intrinsic parallelizability of both the FB encoding and the QFP architecture.

In addition, QFPs have been successfully employed for various quantum information processing tasks, including entanglement certification [131], quantum state tomography [221], quantum walks [218, 222] (see Figure 4.1(d)), and high-dimensional quantum key distribution [167, 168, 169]. However, all these demonstrations rely on the use of bulk- or fiber-based components and the integration of

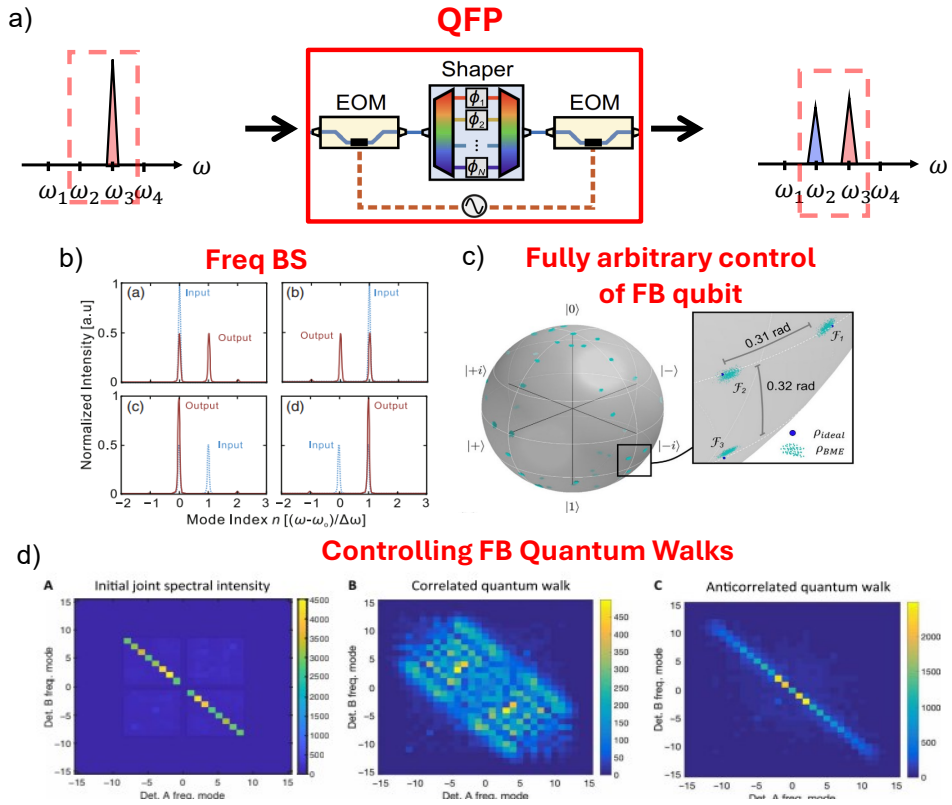



*Figure 4.1:* ***State of the art for QFP–based information processing.*** *(a) Schematic representation of the QFP architecture for unitary FB qubit operations (image adapted from [16]). (b) First demonstration of a frequency beam splitter (source: [216]). (c) First demonstration of arbitrary rotation on a single frequency-bin qubit (source: [217]). (d) Quantum walks of a biphoton frequency comb (source: [218]).*

QFPs on photonic platforms remains relatively unexplored.

While the generation stage is often implemented on chip, thanks to the well-established technique of using single or multiple microring resonators for the generation of biphoton quantum frequency combs (BQFCs) through SFWM, the absence of integrated manipulation stages remains a major drawback. Although efforts have been made to integrate single QFP building blocks, such as the WS [223, 224, 225, 226], these implementations still rely on bulk- or fiber-based components for certain functionalities, thereby limiting the realisation of fully on-chip devices.

This chapter addresses this challenge by presenting the first fully integrated quantum frequency processor, based on a CMOS–compatible silicon photonic circuit, incorporating all the required functionalities for coherent frequency–bin pro-

cessing: generation of a BQFC, spectral phase control, and frequency mixing via phase modulation.

## 4.2 Design and characterization of the silicon chip

The silicon chip is fabricated within an MPW, using the 300 mm Si300 nm photonic pilot line of STMicroelectronics, within their PIC50 technology. Most of the components have been taken from the PDK; these include 50:50 beam splitters, high–speed phase modulator and grating couplers. The foundry offers indeed a large variety of passive and active devices for the realisation of tunable integrated photonic circuits. At the optical wavelength of interest in our work (C-band, around 1550 nm), most of the PDK components are based on the rib waveguide geometry, which has thus been chosen as preferred geometry of our circuit. In particular, the C-band SM rib WGs feature a Si–core thickness of 300 nm, a partial etching depth (D) of 150 nm, and waveguide ($WG_w$) and slab widths of 450 nm and 3050 nm, respectively. The modulators are based on p–n junctions embedded in Si300 nm deep–rib waveguides, while the phase shifters used are simple heaters (see subsection 1.8.1). A simplified cross–section, reporting the full–layers stack employed in this work is reported in Figure 4.2(a). The full technology stack is more complex, comprising also additional materials, such as SiN, which are not listed here as they were not employed in this work.

The designed chip has a size of approximately $4 \times 7$ mm$^2$ (see Figure 4.3), integrating all the fundamental building blocks previously mentioned for obtaining a general–purpose QFP. From IN–1 to OUT–1 grating couplers, following the arrows in Figure 4.2(b,c), these are: a source of BQFC with a frequency spacing of 15 GHz, a carrier–depletion–based silicon phase modulator for frequency mode mixing (PM IN), a line–by–line WS for phase control of a total of eight independent spectral lines, and a second phase modulator (PM OUT). In addition, the source is followed by an asymmetric MZI interferometer with a free spectral range of 500 GHz, used as a pump filter (PF) to reduce the probability of pair generation in the long waveguide traversing the entire circuit. Moreover, it also serves as an additional input (IN–2) and output (OUT–2) for testing the source alone and the QFP alone. This functionality is later exploited for WS calibration and for classical demonstrations, for which the pair generation stage is not required.

The full GDS, together with a photograph of the chip and of the sample holder, are reported in Figure 4.3. The QFP building blocks are all highlighted in the lay-

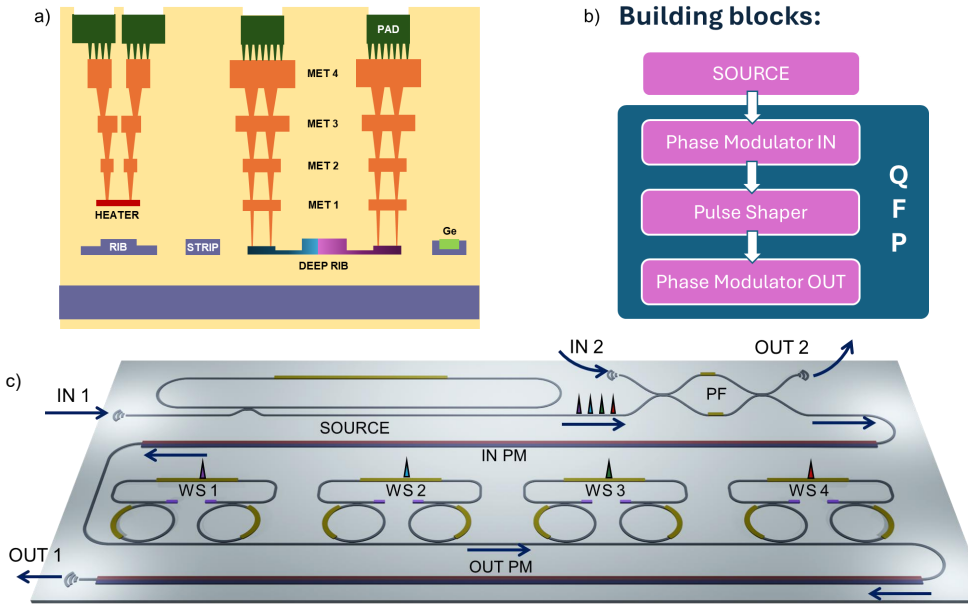



*Figure 4.2:* ***Overview of the silicon chip.*** *(a) Simplified cross–section of the SiPh platform employed in this work. Yellow: $SiO_2$; purple: Si; blue: n-doped Si; magenta: p-doped Si; red: TiN heaters; light green: germanium absorbers; orange: copper metal for electrical routing and vias; dark green: aluminium pads. (b) Circuit's main building blocks. (c) Simplified view of the circuit; for simplicity, only the WS–units used in the experiments are shown, whereas eight units are present on the full chip.*

out view shown in panel (c). In total, the chip contains approximately 28 resistive heaters to tune the response of the optical elements, such as the source coupling coefficient, the light routed by the PF into the QFP (or coupled to OUT–2), the channel wavelength of each WS–unit, and the phase shift applied within each unit. Five additional electrical contacts serve as grounds, for a total of 33 DC electrical aluminium pads, all arranged on the right side of the chip to facilitate wire bonding to the PCB. These contacts are connected through wire bonds to a PCB and driven through computer–controlled voltage sources, enabling easy tuning of the optical components. The 3–mm–long IN and OUT PMs are electrically connected by a single travelling–wave RF line featuring a line impedance of 50 Ω. The line is arranged in a five–electrode geometry, namely ground–signal–ground–signal–ground (GSGSG), connected to five input RF pads for signal injection and 50 Ω terminated at the end of the line. They are driven by two independent RF signals in the tens-of-GHz range using external GSGSG RF probes.

In the following subsections, I provide a detailed description of each build-

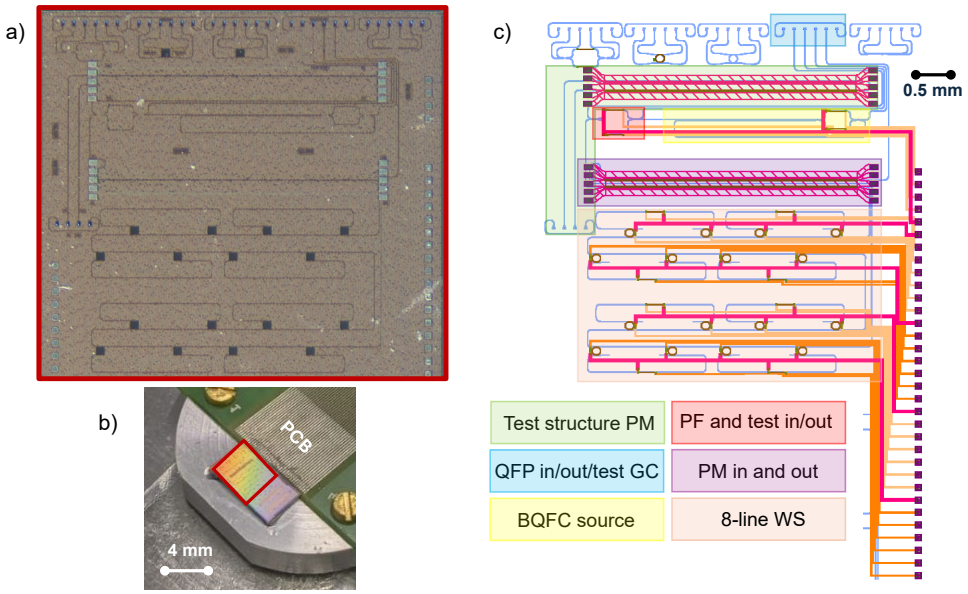



*Figure 4.3:* ***The QFP chip.*** *(a) Photograph of the sample, shown at the same scale as the layout view reported in (c); the different logical building blocks of the chip are delimited by colored squares and listed. (b) Photograph of the sample glued onto the sample holder, with the PCB and the wire bonds for electrical connections visible.*

ing block, including the physical simulations and target performance estimates for those custom devices explicitly designed for this architecture. Their experimental characterizations are also presented, benchmarked against their predicted figures of merit. As previously mentioned, not all components were personally designed, as several were sourced directly from the foundry PDK. Consequently, for these standard devices, the discussion focuses primarily on the experimental validation of their performance in the context of our QFP operation.

### 4.2.1 Biphoton quantum frequency comb source

The biphoton quantum frequency comb source is based on a silicon microring resonator exploiting resonantly enhanced SFWM to generate photon pairs. The MRR is designed to have an FSR of 15 GHz, thus ensuring efficient frequency mode mixing using high–speed silicon phase modulators. Moreover, the MRR is coupled to a bus waveguide through an MZI, which allows for continuous tuning of the coupling coefficient, optimizing the source performance and enabling different operating regimes, such as critical coupling or overcoupling, depending on the target application. This solution is particularly convenient in this case since the footprint of the source, and

even more so of the full circuit, is very large, leaving no room for integrating a circuit DoE to optimize the source, as done in Chapter 3. Therefore, the source incorporates a racetrack MRR, adiabatic curves joined by two long straight WGs, and an MZI, itself composed of two 50:50 directional couplers.

The layout is reported in Figure 4.4(a). The source is followed by a PF, which

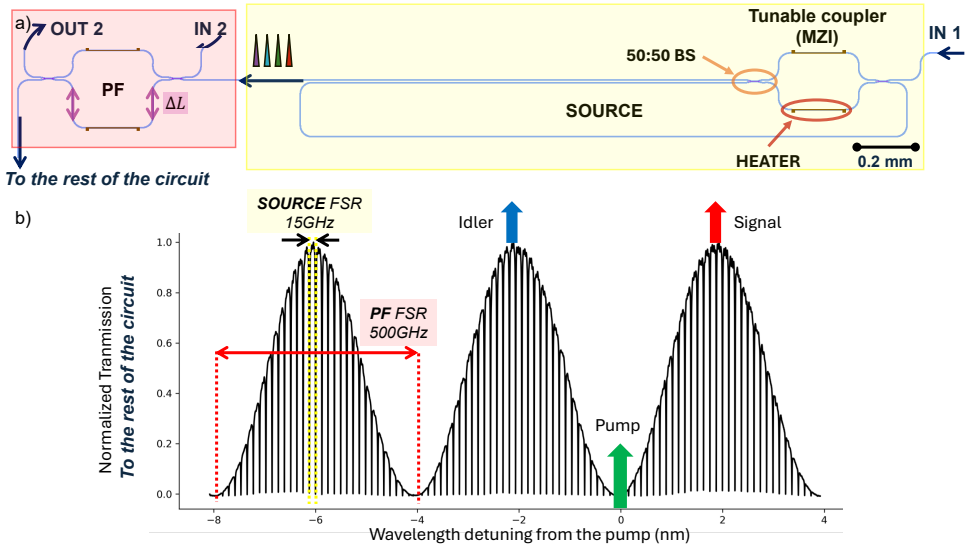



*Figure 4.4:* ***Source layout and working principle.*** *(a) Layout of the source, including the MRR source with the tunable coupler highlighted (yellow region), and the PF (red region). The layout presented here is a zoom of the one reported in Figure 4.3(c). Key elements are highlighted (heater, BS). (b) Typical normalized measured spectrum of the source followed by the PF, illustrating the working principle of this circuit section. The sinusoidal envelope is produced by the PF (an asymmetric MZI, with asymmetry $\Delta L$ reported in (a)), while the deep resonances are caused by the MRR. The spectrum reported here was measured by injecting a tunable laser at IN–1 and collecting the transmitted intensity at OUT–2. Due to the MZI working principle (see section 1.6), the light routed to the rest of the circuit is the exact complement of this response. Thus, to conceptually illustrate the working principle of the generation scheme, here we can consider this spectrum as the one measurable exactly at the port to the rest of the circuit: by pumping the source on–resonance at a minimum of the PF transmission (green arrow), the pump is strongly attenuated, whereas signal and idler photons can be collected at the end of the circuit on the complementary transmission maxima (red and blue arrows).*

is an asymmetric MZI with an FSR of 500 GHz, used to filter out the pump light from the generated photon pairs. The working principle of this section of the circuit is illustrated in Figure 4.4(b), where a typical measured spectrum of the source followed by the PF is reported. The sinusoidal envelope with an FSR of 500 GHz is produced by the PF, while the deep resonances with an FSR of 15 GHz are caused

by the MRR.

To clearly explain the working principle of this circuit portion, let us imagine for simplicity that the spectrum presented in the figure is taken right after the PF, before the light enters the QFP (the port called "to the rest of the circuit" in the figure). More details on how this spectrum has been measured can be found in the caption of Figure 4.4. By pumping the source on resonance at the minimum of the PF transmissivity, the pump is strongly attenuated, while idler and signal photons are collected on high–transmissivity portions of the spectrum and directed to the rest of the circuit. Note that the pump, signal, and idler arrows in Figure 4.4(b), as well as the spectrum itself, are presented as representative examples. The precise wavelengths of the resonances involved in the generation process, along with their measured figures of merit, are reported in detail later in this chapter.

**Simulations and expected figures of merit**

To match the target FSR of both the source and the PF, the modal indices of the waveguide must first be computed (see Equation 1.32 and Equation 1.42, respectively). To minimize simulated–to–fabricated deviations, I chose to use the PDK standard WGs and DCs, as their FoMs (propagation losses and splitting ratios, respectively) are already well established and provided by the foundry, thereby significantly increasing the robustness of the overall circuit performance. Consequently, the source WG geometry was not optimized to obtain enhanced nonlinear effects, as done for example in Chapter 3, but the PDK standard rib SM WG cross–section was used instead. Following the same idea, we will find the same WG geometry also implemented across the other building blocks of the QFP, such as the PF and the WS.

The simulated fundamental TE mode at 1550 nm supported by the WG is shown in the top panel of Figure 4.5. The effective refractive index, group index, and dispersion of the fundamental TE mode around 1550 nm are reported in the lower panel; as expected, the rib geometry does not exhibit anomalous dispersion across any simulated $\mathrm{WG}_w$. At the nominal geometry, the extracted parameters are summarized in Table 4.1. Given the simulated $n_g$, I set the source WG length to approximately 5.160 mm to match the target FSR. For the PF asymmetric MZI, the total arm length difference (highlighted by the purple region $\Delta L$ in Figure 4.4(a)) is about $155\,\mu$m.

The expected FoMs of the MRR were calculated following the approach reported in Section 1.3.3 and are shown in Figure 4.6. As previously mentioned, the FoMs strongly depend on the losses experienced by the light inside the MRR. There-

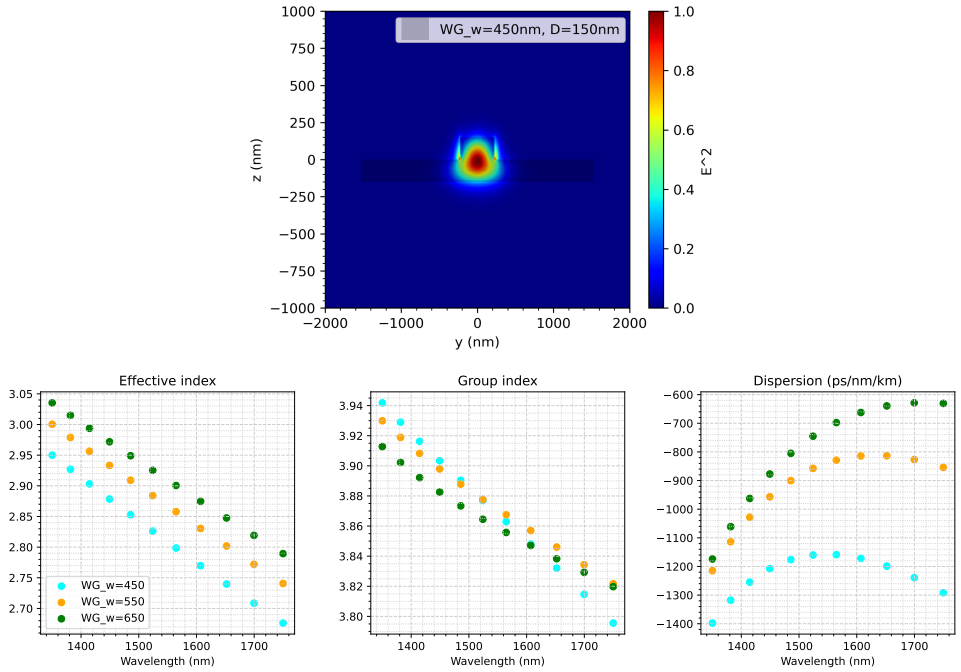



*Figure 4.5:* ***WG simulations.*** *Top panel: simulated mode profile of the standard rib SM WG of the PDK. Bottom panel: effective index, group index, and dispersion as a function of wavelength for different WG geometries.*

| Indices for the SM rib WG at 1.55 $\mu$m | |
|---|---|
| $n_{\text{eff}}$ | 2.788 |
| $n_g$ | 3.874 |
| $\mathcal{D}$ (ps/nm/km) | $-1155$ |
| $A_{\text{eff}}$ ($\mu$m$^2$) | 0.249 |

*Table 4.1: WG simulation results.*

fore, I considered a propagation loss of $1.2 \pm 0.2$ dB/cm, in agreement with PDK values for the considered WG. At the critical coupling condition, corresponding to a cross coefficient $\kappa = 0.4$, I expect a Q–factor of approximately 280000 and a field enhancement of $\sim 2.5$.

### Linear characterizations

Here I report the measured optical spectrum and FoMs obtained for the MRR source. Thanks to the input MZI coupler, the coupling to the bus WG can be effi-

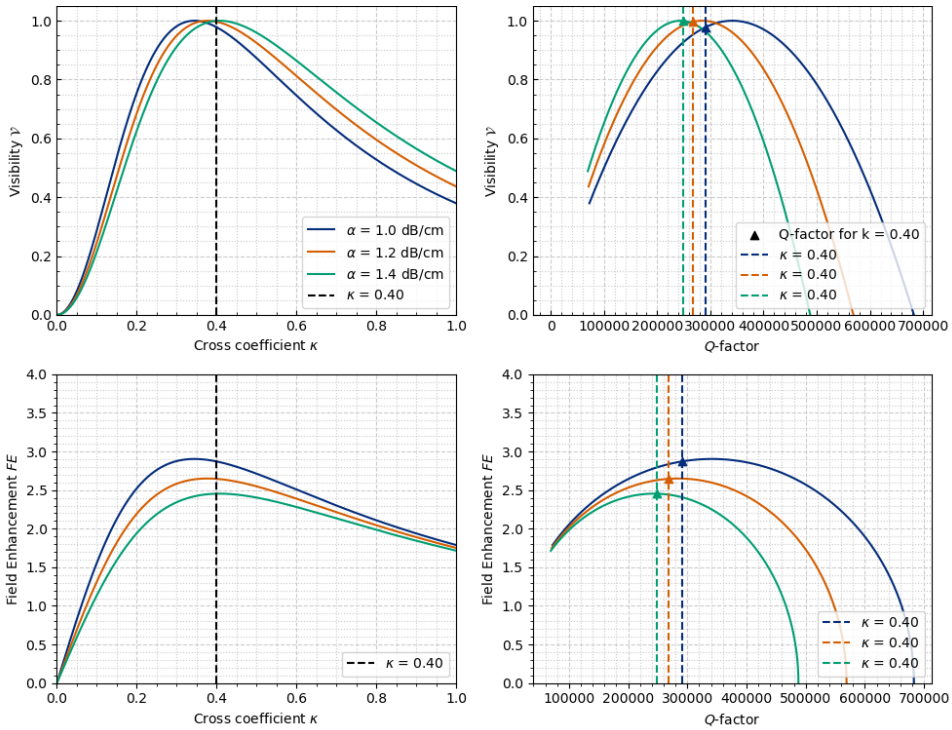



*Figure 4.6:* ***Expected figures of merit of the source MRR.*** *FoMs reported as a function of the coupling coefficient, calculated for propagation losses of* $1.2 \pm 0.2$ *dB/cm. The vertical dashed line indicates the target coupling condition.*

ciently tuned, as clearly shown by the Q–factor and visibility reported in the lower panel of Figure 4.7. The critical coupling condition is reached by applying an electrical power of about 51 mW to one MZI arm, corresponding to a Q–factor of around 240000. The quantum demonstrations were performed in a slightly–overcoupled regime (around 59 mW), which allows for a more efficient extraction of photon pairs from the ring and a narrower resonance shape. The spectrum reported in the top panel corresponds to the idler resonances used in the quantum demonstrations of subsection 4.3.4 and subsection 4.3.5, which are characterized by a quality factor of $3 \times 10^5$. The measured FSR is 15.34 GHz around 1550.0 nm, slightly higher than the target value, but still compatible with the modulation frequency of the PMs.

The characterization of the source in the nonlinear regime, in terms of generation rate and brightness estimation, is reported in Appendix B (see section B.3), as it is not central here given that the focus of this work is on using the full architecture rather than evaluating single–component performance. Moreover, the characteriza-

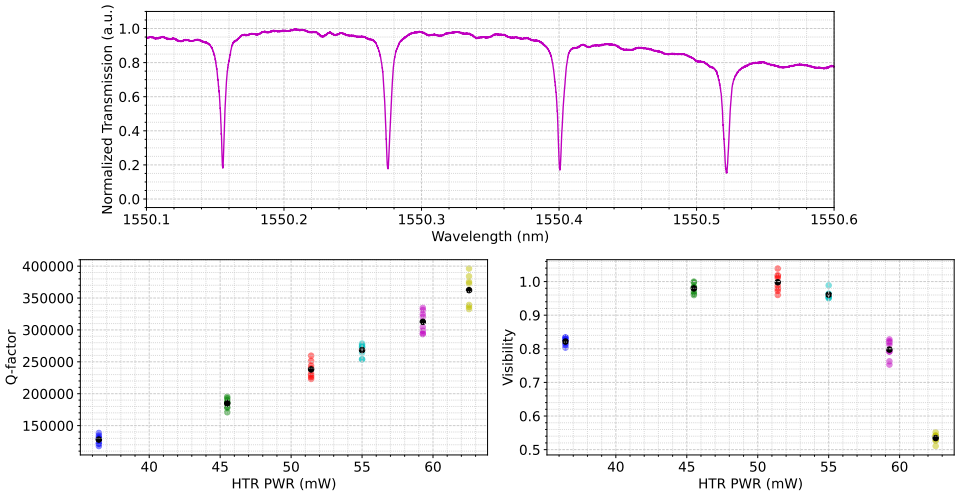



*Figure 4.7:* ***Source linear characterization.*** *Top panel: optical spectrum close to the target performance, achieved at an input MZI heater power of about 59 mW. Bottom panel: observed figures of merit of the MRR source measured as a function of the input MZI heater power (HTR PWR, x–axis). For each setting, each colored point represents the visibility and Q–factor obtained from the Lorentzian fit of a resonance, for a total of eight resonances within the sampled 1–nm range around 1550 nm; the black points indicate the average value for the corresponding setting.*

tion and result analysis procedures follow the approach already extensively reported in section 2.2.1.

Regarding the PF, its measured spectrum was previously shown in Figure 4.4(b). The measured extinction ratio is $\sim$ 30 dB in the wavelength range of interest. As previously mentioned, the goal of the asymmetric MZI is not to completely suppress the pump prior to reaching single–photon detectors, for which a single MZI would not suffice, as known from multiple works on integrated pump–rejection solutions. Its main objective is to attenuate the residual pump immediately after coupling into the source to prevent spurious photon pair generation along the long WGs composing the circuit, which would generate broadband photons and pollute the FB–states generated by the primary source. The measured extinction ratio is already sufficient for this purpose, and its effectiveness is confirmed in the quantum–domain demonstrations in subsection 4.3.4, where no background noise from photon pairs generated off–resonance is observed.

### 4.2.2 p–n phase modulators

The phase modulators are responsible for the mixing of the frequency modes, representing a fundamental building block of the QFP. In silicon WGs, modulation is achieved through plasma dispersion effect, as already described in subsection 1.8.2. Here two PMs are integrated, both based on 3 mm-long p–n junctions embedded in a deep-rib waveguide geometry with a slab thickness of 50 nm and a core width of 360 nm. This is a standard design provided by the foundry; more details on the cross section and fabrication process can be found in Ref. [227, 50]. A GSGSG travelling wave electrode is integrated above the junction, and RF signals are injected (collected) at the input (output) of the line by means of external RF probes. The design of the RF transmission line was also been taken from PDK.

Here, I briefly introduce only the experimental characterization performed to assess the key parameters of the PM, in particular those relevant for the operation of the full circuit. The purpose of these measurements is, indeed, to find the operating regime to fulfill the requirements for the experiments reported in the following sections, such as the modulation bandwidth and the modulation depth at the frequency of interest. In particular, I report the transmission properties of the electrode line under RF driving signals, and the half-wave voltage $V_\pi$ measured at the operating frequency. The characterizations have been performed on the PM test structure, indicated in Figure 4.3, composed of a single 3mm–long p–n junction, accessible optically through an input and output GCs, and electrically connected by a travelling wave electrode, nominally identical to the one implemented in the full circuit, to guarantee consistent analysis.

The RF electrode is characterized in an electrical–electrical configuration by measuring the scattering parameters as a function of the modulation frequency, using two RF probes connected to the input and output of the transmission line. The characterizations have been performed at the laboratory of integrated silicon photonics at CEA–Leti, where a vector network analyzer (VNA) capable of delivering up to 70 GHz–frequency RF tones is available for modulators' bandwidth characterizations. The RF losses are retrieved by measuring the voltage transmitted by the line, normalized by the injected one, in the designed input–output configuration. As a matter of fact, the obtained electrical–electrical RF losses of the line correspond to the magnitude of the scattering parameter $S_{21}$, reported as a function of the driving RF signal frequency in Fig. 4.8 and for different reverse bias voltages. The full scattering matrix, together with the scattering parameter definition, is reported in the Appendix (Figure B.3).

Naturally, the RF losses decrease when the reverse bias voltage is increased, as

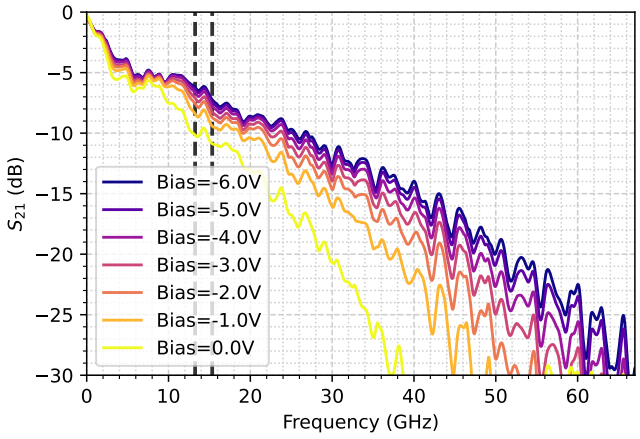



*Figure 4.8:* ***RF line electric–electric characterization.*** *Magnitude of the $S_{21}$–parameter of the integrated RF line as a function of the modulation frequency. It quantifies the voltage transmitted through the line at each RF frequency, obtained by injecting at the input and collecting at the output of the line, with no counter-propagation injection. The dashed vertical line indicates the modulation frequencies used for the full circuit experiments reported in the next sections, i.e.* 15.34 *GHz for the quantum demonstrations and* 13.25 *GHz for the classical demonstrations.*

the depletion region of the p–n junction widens, thus reducing the junction capacitance and consequently the RF losses. At the modulation frequencies used in the full–circuit experiments, around $13 \sim 15\,\text{GHz}$, the measured RF losses are approximately $8 \sim 9\,\text{dB}$ for a reverse bias voltage of $-2\,\text{V}$. However, RF losses are only one of the key parameters to consider to evaluate the best setting for the modulator operation. Increasing the reverse bias voltage pushes the majority carriers away from the junction region, which is located near the center of the optical WG. As a consequence, the overlap between the optical mode and the electrically induced refractive–index modulation is reduced, leading to a lower modulation efficiency. A trade-off must therefore be found between minimizing RF losses and maintaining an efficient electro–optic modulation.

To investigate this trade-off, a second characterization was performed in the electro–optic domain at fixed modulation frequencies. CW laser light around 1546nm, corresponding to the sideband index *0* in Figure 4.9 (a), is injected into the input GC of the PM test structure. The RF signal is injected at the input of the line by the RF probe, while the line termination is $50\,\Omega$, as in the case of the two circuits PMs. Here I report the characterization for 13.25 GHz only, but consistent results

have been found for the other frequency of interest. First, I have verified which was the best reverse bias voltage to apply to the junction, by looking at the generated modulation sidebands in the output spectrum as a function of the reverse bias voltage. At the considered modulation frequencies, the best compromise between RF losses and modulation efficiency is obtained for $-2\,\mathrm{V}$, thus all the following characterizations have been performed at this bias.

The final characterization consisted in sweeping the RF drive power while recording the electro–optical comb spectra collected at the output GC, by means of an optical spectrum analyzer (OSA). According to the well known theoretical treatment [51], the evolution of the relative power of the generated modulation sidebands (Figure 4.9 (b)) should follow the Bessel functions of the first kind $|J_k(\delta)|^2$, whose argument is the modulation depth $\delta = \frac{\pi V_p}{V_\pi}$, where $V_p$ is the peak voltage of the modulation signal. The effective modulation depth and half-wave voltage at the operating frequency are thus obtained by fitting the experimental data with the Bessel functions, obtaining from the fit $V_\pi = 15.5 \pm 1.0\,\mathrm{V}$, where the uncertainty is mainly due to cabling and RF probes loss. This approach has thus provided a practical and direct estimation of the modulator efficiency under the conditions employed in the experimental demonstrations discussed later.

### 4.2.3 Line-by-line waveshaper

The line-by-line waveshaper is the other fundamental building block of the QFP, as it applies arbitrary phase shifts to individual frequency bins. The WS consists of a series of *units*, allocated on a common bus WG, each composed by a pair of add–drop MRRs, looped by a common WG in which the target phase shift is applied by a heater. A unit is illustrated in Figure 4.10 (left panel).

I now briefly describe its working principle. Given a target channel wavelength $\lambda_C$ (green comb line), the resonances of the assigned pair of rings are aligned to $\lambda_C$ by means of the independent heaters integrated on the two. Consequently, the *demux* ring (DR) picks up the comb line, which is coupled to a secondary waveguide by the second point coupler of the AD ring. Here, the desired phase shift $\Phi$ is applied by setting the corresponding heater power, and subsequently the light is reinjected into the common bus waveguide by the *mux* ring (MR). The off-resonance spectral components are not affected by this WS–unit, and propagate straight through the bus WG. This represents an important novelty with respect to other integrated WS architectures, such as that reported in Ref. [225]. By cascading multiple WS–units, it is possible to independently control the phase of multiple comb lines, while pre-

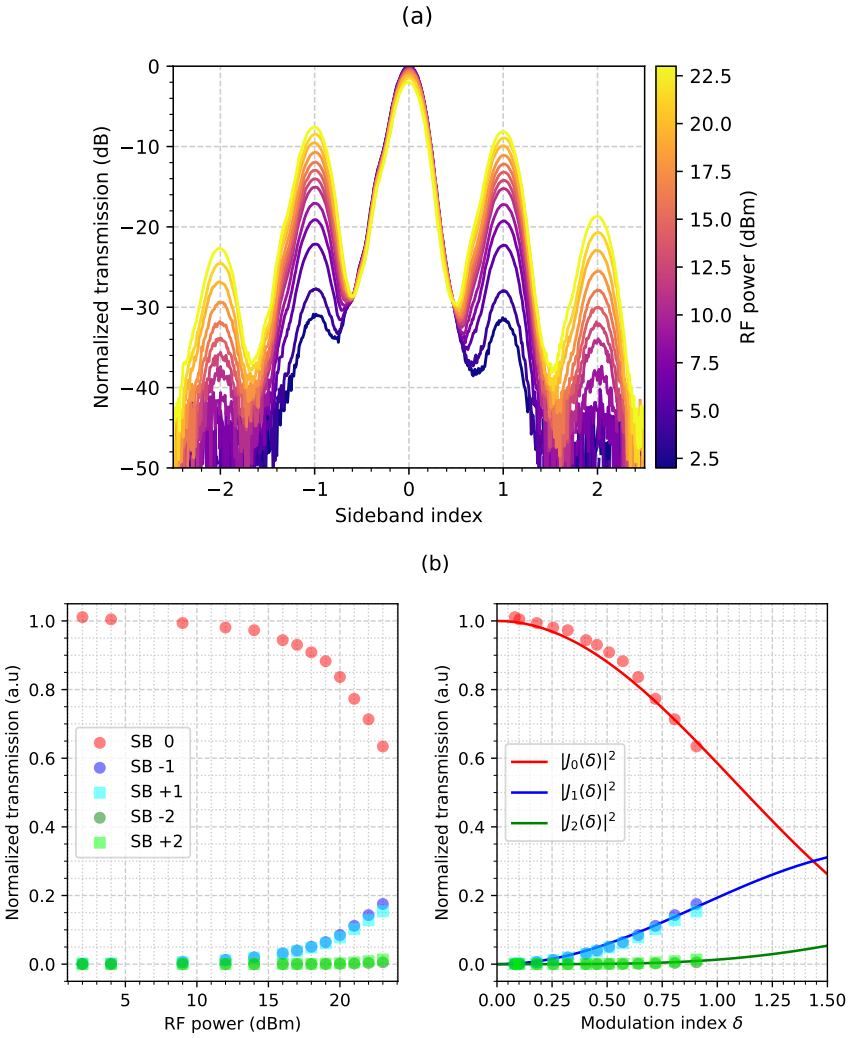



*Figure 4.9:* ***Electro–optical characterization of the PM for a modulation frequency of 13.25 GHz.*** *(a) Spectra recorded with the OSA, normalized with respect to the laser spectral peak measured in the absence of modulation. (b) Relative power of the generated modulation sidebands as a function of the RF driving power. Experimental points: maximum of the corresponding sideband (SB), whose index is defined as in (a). Solid lines: fit of the experimental data with Bessel functions of the first kind. The fit is used to extract the effective modulation depth $\delta$, represented in the x–axis of the right (b)–panel, and the $V_\pi$, obtained to be $15.5 \pm 1.0$ V.*

serving all frequency bins on a single bus waveguide, thus they can be *all* further manipulated with a single PM and ultimately collected out of chip in a single fiber.

Notably, the operation imparted by the WS–units can be reconfigured by set-

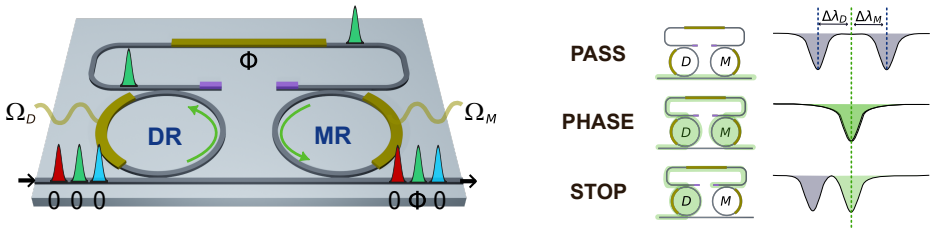



*Figure 4.10:* ***Line-by-line waveshaper.*** *Left: schematic representation of its layout (grey: Si waveguides, purple: Ge absorbers, yellow: heaters) and working principle. The DR collects the target comb line (green) from the common bus WG, while the MR loads it back after the phase shift Φ is applied in the upper WG loop. Right: different WS operations (pass, phase, stop), reconfigurable by tuning the resonance detuning of the ring pair $\Delta\lambda_{D,M}$ with respect to the target channel wavelength (represented by the dotted vertical green line). The resonances of the two MRRs are detuned by means of two heaters, to which independent dither tones ($\Omega_{D,M}$) are added for the calibration procedure (see section B.4).*

ting the resonance detuning $\Delta\lambda_{D,M}$ of the two rings with respect to $\lambda_C$. As above described, when both rings are in resonance with the target channel, the unit operates in the *phase* configuration. On the contrary, when both rings are detuned from the target channel, the WS operates in the *pass* configuration, as the light passes straight through without experiencing either a programmable phase shift or an attenuation. Finally, when only one of the two rings is on resonance with the target channel, the WS operates in the *stop* configuration, since the light is collected by one of the two rings and stopped by one of the absorbers.

Crucial for the *phase* operation of single units is the spectral overlap between the two resonances and the precise control of the applied phase Φ. Therefore, an original calibration technique based on two independent dither tones applied to each ring has been developed. It operates in two steps: first, the optical resonances of the two MRRs are aligned to $\lambda_C$; second, the phase Φ is set to the target value. These steps are implemented using feedback signals derived from the amplitudes of higher–order harmonics in the transmitted intensity, generated by small dither tones applied to the heater voltages of the two rings ($\Omega_{D,M}$ indicated in Figure 4.10). For a given configuration, i.e., modulator driving powers, target wavelength location, and phase setting of each unit, the calibration of a single unit takes approximately 30 minutes, and the procedure is subsequently repeated for all active units. Once

all units are set, potential thermal cross–talk among them is compensated by executing a dedicated voltage optimization routine ($\sim$ 3 minutes per unit). At this point, the optimal settings are stored and stably maintained for all subsequent experimental demonstrations. The comprehensive step–by–step calibration strategy implemented, together with experimental and simulated results, is detailed in Appendix section B.4.

**Design of the MRRs for the WS–units**

The design of the WS units was performed following the approach reported in Sec. 1.3. A low–loss standard SM rib WG geometry was used, consistently with all other circuit sections apart from the PM regions, as previously mentioned. Consistent with the values reported in Table 4.1, the radius was set to $R = 49.265\,\mu$m to obtain an FSR of 250 GHz. The MRRs of the phase shifters were designed to exhibit an FWHM approximately 5 times larger than that of the BQFC resonances, in order to easily accommodate a single comb line of the 15 GHz BQFC while maintaining high visibility. Under this condition, the transmission and phase response of the WS can be assumed to be approximately flat across the entire width of the comb line, thereby avoiding distortion effects. At the same time, high visibility allows most of the comb–line power to be loaded into the WS, minimizing its insertion loss. Therefore, a Q–factor of approximately 40 000 and a visibility close to unity were chosen as target performance metrics for the WS MRRs.

Point–coupler simulations were performed following the methods reported in Sec. 1.3. The target coupling coefficient was estimated to be $\kappa_t \simeq 0.23$, corresponding to a gap of 540 nm for the selected cross–section and curvature radius. Point–coupler simulation results and the computed FoMs of the WS rings as a function of the coupling coefficient are reported in the Appendix (see Figure A.4).

Because the ring resonators employ a rib waveguide geometry, the point couplers retain the same cross–sectional profile. As a consequence, the coupling region is not defined by a fully etched $SiO_2$ gap; instead, the partially etched slab is shared between the bus WGs and the ring waveguide. The resulting geometry is more sensitive to fabrication imperfections, particularly variations in the etching depth, which can lead to systematic deviations from the target coupling coefficient.

In addition, due to the large footprint of the full circuit and the limited space available on the MPW mask, only a single circuit layout was fabricated, without including a DoE for optimizing the WS performance. As a consequence, the performance of the fabricated WS–units was found to deviate from the simulated values, which were based on ideal point–coupler models. This discrepancy is already evid-

ent in the characterization of the individual MRRs, which is therefore presented first, before the evaluation of the WS performance.

### Characterization of the MRRs for the WS–units

The spectra of the MRRs were characterized by injecting a tunable laser into the additional input port of the PF (IN–2 in Figure 4.2) and collecting the transmitted power at the chip output. The spectrum of a single MRR is shown in the left panel of Figure 4.11. The measured Q–factor ranges from 51000 to 53000 across different rings, thus differing from the target value of 40000 previously envisioned. This higher Q–factor does not represent a limitation in itself, as the resonance is nevertheless broad enough to accommodate the comb lines without distortion. However, it leads to consequences that affect the overall WS–unit performance, as discussed in the following section.

To quantify this discrepancy, I modeled the response of the fabricated device. By comparing the measured data against multiple coupling scenarios, I found that the experimental spectra closely resemble the simulated MRR response obtained for $\kappa_{\text{exp}} \simeq 0.15 \sim 0.16$, assuming WG losses about 1.2 dB/cm as expected from PDK values. Given this value, the MRRs operate in a slight undercoupling regime compared to the target coupling coefficient of 0.23 obtained from the previously presented point–coupler simulations.

Having identified this deviation, I will from now on present simulated results considering this experimentally extracted coupling condition. First, the simulated response of a single ring is presented in the upper panel of Figure 4.12, showing both the magnitude squared and phase responses at the Through ($|T|^2$ and $\arg(T)$) and Drop ($|D|^2$ and $\arg(D)$) ports. With this result in mind, I will now present the simulation and characterization of the complete units. All simulated spectra were obtained using the formalism reported in section 1.3 and implemented in Python (see section A.5 for additional details).

### WS–unit design and linear characterization

The expected transmission and phase response of a complete WS–unit were computed using the transfer matrix method (TMM) in the *phase* operation configuration, i.e., with the resonances of the two rings aligned to the target channel wavelength $\lambda_C$. The resulting spectra are shown in Figure 4.12 as a function of the wavelength detuning relative to $\lambda_C$, corresponding to $\Delta\lambda = 0$ in the plots. The model includes all relevant physical quantities, such as propagation losses, the MRR

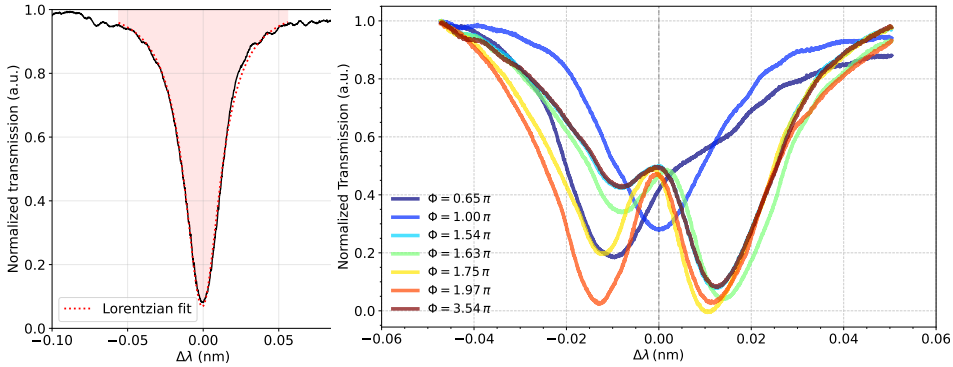



*Figure 4.11:* ***Linear characterization of a single WS MRR and of a WS–unit.*** *Left: transmission spectrum of a single ring resonator, showing a Q-factor of approximately 51000. Right: transmission spectra of the WS–unit for different applied phase shifts* $\Phi$*. The reported phase shifts are associated with an uncertainty of approximately* 0.1 *rad, originating from the heater power–to–phase calibration process (see Figure B.7). The spectra are normalized to the maximum transmitted power measured at the central wavelength around 1550 nm. The dashed vertical line indicates the target channel wavelength* $\lambda_C$*.*

radius, and the experimentally estimated coupling coefficient $\kappa_{\text{exp}} \simeq 0.16$ previously extracted from the single–MRR characterization. The parameters used in the simulations are summarized in Appendix B (section A.5).

Both the transmissivity $|T|^2$ and phase response $\arg(T)$ at the WS–unit Through port are reported in Figure 4.12 as a function of wavelength for different applied phase shifts $\Phi$. The spectra exhibit a strong dependence on the applied phase due to the resonant nature of the device. To clarify the physical origin of this behavior, the operation of the WS–unit is discussed under the optimal condition where the resonance centers of both rings are aligned to $\lambda_C$.

Let us first consider a monochromatic optical signal injected at the input port of the WS–unit with a wavelength exactly equal to $\lambda_C$. In the ideal case of unitary drop efficiency, all optical power is coupled by the DR into the upper waveguide loop, acquires the phase shift $\Phi$ imposed by the heater, and is subsequently coupled back into the common bus waveguide by the MR. Under actual experimental conditions, however, the drop efficiency is reduced by intrinsic intracavity losses, as visible in the simulated drop spectrum of the single MRR (red curve in the top panel). Consequently, the simulated WS–unit transmissivity at zero detuning is lower than unity, corresponding to an estimated insertion loss of approximately $5 \sim 6\,\text{dB}$, with a slight dependence on the applied phase shift $\Phi$. Nevertheless, the

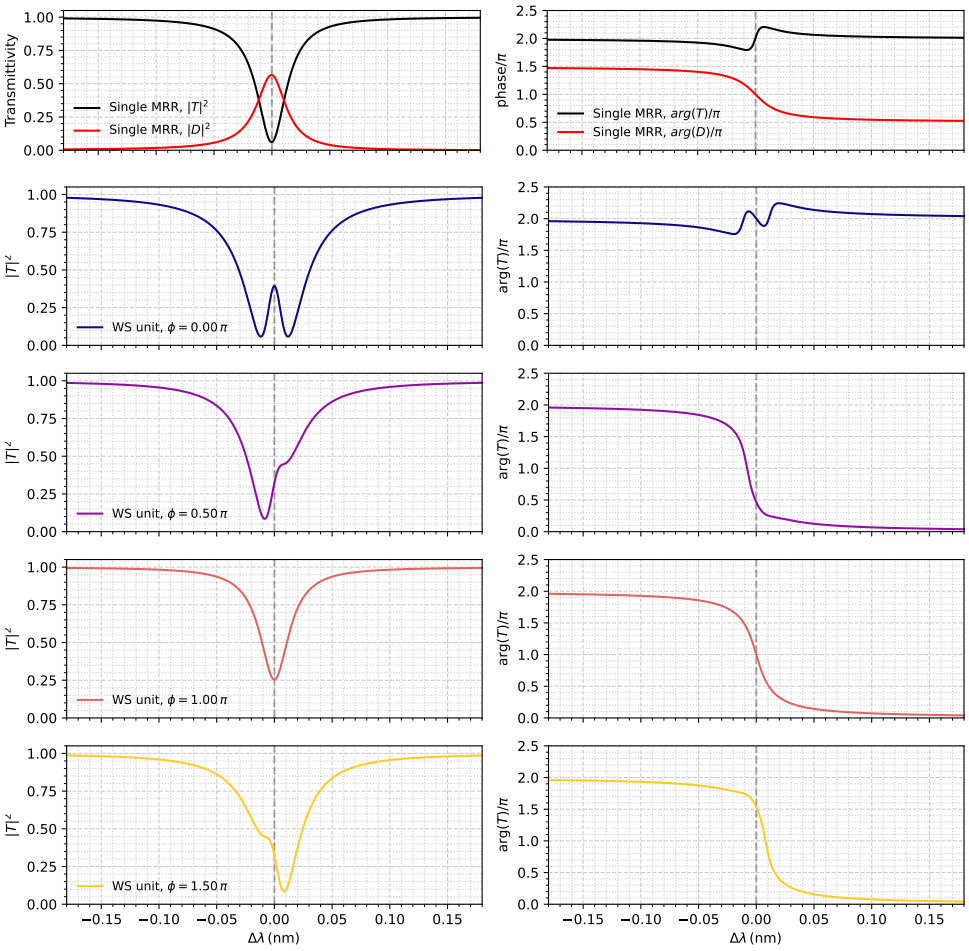



*Figure 4.12:* ***Simulated transmissivity and phase response of a single WS MRR and of a complete WS–unit.*** *The x–axis reports the wavelength detuning relative to the central channel wavelength $\lambda_C$, indicated by the vertical dashed line. Top panel: Through and Drop transmissivity and phase response of a single MRR. Lower panels: simulated spectra of the WS–unit in phase operation for different values of the nominal phase shift $\Phi$ applied by the WS heater (Through port). The simulations incorporate the experimentally estimated coupling coefficient $\kappa_{\text{exp}} \simeq 0.16$. See Appendix B, section A.5 for more simulated $\Phi$ values.*

phase shift imparted to the optical field at $\lambda_C$ matches the target value, as indicated by the intersection between the vertical dashed line at $\Delta\lambda = 0$ and the phase curves reported in the right panel of Figure 4.12.

Away from the central wavelength $\lambda_C$, the optical field is only partially coupled

into the DR due to the Lorentzian line shape of the resonance. As a result, a significant fraction of the input light remains in the bus waveguide and propagates directly to the MR Through port without entering the upper loop. This field interferes at the MR with the portion of light previously dropped by the DR into the upper loop and coupled back into the bus. The resulting interference strongly depends on the applied phase shift $\Phi$, producing the pronounced transmissivity modulation visible away from $\Delta\lambda = 0$. Additionally, the intrinsic phase response of the MRRs introduces a wavelength–dependent phase shift that approaches zero (or $2\pi$) only at the resonance center, as shown in the top panel of Figure 4.12. Consequently, accurate spectral alignment between the resonance wavelengths of the DR and MR and the target wavelength $\lambda_C$ is essential for reliable phase control of the selected spectral line.

Notably, this strong dependence of the WS–unit spectra on the applied phase shift provides a practical feature: by performing a wavelength sweep with a tunable laser, the phase shift applied by the WS can be experimentally retrieved by fitting the measured spectra with the TMM model (see subsection B.4.1 for further details). This approach was initially employed to obtain a baseline estimate of $\Phi$. A drawback of this architecture is the residual variation in insertion loss at $\lambda_C$ as a function of applied phase, clearly visible in the simulated spectra, which leads to a maximum power variation of approximately 0.8 dB in our experimental configuration.

The measured spectra of a WS–unit for various applied phase shifts are shown in the right panel of Figure 4.11, demonstrating good agreement with the theoretical predictions after accounting for the experimentally estimated coupling coefficient.

In summary, the integrated line–by–line waveshaper architecture provides independent phase manipulation of individual frequency bins along a shared bus waveguide. Although the current implementation exhibits an insertion loss of $5 \sim 6$ dB per unit, the performance presented here is consistent with similar integrated implementations [225]. Combined with the automated dither–tone–based calibration routine, this design provides stable, high–fidelity alignment across multiple spectral channels, achieving a phase setting precision of about $\pm 6^\circ$ per channel corresponding to the accuracy of the heater power–to–phase mapping (see technical details in Figure B.7). In the following sections, I will present key experimental demonstrations where the reconfigurable spectral phase control provided by the WS is exploited to demonstrate full processor functionality.

## 4.3 Experimental demonstrations in the classical and quantum domain

The experimental demonstrations reported here were all realized using the photonic chip described above. In Figure 4.13, I report the configuration of the chip for the different operations synthesized (gate synthesis, calibration, quantum walk, and quantum state tomography), together with the off–chip setup personally conceived and implemented. Out of the eight integrated WS–units, four are actively reconfigured to perform the target operations, while the remaining four pairs of rings are detuned from the spectral region of the experiments. Controlling a total of four comb–line phases is sufficient to achieve high performance across all target demonstrations while keeping the complexity of the calibration and control procedure manageable.

The experimental demonstrations are divided into two main categories: classical and quantum. In the classical domain, the performance of the integrated QFP is evaluated by synthesizing a set of target unitary operations on the frequency–bin space, which are then characterized using an optical spectrum analyzer. In the quantum domain, the QFP is employed to manipulate entangled photon pairs generated by the on–chip source, enabling the realisation of a quantum walk and the reconstruction of a two–qubit density matrix through quantum state tomography. The following sections provide detailed descriptions of each experimental demonstration, including the specific configurations of the chip and the corresponding measurement setups.

### 4.3.1 Experimental setup

A tunable continuous–wave (CW) pump laser is employed as the optical source. Its output is first sent to an off–chip electro–optic phase modulator driven by an RF signal at the modulation frequency used in the experiment, namely 13.25 GHz for classical demonstrations or 15.34 GHz for quantum demonstrations, i.e. matching in this case the FSR of the integrated source. It generates an electro–optic frequency comb whose comb–line amplitudes and relative phase shifts are pre–adjusted using an external programmable waveshaper. Prior to coupling the light into the chip, the polarization state is optimized with a fiber polarization controller to match the TE mode supported by the grating couplers. For quantum demonstrations, residual broadband spectral components originating from the modulation process and amplified spontaneous emission are suppressed using an external bandpass filter to

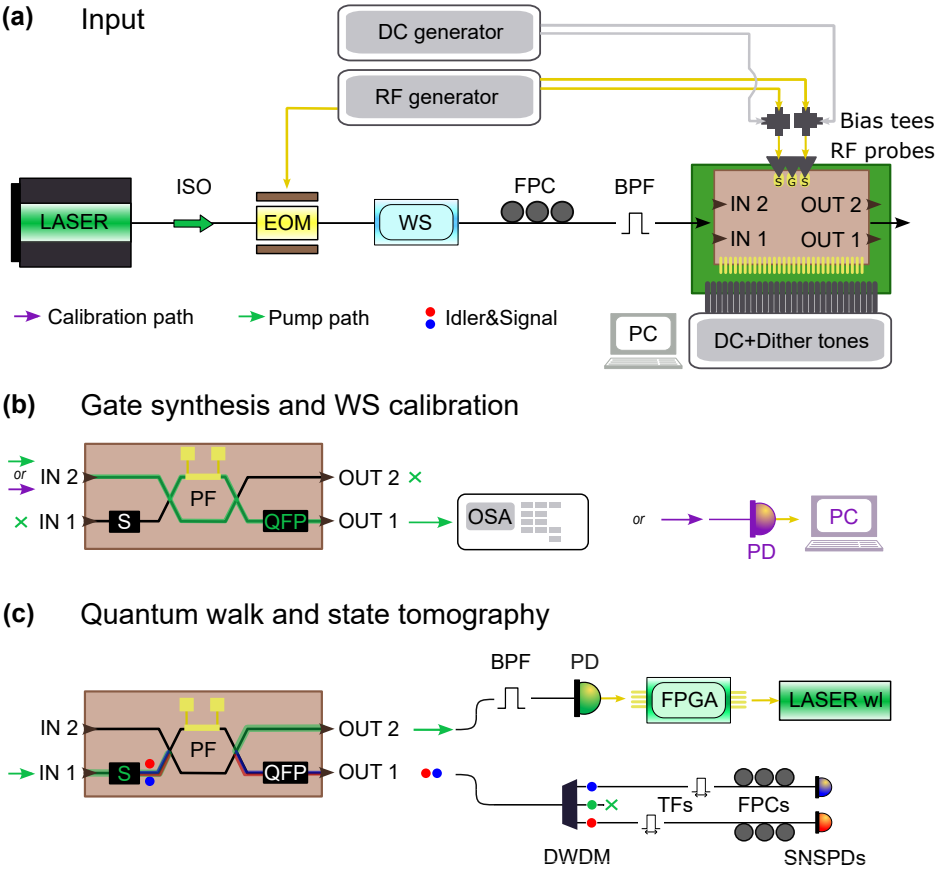



*Figure 4.13:* ***Detailed experimental setup.*** *(a) Schematic of the off–chip optical and electrical apparatus used to drive and characterize the integrated quantum frequency processor. (b) Zoomed–in view illustrating the chip routing configuration during gate synthesis and WS channel calibration, where input laser light is injected at IN–2, bypassing the integrated source (S) through the pump filter (PF) in cross configuration, and directed through the QFP. The light collected at OUT–1 is analyzed either by an OSA (gate synthesis, green light beam) or by a PD (calibration purposes, purple light beam). (c) Zoomed–in view illustrating the chip routing configuration during quantum walk and quantum state tomography experiments, where the pump laser (green) is injected at IN–1, residual pump light is extracted at OUT–2 for active laser wavelength locking, and generated photon pairs (blue and red) are processed by the QFP before output collection at OUT–1, to be finally processed by the frequency–resolved single photon detection apparatus. ISO: isolator; EOM: external electro–optic modulator; WS: external programmable waveshaper; FPC: fiber polarization controller; BPF: bandpass filter; PF: integrated pump filter; S: integrated source; QFP: integrated quantum frequency processor; PD: photodiode; OSA: optical spectrum analyzer; DWDM: ∼ 80 GHz–wide spectral filter; TF: 12 GHz–wide narrowband tunable filter; SNSPD: superconducting nanowire single–photon detector.*

reduce accidental counts at the single–photon detectors. The prepared optical signal is then injected into either the IN–1 or IN–2 port of the device (Figure 4.2), depending on the experimental scheme.

The on–chip photonic circuit is reconfigured by controlling the DC bias applied to the integrated thermal phase shifters using dedicated, computer–controlled voltage drivers. During the calibration of an individual WS–unit, two low–amplitude, independent dither tones are applied to the corresponding MRR pair, as detailed in Appendix B (section B.4). By appropriately adjusting the thermal phase shifter integrated in the PF, different on–chip wavelengths can be selectively routed either toward the rest of the circuit or directly coupled off chip through the OUT–2 port. As previously mentioned, the maximum isolation between the *cross* and *bar* state is given by the extinction ratio of the PF, measured to be about 30 dB in the range of interest. More precisely, in the case of gate synthesis and WS channel calibration, the PF is set to the cross configuration for light injected at IN–2, routing it from the input to the opposite waveguide (bypassing the on–chip source S) and directing it straight into the integrated QFP. After frequency–bin manipulation through the on–chip PMs and WS, the optical signal is coupled off–chip via the OUT–1 grating coupler and characterized using either an OSA (for classical gate characterization) or a photodiode (for WS channel calibration), as shown in Figure 4.13(b).

For the quantum walk and quantum state tomography demonstrations, the pump light is injected into port IN–1 and tuned into resonance with the on–chip source. Most of the pump light is extracted through OUT–2 (with the PF in *cross* configuration at that wavelength) and monitored with a photodiode, while an active feedback loop adjusts the pump laser current to maintain the laser wavelength locked to the center of the pump resonance (Figure 4.13(c)). Under these conditions, the generated biphoton frequency comb, filtered by the sinusoidal transmission response of the PF (in *bar* configuration at the idler and signal selected wavelengths), is routed toward the QFP and manipulated by the WS–units and the output PM. Signal and idler photons are collected from port OUT–1 and directed to a frequency–resolved single–photon detection setup, similar to that presented in Chapter 2, based on dense DWDM filters ($\sim$ 80 GHz bandwidth) and narrowband tunable filters ($\sim$ 12 GHz bandwidth).

#### Additional details on chip calibration and settings

Now that the setup has been described for the different experimental scenarios under test, it is worth outlining how specific on–chip components are properly set

and calibrated, as it is a crucial prerequisite for the experiments to succeed. First, regarding the driving of the on–chip PMs, I have already presented in this chapter the basic characterization performed on a single modulator test structure, which yielded a $V_\pi$ of approximately $15.5 \pm 1.0$ V at the frequency of interest (subsection 4.2.2). To reach the conditions required for the targeted experiments (detailed in their respective sections), the necessary RF signal power is around 23–27 dBm, provided by a dual–channel RF driver and a dedicated amplifier. Importantly, as mentioned earlier, to operate correctly, the p–n junction–based high–speed phase modulators must be driven in the reverse–bias regime. Thus, a bias–tee is used for each modulator (see Figure 4.13(a)) with the DC input biased at $-2$ V to ensure reverse–bias operation. The amplifier gain is 34 dB, while the RF losses from the wiring and each bias–tee are estimated to be about $2 \pm 0.5$ dB per modulator. Although the RF insertion losses associated with the external probes could not be measured directly due to the lack of a vector network analyzer (VNA), this does not limit performance, as only specific modulation depths in the range $\delta \simeq 0.8$–$1.4$ are required; these were calibrated directly by measuring relative sideband intensities with an OSA.

Another crucial parameter for the experiment is the relative phase between the two on–chip PMs, which must be accurately calibrated. To do so, I first identified the $\pi$–dephasing condition. With the WS rings detuned from the target wavelengths and equal modulation depths applied, the electro–optic comb generated by the input PM is mapped back into the optical carrier by the output PM when the relative RF phase is set to exactly $\pi$. All other phase settings are subsequently obtained by adjusting the phase of one RF signal at the RF driver.

Finally, the calibration of the WS units is fundamental. While I have already included a brief description of this procedure in the main text (subsection 4.2.3), its detailed treatment is reported in Appendix B (section B.4).

Now that the experimental setup and the on–chip calibration procedures have been fully described, I will present the experimental demonstrations of the QFP functionality, starting with the two–mode frequency beam splitter (BS) operation.

### 4.3.2 The frequency beam splitter operation

A frequency beam splitter (FBS) coherently mixes two discrete frequency modes in direct analogy to the action of a spatial beam splitter on two optical paths. At the output of a two–mode FBS, one expects to obtain (ideally) two optical output

frequency modes with a programmable splitting ratio (in the classical domain, Figure 4.14(b)). To realize such a transformation, two basic operations are required: a relative phase shift between the modes and mode mixing (interference). For spatial path modes, a simple MZI (see the schematic in Figure 4.14(a)) embeds both operations, enabling a tunable BS whose splitting ratio can be programmably modified by controlling a single phase shifter. In the frequency domain, however, implementing this transformation is less straightforward.

Such an operation is of fundamental importance, as it constitutes a core building block of the Linear Optical Quantum Computing framework (LOQC, [228]), together with phase–shifting operations and single–photon counting. Therefore, I have chosen this operation as the first demonstration to validate the functional operation of the chip.

This operation has been experimentally demonstrated in integrated platforms

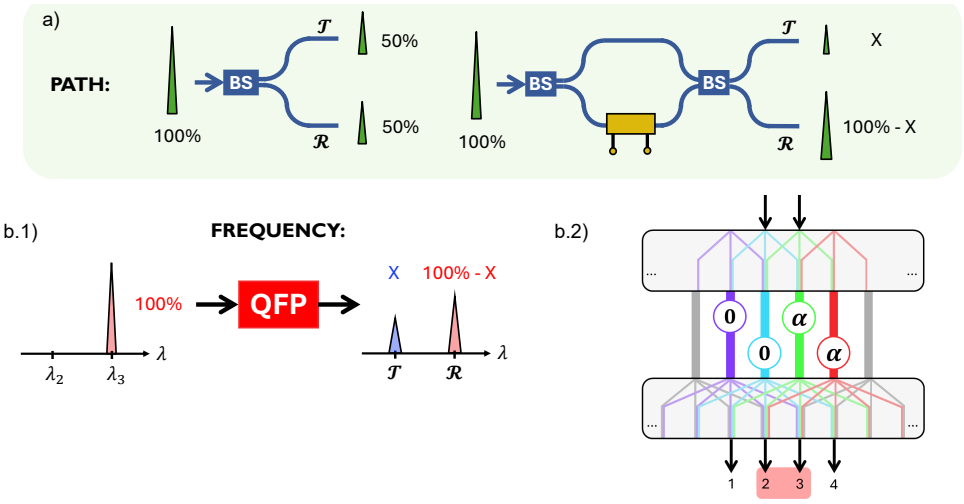



*Figure 4.14:* ***Two–mode beam–splitting operation.*** *(a) In path encoding, a tunable BS is implemented using a Mach–Zehnder interferometer composed of two 50:50 spatial BSs and a phase shifter in one arm (yellow element). The probability $X$ depends on the phase shift between the two arms. (b) In frequency–bin encoding, the operation is less straightforward. (b.1) Example of typical FBS behavior between two target modes labeled with indices 2 and 3: light injected into mode 3 is partially reflected ($\mathcal{R}$, remaining in mode 3) and partially transmitted ($\mathcal{T}$, propagating into mode 2). (b.2) Configuration of the QFP used to realize the FBS operation. The probability $X$, which defines the tunable splitting ratio, is governed by the relative phase shift $\alpha$ (see theoretical explanation in the following paragraph).*

by engineering an electro–optic resonator in thin–film lithium niobate [229]. Within the QFP framework, two notable demonstrations based on the EOM–WS–EOM

architecture are reported in the literature: one using bulk–optics components [216] and a more recent implementation combining bulk EOMs with an integrated WS [224].

In the chip presented in this work, all necessary components for realizing the FBS operation within the QFP architecture are monolithically integrated. The chip configuration is illustrated in Figure 4.14(b.2) and described below.

**Theoretical framework**

The most general unitary operation acting on a single qubit can be parametrized as

$$U(\theta,\lambda,\mu)=\begin{pmatrix}\cos\dfrac{\theta}{2} & e^{i\lambda}\sin\dfrac{\theta}{2}\\ e^{i\mu}\sin\dfrac{\theta}{2} & -e^{i(\mu+\lambda)}\cos\dfrac{\theta}{2}\end{pmatrix}, \tag{4.1}$$

where $\theta\in[0,\pi]$, $\mu\in[0,2\pi)$, and $\lambda\in[0,2\pi)$ are the Euler angles. In fact, this matrix can be decomposed into a sequence of three rotations, $R_z(\mu)R_y(\theta)R_z(\lambda+\pi)$, where $R_J(x)=e^{ixJ}$ and $J=\{Y,Z\}$ are the Pauli matrices. By varying $(\theta,\lambda,\mu)$, any point on the Bloch sphere can be reached, confirming the generality of this formalism.

Coming back to the frequency–bin encoding framework, it has been shown in Ref. [217] that arbitrary single–qubit operations can be implemented by precisely setting a three–element QFP, such as the one integrated on our chip. Specifically, obtaining target frequency–bin gates requires specific settings for the RF driving signals of the two PMs (both power and relative phase), together with the frequency–bin phase shift applied between them by means of the WS.

Focusing now on the realisation of a two–mode 50:50 beam splitter (BS) or Hadamard gate within the general unitary transformation framework of Equation 4.1 (which holds independently of the chosen encoding), the 50:50 splitting operation corresponds to $H=U\left(\frac{\pi}{2},0,0\right)$. Within the QFP framework, a continuously tunable beam splitter is realized when the two RF signals are $\pi$–shifted and a phase jump $\alpha$ between the left and right frequency modes is applied by the WS, a configuration schematically illustrated in Figure 4.14(b.2). Under these conditions, the $U$ matrix reduces to [220]:

$$U(\alpha)=\begin{pmatrix}U_{00}(\alpha) & U_{01}(\alpha)\\ U_{10}(\alpha) & U_{11}(\alpha)\end{pmatrix}. \tag{4.2}$$

By varying the left–right phase difference $\alpha$, one obtains a tunable beam splitter whose reflectivity and transmissivity are given by the squared modulus of the matrix

elements:

$$\begin{aligned}\mathcal{T}_{0\to1} = \mathcal{T}_{1\to0} = |U_{10}(\alpha)|^2 &= \left|\left(1-e^{i\alpha}\right)\sum_{k=1}^{\infty} J_k(\delta)J_{k-1}(\delta)\right|^2, \\ \mathcal{R}_{0\to0} = |U_{00}(\alpha)|^2 &= \left|J_0^2(\delta) + \left(1+e^{i\alpha}\right)\frac{1-J_0^2(\delta)}{2}\right|^2, \\ \mathcal{R}_{1\to1} = |U_{11}(\alpha)|^2 &= \left|e^{i\alpha}J_0^2(\delta) + \left(1+e^{i\alpha}\right)\frac{1-J_0^2(\delta)}{2}\right|^2,\end{aligned} \tag{4.3}$$

where $J_k(\delta)$ are Bessel functions of the first kind and $\delta$ is the modulation index ($\delta \simeq 0.82$, extracted from simulations as reported in Ref. [217]). The resulting reflectivity $\mathcal{R}_{0\to0} = \mathcal{R}_{1\to1} \equiv \mathcal{R}$ and transmissivity $\mathcal{T}_{0\to1} = \mathcal{T}_{1\to0} \equiv \mathcal{T}$ are plotted in Figure 4.15 as a function of $\alpha$, together with the corresponding $\theta$ and $\lambda$ angles as a function of the parameter $\alpha$ of Equation 4.1.

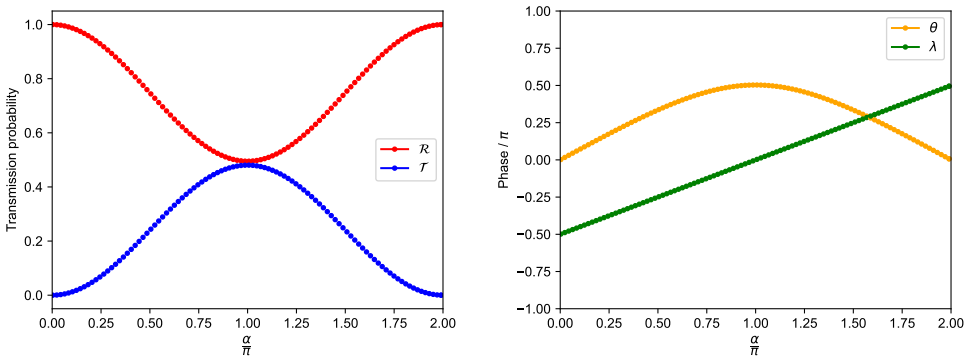



*Figure 4.15:* ***Theoretical response of the tunable frequency beam splitter.*** *Left panel: expected BS splitting ratio as a function of the left–right phase difference $\alpha$. Right panel: corresponding theoretical phases $\theta$ and $\lambda$ of Equation 4.1 as a function of $\alpha$. The phase $\mu$ is not reported, since it coincides with $\lambda$ in our formalism.*

As anticipated, for the specific case $\alpha = \pi$, the standard Hadamard gate is obtained:

$$U(\pi) = H = \frac{1}{\sqrt{2}}\begin{pmatrix}1 & 1\\ 1 & -1\end{pmatrix}. \tag{4.4}$$

This is the first classical gate demonstration presented here.

### Figures of merit

Before presenting the experimental results, it is necessary to introduce the metrics used to verify the quality of the implemented gate. Two figures of merit are employed: the fidelity $\mathcal{F}$, which compares the measured transformation with the ideal one, and the success probability $\mathcal{P}$, which quantifies the fraction of light remaining in the two target modes with respect to the total spectral intensity. Following [216], they are calculated as:

$$\begin{aligned} \mathcal{P} &= \frac{1}{d}\,\mathrm{Tr}\big(U^\dagger U\big)\,, \\ \mathcal{F} &= \frac{1}{\mathcal{P}\,d^2}\,\big|\mathrm{Tr}\big(U^\dagger U_T\big)\big|^2\,, \end{aligned} \tag{4.5}$$

where $U$ is the measured transformation matrix and $U_T$ is the target one. Both are truncated to the $d \times d$ subspace of the BS operation, with $d = 2$ in our case. To assess the quality of the implemented operation itself, I disregard the overall insertion loss before computing these quantities, as usually done in this type of demonstrations [216, 230]. The total loss will anyway be clearly stated.

### Results, the 50:50 case

Let us consider four classical FB modes, whose frequency spacing is $f = 13.25\,\mathrm{GHz}$, labeled 1 through 4 in Figure 4.14(b.2). The two central bins (2 and 3) are the target modes for the realisation of the tunable BS operation, while the outer bins (1 and 4) serve as auxiliary modes. Using the on–chip WS, the phases $\{\Phi_j\}_{j=1}^4$ associated with each FB are independently controlled and set according to the theoretical model. In addition to these modal phases, the calibration procedure also includes the setting of the modulation depth $\delta$ of the two PMs, and the relative phase between the two RF signals, driven at frequency $f$. The methods used for those calibrations are already reported in subsection 4.3.1, while here I summarize the implemented values and settings, according to the experimental procedure reported in Ref. [216]:

- **IN PM:** the modulation depth is set to $\delta = 0.82 \pm 0.02$, corresponding to a power difference between the carrier and the first–order sidebands of $-6.9 \pm 0.1\,\mathrm{dB}$. In our setup, this requires an RF power of $P_{RF}^{\mathrm{in}} = 23.0 \pm 0.5\,\mathrm{dBm}$.

- **OUT PM:** the same modulation depth as the IN PM is used, requiring an RF power of $P_{RF}^{\mathrm{out}} = 23.5 \pm 0.5\,\mathrm{dBm}$. The relative RF phase between the two PMs is set to $\pi$.

For a 50:50 splitting ratio, the phase pattern along the four FBs must be $[0, 0, \pi, \pi]$. Since the physically relevant quantity is the phase difference between the *left* and *right* modes, the absolute phases can be freely adjusted. In practice, I select the phase configuration that minimizes the transmissivity imbalance at the target modes, thereby reducing unbalanced losses according to the spectra reported above (Figure 4.12), namely $[\pi/2, \pi/2, 3\pi/2, 3\pi/2]$.

The top panel of Figure 4.16 shows the resulting spectrum after calibration of the four WS units, i.e., after optimizing both ring alignment and applied phase. Finally, the exact frequency of the input laser comb is fine–tuned (within $\sim 20\,\mathrm{pm}$ from the target one) by monitoring the output spectrum on the OSA, in order to optimize the performance.

The resulting BS operation is shown in the bottom panels of Figure 4.16. When injecting a pure state, i.e., when the off–chip waveshaper selects either the left (blue) or right (red) comb line, the light is split between the two target modes. Without changing the configuration, the capability of the processor to coherently manipulate the FB modes is showcased by injecting a superposition state (two comb lines in the target modes, in green). As reported by the two lower spectra, routing all the light into either one or the other target mode is possible by only modifying the relative phase between the two input comb lines (i.e., the phase of the external PM $\gamma$, from 0 to $\pi$). These four spectra are sufficient to reconstruct the experimental complex $2\times2$ scattering matrix $U$ representing the implemented BS operation, which is reported in the top panel of Figure 4.18. The procedure used to characterize the scattering matrix closely follows the approach described in Ref. [231] and implemented in the frequency–bin platform of Ref. [216].

The resulting figures of merit are $\mathcal{P} = 0.94 \pm 0.01$ and $\mathcal{F} = 0.999 \pm 0.001$, according to the equations defined above (Equation 4.5). These values are particularly good when compared both with the single–PM case, for which the success probability is theoretically limited to 0.667, and with the theoretical prediction obtained after parameter optimization in the 4–bin phase–setting case ($\mathcal{P} = 0.964 \pm 0.002$ for a target fidelity of 0.99999). To evaluate the operation–related loss, I compare the BS spectrum with a calibration measurement taken with the WS rings detuned from the input comb wavelengths. Apart from the WS, the rest of the setup is kept unchanged, yielding an estimated WS–induced loss of about 5.4 dB for this operation. The BS plots reported here are normalized by this quantity.

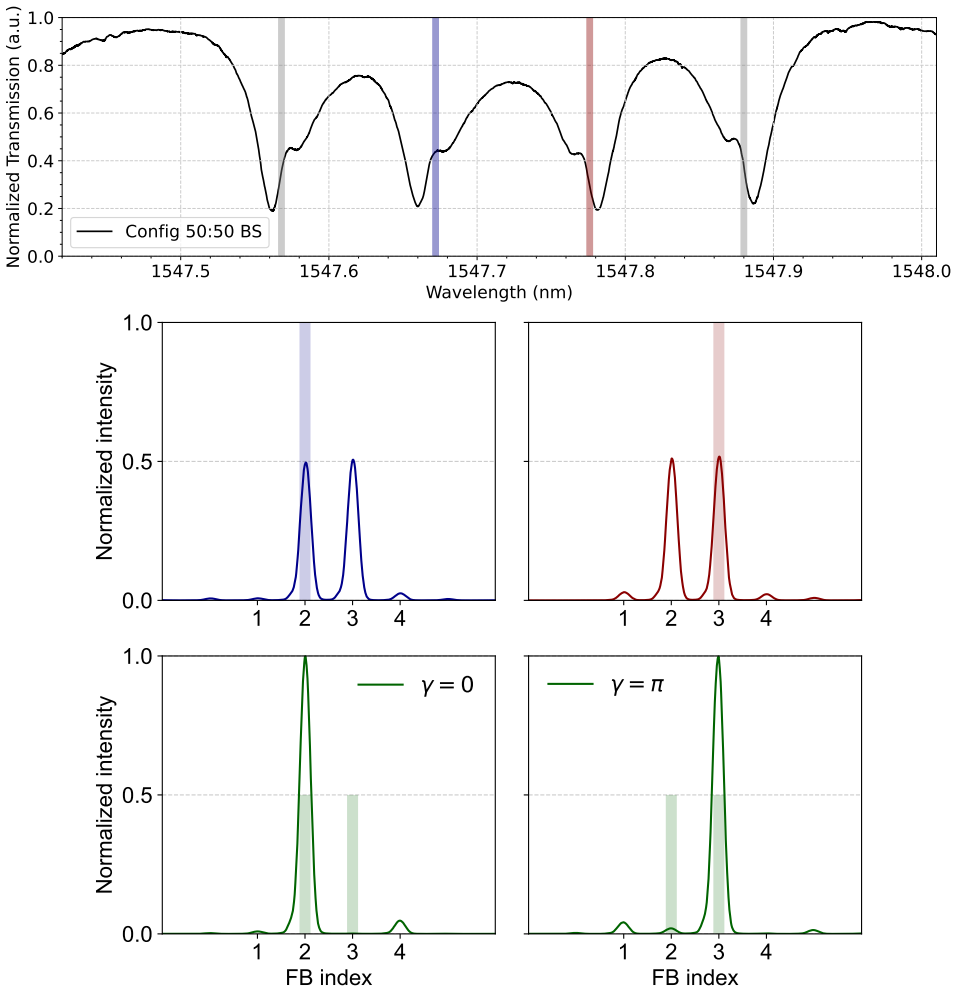



*Figure 4.16:* ***50:50 frequency beam splitter.*** *Top panel: WS output spectrum after calibration of the four units. The applied phases, from left to right, are* $[\pi/2, \pi/2, 3\pi/2, 3\pi/2]$. *Colored vertical lines indicate the positions of the relevant frequency bins. Bottom panels: measured spectra for the four input conditions. Top: input pure states in the 2 (blue) or 3 (red) target modes. Bottom: input superposition state of the two target modes, with the external PM phase* $\gamma$ *adjusted to direct all light into one or the other output frequency bin. All spectra are normalized to a common factor accounting for the total spectral power and for the WS loss.*

### Results, tunable splitting ratio

Following the same settings listed for the 50:50 BS, the set of four measurements performed to fully reconstruct the implemented transformation is repeated for five

different values of the phase step $\alpha$ to demonstrate programmable tuning of the splitting ratio, according to the theoretical transmissivity and reflectivity equations (Equation 4.3), shown in Figure 4.15. The *left–right* mode phase difference $\alpha$ imparted by the on–chip WS is calibrated for each setting by iterating the calibration procedure for each individual WS–unit. The uncertainty on the horizontal axis arises from the uncertainty in the $P_{2\pi}$ estimation for each WS–unit ($\pm 1.0\,\mathrm{mW}$). The results are shown in Figure 4.17.

The reflectivity and transmissivity reported in the top panel are taken as the

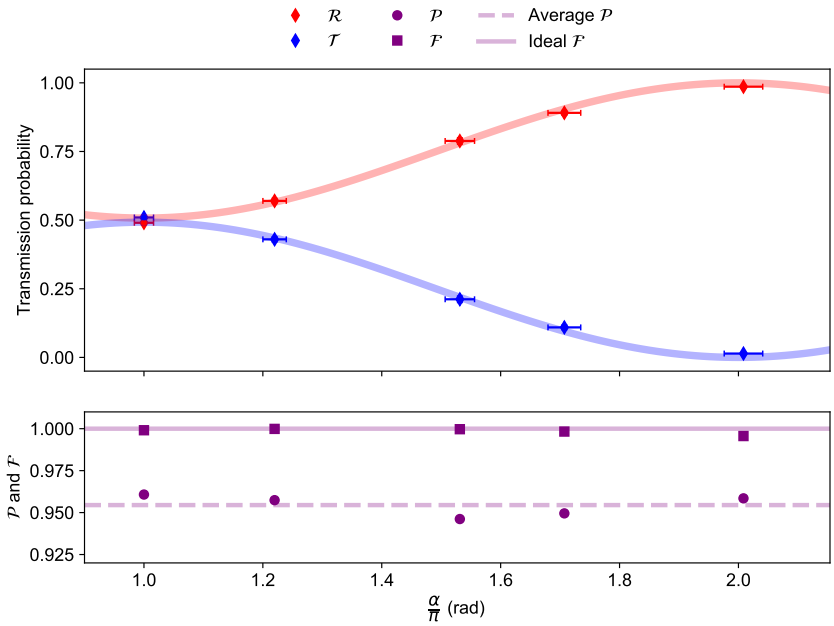



*Figure 4.17:* ***Experimental tunable frequency beam splitter.*** *Top panel: measured reflectivity and transmissivity as a function of the left–right phase difference $\alpha$ (points), compared with the theoretical prediction from Equation 4.3 for $\delta = 0.82 \pm 0.01$ (solid lines). The horizontal error bars are directly obtained from the heater power–to–phase conversion, rigorously reported in section B.4. Bottom panel: corresponding success probability $\mathcal{P}$ and fidelity $\mathcal{F}$ for each configuration. The horizontal lines indicate the average experimental success probability and the ideal fidelity for reference. Error bars are smaller than the marker size.*

average between the two complementary input conditions (pure state in mode 2 and pure state in mode 3). The difference between these two measurements is used as the vertical error bar, which is smaller than the marker size. The fidelity and success probability for each configuration are shown in the bottom panel. For the fidelity, the calculation is repeated considering a family of ideal matrices obtained by varying

the theoretical phase according to the uncertainty estimated from $P_{2\pi}$; the resulting vertical spread is again shown and is smaller than the marker size. The uncertainty on the success probability is determined by the OSA resolution and is also negligible on the scale of the plot. By assuming a modulation index $\delta = 0.82 \pm 0.01$, the theoretical behavior is calculated (solid curves in the top panel), finally confirming that the experimental trends follow the expected behavior very closely.

### 4.3.3 General single-qubit gates

An arbitrary unitary qubit operation described by the matrix in Equation 4.1 can be realized by a sequence of three rotations, parametrized by the angles $(\theta, \lambda, \mu)$. Their combination results in a rotation around an arbitrary axis in three-dimensional space, which—in the quantum mechanical context—corresponds to a general single-qubit gate, i.e., an arbitrary qubit rotation on the Bloch sphere. The frequency–bin qubit transformations implemented in the previous paragraphs showcase tunability by varying the phase step $\alpha$ at a fixed modulation depth $\delta$, which in turn controls the angles $(\theta, \lambda, \mu)$ in a mutually dependent manner. In other words, $(\alpha, \delta)$ represent a set of tunable parameters from which all three rotation angles are simultaneously determined, as described by Equation 4.3.

Therefore, to demonstrate fully arbitrary qubit operations, the capability of synthesizing transformations with independently adjustable phases is crucial. This requires two additional rotations: $R_z(\lambda) = e^{i\lambda Z}$ and $R_z(\mu) = e^{i\mu Z}$, applied before and after $R_y(\theta)$, respectively.

Without loss of generality, I focus on the specific setting $\theta = \pi/2$ (thus keeping a 50:50 splitting ratio), $\lambda = \pi/2$, and $\mu = 0$, but arbitrary rotation angles can be similarly implemented. The resulting transformation is given by:

$$U\left(\frac{\pi}{2}, \lambda, 0\right) = \frac{1}{\sqrt{2}} \begin{pmatrix} 1 & e^{i\lambda} \\ 1 & -e^{i\lambda} \end{pmatrix} . \tag{4.6}$$

The transmissivity and reflectivity remain those of a 50:50 BS, but the matrix elements acquire a controllable phase shift $\lambda \neq 0$.

This $\lambda$-shift can be measured by exploiting the following effect. Let us consider an input superposition state with equal amplitudes in the two target modes and a relative phase $\gamma$ (in practice tunable by acting on the phase of the RF signal driving

the external PM):

$$\begin{pmatrix} A_2 \\ A_3 \end{pmatrix} = U\Big(\frac{\pi}{2}, \lambda, 0\Big) \cdot \frac{1}{\sqrt{2}} \begin{pmatrix} 1 \\ e^{i\gamma} \end{pmatrix} = \frac{1}{2} \begin{pmatrix} 1 + e^{i(\lambda-\gamma)} \\ 1 - e^{i(\lambda-\gamma)} \end{pmatrix} , \tag{4.7}$$

where $A_2$ and $A_3$ are the complex amplitudes of the output target modes. By varying $\gamma$, the output power in one of the two target modes oscillates between a maximum and a minimum value, following a cosine behavior:

$$\begin{aligned} |A_2|^2 &= \frac{1}{2}\left[1 + \cos(\lambda - \gamma)\right] , \\ |A_3|^2 &= \frac{1}{2}\left[1 - \cos(\lambda - \gamma)\right] . \end{aligned} \tag{4.8}$$

The position of the maximum (or minimum) is shifted by an effective shift $-\lambda$ with respect to the standard 50:50 case, where $\lambda = 0$. In particular, by monitoring mode 3 ($|A_3|^2$), the minimum is obtained at $\gamma = \lambda$, thus if we arbitrary chose $\lambda = -\pi/2$ it is obtained at $\gamma = -\pi/2$.

**Results**

To experimentally implement the transformations described above with this additional gate programmability using our QFP, I followed the procedure reported in Ref. [217]. Starting from a general configuration $U(\theta, 0, 0)$, the shifted transformation $U(\theta, \lambda, 0)$ is obtained by delaying the RF signal of the IN PM by $\tau^{\text{in}} = -\frac{\lambda}{2\pi f}$, where $f$ is the modulation frequency corresponding to the mode frequency spacing ($f = 13.25\,\text{GHz}$), and by adding a linear spectral phase ramp $\phi_j \mapsto \phi_j + j\lambda$ to each WS channel $j$. The effective shift obtained is $-\lambda$ with respect to the initial transformation considered. Equivalently, the same procedure can be applied to achieve a phase shift $-\mu$ corresponding to the final rotation $R_z(\mu)$, by delaying the OUT PM RF signal by $\tau^{\text{out}} = -\frac{\mu}{2\pi f}$ and adding the linear spectral phase ramp $\phi_j \mapsto \phi_j + j\mu$. As previously mentioned, I restrict the discussion here to a specific case to demonstrate that this experimental procedure is effective, but the same approach can be applied to achieve arbitrary phase shifts $\lambda$ and $\mu$.

Starting from the standard 50:50 configuration, whose PM and WS settings are summarized in Figure 4.19(a), a target $\lambda$-shift is set: $U(\theta = \pi/2, \lambda = -\pi/2, 0)$, obtained by shifting the input PM phase by $\lambda$ and applying phases $[\frac{\pi}{2} + \lambda, \frac{\pi}{2} + 2\lambda, \frac{3\pi}{2} + 3\lambda, \frac{3\pi}{2} + 4\lambda]$ to the four WS elements. The exact settings are reported in

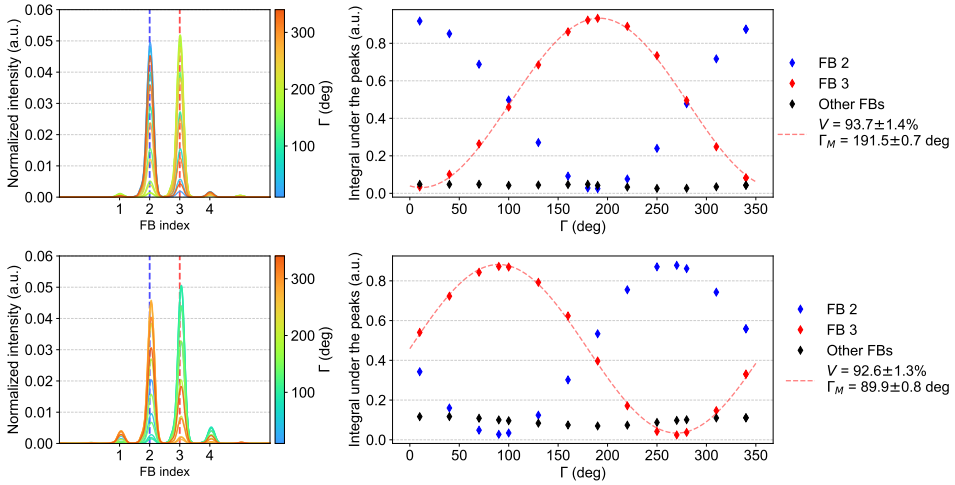



*Figure 4.18:* ***Characterization of the single-qubit gate $\lambda$-shift.*** *Left: spectra obtained as a function of the RF phase of the external EOM $\Gamma$, reported prior to calibration. The spectra are normalized to the total output power, i.e., to the integral over the entire spectrum. Right: interference fringes extracted from the spectra (using the same normalization) shown on the left; in red (blue), the integral under peak 2 (3); in black, the remaining spectral intensity (fraction of light scattered into non-target modes). Top panel: spectra and reconstructed interference fringes for the standard 50:50 case ($\lambda_t = 0°$). Bottom panel: spectra and reconstructed interference fringes for the phase-shifted 50:50 BS ($\lambda_t = 90°$).*

Figure 4.19(b).

To characterize the resulting transformation, I repeat the same set of measurements as for the 50:50 case, i.e., injecting the same three input states (two pure states and the superposition state) and measuring the output spectra. The only difference is that, in the case of the input superposition state, multiple spectra are recorded as a function of the phase of the external EOM $\gamma$ generating the two input comb lines, aiming to reconstruct the interference fringes described in Equation 4.8. The resulting spectra and the reconstructed fringes obtained from the integral under the peaks localized in the two target modes (blue for mode 2 and red for mode 3) are shown in Figure 4.18. In the top panel, I report the standard 50:50 configuration, corresponding to $U(\pi/2, 0, 0)$, while in the bottom panel I show the results for the new configuration $U(\pi/2, -\pi/2, 0)$.

In the graphs, $\Gamma$ (deg) is indicated on the x–axis, emphasizing that this value is reported prior to calibration, i.e., it corresponds to the actual phase set at the RF driver level. In fact, different lengths of the two PM RF cables and the initial phase of the light beam entering the PMs produce a phase shift $\gamma_0 \neq 0$; thus,

the true interference phase is $\gamma = \Gamma - \gamma_0$. Therefore, a calibration procedure is required to determine the actual phase $\gamma$ corresponding to the RF phase $\Gamma$. This calibration is performed by comparing the measured interference fringes for a reference case, chosen to be the standard 50:50 BS, with the theoretical expectation. In the starting configuration, i.e., before the phase shift is applied, the maximum of the mode 3 fringe is expected at $\gamma = \pi$, which corresponds to a measured value $\Gamma_M^{\text{std}}$. When a phase-shifted configuration is applied, the maximum of the mode 3 fringe is expected to shift to $\gamma = \pi + \lambda$, as described in Equation 4.8. The interference fringe is thus fitted with a cosine–like function $\propto [1 + V\cos(\Gamma - \Gamma_M)]$, and the phase corresponding to the maximum in this configuration, $\Gamma_M^{\text{shift}}$, is also extracted. By comparing these two measurements, the effective phase shift $\lambda$ is measured to be $\lambda = \Gamma_M^{\text{std}} - \Gamma_M^{\text{shift}} \simeq 101°$, which thus corresponds to a transformation $U(\pi/2, -101°, 0)$ as previously explained. All the fitting values are reported in the legend of Figure 4.18.

By repeating the pure-state input measurements as well, I reconstruct the full $U$ matrix reported in Figure 4.19; the associated figures of merit are summarized in Figure 4.2.

The success probabilities reflect the amount of light scattered outside the two target modes, also reported as black points in Figure 4.18. The standard 50:50 case ($\lambda_t = 0°$) corresponds to a different measurement set from the one shown in Figure 4.16, but yields comparable performance, confirming the repeatability of our measurements. For the phase-shifted case (bottom panel), the measured phase shift differs from the target value $\lambda_t = 90°$ by $\sim 10°$, and the success probability is about 5% lower than in the standard case. These deviations are likely due to a non-ideal phase pattern applied by the WS.

Indeed, this operation requires a full WS recalibration, since all phases are changed with respect to the initial configuration. As mentioned previously, the phase error estimated for each WS unit is $\Delta\Phi \simeq 6°$, which is not negligible and can account for both the reduced success probability and the small deviation of the measured phase from the target value. Nevertheless, the reported performance remains significantly higher than what can be achieved with a single-EOM configuration (whose maximum success probability is limited to 66.6%), thus confirming the overall quality of the implemented operation.

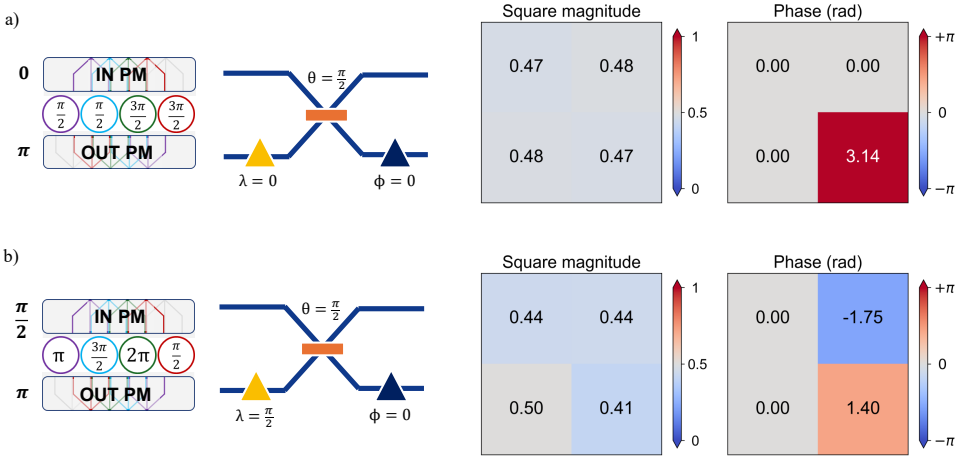



*Figure 4.19:* ***General single-qubit gate.*** *Right: QFP configuration; center: equivalent transformation, illustrated using dual-rail encoding; left: reconstructed* $2 \times 2$ *transformation matrices. The top section (a) corresponds to the 50:50 BS in the standard configuration* ($\lambda_t = 0°$)*. In the bottom section (b), I report the shifted case with* $\lambda_t = -90°$ *and experimental shift* $-\lambda = 101°$*, according to the measurements shown in Figure 4.18. The extracted success probabilities and fidelities are listed in Figure 4.2.*

*Table 4.2: Figures of merit of the single-qubit gates for the two target λ-shifts considered.*

| $\lambda_t$ (deg) | $\mathcal{P}$ | $\mathcal{F}$ |
|---|---|---|
| 0 | $0.95 \pm 0.01$ | $0.999 \pm 0.001$ |
| 90 | $0.90 \pm 0.01$ | $0.993 \pm 0.001$ |

### 4.3.4 Quantum walk manipulation

Quantum walks (QWs), the quantum analogues of classical random walks, describe the evolution of a quantum carrier (the *walker*) in a discrete space. Their behavior is expected to be radically different from the classical case, being governed by the rules of quantum mechanics. Among the various available DoFs, a photon can undergo a QW also in frequency-bin space. This can be easily implemented using a single PM, which stochastically scatters photons across neighboring frequency modes. The first realisation of this approach was reported by P. Imany *et al.* in Ref. [218] using bulk optical devices, and demonstrated in particular two distinct evolution regimes, namely the *anticorrelated* and the *correlated* regimes, thus proving the coherent manipulation of BQFC.

In this section, I report the realisation and coherent manipulation of a QW performed entirely on-chip, namely by using our integrated QFP architecture and

the on-chip MRR source. In particular, the ability to control the relative phase between adjacent frequency bins is exploited to convert the quantum walk from the correlated to the anticorrelated regime, following the theoretical framework extensively reported in the Supplemental Material of Ref. [218].

**Results**

We now demonstrate the capability of the integrated QFP to manipulate the BQFC generated by the on-chip source. To this end, we have implemented the setup shown in Figure 4.13, which I briefly recall here for clarity. A CW laser beam resonantly excites the MRR source, whose wavelength is actively stabilized by a feedback loop by sending most of the pump light to an external photodiode by means of the integrated PF. The feedback loop is implemented by an FPGA, which adjusts the current of the pump laser to keep the wavelength locked to the center of the MRR resonance. The PF, providing approximately 30 dB of attenuation at the chosen pump wavelength (1555.9 nm), is crucial to prevent SFWM along the long integrated circuit WG, where residual pump light would otherwise continue to circulate, generating background noise from photon pairs produced off-resonance. The PF shapes the generated BQFC routed to the on-chip QFP with its sine-like transmission function. Due to the availability of high-extinction-ratio off-chip filters necessary for single-photon detection with SNSPDs, the photon pairs used for the quantum demonstrations are selected from the broad generated spectrum located about 5 nm away from the pump, with the idler at approximately 1550.3 nm and the signal at 1561.6 nm. A typical spectrum of the resonances involved in the SFWM process (the idler) is shown in the top panel of Figure 4.7, corresponding to an average quality factor of $3 \times 10^5$. In this configuration, the measured on-chip rate is $\sim 1$ MHz (see Appendix B, section B.3, for further source characterizations and details on the pump settings).

The generated BQFC is then routed to the on-chip QFP, where one PM and the WS are used to manipulate the state. Specifically for this demonstration, the OUT PM is used to apply the required modulation for the quantum walk, driven by a single RF tone at 15.34 GHz, matching the FSR of the resonator, with a modulation depth arbitrarily chosen to be $\delta \simeq 0.80$ rad. The IN PM is kept off, while the four WS units are used to apply the phase pattern to the photon pair states by aligning them with four idler frequency bins, as schematically depicted in the top panel of Figure 4.20. In what follows, the dynamics of the QW is monitored by looking at the frequency-resolved coincidence measurements performed between the four idler and corresponding four signal bins, using the setup in Figure 4.13. The

resulting $4 \times 4$ correlation matrices are reported in the lower panel of Figure 4.20, together with the simulated coincidence patterns obtained following the methods of Ref. [218] and briefly summarized in Appendix B (section B.5).

Panel (a) shows the frequency-resolved coincidence measurement over this

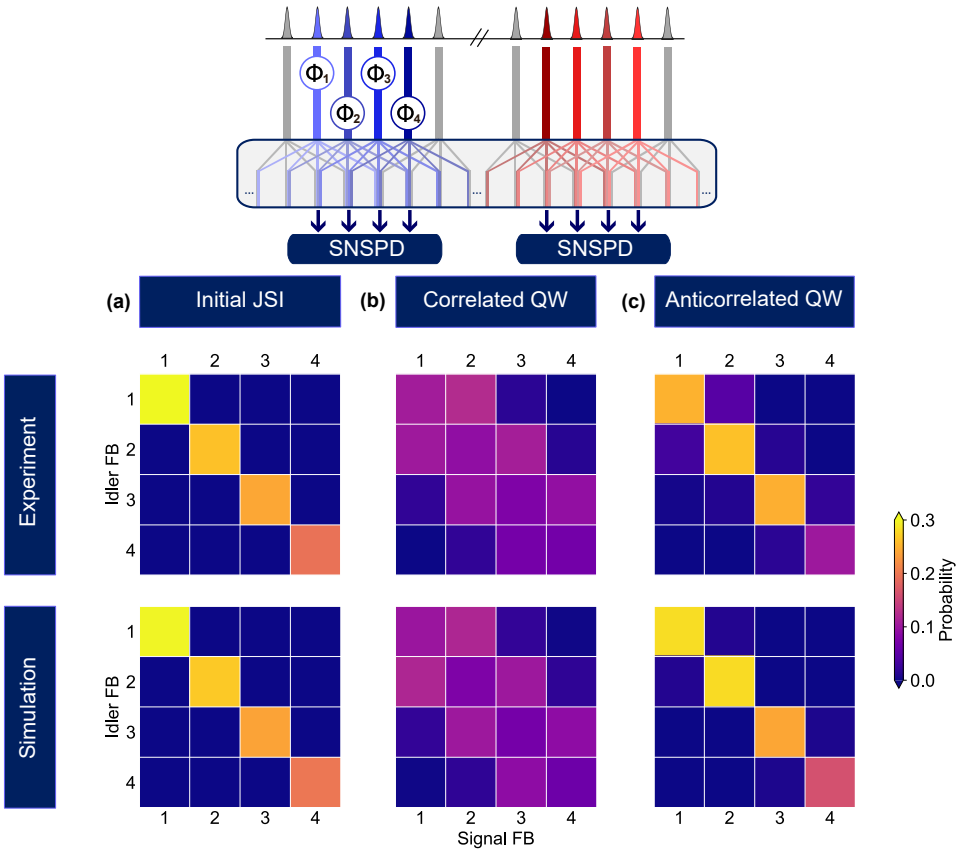



*Figure 4.20:* ***Quantum walk in frequency space.*** *Top panel: Schematic representation of the implemented chip configuration for realizing the QW presented here in the considered $4 \times 4$ subspace. The blue and red bins represent, respectively, the four idler and signal frequency bins under test, which are detected off–chip through SNSPDs. Bottom panel: Measured (top) and simulated (bottom) coincidence patterns for three configurations of the quantum walk: (a) without modulation, (b) with modulation in the correlated regime, and (c) with modulation and a $\pi$-phase shift between adjacent idler bins, i.e. in the anti-correlated regime.*

sixteen-dimensional space, namely the initial joint spectral intensity (JSI) measured immediately after the source (i.e., with the PMs off and the WS detuned from the resonances of interest). The expected BQFC state generated by an MRR source

in the subspace of interest has the form $|\psi\rangle \propto \sum_{k=1}^{4} \beta_k |kk\rangle$, where $\beta_k$ are complex coefficients. Thus, coincidences are expected to arise only for identical idler and signal indices; as expected, the JSI coincidence counts are clearly localized along the main diagonal, indicating strong frequency correlations between signal and idler photons. The small decrease along the diagonal is due to the response of the PF, since the four pairs are not located precisely at the peak of the sine-like envelope. This issue can be attributed to the choice of the off-chip filtering stages for pump, idler, and signal (chosen to have three energy-matched regions among the filters available in the laboratory) rather than a physical constraint. The mentioned decrease in coincidence counts along the diagonal is indeed in agreement with the measured bin losses, which have been considered in the simulations reported in the figure.

In panel (b), the OUT PM was turned on in the regime previously mentioned, while keeping the WS channels in the *pass* configuration. The applied RF signal coherently mixes frequency bins within both the signal and idler subspaces, inducing a frequency-domain *correlated QW* of depth $\delta$. In Ref. [218], the authors report the theoretical treatment of QWs of highly correlated events, showing that it strongly depends on the relative phase $\Delta = \mathrm{Arg}(\beta_{k+1}) - \mathrm{Arg}(\beta_k)$ between adjacent frequency bins prior to the walk. In particular, for $\Delta = 0$, the QW is expected to be correlated, with a spread of coincidences away from the diagonal, while for $\Delta = \pi$ the QW is expected to be anticorrelated, with a strong confinement along the diagonal. The pattern in panel (b) shows a clear spreading of coincidences away from the diagonal, indicating that the quantum walk is in the correlated regime. Moreover, the experimental pattern matches the simulation with a fidelity of $\mathcal{F} = \frac{\mathrm{Tr}(AB^T)}{\sqrt{\mathrm{Tr}(AA^T)\,\mathrm{Tr}(BB^T)}} = 99.38(5)\%$, where $A$ and $B$ are the measured and simulated coincidence matrices, respectively. The relative phase shifts extracted by fitting the experimental data to the theoretical model, producing the simulated JSI reported in the plot, lie within the range $\Delta = 0 \pm 0.1\,\mathrm{rad}$ across all four bin pairs, further confirming good agreement with theoretical expectations. The reader can refer to section B.5 for more detail on the QW simulations.

Finally, to demonstrate the capability of the full QFP to coherently manipulate the BQFC, we show the conversion of the walk to *anticorrelated* in the right panel. A strong confinement along the diagonal is recovered, effectively compensating for the OUT PM effect by adjusting the phase between adjacent pairs on-chip using the WS. I applied a relative phase $\Delta = \pi \pm 0.1\,\mathrm{rad}$ (according to the phase-calibration uncertainty already discussed) between adjacent idler frequency bins. The fidelity calculated between the simulated and experimental coincidence pat-

terns is $\mathcal{F} = 98.7(5)\%$. In performing this conversion, one has to consider the WS-induced losses, which are estimated to be $\sim 6\,\mathrm{dB}$ for the phase pattern applied.

### 4.3.5 Bell-curve measurements and quantum state tomography

The integrated chip architecture presented in this chapter incorporates all the necessary components to perform Bell-state measurements and quantum state tomography of two-qubit states encoded in frequency bins. As previously mentioned, the combination of the on-chip WS and PM allows for the implementation of arbitrary single-qubit gates, which are essential for performing projective measurements in different bases required for QST. More information on the employed method can be found in Chapter 2 (section 2.2.3) and in Ref. [210].

#### Results

Exploiting the same setup as in the previous section, I now demonstrate the capability of the integrated QFP to perform quantum state tomography of a frequency-bin state generated on the same chip. To this end, the same four idler-signal FBs already exploited in subsection 4.3.4 are selected off-chip through the DWDM filters, but this time the BQFC is further shaped on-chip using the integrated WS. Upon creation of guard bands around the central pair of energy-correlated bins, as schematically reported in the top panel of Figure 4.21, only two signal and idler energy-matched bins are isolated from the rest of the generated comb. In this way, a state closely approximating the Bell state

$$|\Phi^+\rangle = \frac{1}{\sqrt{2}} \left(|00\rangle_{si} + |11\rangle_{si}\right)$$

is obtained.

Across this thesis, I have already presented a frequency analyzer used to fully characterize frequency-bin-encoded quantum states, specifically in section 2.2.3. Here, I perform a similar set of projective measurements, but using the integrated QFP to analyze the on-chip-generated Bell-like state. In this configuration, both idler and signal photons pass through the same PM; therefore, the phase shift required to implement different projectors is synthesized by the WS, acting on the pair of idler FBs, rather than by the phase of the RF driving signal, as in the previously introduced analyzer based on two distinct PMs. Here, the OUT PM is used to mix both idler and signal FBs after the phase shift is applied.

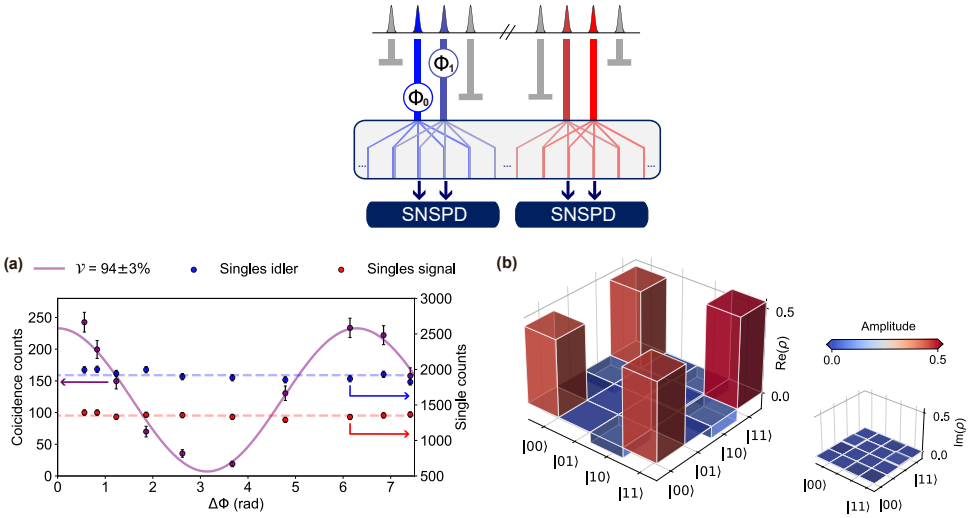



*Figure 4.21:* ***Quantum state tomography of a two-qubit frequency-bin state.*** *Top panel: schematic representation of the implemented chip configuration for realizing the here presented QST. The blue and red bins represent, respectively, the two idler and signal frequency bins under test, which are detected off–chip through SNSPDs. Bottom panel: (a) Bell-curve measurement obtained by recording coincidence (purple) and single counts (blue and red) as a function of the relative phase shift* $\Delta\Phi = \Phi_0 - \Phi_1$ *applied by the WS between the two idler bins before mixing, with the modulation depth set to* $\delta \sim 1.4$ *rad. The solid line represents a sinusoidal fit to the coincidence counts. (b) Real and imaginary parts of the reconstructed density matrix of the generated state, obtained via maximum-likelihood estimation.*

By continuously tuning the phase shift applied by the WS, $\Delta\Phi = \Phi_0 - \Phi_1$, as indicated in the schematic, and setting the modulation depth to $\delta \sim 1.4$ rad, corresponding to near equalization of the carrier and first-order sidebands, coincidence counts are recorded. Specifically, the idler and signal tunable filters are centered at the wavelengths corresponding to $|0\rangle_s$ and $|0\rangle_i$, and the resulting coincidence and single counts are reported in Figure 4.21(a). The results clearly show the expected interference fringes arising from two-photon interference, already introduced in subsection 2.3.1; the visibility extracted from the sinusoidal fit (solid purple line) is $V = 0.94 \pm 0.03$. At the same time, the single counts remain constant over the full $2\pi$ phase range, confirming the absence of phase-dependent losses and the Bell-like nature of the observed interference, thus proving entanglement.

Finally, by performing a complete set of projective measurements, I reconstruct the density matrix of the generated state using the maximum-likelihood estimation method described in Ref. [166]. In particular, projectors onto superposition bases are implemented using the same approach as for the Bell-curve measurements,

while projectors onto the computational basis are obtained by turning off the PM and measuring the full $2 \times 2$ frequency-resolved coincidence pattern by tuning the central wavelengths of the tunable filters. The resulting density matrix is shown in Figure 4.21(b). The computed fidelity with respect to the target Bell state $|\Phi^+\rangle$ is $95.7 \pm 0.3\%$, while the purity is $93.8 \pm 0.5\%$. These results demonstrate the capability of the integrated QFP to perform quantum state tomography of frequency-bin states, providing a crucial tool for the characterization and validation of quantum states generated and manipulated on-chip.

## 4.4 Conclusions and further perspectives

In this chapter, I reported the key aspects of a project spanning more than two years, in which I was involved from the beginning to the end. I presented the design, numerical simulations, preliminary linear characterization of individual components, and final experimental demonstrations in both the classical and quantum domains of the full device, showcasing a monolithic silicon quantum frequency processor.

The key performance metrics of all integrated components were reported, as obtained from optical and electrical characterizations performed mostly at the Quantum Photonics Laboratory in Pavia, with the exception of the PM electrical RF-response characterization, which I performed at the Laboratory of Silicon Photonics at CEA-Leti in Grenoble. The results showed that overall the components were functional and exhibited performance in line with expected values, confirming the quality of the design and fabrication process. A small discrepancy between simulation and measurement was observed in the coupling coefficient of the MRRs integrated in our WS architecture, but this did not compromise the effective functioning of the device.

After this preliminary characterization, I demonstrated the capability of the integrated QFP to perform coherent manipulations of frequency-bin encoded quantum states. This was first achieved by implementing a series of single-qubit gates using classical frequency modes; specifically, a high-fidelity, tunable frequency beam splitter with strong suppression of leakage into neighboring modes. The obtained success probability was higher than 94% for all implemented splitting ratios, greatly exceeding the single-phase-modulator limit. More general single-qubit rotations were also shown to be realizable by applying an arbitrary phase shift to the input modes while maintaining the splitting ratio, achieving a success probability of $90 \pm 1\%$. These results showed that the integrated architecture could implement precise and reconfigurable frequency-domain transformations with high fidelity and low crosstalk,

providing a solid foundation for future quantum-optical experiments.

I then moved to the quantum domain by demonstrating the capability of the integrated QFP to manipulate the BQFC generated by the on-chip MRR source. In particular, I implemented a quantum walk in frequency space, showing the transition from the correlated to the anti-correlated regime by applying relative phase shifts between adjacent frequency bins via the WS. The measured coincidence patterns showed a fidelity higher than 98% with respect to numerical simulations, confirming the high quality of the implemented transformations. Finally, I demonstrated quantum state tomography of two-qubit states by reconstructing the density matrix of a Bell-like state generated on chip with a fidelity of 95.7% with respect to the target Bell state $|\Phi^+\rangle$.

Future efforts will be devoted to improving the performance of the integrated devices, for example by reducing the WS insertion loss, as well as the $V_\pi$ and propagation loss of the on-chip silicon modulators. In particular, the WS design can be straightforwardly optimized by increasing the coupling strength between the microring resonators and the bus waveguides, or by implementing asymmetric designs to increase the drop efficiency. The modulator performance can be further improved by optimizing the design of the p-n junction [232], or by moving to hybrid approaches, such as the integration of CMOS-compatible electro-optic polymers [233] or thin-film lithium niobate [234]. In addition to physical hardware optimizations, a promising strategy to scale the information capacity of the processor lies in driving the phase modulators with multiple RF harmonics. This approach allows the implementation of high-dimensional unitary transformations without increasing the physical circuit depth or adding further optical losses [235].

This work represents, to the best of my knowledge, the first fully integrated frequency processor including all the necessary components for the generation, manipulation, and analysis of frequency-bin-encoded quantum states, leveraging the intrinsic advantages of silicon photonics such as compactness, phase stability, and compatibility with CMOS fabrication. It represents a significant step toward scalable and efficient quantum-photonic systems and lays the foundation for future advancements in quantum-information processing based on frequency-bin encoding. The results reported here are published in Ref. [210].

# Conclusions

In this research work, I developed novel silicon integrated photonic circuits for the generation and manipulation of quantum states of light. The devices introduced here aimed to increase both the dimensionality and the programmability of frequency–bin–encoded states, which are particularly relevant for quantum communications thanks to their large native Hilbert space and their compatibility with standard telecommunication infrastructures.

The first chapter was dedicated to the silicon–on–insulator photonic platform in which the circuits were integrated, within multi–project fabrication runs offered by CEA-Leti and STMicroelectronics. A broad overview of the components required to build a functional silicon photonic circuit was provided, highlighting the linear and nonlinear properties of silicon devices. Special attention was given to the most critical aspects related to the design of the fundamental building blocks exploited in the research projects here presented, with the goal of providing a tutorial–style reference for readers interested in silicon photonic simulation and layout.

The following chapters were devoted to the implementation of silicon photonic circuits for novel quantum demonstrations. Chapter 2 presented the realisation of a hyperentangled source of 16–dimensional states based on multiple high–brightness microring resonators. Previous demonstrations [165, 166] had addressed the typical brightness–FSR trade–off by using multiple small–radius rings to generate photon pairs at tens of $\mathrm{MHz/mW^2}$, but had not extended this approach to include additional DoFs. The first step taken in this thesis was therefore to use the same device and show its suitability for hyperentanglement by including the time–bin DoF. The generation of the target state was verified by observing entanglement in the two separate DoFs, exceeding the classical bounds by more than 27 standard deviations in both of them, and finally measuring a hyperentanglement witness that violated the bound for non–hyperentangled states by 60 standard deviations. These results are discussed in detail in the dedicated chapter and were published in a peer–

reviewed journal [145].

Building on this achievement, Chapter 3 introduced a new generation of quantum circuits with the goal of including additional DoFs, such as path and polarization. This would produce an increase in the quantum state dimensionality and information capacity per photon, which may be exploited in future quantum demonstrations. The preliminary results presented included wafer–scale morphological and linear optical characterizations that validated the fabrication of the passive components on the 300–mm wafers. Most measurements showed good agreement with the reported simulations, and a systematic wavelength offset was identified that can be compensated in the next fabrication run, giving confidence that the intended quantum experiments can be carried out once fabrication is fully completed. Several additional circuits were also designed and included in this CEA-Leti fabrication run but were not discussed in this manuscript, including circuits incorporating high–extinction–ratio pump–rejection filters. Furthermore, strategies to suppress on–chip scattered pump light were also developed, which led to three published patent applications [236, 237, 238].

The manuscript concluded with Chapter 4, which presented a monolithic silicon–integrated platform for the generation and manipulation of high–dimensional frequency–bin states. Device simulations, integration within the STMicroelectronics PIC50 technology, and linear characterization of the individual components confirmed once again that the design strategies developed in Chapter 1 are well suited for complex quantum photonic circuits.

The full potential of the integrated quantum frequency processor was then shown through the realisation of a post–selection–free, reconfigurable two–mode frequency beam splitter, exhibiting leakage to unwanted frequency modes below 6% across the considered 50:50 to 100:0 splitting–ratio range. More general single–qubit operations were also realized by applying a controlled phase shift while maintaining the desired splitting ratio. The final validation was performed in the quantum regime, showcasing the manipulation of the biphoton quantum frequency comb generated by the on–chip microring source. In particular, I reported the realisation of quantum walks in frequency space, showing the transition from correlated to anticorrelated regimes through controlled phase shifts between adjacent frequency bins. Close agreement between experimental and simulated coincidence patterns, with fidelities above 98%, confirmed the accuracy of the implemented transformations. The processor also enabled on–chip quantum state tomography of a two–qubit state, achieving a fidelity of 95.7% with respect to the target Bell state.

These results, published in Ref. [210], demonstrate for the first time the full in-

tegration of a quantum frequency processor on a monolithic silicon chip, including coherent generation, manipulation, and analysis of frequency–bin–encoded quantum states.

Overall, the results presented in this thesis position silicon photonics as a powerful platform for quantum information processing. High–brightness integrated photon–pair sources, multidimensional encoding through hyperentanglement, and programmable quantum frequency processors were demonstrated on silicon–on–insulator chips, thus contributing toward fully integrated frequency–bin quantum photonic systems. The research work presented in this manuscript may therefore pave the way to large–scale quantum photonic systems capable of supporting complex, high–dimensional quantum protocols, leveraging both CMOS–compatible fabrication and telecommunication–compatible frequency–bin encoding.

# Appendix A

# Supplementary device modeling and simulations

In this appendix, I collect supplementary numerical simulations, theoretical modeling, and design references that support the design of the passive photonic building blocks discussed in chapter 1, chapter 3, and chapter 4.

Specifically, I report finite–difference eigenmode (FDE) simulations characterizing the dispersion and nonlinear properties of the 300 nm silicon photonics platform, and I compare different theoretical formulations for the nonlinear parameter $\gamma$ in high–index–contrast waveguides. I also provide a design reference table summarizing the exact and approximate figures of merit for microring resonators in both all–pass and add–drop configurations. Finally, I present finite–difference time–domain (FDTD) point coupler simulations for devices fabricated at the CEA–Leti and STMicroelectronics pilot lines, along with a custom Transfer Matrix Method (TMM) model, implemented in Python, to calculate the complex spectral transmission and phase response of the integrated double–ring line–by–line waveshaper.

## A.1 Si300nm WG simulations

Here I report additional simulations of silicon waveguides, showing the effective index, group index, and dispersion, according to the definitions given in the main text (see Equation 1.5). In particular, the simulations reported here refer to the fundamental $TE_{00}$ mode of both strip and rib waveguides on the Si 300 nm platform, for multiple waveguide widths ($WG_w$). They were performed following the methods

described in the main text (see section 1.2), using the FDE solver of the Lumerical MODE software [97]. The results for the Si 220 nm SOI platform are reported in the main text (Figure 1.6).

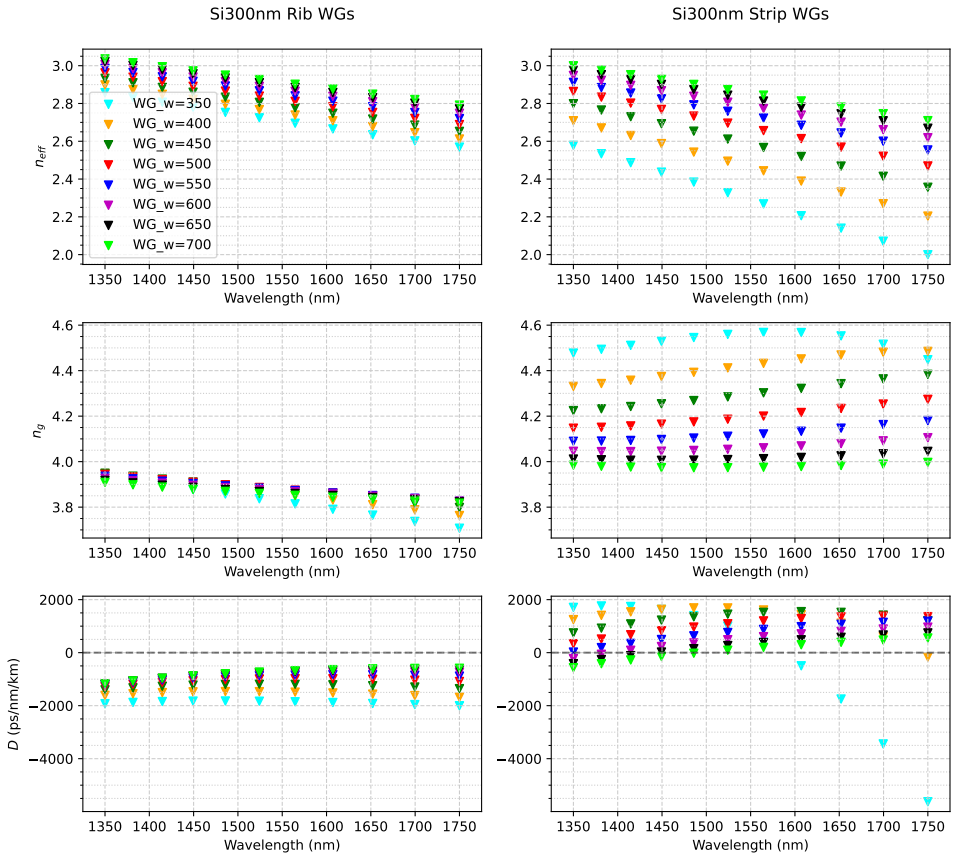



*Figure A.1:* ***WG dispersion simulations.*** *WG properties as a function of the wavelength for fundamental $TE_{00}$ mode of strip and rib WG for the platform Si300nm, for different $WG_w$.*

## A.2 Si WG nonlinear parameter estimations

The analysis presented in this section is not intended to be exhaustive: it focuses on a single representative strip WG geometry with a cross–section of $300 \times 600$ nm$^2$. Its aim is instead to provide a clear, quantitative insight into how the parameter estimates differ depending on the formulation adopted. All the physical and mathematical assumptions established in the main text (section 1.1.2) remain valid here,

including the tensor symmetries of the third–order susceptibility $\chi^{(3)}$, with the effective susceptibility $\chi^{(3)}_{\text{eff}}$ taken equal to $\chi^{(3)}_{1111}$ [61].

To this end, I report the nonlinear parameter estimates for the fundamental $\text{TE}_{00}$ mode of this WG as a function of wavelength. The calculations were performed using the formulas reported in Sec. 1.1.2, and the results are shown in Figure A.2. The values of $A^{(F)}_{\text{eff}}$ were obtained from FDE simulations, while the Kerr coefficient and the third–order susceptibility ($n_2$, and the real and imaginary parts of $\chi^{(3)}_{1111}$) were taken from the literature (specifically, Figure 7 of [56]). The values of $\gamma^{(F)}$ and $\gamma^{(SOI)}$ in the right–hand plots were obtained through Equation 1.15 and Equation 1.14, respectively. Following the calculations in [56], also recalled in [58], the $\gamma$ values are reported under two conditions: with and without dispersion of the nonlinear coefficients. The dashed lines account only for the WG mode dispersion, i.e., the wavelength dependence of the linear materials indexes (both silicon and silica), thus it accounts for the mode refractive indices and effective area chromatic dispersion. The solid lines also include nonlinear material dispersion, i.e., in addition, it includes the wavelength dependence of $n_2$ and $\chi^{(3)}_{1111}$ of the core material (silicon; the contribution of silica is neglected). The values of $\gamma^{(SOI)}$ agree well with those reported in [56], where the same WG geometry was evaluated.

As mentioned in the main text, the two nonlinear parameters are expected to differ between the two formulations because of the high refractive–index contrast of the SOI platform compared to standard optical fibers. Specifically, at 1550 nm the SOI formulation gives a value of $\gamma^{(SOI)}$ more than two times larger than $\gamma^{(F)}$. Nevertheless, this discrepancy does not limit the analysis of the nonlinear processes considered in this work: a precise estimate of the nonlinear parameter alone does not translate directly into an exact quantification of real–world nonlinear effects. Experimental quantities, such as the photon–pair generation rate in SFWM–based sources, are also strongly influenced by practical factors, including linear and nonlinear propagation losses in the WG, fiber–to–chip coupling efficiency, and the internal pump power distribution. The theoretical nonlinear parameter is therefore only one component of the broader experimental framework governing the generation rates.

## A.3 List of ring resonator figures of merit

Analytical approximate expressions for the main figures of merit of microring resonators are summarized here for both AP and AD configurations. Two standard approximations are assumed: $a \simeq 1 - \tilde{\alpha} L_{rt}/2$ and $t \simeq 1 - \kappa^2/2$ (see [66, 239] for further details). The notation is consistent with Sec. 1.3, to which the reader is

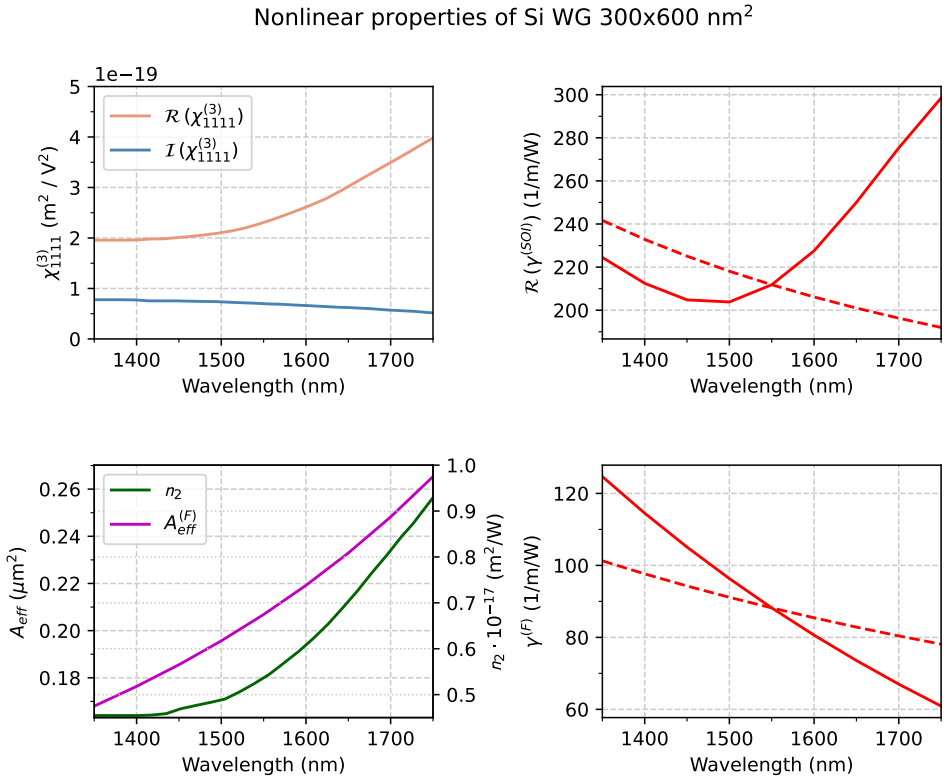



*Figure A.2:* ***Nonlinear parameter estimations.*** *Calculated WG optical properties and nonlinear parameters as a function of wavelength for the fundamental $TE_{00}$ mode of a $300\times600$ $nm^2$ strip WG. The panels present the effective area $A^{(F)}_{eff}$, the silicon parameters ($n_2$ and $\chi^{(3)}_{1111}$), and the comparison between $\gamma^{(F)}$ and $\gamma^{(SOI)}$, evaluated both with (solid lines) and without (dashed lines) material dispersion.*

referred for the full derivation and the underlying hypotheses. I recall here the meaning of the quantities appearing in the equations: $t$ and $\kappa$ are the coupling coefficients (bar and cross, respectively), with $t^2+\kappa^2=1$; $a=\exp(-\tilde{\alpha}L_{rt}/2)$ is the round–trip attenuation; $\tilde{\alpha}$ is the power attenuation coefficient, in $[\mathrm{m}^{-1}]$; $L_{rt}$ is the round–trip length; and $\theta(\omega)$ is the accumulated phase.

| **FoM** | **All–Pass (AP)** | **Add–Drop (AD)** |
|---|---|---|
| Through power transmission $T(\omega)$ | $\frac{t^2+a^2-2at\cos(\theta)}{1+a^2t^2-2at\cos(\theta)}$ | $\frac{t_1^2+a^2t_2^2-2at_1t_2\cos(\theta)}{1+a^2t_1^2t_2^2-2at_1t_2\cos(\theta)}$ |
| Through transmission @ resonance $T(\omega_m)$ | $\frac{(a-t)^2}{(1-at)^2}$ | $\frac{(at_2-t_1)^2}{(1-at_1t_2)^2}$ |
| Drop power transmission $T_{DROP}(\omega)$ | – | $\frac{\kappa_1^2\kappa_2^2 a}{1+a^2t_1^2t_2^2-2at_1t_2\cos(\theta)}$ |
| Drop transmission @ resonance $T_{DROP}(\omega_m)$ | – | $\frac{(1-t_1^2)(1-t_2^2)\,a}{(1-at_1t_2)^2}$ |
| Critical coupling | $a=t$ | $at_2=t_1$ |
| Free Spectral Range (FSR) | $\frac{\lambda^2}{n_g\,L_{rt}}$ | |
| Quality factor $Q$ | $\frac{2\pi n_g L_{rt}}{\lambda\left(\sum_c \kappa_c^2+\tilde{\alpha}L_{rt}\right)}=\left(\frac{1}{Q_i}+\sum_c\frac{1}{Q_c}\right)^{-1}$ | |
| Finesse $\mathcal{F}$ | $\frac{FSR}{\Delta\lambda}=2\pi M$, with $M$ the number of round trips | |
| Field enhancement (FE) | $\left\lvert\frac{\kappa}{1-a\,t\,e^{-i\theta(\omega)}}\right\rvert$ | $\left\lvert\frac{\kappa_1}{1-a\,t_1t_2\,e^{-i\theta(\omega)}}\right\rvert$ |
| FE @ resonance $FE(\omega_m)$ | $\left\lvert\frac{\kappa}{1-at}\right\rvert$ | $\left\lvert\frac{\kappa_1}{1-at_1t_2}\right\rvert$ |
| FE @ resonance (approx.) | $\left\lvert\frac{2\kappa}{\kappa^2+\tilde{\alpha}L_{rt}}\right\rvert$ | $\left\lvert\frac{2\kappa_1}{\kappa_1^2+\kappa_2^2+\tilde{\alpha}L_{rt}}\right\rvert$ |
| Visibility $\mathcal{V}$ | $1-\frac{T(\theta=2\pi)}{T(\theta=\pi)}$ | |
| Visibility (approx.) | $1-\left\lvert\frac{\kappa^2-\tilde{\alpha}L_{rt}}{\kappa^2+\tilde{\alpha}L_{rt}}\right\rvert^2$ | $1-\left\lvert\frac{\kappa_1^2-\kappa_2^2-\tilde{\alpha}L_{rt}}{\kappa_1^2+\kappa_2^2+\tilde{\alpha}L_{rt}}\right\rvert^2$ |

*Table A.1:* ***Main figures of merit for AP and AD MRRs.*** *General expressions for the main FoMs of MRRs, including the low–loss and weak–coupling approximations (i.e., $a\simeq 1-\frac{\tilde{\alpha}L_{rt}}{2}$ and $t_i\simeq 1-\frac{\kappa_i^2}{2}$). The quantities are used in the main text to design and analyze the integrated photonic building blocks presented in chapter 1, chapter 3, and chapter 4.*

This table is intended as a design reference: the *@resonance* rows are particularly useful for quick checks of coupling conditions and power transfer at the central resonance wavelength, while the general expressions allow for more accurate spectral calculations. These expressions were used for the design throughout the thesis. Visibility, quality factor, and field enhancement, calculated directly from these formulas as a function of the coupling coefficient, are reported in Figure A.3 and Figure A.4 for the AD MRRs used in chapter 3 and chapter 4, respectively.

## A.4 Additional point coupler simulations

Here I report additional point coupler simulations, performed for the AD MRRs used in chapter 3 and chapter 4. The point coupler simulations and the analytical FoM calculations follow the methods described in section 1.4.

### A.4.1 Si300nm platform, integrated in CEA-Leti pilot line

The FoMs (visibility, Q-factor, and field enhancement) of AD rings with strip WGs ($300 \times 550\,\mathrm{nm}^2$) are shown here as a function of the cross–coupling coefficient. The results, reported in Figure A.3, were obtained for a ring radius $R = 57.94\,\mu$m and a wavelength $\lambda = 1550\,$nm. The FoMs were calculated using the formulas reported in Table A.1. This design was implemented on the Si300nm platform of the CEA-Leti 300 mm pilot line, and the corresponding experimental results are reported in Figure 3.16.

### A.4.2 Si300nm platform, integrated in STMicroelectronics pilot line

Additional point coupler simulations and FoM calculations are presented here for the AD MRRs of the STMicroelectronics chip described in chapter 4. The cross–section is the standard single–mode rib geometry, used all along the quantum frequency processor circuit, and the radius was set to $R = 49.265\,\mu$m to obtain an FSR of 250 GHz. The target coupling coefficient was set to $\kappa = 0.23$, corresponding to a target Q-factor of about 40000 (dashed vertical line in the bottom panel of Figure A.4). The results of the FDTD point coupler simulation are reported in the top panel; the resulting gap is $GAP = 540\,$nm. The spectrum measured after fabrication (Figure 4.11) shows a visibility and Q-factor slightly different from the target values, consistent with under–coupling relative to the simulation. See the

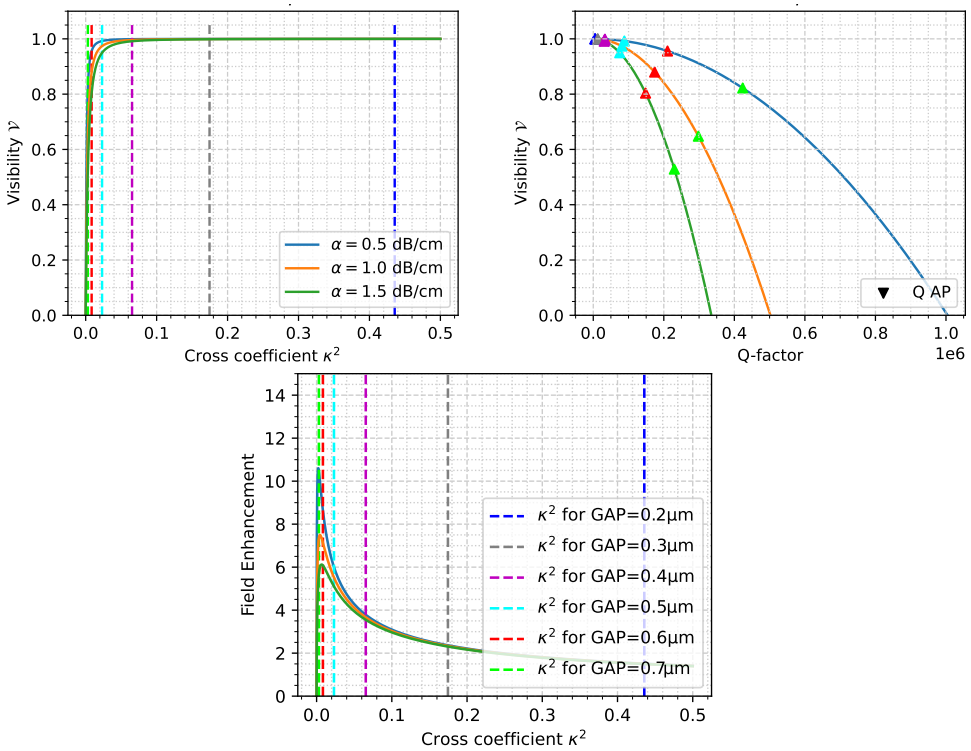



*Figure A.3:* ***AD MRR FoMs.*** *The figure shows the FoMs of the AD MRRs (*$300 \times 550\,nm^2$ *cross–section) of radius* $57.94\,\mu m$ *as a function of the cross coefficient and propagation loss.*

main text (subsection 4.2.3) for further details on the design and characterizations of the device.

## A.5 TMM for structures based on ring resonators

Using the Transfer Matrix Method (TMM), it is possible to compute the transmission functions of complex photonic structures, such as coupled ring resonators. As an example, I report here the double–ring line–by–line waveshaper introduced in Sec. 4.2.3, whose structure is schematically shown in Figure A.5. It consists of a pair of identical AD rings, with the drop port of the left ring (DEMUX ring, $D$) connected to the add port of the right one (MUX ring, $M$). Between the two rings, a phase shifter (heater, shown in yellow) is integrated to control the phase shift $\Phi$ of the light dropped by the $D$–ring and loaded back into the $M$–ring. Finally, the two rings are also connected through the bus WG: the through port of the $D$–ring

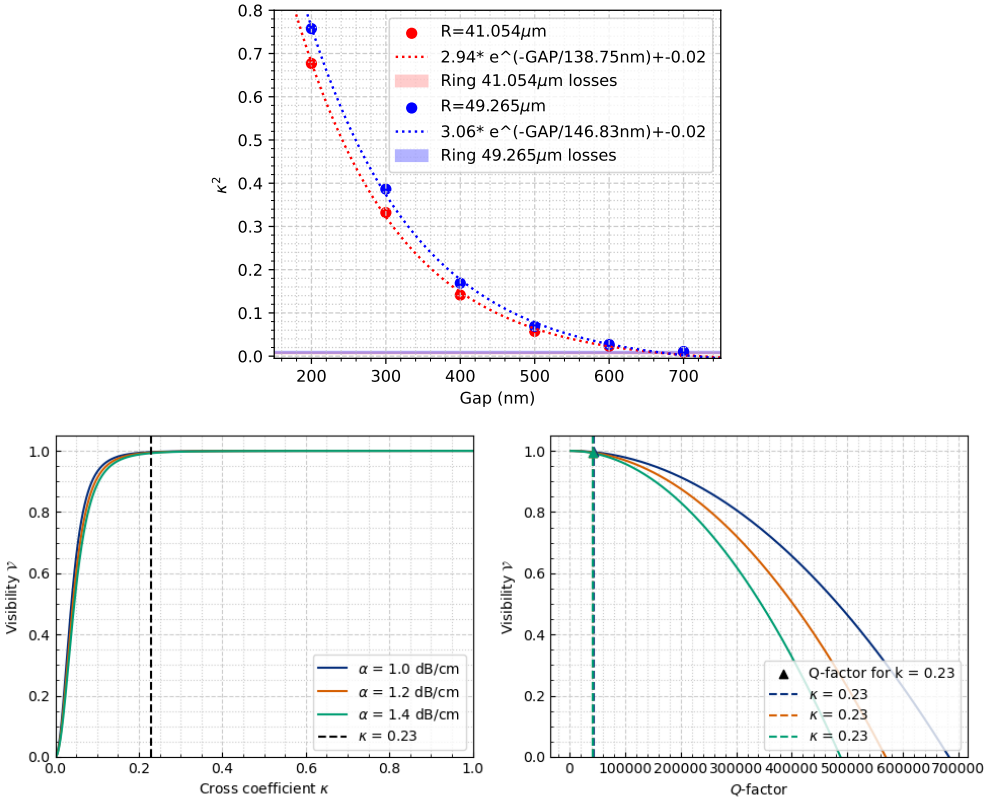



*Figure A.4:* ***AD MRR FoMs.*** *Top panel: FDTD simulation of the rib point coupler, as a function of the gap. Bottom panel: expected visibility and Q-factor of the single WS ring resonators as a function of the coupling coefficient, calculated for propagation losses around* $1.2 \pm 0.2$ *dB/cm. The dashed vertical line indicates the target coupling condition.*

is connected to the input of the $M$–ring.

By cascading the transfer matrices of each region, represented by the numbered sections in the scheme, the expected transmission and phase at the WS–unit OUT port are calculated as a function of wavelength. In particular, the *purple* regions are treated with the point–coupler formalism reported in Sec. 1.3, while the *pink* regions are described by free–propagation matrices. The latter are diagonal, with elements given by the phase accumulated in the region, $e^{i\theta_i(\lambda)}$, which depends on the wavelength and on the region length $L_i$: $\theta_i(\lambda) = n_{eff}(\omega)\frac{2\pi}{\lambda} \cdot L_i + i\,\tilde{\alpha}/2\,L_i$.

The field at the OUT port is calculated by propagating the input field through the entire structure, with the calculations implemented in Python. The resulting transmissivity $|T|^2 = |\frac{E_{t\,1\,M}}{E_{i\,1\,D}}|^2$ and phase $\arg(T)$ are reported in Figure A.6 as a func-

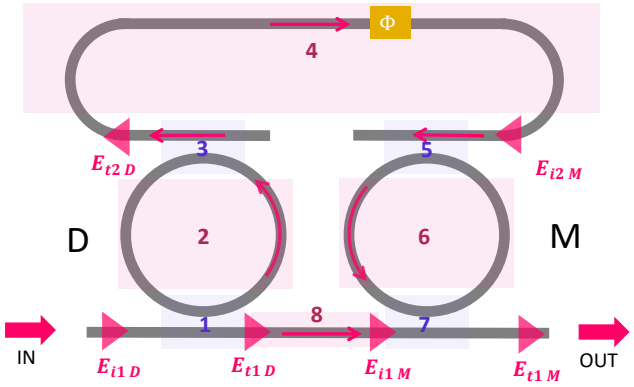



*Figure A.5:* ***Double-ring waveshaper scheme.*** *The free-propagation (pink) and point coupler (purple) regions are highlighted in different colors. The matrix-based calculation propagates the field injected in the lower-left WG ($E_{i\,1\,D}$).*

tion of the detuning from the target channel wavelength $\lambda_C$, at which both rings are aligned ($\Delta\lambda = 0$ in the plots). Notably, an interference effect arises between the fraction of light remaining in the bus WG away from $\lambda_C$ and the light dropped into the upper WG. This mechanism is fully accounted for in the TMM model; the spectra are computed for different values of the phase shift $\Phi$.

The spectra shown here were obtained with the following parameters: propagation loss $\alpha = 1.2\,\mathrm{dB/cm}$, ring radius $R = 49.265\,\mu\mathrm{m}$, and the experimentally extracted coupling coefficient $\kappa_1 = \kappa_2 = 0.16$ (see the main text) for both couplers of each ring, i.e., each AD ring is symmetric and the two rings are nominally identical. In the model, the path difference between the lower bus WG (region 8) and the upper bus WG (region 4) is assumed to be zero. In the physical device, there is a path difference of approximately $\Delta L_0 = 1.5\,\mathrm{mm}$, which introduces a fixed phase offset $\Phi_0$ in addition to the shift $\Phi$ applied by the integrated heater. Fabrication imperfections and the wavelength dependence of the phase contribute to small deviations from $\Phi_0$. The model therefore uses a generic phase shift $\Phi$, which in practice is the sum of the initial offset $\Phi_0$ and the shift induced by the power dissipated in the heater. $\Phi_0$ can be easily calibrated for each WS unit by aligning its resonances to the target $\lambda_C$ (i.e., acting on the MRR heaters) with the phase–shifter heater turned off.

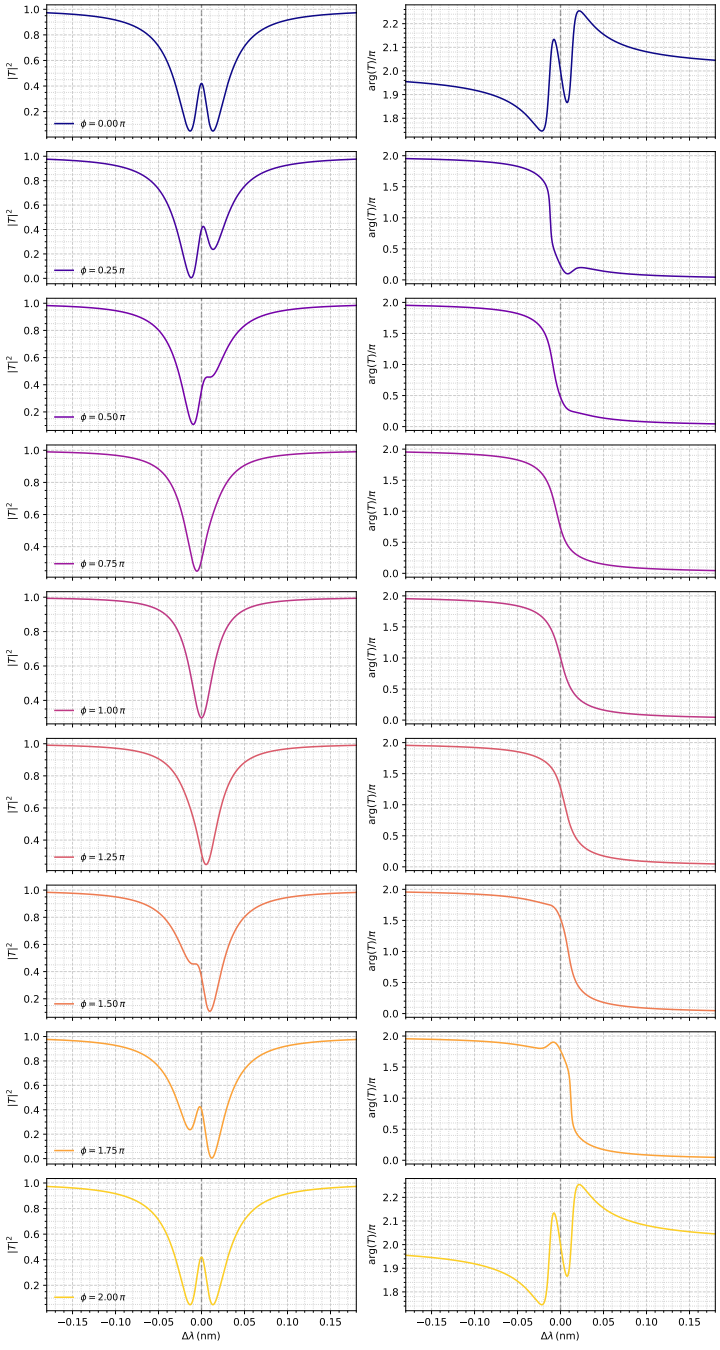



*Figure A.6:* ***Double-ring waveshaper calculated spectra.*** *Expected transmittivity and phase at the through port of the WS unit, as a function of the wavelength detuning with respect to the target channel $\lambda_C$ (vertical dashed line). Different values of the phase shift $\Phi$ applied in the WS unit are reported. The results were calculated using the TMM, with the parameters reported in the text.*

# Appendix B

# Supplementary experimental methods and characterizations

In this appendix, I provide supplementary experimental details, test structure layouts, dedicated component characterizations, and numerical simulation workflows that support the results presented in chapter 3 and chapter 4.

I first present the layout and wafer–scale performance of passive test structures, specifically directional couplers and microring resonators, fabricated on the 300 nm silicon photonics platform at CEA–Leti. Next, I report the electrical characterization in the radio–frequency domain of the traveling–wave electrodes driving the integrated p–n phase modulators ($S$–parameters), measured with a vector network analyzer.

I then detail characterizations and experimental methods related to the integrated quantum frequency processor (chapter 4). First, I report the internal pair–generation rates and coincidence–to–accidental ratios of the 15 GHz–FSR biphoton source. I also describe the calibration routines developed for the integrated double–ring line–by–line waveshaper units, focusing on the dither–tone–based calibration method I implemented for resonance alignment and power–to–phase mapping. Finally, I present supplementary linear transmission spectra and the numerical optimization framework used to model frequency–domain quantum walks.

# B.1 Layout and characterization of circuit test structures

In chapter 3 I introduced a novel generation of HE sources, whose fabrication at the CEA-Leti cleanroom (Grenoble), on the Si300nm platform, is currently being completed. These devices incorporate photon–pair generation, routing, and filtering to enable the combination of frequency–bin and, potentially, time–bin entanglement with additional degrees of freedom such as path and polarization. The preliminary results on the single components integrated within the full circuits are reported in the main text. Here I report the layout of the test structures dedicated to MRRs and DCs, from which the spectra and FoMs reported in section 3.5 were extracted.

In this section, I report the wafer–scale characterizations of Si300 nm components fabricated in the 300 mm silicon photonics pilot line at CEA-Leti. The fabrication details are reported in Sec. 3.3.

## B.1.1 Directional coupler characterization

As reported in subsection 3.2.1, I included in the HE source design some versions incorporating idler–signal routing via cascaded MZI demultiplexers. Referring to the theoretical framework in subsection 1.6.1, the architecture selected for this design requires a total of four DCs, with splitting ratios of 50:50, 20:80, 20:80, and 04:96. To optimize the performance of the demultiplexer in future runs, I included in the mask not only the full cascaded structure with the nominal DCs, i.e., the best design according to the FDTD simulations, but also test structures with multiple DC lengths, in order to identify trends that may guide future optimizations. Here I report the characterization of these additional DC test structures (Fig. B.2).

The spectra indicate that the shortest DCs perform best at the target wavelength (1550 nm). For the next fabrication run, designs with even shorter coupling lengths should be included to achieve the target splitting ratios.

# B.2 Additional characterization of the silicon phase modulators

The electrical–electrical characterization of the traveling–wave electrode driving the silicon modulators integrated in the quantum frequency processor (see chapter 4) chip is reported here. To characterize the RF response of the device under test, RF tones are injected into one port, and the transmitted and reflected signals are




*Figure B.1:* ***Test structure layouts integrated in the 300mm pilot line at CEA-Leti.*** *Top panel: Zoomed–in view of a microring resonator test structure. Unless otherwise specified, the waveguide width is* 550 *nm for AD microring resonators and* 600 *nm for AP microring resonators. Bottom panel: Zoomed–in view of a single directional coupler test structure.*

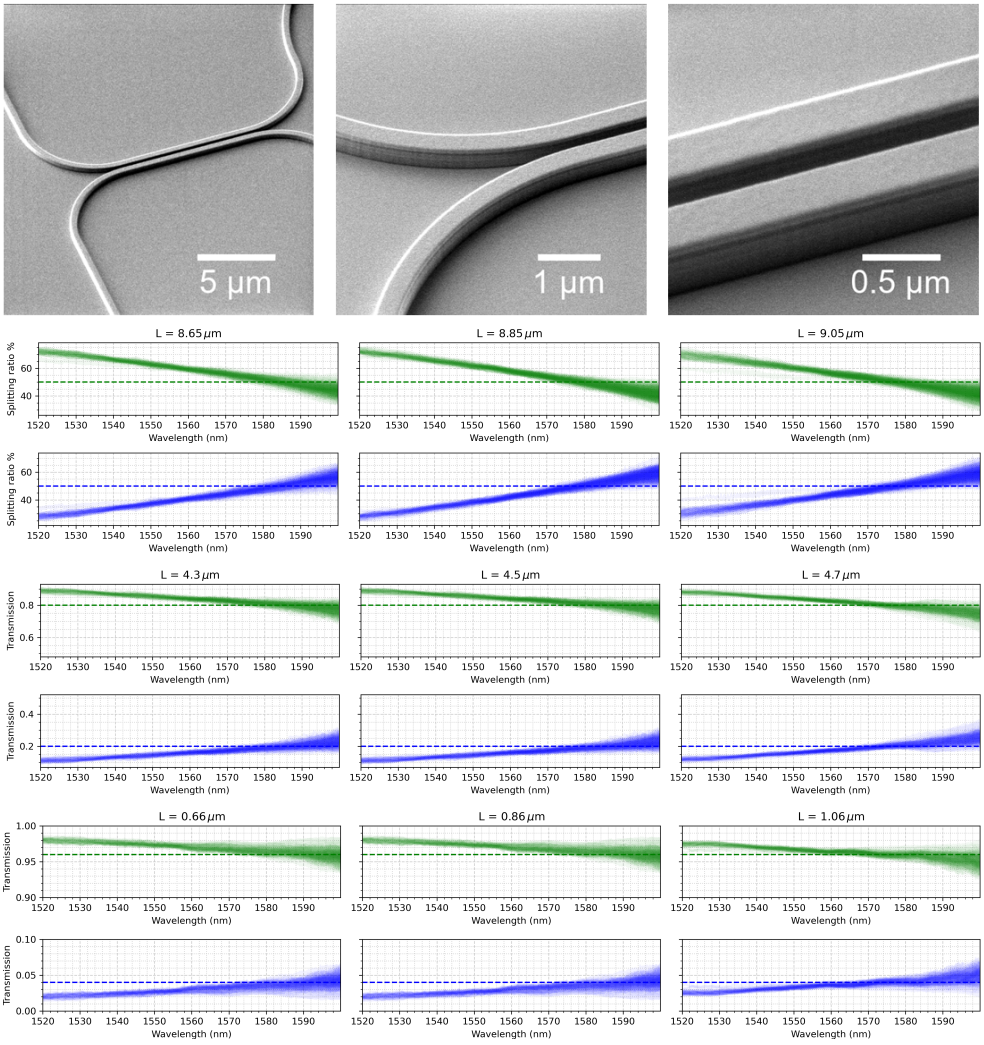



*Figure B.2:* ***DCs fabricated on the Si300 nm platform.*** *Top: SEM image of a DC with gap of* 200 *nm and length* $L = 8.85\,\mu m$*. Bottom: wafer-scale characterization of the DCs test structures (layout in Figure B.1) with nominal coupling ratios: 50:50, 20:80, and 04:96. The reported spectra have been normalized to reference straight WGs to remove the grating couplers' response, and were taken across 17 dies over the 300 mm wafer to show the uniformity of the fabrication process.*

analyzed with a VNA. This yields four scattering parameters, defined in Figure B.3, which are shown as a function of frequency to reconstruct the full RF response of the device. The magnitude of all the $S$–parameters is presented for different bias voltages applied across the p–n junction. The $S_{21}$ parameter is also reproduced in the main text, as it is the most relevant one for characterizing RF losses in the modulator.

## B.3 Source generation rate characterizations

The internal generation rate and the coincidence–to–accidental ratio of the 15 GHz source integrated in the quantum frequency processor chip (described in chapter 4) are presented here. Using the method described in section 2.2.1, the brightness is extracted as $288 \pm 2$ kHz/mW$^2$. The quantum demonstrations, i.e., both the QWs and the QST, were performed by resonantly exciting the MRR with a pump power of 2.5 mW. This generates signal–idler photon pairs, for each resonance pair, with an on–chip rate of $\sim 1.0$ MHz and a CAR of $55 \pm 12$. The setup employed is described in the main text (see subsection 4.3.1).

## B.4 Integrated WS calibration technique

The integrated waveshaper introduced in subsection 4.2.3 is a key component of the quantum frequency processor, as it enables the application of arbitrary spectral phase profiles to the on–chip generated frequency–bin state. Its calibration is therefore crucial for the correct operation of the processor, and the details of the procedure are reported here. Two approaches were used for resonance alignment and phase calibration: the first is based on the analysis of the spectra transmitted by the WS unit, the second on the analysis of the harmonics generated by two independent dither tones applied to the heaters of the two rings. Both methods are described in detail below.

### B.4.1 Spectra–based calibration procedure

As shown in the simulated single–MRR spectra (see top panel of Figure 4.12), the phase response of a ring depends strongly on wavelength. As a consequence, the interference between the two rings of a WS unit is also strongly wavelength–dependent, and the resulting spectra are highly sensitive to the applied phase shift $\Phi$. This property can be exploited to calibrate the WS unit by analyzing the transmitted

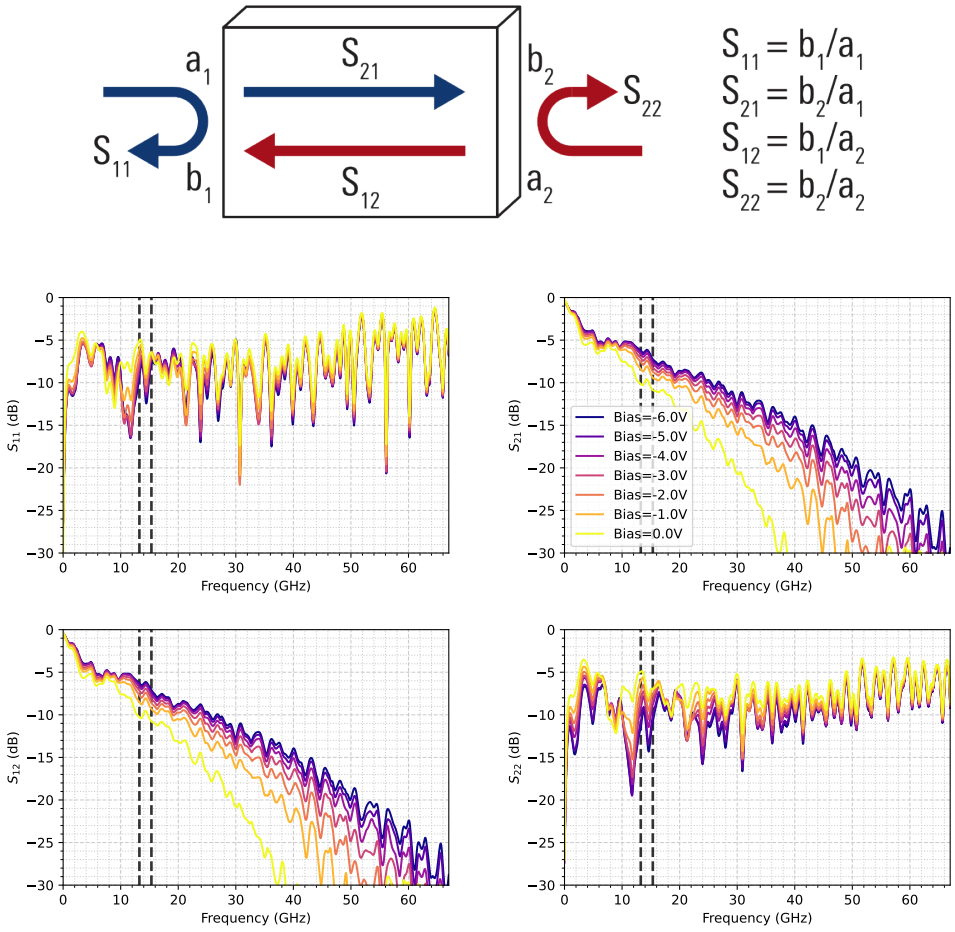



*Figure B.3:* ***RF line electrical–electrical characterization.*** *Top panel: schematic representation and definition of the S–parameters, taken from [240]. Bottom panel: magnitude of the S–parameters of the RF line as a function of the modulation frequency (x–axis) and of the bias voltage (line color). The dashed vertical line indicates the modulation frequencies used for the full–circuit experiments described in the main text, i.e.,* 15.34 *GHz for the quantum demonstrations and* 13.25 *GHz for the classical demonstrations.*

spectra. In particular, the phase shift $\Phi$ can be estimated by fitting the measured spectra with the TMM model, thus obtaining a mapping between the dissipated heater power and the applied phase shift. The heater power required to achieve a target phase shift $\Phi_0$ is determined by minimizing the difference between the measured and simulated spectra, which gives a reference power $P_0$. Since nonlinear

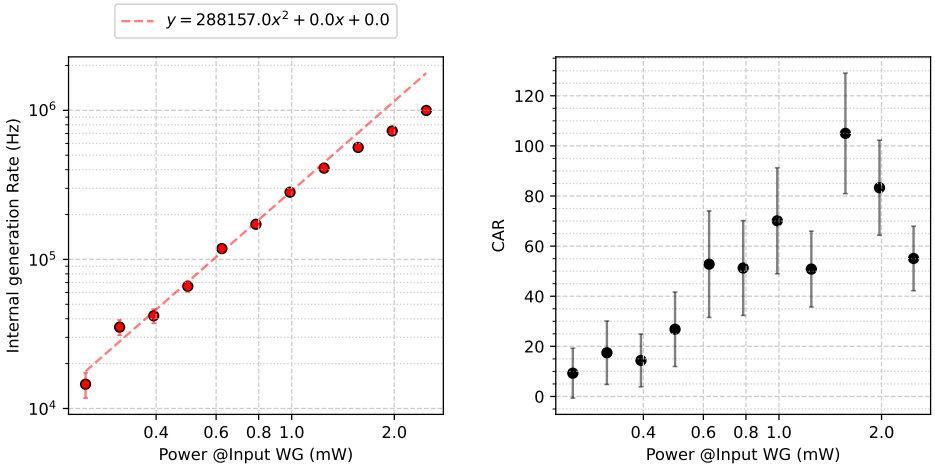



*Figure B.4:* ***Internal generation rate of the QFP 15GHz-FSR source.*** *Measured generation rate and CAR of the source.*

relations between electrical power and phase shift were experimentally found to be negligible within the explored operating range (from 0 to approximately 70 mW), the power–to–phase conversion can be approximated as linear and expressed as $\Phi(P)_{tot} = \Phi_0 + 2\pi \frac{P}{P_{2\pi}}$, where $P_{2\pi}$ is the electrical power required to obtain an additional $2\pi$ phase shift, while $\Phi_0$ is the phase shift corresponding to heater power set to zero.

An example of the extraction of $P_{2\pi}$ is already visible in the experimental spectra shown in the main text (Figure 4.11). Starting from the curve labeled $1.54\pi$, the heater power is increased until a spectrum nearly overlapping the original one is obtained again. This condition corresponds to an additional $2\pi$ phase shift; the resulting spectrum is therefore labeled $3.54\pi$. The electrical power required for this additional phase shift, i.e., $P_{2\pi}$, was estimated to lie between 65 and 70 mW across different WS units.

This was the first calibration approach implemented. Since it requires a wavelength sweep, however, it becomes impractical when operating with narrow frequency combs instead of a tunable laser. During the experiments with the fully operating circuit, where monochromatic comb lines are injected, I therefore employed a more precise procedure that avoids wavelength–sweep–based calibration. It is described in the next subsection.

### B.4.2 Dither–tone–based calibration procedure

The automated calibration protocol has been developed to work with fixed frequency combs, as is the case of our classical and quantum experimental demonstrations. The technique here reported has been applied to the four WS units used in the experiments, leading to the saving of multiple calibrated settings including both the integrated modulator drive powers and the target WS channel wavelength and phase shift. The method involves two independent low–amplitude dither tones superimposed on the DC bias of each ring heater ($\Omega_D$ for the demux ring, DR, and $\Omega_M$ for the mux ring, MR). To account for background thermal dissipation during the actual operation, all calibrations are executed while the p–n phase modulators are driven at the experimental RF power levels.

The calibration protocol comprises two main stages: resonance alignment and power–to–phase mapping.

#### Alignment of the ring resonances

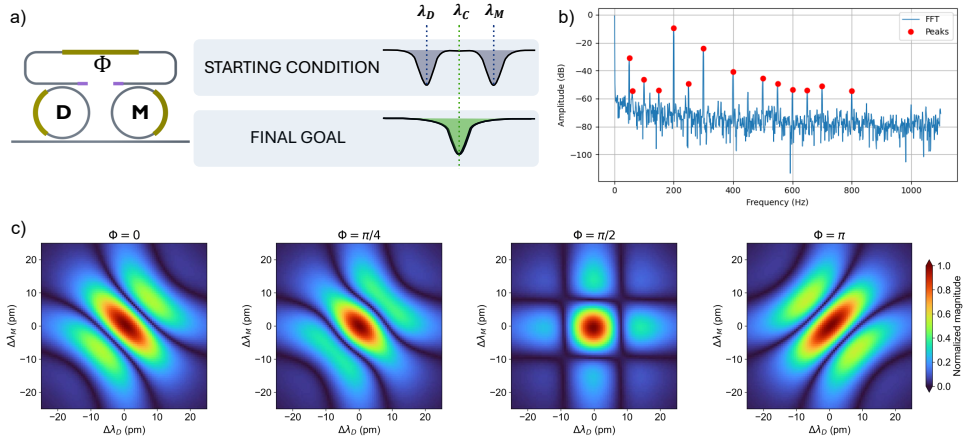



*Figure B.5:* ***WS calibration: alignment of ring resonances.*** *(a) Schematic illustration of the calibration target. (b) Representative FFT spectrum retrieved from light transmitted through a WS unit during the grid–search routine. (c) Numerical simulation of the magnitude of the $2(\Omega_D + \Omega_M)$ harmonic as a function of the resonance detunings for various phases.*

In the first stage, the resonance wavelengths of the DR and MR within a WS unit are aligned to the central channel wavelength $\lambda_C$, as illustrated in Figure B.5(a). Laser light at $\lambda_C$ is injected through port IN–2 and collected at port OUT–1 (see Figure 4.2). Dither tones at $\Omega_D/2\pi = 150$ Hz and $\Omega_M/2\pi = 250$ Hz are applied

to the DR and MR heaters, respectively, modulating their resonance wavelengths with equal amplitude $\Lambda$. The transmitted intensity $I(t)$ is monitored with a photodiode, and its spectral content is extracted using a fast Fourier transform (FFT, implemented in Python), yielding the characteristic harmonic response shown in Figure B.5(b).

Due to the strongly nonlinear transfer function of the resonant WS channel, multiple harmonics are generated. Using the scattering–matrix model described in section A.5, the time–dependent response under wavelength modulation $\lambda_{D(M)}(t) = \bar{\lambda}_{D(M)} + \Lambda \sin(\Omega_{D(M)} t)$ shows that the magnitude of the harmonic at frequency $2(\Omega_D + \Omega_M)$ reaches an absolute maximum when the relative detunings vanish ($\Delta\lambda_M = \Delta\lambda_D = 0$). As shown by the simulations in Figure B.5(c), this maximum does not depend on the internal phase shift $\Phi$.

In practice, the alignment procedure is structured into three sequential steps:

1. **Initial coarse alignment:** A tunable laser is swept continuously across the C–band, the spectrum is recorded, and the heaters are adjusted to coarsely bring the two resonances of interest close to $\lambda_C$ ($\sim$ 5 minutes, executed once at system initialization). This places the two resonances within the $\sim$ 40 pm span of the subsequent wide grid search. During this step, the dither tones are not applied and the FFT analysis is not performed.

2. **Wide grid search:** With the laser fixed at $\lambda_C$ and the dither tones applied, a wide grid search over the heater currents, covering a wavelength span of $\Delta\lambda \sim 40$pm, is performed to maximize the magnitude of the $2(\Omega_D + \Omega_M)$ harmonic ($\sim$ 20 minutes per unit). This procedure is executed once, sequentially, on the four WS units. A single global maximum is experimentally observed, corresponding, as expected, to the condition $\Delta\lambda_M = \Delta\lambda_D = 0$. The measured normalized harmonic magnitude recorded while scanning can be directly compared with the theoretical prediction in Figure B.6, showing good agreement. To validate the approach, the same figure also reports the other harmonics, which are not used for calibration and show a different dependence on the detuning, but also follow the theoretical predictions closely.

3. **Narrow grid search for cross–talk mitigation:** Since the previous step is performed sequentially, i.e. one WS–unit at a time, some residual inter–unit thermal cross–talk is expected. Once all units have been calibrated, a grid search over a restricted span of $\Delta\lambda \sim 10$ pm ($\sim$ 3 minutes per unit) is executed to mitigate this effect.

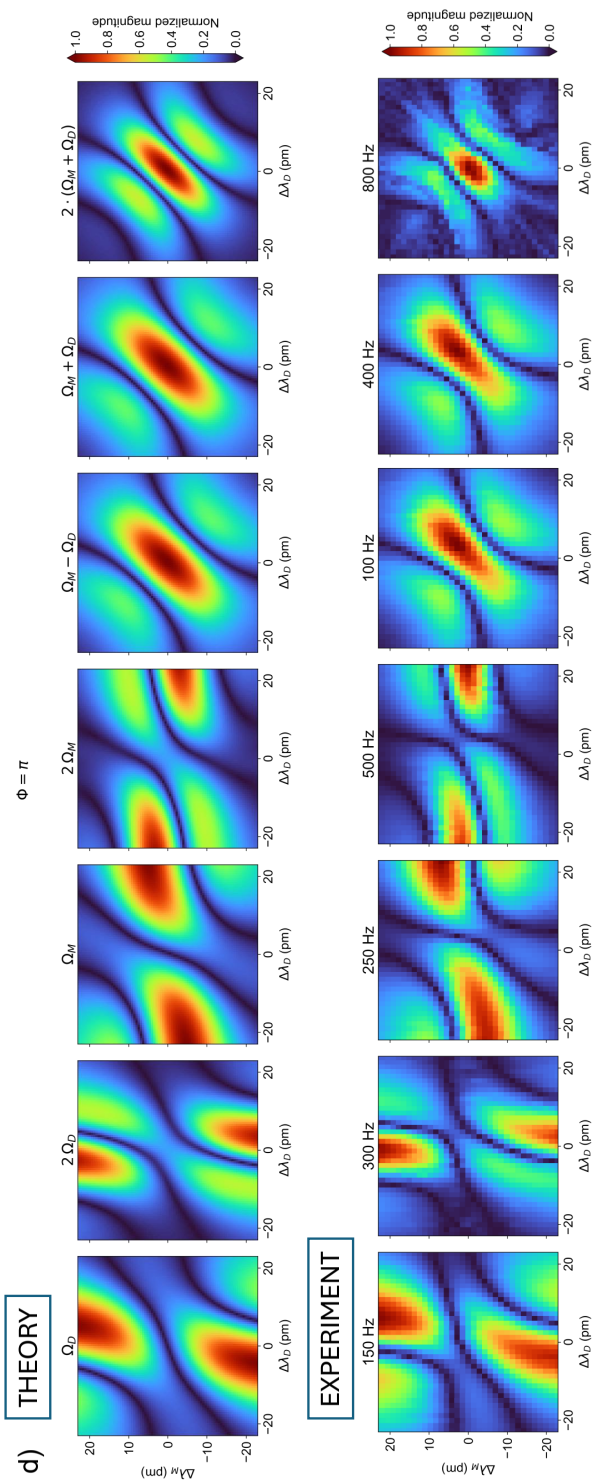



*Figure B.6:* ***WS calibration: harmonic magnitude comparison while scanning.*** *Comparison between theoretical and measured magnitudes of higher–order harmonics across different frequencies for a representative phase setting ($\Phi = \pi$). The panel on the right ($2(\Omega_D + \Omega_M)$) is the one used for the resonance alignment calibration procedure, while the other harmonics are reported for comparison. The experimental data are in good agreement with the theoretical predictions, confirming the validity of both the calibration method and the TMM model used.*

### Mapping of heater power to phase shift Φ

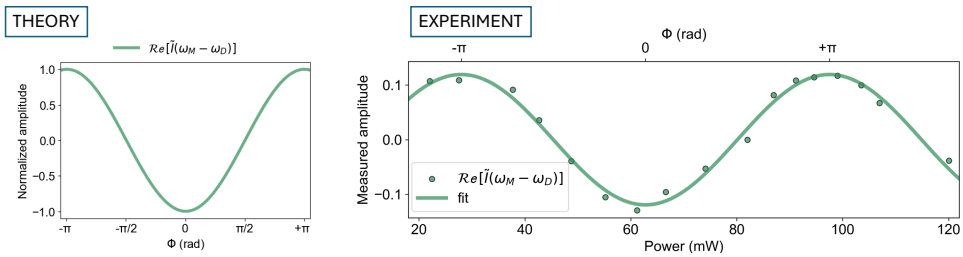



*Figure B.7:* ***WS calibration: phase setting.*** *Numerical simulation and experimental fit of the real part of the harmonic at $\Omega_M - \Omega_D$. The fit of the experimental data yields a power–to–phase conversion parameter of $P_{2\pi} = 69 \pm 1$ mW for the characterized WS unit.*

Once the MRR heater powers have been set by the resonance alignment, the second stage determines the exact mapping between the electrical power $P$ applied to the phase–shifter heater (located between the DR and MR) and the resulting phase Φ. Under the $\Delta\lambda_{D(M)} = 0$ conditions, the real part of the harmonic at frequency $\Omega_M - \Omega_D$ follows the sinusoidal relation:

$$\mathrm{Re}\left[\tilde{I}(\Omega_M - \Omega_D)\right] = \tilde{I}_0 \cos(\Phi(P)_{tot}) \tag{B.1}$$

where $\Phi(P)_{tot} = \Phi_0 + 2\pi \frac{P}{P_{2\pi}}$ and $\Phi_0$ is the intrinsic phase offset, i.e., the phase at $P = 0$.

To extract the calibration curve, the heater power $P$ is swept over a full fringe, as shown in Figure B.7. To compensate for the localized thermal cross–talk induced by the phase heater on the adjacent DR and MR resonators, the narrow grid search ($\sim 3$ minutes) is repeated at each power step. The measured fringe is fitted using:

$$\mathrm{Re}\left[\tilde{I}(\Omega_M - \Omega_D)\right] = \tilde{I}_0 \cos\left(2\pi \frac{P}{P_{2\pi}} + \Phi_0\right) \tag{B.2}$$

with $P_{2\pi}$ and $\Phi_0$ as free fitting parameters. For the unit characterized in Figure B.7, the extracted power required for a $2\pi$ phase shift is $P_{2\pi} = 69 \pm 1$ mW. The resulting linear relation of $\Phi(P)$ above defined thus determines the phase setting.

### Parallelization considerations and operational workflow

Although the calibration protocol was executed sequentially, one unit at a time, for this proof–of–principle demonstration, the underlying methodology supports

parallelized multi–channel execution:

- **Spatial demultiplexing scheme:** An electro–optic frequency comb (generated off–chip or on–chip via PM IN) can be injected simultaneously across all WS units. Demultiplexing the comb lines at the chip output and measuring each time–dependent signal with a dedicated photodiode (one per phase channel) would allow the same dither frequency pair $(\Omega_D, \Omega_M)$ to be reused simultaneously across all WS units.

- **Frequency multiplexing scheme:** Alternatively, distinct dither frequency pairs $(\Omega_{D,i}, \Omega_{M,i})$ can be assigned to each WS unit $i$, avoiding overlap between the harmonics and enabling parallel calibration on a single combined output detector, without the need for spatial demultiplexing.

In this work, the dither–tone–based calibration method was implemented sequentially on single units, requiring about $\sim 20$ minutes per WS–unit at the initialization stage and about 3 minutes per unit for subsequent small phase adjustments. This approach was already sufficient for our proof–of–principle demonstrations. However, the above parallelization strategies could significantly reduce the overall calibration time.

## B.5 Additional quantum frequency processor characterizations and simulations

Additional characterizations and details on the numerical simulations of the quantum frequency processor are reported to support the interpretation of the experimental results and to confirm the validity of the implemented transformations. The simulations are based on the methods described in Ref. [218].

### B.5.1 Additional linear characterizations

The spectra of the WS for all the implemented transformations are recorded to extract the losses at the FB–mode wavelengths. This is achieved by routing the light between the main input/output channels and the two additional ones provided by the PF MZI. These additional ports allow the light either to be sent through the WS section only (and collected at the full–circuit output), or to be collected after the source–only section (in which case it is injected through the main input). Examples of the spectra are shown in Figure B.8; the losses extracted at the resonant

wavelengths are included in the analysis of the corresponding coincidence measurements.

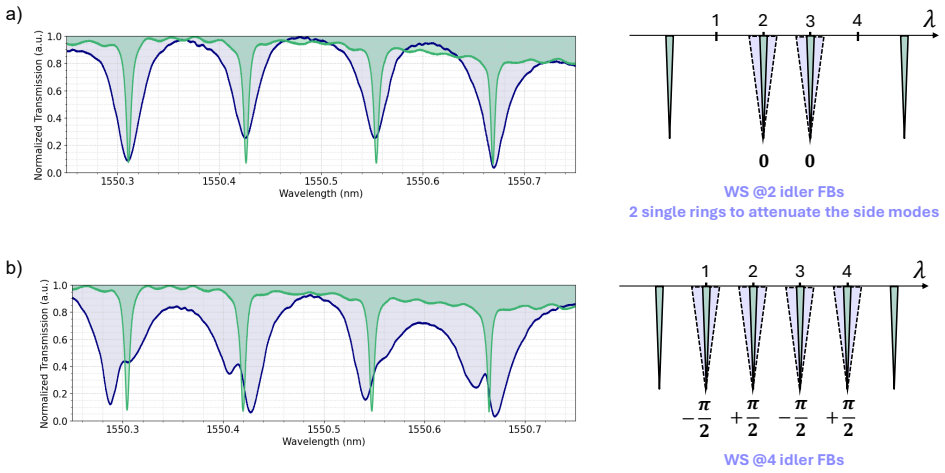



*Figure B.8:* ***WS and source spectra.*** *(a) WS spectra (blue) for the QST configuration, in the specific case where the phase difference between the idler modes is set to zero. (b) WS spectra (blue) implemented for the anticorrelated QW. The source spectrum (green) is superimposed to visualize the exact resonance positions.*

### B.5.2 Quantum walk data analysis and simulations

The quantum walks shown in Figure 4.20 include both experimental and simulated results. Here, I report additional details regarding the simulations of the quantum–walk dynamics.

The state at the input of the OUT PM, generated by the on-chip source, can be written as $|\Psi\rangle = \frac{1}{\mathcal{N}} \sum_{l=0}^{5} \beta_l \, |ll\rangle_{si}$, where $\mathcal{N}$ is a normalization constant. The four frequency bins labeled 1 to 4 in Figure B.8 span the $4 \times 4$ Hilbert space of interest, within which frequency-resolved coincidence measurements are performed. The outer bins, labeled 0 and 5, also participate in the quantum walk but cannot be measured due to the limited bandwidth ($\sim 80\,\mathrm{GHz}$) of the off-chip filters used for pump suppression. Frequency bins with indices $l < 0$ or $l > 5$ are excluded from the simulations owing to the relatively small modulation depth ($\delta \sim 0.8\,\mathrm{rad}$) applied to the OUT PM, which confines frequency-bin scrambling primarily to nearest neighbors.

The coefficients $|\beta_l|^2$ for $l = 1$–$4$ are extracted directly from the measured JSI of the source. The dominant source of inhomogeneity among the coefficients, clearly

visible as a decreasing intensity along the main diagonal in the initial JSI panel, is due to the pump-rejection filter, which imposes a sinusoidal envelope with a free spectral range of 500 GHz on the broadband frequency comb. This envelope is used to extrapolate the values of $|\beta_0|$ and $|\beta_5|$.

To extract the relative phases between the input frequency bins, the state $|\Psi\rangle$ was sent through the OUT PM with a modulation depth set to $\delta = 0.8$ rad, and the resulting JSI was measured, as shown in Fig. 4.20(b). We then employed a numerical optimization procedure (`scipy.optimize.minimize`) to maximize the overlap between the experimental JSI and the simulated distribution. The free parameters in the optimization are the relative phases $\mathrm{Arg}(\beta_l)$ for $l = 1$–5, with $\mathrm{Arg}(\beta_0) = 0$ serving as a reference. All other parameters were fixed based on independent experimental calibrations, including the modulation depth $\delta$, the losses of each WS channel, and the applied spectral phases $\{\Phi_l\}_{l=1}^{4}$, which were all set to zero. We find that the phases $\mathrm{Arg}(\beta_l)$ maximizing the overlap between the simulated ($\mathrm{JSI_t}$) and experimental ($\mathrm{JSI_e}$) JSIs all lie within $\pm 0.1$ rad. The simulation, shown in Fig. 4.20(b), yields a fidelity of $\mathcal{F} = \frac{\mathrm{Tr}(AB^T)}{\sqrt{\mathrm{Tr}(AA^T)\,\mathrm{Tr}(BB^T)}} = 99.38(5)\%$, where $A =$JSI$_\mathrm{t}$ (theoretical model, fitted) and $B =$JSI$_\mathrm{e}$ (experimental). This indicates that the input frequency bins are mutually phase-aligned within experimental and numerical uncertainty. Consequently, the generated photon pairs undergo a correlated quantum walk, characterized by frequency correlations spreading away from the main diagonal of the JSI [218].

To convert this behavior into an anti-correlated quantum walk, where frequency correlations remain confined along the main diagonal, the input state must be transformed into $|\Psi\rangle_{\mathrm{ac}} = \frac{1}{\mathcal{N}} \sum_{l=0}^{5} |\beta_l| e^{il\pi} |ll\rangle_{si}$; thus, a relative $\pi$ phase shift must be introduced between consecutive frequency bins. We achieve this transformation using the four-channel WS. Specifically, we apply to the four controlled modes the phase pattern $\Phi_{1-4} = [-0.5\pi, 0.5\pi, -0.5\pi, 0.5\pi]$. The resulting WS spectrum is reported in Fig. B.8(b). The experimentally measured JSI corresponding to this configuration is shown in Fig. 4.20(c). After the OUT PM, the frequency correlations remain confined along the main diagonal, clearly indicating the transition to an anti-correlated quantum walk. The fidelity between the experimental JSI and the corresponding numerical simulation, accounting for both the introduced channel losses and the $\Phi_{1-4}$ pattern, is $\mathcal{F} = 98.7(5)\%$.

# List of publications and conferences

## Journals

1. **Congia, S.**[*], Virot, L., Rovetta, E., Fincato, A., Boeuf, F. *et al.* Fully integrated quantum frequency processor on a silicon chip. *Nature Communications* (2026). DOI: https://doi.org/10.1038/s41467-026-77287-5

2. **Congia, S.**[*], Borghi, M., Brusaschi, E., Sabattoli, F. A., El Dirani, H. *et al.* Generation of hyperentangled photon pairs in the time and frequency domain on a silicon photonic chip. *Opt. Lett.* **50**, 5117–5120 (2025). DOI: https://doi.org/10.1364/OL.562079

3. Bernardi, A.[*], Clementi, M., Bacchi, M., Bolaños, M. R., **Congia, S.** *et al.* Gigahertz-rate thin-film lithium niobate receiver for time-bin quantum communication. *Light Sci. Appl.* **15**, 237 (2026). DOI: https://doi.org/10.1038/s41377-026-02306-5

4. Bacchi, M.[*], Bernardi, A., Clementi, M., **Congia, S.**, Garrisi, F. *et al.* Post-selection-free time-bin entanglement on a thin-film lithium niobate photonic chip. *Physical Review Applied 25.6* 064045 (2026). DOI: https://doi.org/10.1103/1sjz-tw85

5. Gianini, L., Barone, A., Bacchi, M., **Congia, S.**[*], Tagliavacche, N. *et al.* A silicon integrated source of hyper-entangled photon pairs with rate exceeding 1 billion pairs per second. *npj Nanophotonics* **3**, 1 (2026). DOI: https://doi.org/10.1038/s44310-025-00093-2

## Preprints

1. Compagnini, D., Tagliavacche, N., **Congia, S.**, Bernardi, A., *et al.* A Universal All-Fiber Quantum Buffer for the Telecom Band. *arXiv* 2606.24681 (2026). Currently under peer review.

## Conference proceedings

1. **Congia, S.**, Rovetta, E., Virot, L., Fincato, A., Boeuf, F. & Borghi, M. A Silicon integrated Quantum Frequency Processor. Presented at *Quantum 2.0.* (Optica Publishing Group, 2026).

2. **Congia, S.***, Rovetta, E., Virot, L., Fincato, A., Boeuf, F. & Borghi, M. Generation and processing of quantum optical microcombs on a silicon photonic chip. Presented at *Conference on Lasers and Electro-Optics (CLEO)* (Optica Publishing Group, 2026).

3. Bernardi, A., Clementi, M.*, Bacchi, M., Bolaños, M. R., **Congia, S.** *et al.* Thin-film lithium niobate receiver for time-bin quantum communication. Presented at *Conference on Lasers and Electro-Optics (CLEO)* (Optica Publishing Group, 2026).

4. **Congia, S.***, Borghi, M., Brusaschi, E., Liscidini, M., Rothman, J. *et al.* Generation of hyperentangled photon pairs encoded in the time-bin and frequency-bin degree of freedom from silicon microrings. In *25th Anniversary International Conference on Transparent Optical Networks (ICTON)*, 1–3 (IEEE, 2025).

5. **Congia, S.***, Borghi, M., Sabattoli, F. A., El Dirani, H., Youssef, L. *et al.* Generation of hyperentangled photon pairs in the frequency-bin and time-bin domains with a silicon photonic chip. In *CLEO/Europe–EQEC*, 1 (IEEE, 2025).

6. Bernardi, A.*, Bacchi, M., Clementi, M., **Congia, S.**, Garrisi, F. *et al.* High switching-rate post-selection-free time-bin entanglement in thin-film lithium niobate. In *25th Anniversary International Conference on Transparent Optical Networks (ICTON)*, 1–3 (IEEE, 2025).

7. Bacchi, M.*, Bernardi, A., Clementi, M., **Congia, S.**, Garrisi, F. *et al.* Ultrafast post-selection-free time-bin entanglement on a thin-film lithium niobate photonic chip. In *CLEO/Europe–EQEC*, 1 (IEEE, 2025).

8. Gianini, L.*, Barone, A., Bacchi, M., Faugier-Tovar, J., **Congia, S.** *et al.* Hyperentangled photon pairs emitted from an integrated source delivering more than 1 Gpair/s. In *CLEO: Fundamental Science*, FF2K–4 (Optica Publishing Group, 2024).

9. Szelag, B., Garcia, S., Adelmini, L., KazarMendes, M., Guerber, S., **Congia, S.** *et al.* High-performance 300 mm silicon photonics platform for R&D and product prototyping. In *IEEE Photonics Conference (IPC)*, 1–2 (IEEE, 2022).

## Conference presentations

1. **Congia, S.**, Rovetta, E., Virot, L., Fincato, A., Boeuf, F. & Borghi, M. Generation and processing of quantum optical microcombs on a silicon photonic chip. Presented at *Conference on Lasers and Electro-Optics (CLEO)* (Optica Publishing Group, 2026).

2. Bernardi, A., Clementi, M., Bacchi, M., Bolaños, M. R., **Congia, S.** *et al.* Thin-film lithium niobate receiver for time-bin quantum communication. Presented at *Conference on Lasers and Electro-Optics (CLEO)* (Optica Publishing Group, 2026).

3. **Congia, S.**, Borghi, M., Brusaschi, E., Liscidini, M., Rothman, J. *et al.* Generation of hyperentangled photon pairs encoded in the time-bin and frequency-bin degree of freedom from silicon microrings. Presented at *25th Anniversary International Conference on Transparent Optical Networks (ICTON)* (2025).

4. **Congia, S.**, Borghi, M., Sabattoli, F. A., El Dirani, H., Youssef, L. *et al.* Generation of hyperentangled photon pairs in the frequency-bin and time-bin domains with a silicon photonic chip. Presented at *CLEO/Europe–EQEC* (2025).

## Patents

1. **Congia, S.** *et al.* US Patent Application US 20260072212 A1 (published 12 March 2026).

2. **Congia, S.** *et al.* French Patent Application FR 3166229 A1 (published 13 March 2026).

3. **Congia, S.** *et al.* French Patent Application FR 3166228 A1 (published 13 March 2026).

*Corresponding author

# Bibliography


[1] Henning Soller, Duc Nam Nguyen and Martina Gschwendtner. *Quantum technology investment hits a magic moment'*. https://www.mckinsey.com/capabilities/tech-and-ai/our-insights/tech-forward/quantum-technology-investment-hits-a-magic-moment. Accessed: 2025-10-27. McKinsey & Company, Oct. 2025.

[2] Ministero dell'Università e della Ricerca (MUR). *Italian Strategy for Quantum Technologies*. https://www.mur.gov.it/sites/default/files/2025-09/Strategia_italiana_tecnologie_quantistiche_ENG.pdf. Accessed: 2025-10-27. Ministero dell'Università e della Ricerca, Governo Italiano, Sept. 2025.

[3] France 2030. *La Stratégie Nationale Quantique*. https://quantique.france2030.gouv.fr/. Accessed: 2025-10-27. Gouvernement de la République française, 2025.

[4] Muhammad AbuGhanem. 'Photonic quantum computers'. In: *arXiv preprint arXiv:2409.08229* (2024).

[5] Nicolas Gisin and Rob Thew. 'Quantum communication'. In: *Nature photonics* 1.3 (2007), pp. 165–171.

[6] Ivonne Bente et al. 'The potential of multidimensional photonic computing'. In: *Nature Reviews Physics* 7.8 (2025), pp. 439–450.

[7] Emanuele Pelucchi et al. 'The potential and global outlook of integrated photonics for quantum technologies'. In: *Nature Reviews Physics* 4.3 (2022), pp. 194–208.

[8] Hui Wang et al. 'Scalable photonic quantum technologies'. In: *Nature Materials* (2025), pp. 1–15.

[9] Laurent Labonté et al. 'Integrated photonics for quantum communications and metrology'. In: *PRX Quantum* 5.1 (2024), p. 010101.

[10] Paolo Piergentili et al. ‘Quantum information with integrated photonics’. In: *Applied Sciences* 14.1 (2023), p. 387.

[11] Galan Moody et al. ‘2022 Roadmap on integrated quantum photonics’. In: *Journal of Physics: Photonics* 4.1 (2022), p. 012501.

[12] Taira Giordani et al. ‘Integrated photonics in quantum technologies’. In: *La Rivista del Nuovo Cimento* 46.2 (2023), pp. 71–103.

[13] Wei Luo et al. ‘Recent progress in quantum photonic chips for quantum communication and internet’. In: *Light: Science & Applications* 12.1 (2023), p. 175.

[14] Jianwei Wang et al. ‘Integrated photonic quantum technologies’. In: *Nature photonics* 14.5 (2020), pp. 273–284.

[15] Yufei Liu et al. ‘Silicon photonic transceivers in the field of optical communication’. In: *Nano communication networks* 31 (2022), p. 100379.

[16] Hsuan-Hao Lu et al. ‘Frequency-bin photonic quantum information’. In: *Optica* 10.12 (2023), pp. 1655–1671.

[17] Karthik V Myilswamy et al. ‘On-chip frequency-bin quantum photonics’. In: *Nanophotonics* 14.11 (2025), pp. 1879–1894.

[18] Michael Kues et al. ‘Quantum optical microcombs’. In: *Nature Photonics* 13.3 (2019), pp. 170–179.

[19] Antoine Henry et al. ‘Parallelizable synthesis of arbitrary single-qubit gates with linear optics and time-frequency encoding’. In: *Physical Review A* 107.6 (2023), p. 062610.

[20] Antoine Henry et al. ‘Parallelization of frequency domain quantum gates: manipulation and distribution of frequency-entangled photon pairs generated by a 21 GHz silicon microresonator’. In: *Advanced Photonics* 6.3 (2024), pp. 036003–036003.

[21] Avik Dutt et al. ‘Nonlinear and quantum photonics using integrated optical materials’. In: *Nature Reviews Materials* 9.5 (2024), pp. 321–346.

[22] Paul G Kwiat. ‘Hyper-entangled states’. In: *Journal of modern optics* 44.11-12 (1997), pp. 2173–2184.

[23] Fabian Steinlechner et al. ‘Distribution of high-dimensional entanglement via an intra-city free-space link’. In: *Nature communications* 8.1 (2017), p. 15971.

[24] Fu-Guo Deng, Bao-Cang Ren and Xi-Han Li. 'Quantum hyperentanglement and its applications in quantum information processing'. In: *Science bulletin* 62.1 (2017), pp. 46–68.

[25] Liangliang Lu et al. 'Advances in chip-scale quantum photonic technologies'. In: *Advanced Quantum Technologies* 4.12 (2021), p. 2100068.

[26] Carsten Schuck et al. 'Complete deterministic linear optics Bell state analysis'. In: *Physical review letters* 96.19 (2006), p. 190501.

[27] Tzu-Chieh Wei, Julio T Barreiro and Paul G Kwiat. 'Hyperentangled Bell-state analysis'. In: *Physical Review A-Atomic, Molecular, and Optical Physics* 75.6 (2007), p. 060305.

[28] Julio T Barreiro, Tzu-Chieh Wei and Paul G Kwiat. 'Beating the channel capacity limit for linear photonic superdense coding'. In: *Nature physics* 4.4 (2008), pp. 282–286.

[29] Brian P Williams, Ronald J Sadlier and Travis S Humble. 'Superdense coding over optical fiber links with complete Bell-state measurements'. In: *Physical review letters* 118.5 (2017), p. 050501.

[30] Kai Chen et al. 'Experimental Realization of One-Way Quantum Computing with Two-Photon Four-Qubit Cluster States'. In: *Physical review letters* 99.12 (2007), p. 120503.

[31] Giuseppe Vallone et al. 'One-way quantum computation with two-photon multiqubit cluster states'. In: *Physical Review A-Atomic, Molecular, and Optical Physics* 78.4 (2008), p. 042335.

[32] Christian Reimer et al. 'High-dimensional one-way quantum processing implemented on d-level cluster states'. In: *Nature Physics* 15.2 (2019), pp. 148–153.

[33] Jin-Hun Kim et al. 'Noise-resistant quantum communications using hyperentanglement'. In: *Optica* 8.12 (2021), pp. 1524–1531.

[34] Dan Xu et al. 'Entanglement distillation based on polarization and frequency hyperentanglement'. In: *IEEE Journal of Selected Topics in Quantum Electronics* 30.1: Single-Photon Technologies and Applications (2023), pp. 1–8.

[35] Xiaojiong Chen et al. 'Quantum entanglement on photonic chips: a review'. In: *Advanced Photonics* 3.6 (2021), pp. 064002–064002.

[36] Hong Deng et al. 'Single-chip silicon photonic engine for analog optical and microwave signals processing'. In: *Nature Communications* 16.1 (2025), p. 5087.

[37] Jianwei Wang et al. 'Multidimensional quantum entanglement with large-scale integrated optics'. In: *Science* 360.6386 (2018), pp. 285–291.

[38] Xiaogang Qiang et al. 'Large-scale silicon quantum photonics implementing arbitrary two-qubit processing'. In: *Nature photonics* 12.9 (2018), pp. 534–539.

[39] Jueming Bao et al. 'Very-large-scale integrated quantum graph photonics'. In: *Nature Photonics* 17.7 (2023), pp. 573–581.

[40] Joseph M Lukens and Pavel Lougovski. 'Frequency-encoded photonic qubits for scalable quantum information processing'. In: *Optica* 4.1 (2016), pp. 8–16.

[41] R. Soref and J. Larenzo. 'All-silicon active and passive guided-wave components for l=1.3 and 1.6um'. In: *IEEE Journal of Quantum Electronics* 22.6 (1986), pp. 873–879.

[42] Chong Zhang et al. 'Integrated photonics beyond communications'. In: *Applied Physics Letters* 123.23 (Dec. 2023), p. 230501. ISSN: 0003-6951. URL: https://xdoi.org/10.1063/5.0184677.

[43] S. Y. Siew et al. 'Review of Silicon Photonics Technology and platform development'. In: *Journal of Lightwave Technology* 39.13 (July 2021), pp. 4374–4389.

[44] Sudip Shekhar et al. 'Roadmapping the next generation of Silicon Photonics'. In: *Nature Communications* 15.1 (Jan. 2024).

[45] Mordor Intelligence Research & Advisory. *Silicon Photonics Market Size & Share Analysis - Growth Trends & Forecasts (2024 - 2029)*. 2024. URL: https://www.mordorintelligence.com/industry-reports/silicon-photonics-market (visited on 07/02/2024).

[46] Wei Shi, Ye Tian and Antoine Gervais. 'Scaling capacity of fiber-optic transmission systems via silicon photonics'. In: *Nanophotonics* 9.16 (2020), pp. 4629–4663.

[47] Xia Chen et al. 'The emergence of silicon photonics as a flexible technology platform'. In: *Proceedings of the IEEE* 106.12 (Dec. 2018), pp. 2101–2116.

[48] Quentin Wilmart et al. 'A Complete Si Photonics Platform Embedding Ultra-Low Loss Waveguides for O- and C-Band'. In: *Journal of Lightwave Technology* 39.2 (2021), pp. 532–538.

[49] B. Szelag et al. 'High performance 300mm silicon photonics platform for R&D and product prototyping'. In: *2022 IEEE Photonics Conference (IPC)*. 2022, pp. 1–2.

[50] F. Boeuf et al. 'Silicon Photonics Beyond Optical Interconnects'. In: *2021 IEEE International Electron Devices Meeting (IEDM)*. 2021, pp. 29.2.1–29.2.4.

[51] A. Yariv and P. Yeh. *Photonics*. Oxford Series in Electrical and Computer Engineering. Oxford University Press, 2007.

[52] Abdul Rahim et al. 'Taking silicon photonics modulators to a higher performance level: State-of-the-art and a review of New Technologies'. In: *Advanced Photonics* 3.02 (Apr. 2021).

[53] Lukas Chrostowski and Michael Hochberg. *Silicon Photonics Design*. Cambridge University Press, 2019.

[54] Robert W. Boyd. *Nonlinear optics*. Elsevier, AP Academic Press, 2020.

[55] Y R Shen. *Principles of nonlinear optics*. Jan. 1984.

[56] R. M. Osgood Jr. et al. 'Engineering nonlinearities in Nanoscale Optical Systems: Physics and applications in dispersion-engineered silicon nanophotonic wires'. In: *Advances in Optics and Photonics* 1.1 (Jan. 2009), p. 162.

[57] J. Leuthold, C. Koos and W. Freude. 'Nonlinear silicon photonics'. In: *Nature Photonics* 4.8 (July 2010), pp. 535–544.

[58] M Borghi et al. 'Nonlinear silicon photonics'. In: *Journal of Optics* 19.9 (Aug. 2017), p. 093002.

[59] Luigi Sirleto and Giancarlo C. Righini. 'An introduction to nonlinear integrated photonics devices: Nonlinear effects and materials'. In: *Micromachines* 14.3 (Mar. 2023), p. 604.

[60] Q. Lin, Oskar J. Painter and Govind P. Agrawal. 'Nonlinear optical phenomena in Silicon Waveguides: Modeling and applications'. In: *Optics Express* 15.25 (2007), p. 16604.

[61] X. Chen, N.C. Panoiu and R.M. Osgood. 'Theory of raman-mediated pulsed amplification in silicon-wire waveguides'. In: *IEEE Journal of Quantum Electronics* 42.2 (Feb. 2006), pp. 160–170.

[62] H K Tsang and Y Liu. 'Nonlinear Optical Properties of Silicon Waveguides'. In: *Semiconductor Science and Technology* 23.6 (May 2008), p. 064007.

[63] M. Dinu, F. Quochi and H. Garcia. 'Third-order nonlinearities in silicon at telecom wavelengths'. In: *Applied Physics Letters* 82.18 (May 2003), pp. 2954–2956.

[64] Alan D Bristow, Nir Rotenberg and Henry M Van Driel. 'Two-photon absorption and Kerr coefficients of silicon for 850–2200nm'. In: *Applied physics letters* 90.19 (2007).

[65] Stefano Azzini. 'Classical and Quantum Nonlinear Emission of Light from Photonic Micro- and Nano-cavities'. Submitted to the Graduate School of Physics for the degree of Doctor of Philosophy in Physics at the University of Pavia. PhD thesis. 2013. URL: `https://www.researchgate.net/publication/268808780_Classical_and_Quantum_Nonlinear_Emission_of_Light_from_Photonic_Micro-_and_Nano-cavities`.

[66] Federico Andrea Sabattoli. 'Silicon Photonics Integrated Circuits for Quantum Applications'. Submitted to the Graduate School of Physics for the degree of Doctor of Philosophy in Physics at the University of Pavia. PhD thesis. 2021. URL: `http://hdl.handle.net/11571/1437334`.

[67] Govind P. Agrawal. *Nonlinear Fiber Optics*. 6th. London: Academic Press, 2019. ISBN: 978-0-12-817043-4.

[68] Alwyn C. Scott and P. L. Christiansen. *Nonlinear science at the dawn of the 21st century*. Springer, 2000.

[69] Shivani Sharma et al. 'Nanowaveguide Designs in 220-nm SOI for Ultra-Broadband FWM at Telecom Wavelengths'. In: *IEEE Journal of Quantum Electronics* 56.5 (2020), pp. 1–8.

[70] Zhenshan Yang, Marco Liscidini and J. E. Sipe. 'Spontaneous parametric down-conversion in waveguides: A backward Heisenberg picture approach'. In: *Phys. Rev. A* 77 (3 Mar. 2008), p. 033808.

[71] L. G. Helt et al. 'Spontaneous four-wave mixing in microring resonators'. In: *Opt. Lett.* 35.18 (Sept. 2010), pp. 3006–3008.

[72] Lukas G. Helt, Marco Liscidini and John E. Sipe. 'How does it scale? Comparing quantum and classical nonlinear optical processes in integrated devices'. In: *J. Opt. Soc. Am. B* 29.8 (Aug. 2012), pp. 2199–2212.

[73] R Dekker et al. 'Ultrafast nonlinear all-optical processes in silicon-on-insulator waveguides'. In: *Journal of Physics D: Applied Physics* 40.14 (June 2007).

[74] R. Claps et al. 'Influence of nonlinear absorption on Raman amplification in silicon waveguides'. In: *Optics Express* 12.12 (2004), p. 2774.

[75] T. K. Liang and H. K. Tsang. 'Role of free carriers from two-photon absorption in Raman amplification in silicon-on-insulator waveguides'. In: *Applied Physics Letters* 84.15 (Apr. 2004), pp. 2745–2747.

[76] Vilson R. Almeida and Michal Lipson. 'Optical bistability on a Silicon Chip'. In: *Optics Letters* 29.20 (Oct. 2004), p. 2387.

[77] Qianfan Xu and Michal Lipson. 'Carrier-induced optical bistability in silicon ring resonators'. In: *Optics Letters* 31.3 (2006), p. 341.

[78] Andrey A. Nikitin et al. 'Carrier-induced optical bistability in the silicon micro-ring resonators under continuous wave pumping'. In: *Optics Communications* 480 (Feb. 2021), p. 126456.

[79] Vilson R. Almeida et al. 'All-optical switching on a silicon chip'. In: *Optics Letters* 29.24 (Dec. 2004), p. 2867.

[80] Masaya Notomi et al. 'Optical bistable switching action of SI high-Q photonic-crystal nanocavities'. In: *Optics Express* 13.7 (2005), p. 2678.

[81] Michele Belotti et al. 'All-optical switching in 2D silicon photonic crystals with low loss waveguides and optical cavities'. In: *Optics Express* 16.15 (July 2008), p. 11624.

[82] Qianfan Xu and Michal Lipson. 'All-optical logic based on silicon micro-ring resonators'. In: *Optics Express* 15.3 (2007), p. 924.

[83] Qianfan Xu, Po Dong and Michal Lipson. 'Breaking the delay-bandwidth limit in a photonic structure'. In: *Nature Physics* 3.6 (Apr. 2007), pp. 406–410.

[84] Michal Lipson. 'Storing light on chip: Breaking the delay-bandwidth limit'. In: *Integrated Photonics and Nanophotonics Research and Applications / Slow and Fast Light* (2007).

[85] Libin Zhang et al. 'Experimental observations of thermo-optical bistability and self-pulsation in silicon microring resonators'. In: *Journal of the Optical Society of America B* 31.2 (Jan. 2014), p. 201.

[86] Richard A. Soref and Brian R. Bennett. 'Kramers-Kronig Analysis of electro-optical switching in Silicon'. In: *SPIE Proceedings* (Mar. 1987).

[87] R. Soref and B. Bennett. 'Electrooptical effects in Silicon'. In: *IEEE Journal of Quantum Electronics* 23.1 (Jan. 1987), pp. 123–129.

[88] Alexis Abraham. 'Development of low power consumption silicon optical modulators for the next generation of optical interconnects'. Optique photonique. Université Paris Saclay (COmUE), 2016. Français. NNT : 2016SACLS338. tel-01433574. PhD thesis. 2016.

[89] Graham T. Reed and Andrew P. Knights. *Silicon Photonics: An introduction.* Wiley, 2005.

[90] Graham T. Reed and C.E. Jason Png. 'Silicon Optical Modulators'. In: *Materials Today* 8.1 (Jan. 2005), pp. 40–50.

[91] G. T. Reed et al. 'Silicon Optical Modulators'. In: *Nature Photonics* 4.8 (July 2010), pp. 518–526.

[92] Haisheng Rong et al. 'Low-threshold continuous-wave Raman Silicon Laser'. In: *Nature Photonics* 1.4 (Apr. 2007), pp. 232–237.

[93] Thomas J. Johnson, Matthew Borselli and Oskar Painter. 'Self-induced optical modulation of the transmission through a high-Q Silicon Microdisk resonator'. In: *Optics Express* 14.2 (2006), p. 817.

[94] Vilson R. Almeida et al. 'All-optical control of light on a Silicon Chip'. In: *Nature* 431.7012 (Oct. 2004), pp. 1081–1084.

[95] G. Cocorullo and I. Rendina. 'Thermo-optical modulation at 1.5um in silicon etalon'. In: *Electronics Letters* 28.1 (Jan. 1992), pp. 83–85.

[96] Stefano Signorini et al. 'Intermodal four-wave mixing in silicon waveguides'. In: *Photonics Research* 6.8 (2018), pp. 805–814.

[97] ANSYS, Inc. *MODE - Finite Difference Eigenmode (FDE) solver (Lumerical software ULC).* Version 7.18.2779. 2024. URL: `https://optics.ansys.com/hc/en-us/articles/360034917233-MODE-Finite-Difference-Eigenmode-FDE-solver-introduction` (visited on 12/02/2024).

[98] Yuning Zhang et al. 'Enhanced Kerr nonlinearity and nonlinear figure of merit in silicon nanowires integrated with 2D graphene oxide films'. In: *ACS Applied Materials & Interfaces* 12.29 (2020), pp. 33094–33103.

[99] Yuxing Yang et al. 'Efficient and Broadband Four-Wave Mixing in a Compact Silicon Subwavelength Nanohole Waveguide'. In: *Advanced Optical Materials* 7.21 (2019), p. 1900810.

[100] B.E. Little et al. 'Microring resonator channel dropping filters'. In: *Journal of Lightwave Technology* 15.6 (1997), pp. 998–1005.

[101] Jun Rong Ong, Ranjeet Kumar and Shayan Mookherjea. 'Ultra-High-Contrast and Tunable-Bandwidth Filter Using Cascaded High-Order Silicon Microring Filters'. In: *IEEE Photonics Technology Letters* 25.16 (2013), pp. 1543–1546.

[102] Wim Bogaerts et al. 'Silicon-on-Insulator Spectral Filters Fabricated With CMOS Technology'. In: *IEEE Journal of Selected Topics in Quantum Electronics* 16.1 (2010), pp. 33–44.

[103] Daniele Bajoni and Matteo Galli. 'Nonclassical light sources for silicon photonics'. In: *Photonics and Nanostructures - Fundamentals and Applications* 26 (2017), pp. 24–34. ISSN: 1569-4410.

[104] P. P. Absil et al. 'Wavelength conversion in GaAs micro-ring resonators'. In: *Opt. Lett.* 25.8 (Apr. 2000), pp. 554–556.

[105] Joshua W Silverstone et al. 'Silicon quantum photonics'. In: *IEEE Journal of Selected Topics in Quantum Electronics* 22.6 (2016), pp. 390–402.

[106] ANSYS, Inc. *Finite Difference IDE (Lumerical software ULC)*. Version 8.26.2779. 2021. URL: `https://www.lumerical.com/products/fdtd/` (visited on 18/05/2021).

[107] Warren Kut King Kan et al. '2x2 ultra-broadband multimode interference coupler with subwavelength gratings fabricated by immersion lithography'. In: *2023 Photonics North (PN)*. IEEE. 2023, pp. 1–1.

[108] Wim Bogaerts and Lukas Chrostowski. 'Silicon Photonics Circuit Design: Methods, Tools and Challenges'. In: *Laser & Photonics Reviews* 12.4 (2018), p. 1700237.

[109] Hongnan Xu and Yaocheng Shi. 'Flat-Top CWDM (De)Multiplexer Based on MZI With Bent Directional Couplers'. In: *IEEE Photonics Technology Letters* 30.2 (2018), pp. 169–172.

[110] Zeqin Lu et al. 'Broadband silicon photonic directional coupler using asymmetric-waveguide based phase control'. In: *Opt. Express* 23.3 (Feb. 2015), pp. 3795–3808.

[111] JC Mikkelsen et al. 'Polarization-insensitive silicon nitride Mach-Zehnder lattice wavelength demultiplexers for CWDM in the O-band'. In: *Optics express* 26.23 (2018), pp. 30076–30084.

[112] Linda Gianini. 'High-rate multiplexed silicon-integrated sources of entangled states of light for quantum communication'. Submitted to the Graduate School of the department of Electrical, Computer and Biomedical Engineering for the degree of Doctor of Philosophy in Microelectronics at the University of Pavia. PhD thesis. 2024.

[113] Xin Mu et al. 'Edge couplers in silicon photonic integrated circuits: A review'. In: *Applied Sciences* 10.4 (2020), p. 1538.

[114] Lirong Cheng et al. 'Grating couplers on silicon photonics: Design principles, emerging trends and practical issues'. In: *Micromachines* 11.7 (2020), p. 666.

[115] Frédéric Boeuf et al. '300mm Silicon Photonics Platforms from Datacommunication to LiDAR'. In: *JSAP-Optica Joint Symposia*. Optica Publishing Group. 2025, 8p_N203_1.

[116] FJ Ferraro et al. 'Imec silicon photonics platforms: performance overview and roadmap'. In: *Next-Generation Optical Communication: Components, Sub-Systems, and Systems XII*. Vol. 12429. SPIE. 2023, pp. 22–28.

[117] Frederik Van Laere et al. 'Compact focusing grating couplers for silicon-on-insulator integrated circuits'. In: *IEEE Photonics Technology Letters* 19.23 (2007), pp. 1919–1921.

[118] Warren Kut King Kan. 'Design and characterization of subwavelength grating (SWG) engineered silicon photonics devices fabricated by immersion lithography'. PhD thesis. Université Paris-Saclay, 2024.

[119] Niklas Hoppe et al. 'Ultra-efficient silicon-on-insulator grating couplers with backside metal mirrors'. In: *IEEE Journal of Selected Topics in Quantum Electronics* 26.2 (2019), pp. 1–6.

[120] Yannong Luo et al. 'Low-loss two-dimensional silicon photonic grating coupler with a backside metal mirror'. In: *Optics letters* 43.3 (2018), pp. 474–477.

[121] Günther Roelkens, Dries Van Thourhout and Roel Baets. 'High efficiency Silicon-on-Insulator grating coupler based on a poly-Silicon overlay'. In: *Optics Express* 14.24 (2006), pp. 11622–11630.

[122] Dirk Taillaert et al. 'A compact two-dimensional grating coupler used as a polarization splitter'. In: *IEEE Photonics Technology Letters* 15.9 (2003), pp. 1249–1251.

[123] B Chen et al. 'Two-dimensional grating coupler on silicon with a high coupling efficiency and a low polarization-dependent loss'. In: *Optics Express* 28.3 (2020), pp. 4001–4009.

[124] Frederik Van Laere et al. 'Focusing polarization diversity grating couplers in silicon-on-insulator'. In: *Journal of Lightwave Technology* 27.5 (2009), pp. 612–618.

[125] María Félix Rosa et al. 'Novel design of two-dimensional grating couplers with backside metal mirror in 250 nm silicon-on-insulator'. In: *2017 International Conference on Numerical Simulation of Optoelectronic Devices (NUSOD)*. IEEE. 2017, pp. 81–82.

[126] Lee Carroll et al. 'Broad parameter optimization of polarization-diversity 2D grating couplers for silicon photonics'. In: *Optics express* 21.18 (2013), pp. 21556–21568.

[127] Simon Plantier et al. 'Impact of scattering element shape on polarisation dependent loss in two dimensional grating couplers'. In: *2016 IEEE 13th International Conference on Group IV Photonics (GFP)*. IEEE. 2016, pp. 76–77.

[128] Daniel Benedikovic et al. 'Silicon–germanium receivers for short-wave-infrared optoelectronics and communications'. In: *Nanophotonics* 10.3 (2021), pp. 1059–1079.

[129] Hiroshi Murata et al. 'Optical pulse generation by electrooptic-modulation method and its application to integrated ultrashort pulse generators'. In: *IEEE Journal of Selected Topics in Quantum Electronics* 6.6 (2002), pp. 1325–1331.

[130] Michael Kues et al. 'On-chip generation of high-dimensional entangled quantum states and their coherent control'. In: *Nature* 546.7660 (2017), pp. 622–626.

[131] Poolad Imany et al. 'Characterization of coherent quantum frequency combs using electro-optic phase modulation'. In: *Physical Review A* 97.1 (2018), p. 013813.

[132] Wei-Ta Huang et al. 'Emerging Modulator Technologies in Silicon Photonics'. In: *IEEE Nanotechnology Magazine* (2025).

[133] Cheng Wang et al. 'Integrated lithium niobate electro-optic modulators operating at CMOS-compatible voltages'. In: *Nature* 562.7725 (2018), pp. 101–104.

[134] Anthony J Mercante et al. 'Thin film lithium niobate electro-optic modulator on silicon up to 50 GHz'. In: *Optics Express* 26.12 (2018), pp. 14810–14816.

[135] Nan Qi et al. 'Co-design and demonstration of a 25-Gb/s silicon-photonic Mach–Zehnder modulator with a CMOS-based high-swing driver'. In: *IEEE Journal of Selected Topics in Quantum Electronics* 22.6 (2016), pp. 131–140.

[136] Jeremy Witzens. 'High-speed silicon photonics modulators'. In: *Proceedings of the IEEE* 106.12 (2018), pp. 2158–2182.

[137] Juerg Leuthold et al. 'High-speed, low-power optical modulators in silicon'. In: *2013 15th International Conference on Transparent Optical Networks (ICTON)*. IEEE. 2013, pp. 1–4.

[138] Xiaoguang Tu et al. 'Silicon optical modulator with shield coplanar waveguide electrodes'. In: *Optics express* 22.19 (2014), pp. 23724–23731.

[139] Ran Ding et al. 'High-speed silicon modulator with slow-wave electrodes and fully independent differential drive'. In: *Journal of Lightwave Technology* 32.12 (2014), pp. 2240–2247.

[140] Thomas Ferrotti. 'Design, fabrication and characterization of a hybrid III-V on silicon transmitter for high-speed communications'. THESE de DOCTORAT DE L'UNIVERSITE DE LYON, opérée au sein de l'Ecole centrale de Lyon. PhD thesis. 2016. URL: `https://theses.hal.science/tel-01529424/`.

[141] STMicroelectronics. *Update: PIC100 or ST's 1st Silicon Photonics Technology Offers Performance, Efficiency, and a Vision of What the Future Looks Like in Data Centers*. Mar. 2026. URL: `https://blog.st.com/pic100/` (visited on 17/09/2026).

[142] Mingbo He et al. 'High-performance hybrid silicon and lithium niobate Mach–Zehnder modulators for 100 Gbit s- 1 and beyond'. In: *Nature photonics* 13.5 (2019), pp. 359–364.

[143] Arif Rahman et al. 'High-performance hybrid lithium niobate electro-optic modulators integrated with low-loss silicon nitride waveguides on a wafer-scale silicon photonics platform'. In: *arXiv preprint arXiv:2504.00311* (2025).

[144] Ligentec. *MPW: Multi Project Wafer Runs*. Mar. 2026. URL: `https://www.ligentec.com/ligentec-labs/` (visited on 17/09/2026).

[145] Sara Congia et al. 'Generation of hyperentangled photon pairs in the time and frequency domain on a silicon photonic chip'. In: *Optics Letters* 50.16 (2025), pp. 5117–5120.

[146] Julio T. Barreiro et al. 'Generation of Hyperentangled Photon Pairs'. In: *Phys. Rev. Lett.* 95 (26 Dec. 2005), p. 260501.

[147] Raino Ceccarelli et al. 'Experimental Entanglement and Nonlocality of a Two-Photon Six-Qubit Cluster State'. In: *Phys. Rev. Lett.* 103 (16 Oct. 2009), p. 160401.

[148] Giuseppe Vallone et al. 'Hyperentanglement of two photons in three degrees of freedom'. In: *Physical Review A-Atomic, Molecular, and Optical Physics* 79.3 (2009), p. 030301.

[149] Hsuan-Hao Lu et al. 'Generation and characterization of ultrabroadband polarization–frequency hyperentangled photons'. In: *Optics Letters* 48.22 (2023), pp. 6031–6034.

[150] Zhenda Xie et al. 'Harnessing high-dimensional hyperentanglement through a biphoton frequency comb'. In: *Nature Photonics* 9.8 (2015), pp. 536–542.

[151] Wei-Bo Gao et al. 'Experimental demonstration of a hyper-entangled ten-qubit Schrödinger cat state'. In: *Nature physics* 6.5 (2010), pp. 331–335.

[152] Ramesh Kumar, Vikash Kumar Yadav and Joyee Ghosh. 'Postselection-free, hyperentangled photon pairs in a periodically poled lithium-niobate ridge waveguide'. In: *Physical Review A* 102.3 (2020), p. 033722.

[153] Yiwen Huang et al. 'High-performance hyperentanglement generation and manipulation based on lithium niobate waveguides'. In: *Physical Review Applied* 17.5 (2022), p. 054002.

[154] Lucia Caspani et al. 'Integrated sources of photon quantum states based on nonlinear optics'. In: *Light: Science & Applications* 6.11 (2017), e17100–e17100.

[155] Jing Suo et al. 'Generation of hyper-entanglement on polarization and energy-time based on a silicon micro-ring cavity'. In: *Opt. Express* 23.4 (Feb. 2015), pp. 3985–3995.

[156] Linda Gianini et al. 'A silicon integrated source of hyper-entangled photon pairs with rate exceeding 1 billion pairs per second'. In: *npj Nanophotonics* 3.1 (2026), p. 1.

[157] Hyperspace International. *Hyperspace International*. `https://hyperspace.international/`. Accessed: 2026-02-26. n.d.

[158] Ivan Marcikic et al. 'Distribution of time-bin entangled qubits over 50 km of optical fiber'. In: *Physical review letters* 93.18 (2004), p. 180502.

[159] Rupert Ursin et al. 'Entanglement-based quantum communication over 144 km'. In: *Nature physics* 3.7 (2007), pp. 481–486.

[160] Giuseppe Vallone et al. 'Interference at the single photon level along satellite-ground channels'. In: *Physical review letters* 116.25 (2016), p. 253601.

[161] Ilaria Vagniluca et al. 'Efficient time-bin encoding for practical high-dimensional quantum key distribution'. In: *Physical Review Applied* 14.1 (2020), p. 014051.

[162] Hao Yu et al. 'Quantum key distribution implemented with d-level time-bin entangled photons'. In: *Nature Communications* 16.1 (2025), p. 171.

[163] Andrea Bernardi et al. 'Gigahertz-rate thin-film lithium niobate receiver for time-bin quantum communication'. In: *Light: Science & Applications* 15.1 (2026), p. 237.

[164] Simon JU White et al. 'A robust approach for time-bin encoded photonic quantum information protocols'. In: *arXiv preprint arXiv:2404.16106* (2024).

[165] Marco Clementi et al. 'Programmable frequency-bin quantum states in a nano-engineered silicon device'. In: *Nature Communications* 14.1 (2023), p. 176.

[166] Massimo Borghi et al. 'Reconfigurable silicon photonic chip for the generation of frequency-bin-entangled qudits'. In: *Physical Review Applied* 19.6 (2023), p. 064026.

[167] Noemi Tagliavacche et al. 'Frequency-bin entanglement-based quantum key distribution'. In: *npj Quantum Information* 11.1 (2025), p. 60.

[168] Anahita Khodadad Kashi and Michael Kues. 'Frequency-bin-encoded entanglement-based quantum key distribution in a reconfigurable frequency-multiplexed network'. In: *Light: Science & Applications* 14.1 (2025), p. 49.

[169] George Claudiu Crisan et al. 'Multi-dimensional frequency-bin entanglement-based quantum key distribution network'. In: *npj Quantum Information* (2026).

[170] Marco Liscidini and JE Sipe. 'Scalable and efficient source of entangled frequency bins'. In: *Optics Letters* 44.11 (2019), pp. 2625–2628.

[171] J. Brendel et al. 'Pulsed Energy-Time Entangled Twin-Photon Source for Quantum Communication'. In: *Phys. Rev. Lett.* 82 (12 Mar. 1999), pp. 2594–2597.

[172] Hiroki Takesue and Yuita Noguchi. 'Implementation of quantum state tomography for time-bin entangled photon pairs'. In: *Optics express* 17.13 (2009), pp. 10976–10989.

[173] J. D. Franson. 'Bell inequality for position and time'. In: *Phys. Rev. Lett.* 62 (19 May 1989), pp. 2205–2208.

[174] Massimo Borghi et al. 'Quantum interference with time-frequency modes and multiple-photons generated by a silicon nitride microresonator'. In: *arXiv preprint arXiv:2502.00491* (2025).

[175] J. D. Franson. 'Inconsistency of local realistic descriptions of two-photon interferometer experiments'. In: *Phys. Rev. A* 61 (1 Dec. 1999), p. 012105.

[176] John F Clauser et al. 'Proposed experiment to test local hidden-variable theories'. In: *Physical review letters* 23.15 (1969), p. 880.

[177] Giuseppe Giuseppe Vallone et al. 'Hyperentanglement witness'. In: *Physical Review A-Atomic, Molecular, and Optical Physics* 78.6 (2008), p. 062305.

[178] Géza Tóth and Otfried Gühne. 'Entanglement detection in the stabilizer formalism'. In: *Physical Review A-Atomic, Molecular, and Optical Physics* 72.2 (2005), p. 022340.

[179] Géza Tóth and Otfried Gühne. 'Detecting genuine multipartite entanglement with two local measurements'. In: *Physical review letters* 94.6 (2005), p. 060501.

[180] Artur Czerwinski. 'Quantifying entanglement of two-qubit Werner states'. In: *Communications in Theoretical Physics* 73.8 (2021), p. 085101.

[181] Giovanni Garberoglio et al. *Enhanced Compressive Threshold Quantum State Tomography for Qudit Systems*. 2025. arXiv: 2502.10031 [quant-ph].

[182] H Aghaee Rad et al. 'Scaling and networking a modular photonic quantum computer'. In: *Nature* 638.8052 (2025), pp. 912–919.

[183] Ming Lai Chan et al. 'Tailoring fusion-based photonic quantum computing schemes to quantum emitters'. In: *PRX Quantum* 6.2 (2025), p. 020304.

[184] Sara Bartolucci et al. 'Fusion-based quantum computation'. In: *Nature Communications* 14.1 (2023), p. 912.

[185] Hua-Liang Liu et al. 'Robust quantum computational advantage with programmable 3050-photon Gaussian boson sampling'. In: *arXiv preprint arXiv:2508.09092* (2025).

[186] PsiQuantum team. 'A manufacturable platform for photonic quantum computing'. In: *Nature* 641.8064 (2025), pp. 876–883.

[187] Jieshan Huang et al. 'Demonstration of hypergraph-state quantum information processing'. In: *Nature Communications* 15.1 (2024), p. 2601.

[188] Daniel Llewellyn et al. 'Chip-to-chip quantum teleportation and multi-photon entanglement in silicon'. In: *Nature Physics* 16.2 (2020), pp. 148–153.

[189] Stefano Paesani et al. 'Generation and sampling of quantum states of light in a silicon chip'. In: *Nature Physics* 15.9 (2019), pp. 925–929.

[190] Juan M Arrazola et al. 'Quantum circuits with many photons on a programmable nanophotonic chip'. In: *Nature* 591.7848 (2021), pp. 54–60.

[191] Je-Hyung Kim et al. 'Hybrid integration methods for on-chip quantum photonics'. In: *Optica* 7.4 (2020), pp. 291–308.

[192] Haoyang Wang et al. 'Progress on chip-based spontaneous four-wave mixing quantum light sources'. In: *Advanced Devices & Instrumentation* 5 (2024), p. 0032.

[193] Jong-Moo Lee et al. 'Quantum states generation and manipulation in a programmable silicon-photonic four-qubit system with high-fidelity and purity'. In: *Apl Photonics* 9.7 (2024).

[194] Laurent Olislager et al. 'Silicon-on-insulator integrated source of polarization-entangled photons'. In: *Optics letters* 38.11 (2013), pp. 1960–1962.

[195] Xin Hua et al. 'A bright polarization-entangled photon pair source based on silicon photonics integration'. In: *APL Photonics* 10.6 (2025).

[196] Colin Vendromin, JE Sipe and Marco Liscidini. 'Programmable integrated source of polarization and frequency-bin hyperentangled photon pairs'. In: *Physical Review A* 111.4 (2025), p. 043711.

[197] Liang Zhang et al. 'On-chip parallel processing of quantum frequency comb'. In: *npj Quantum Information* 9.1 (2023), p. 57.

[198] S Francesconi et al. 'On-chip generation of hybrid polarization-frequency entangled biphoton states'. In: *Photonics Research* 11.2 (2023), pp. 270–278.

[199] Dongpeng Kang et al. 'Hyperentangled photon sources in semiconductor waveguides'. In: *Physical Review A* 89.2 (2014), p. 023833.

[200] Guangqiang He et al. 'Generation of path-polarization hyperentanglement using quasi-phase-matching in quasi-periodic nonlinear photonic crystal'. In: *Scientific Reports* 7.1 (2017), p. 4954.

[201] Mario Arnolfo Ciampini et al. 'Path-polarization hyperentangled and cluster states of photons on a chip'. In: *Light: Science & Applications* 5.4 (2016), e16064–e16064.

[202] Yonghe Yu et al. 'Chip-to-chip hyperentanglement distribution and entanglement purification using silicon integrated photonics'. In: *arXiv preprint arXiv:2510.18562* (2025).

[203] Cadence Design Systems. *Virtuoso layout suite Cadence design systems.* `https://www.cadence.com/en_US/home/tools/custom-ic-analog-rf-design/layout-design/virtuoso-layout-suite.html`. Accessed: 2026-02-26. n.d.

[204] Tsuyoshi Horikawa et al. 'A 300-mm Silicon Photonics Platform for Large-Scale Device Integration'. In: *IEEE Journal of Selected Topics in Quantum Electronics* 24.4 (2018), pp. 1–15.

[205] Ken Giewont et al. '300-mm Monolithic Silicon Photonics Foundry Technology'. In: *IEEE Journal of Selected Topics in Quantum Electronics* 25.5 (2019), pp. 1–11.

[206] Vladimir Bliznetsov and Kelvin Loh Wei Loong. 'Development of trilayer mask etching for fabrication of high aspect ratio structures'. In: *2019 Electron Devices Technology and Manufacturing Conference (EDTM)*. 2019, pp. 127–129.

[207] Dritan Celo et al. 'Optical proximity correction in geometry sensitive silicon photonics waveguide crossings'. In: *2017 IEEE 14th International Conference on Group IV Photonics (GFP)* (2017), pp. 45–46.

[208] Bastien Orlando et al. 'OPC for curved designs in application to photonics on silicon'. In: *Optical Microlithography XXIX*. Ed. by Andreas Erdmann and Jongwook Kye. Vol. 9780. International Society for Optics and Photonics. SPIE, 2016, pp. 260–265.

[209] Ang Li et al. 'Backscattering in silicon microring resonators: a quantitative analysis'. In: *Laser & Photonics Reviews* 10.3 (2016), pp. 420–431.

[210] Sara Congia et al. 'Fully integrated quantum frequency processor on a silicon chip'. In: *Nature Communications* (2026).

[211] Hsuan-Hao Lu et al. 'Quantum information processing with frequency-comb qudits'. In: *IEEE Photonics Technology Letters* 31.23 (2019), pp. 1858–1861.

[212] Hsuan-Hao Lu et al. 'Characterization of quantum frequency processors'. In: *IEEE Journal of Selected Topics in Quantum Electronics* 29.6: Photonic Signal Processing (2023), pp. 1–12.

[213] Stéphane Clemmen et al. 'Ramsey interference with single photons'. In: *Physical review letters* 117.22 (2016), p. 223601.

[214] Toshiki Kobayashi et al. 'Frequency-domain Hong–Ou–Mandel interference'. In: *Nature photonics* 10.7 (2016), pp. 441–444.

[215] Joseph M Lukens et al. 'All-optical frequency processor for networking applications'. In: *Journal of Lightwave Technology* 38.7 (2019), pp. 1678–1687.

[216] Hsuan-Hao Lu et al. 'Electro-optic frequency beam splitters and tritters for high-fidelity photonic quantum information processing'. In: *Physical review letters* 120.3 (2018), p. 030502.

[217] Hsuan-Hao Lu et al. 'Fully arbitrary control of frequency-bin qubits'. In: *Physical Review Letters* 125.12 (2020), p. 120503.

[218] Poolad Imany et al. 'Probing quantum walks through coherent control of high-dimensionally entangled photons'. In: *Science Advances* 6.29 (2020), eaba8066.

[219] Hsuan-Hao Lu et al. 'A controlled-NOT gate for frequency-bin qubits'. In: *npj Quantum Information* 5.1 (2019), p. 24.

[220] Hsuan-Hao Lu et al. 'Quantum interference and correlation control of frequency-bin qubits'. In: *Optica* 5.11 (2018), pp. 1455–1460.

[221] Poolad Imany et al. '50-GHz-spaced comb of high-dimensional frequency-bin entangled photons from an on-chip silicon nitride microresonator'. In: *Optics express* 26.2 (2018), pp. 1825–1840.

[222] Raktim Haldar et al. 'Steering of Quantum Walks through Coherent Control of High-dimensional Bi-photon Quantum Frequency Combs with Tunable State Entropies'. In: *arXiv preprint arXiv:2210.06305* (2022).

[223] Kaiyi Wu et al. 'On-chip pulse shaping of entangled photons'. In: *Physical Review Research* 7.3 (2025), p. 033015.

[224] Chen-You Su et al. 'High-resolution tunable frequency beamsplitter enabled by an integrated silicon pulse shaper'. In: *arXiv preprint arXiv:2601.23028* (2026).

[225] Lucas M Cohen et al. 'Silicon photonic microresonator-based high-resolution line-by-line pulse shaping'. In: *Nature Communications* 15.1 (2024), p. 7878.

[226] Benjamin E Nussbaum et al. 'Design methodologies for integrated quantum frequency processors'. In: *Journal of Lightwave Technology* 40.23 (2022), pp. 7648–7657.

[227] F Boeuf et al. 'A silicon photonics technology for 400 Gbit/s applications'. In: *2019 IEEE international electron devices meeting (IEDM)*. IEEE. 2019, pp. 33–1.

[228] Emanuel Knill, Raymond Laflamme and G Milburn. 'Efficient linear optics quantum computation'. In: *arXiv preprint quant-ph/0006088* (2000).

[229] Yaowen Hu et al. 'On-chip electro-optic frequency shifters and beam splitters'. In: *Nature* 599.7886 (2021), pp. 587–593.

[230] Chen-You Su et al. '3 GHz-Spaced Frequency Beam Splitter Using an On-Chip Pulse Shaper'. In: *2025 Conference on Lasers and Electro-Optics (CLEO)*. IEEE. 2025, pp. 1–2.

[231] Saleh Rahimi-Keshari et al. 'Direct characterization of linear-optical networks'. In: *Optics express* 21.11 (2013), pp. 13450–13458.

[232] Stephane Monfray et al. 'Optimization of deep rib high speed phase modulators on 300mm industrial Si-photonics platform'. In: *Integrated Photonics Platforms: Fundamental Research, Manufacturing and Applications*. Vol. 11364. SPIE. 2020, pp. 7–14.

[233] Iman Taghavi et al. 'Polymer modulators in silicon photonics: review and projections'. In: *Nanophotonics* 11.17 (2022), pp. 3855–3871.

[234] Huangpu Han, Shuangchen Ruan and Bingxi Xiang. 'Heterogeneously integrated photonics based on thin film lithium niobate platform'. In: *Laser & Photonics Reviews* 19.1 (2025), p. 2400649.

[235] Hsuan-Hao Lu et al. 'High-dimensional discrete Fourier transform gates with a quantum frequency processor'. In: *Optics Express* 30.6 (2022), pp. 10126–10134.

[236] Sara Congia, Pierre Chausse and Sylvain Guerber. *PHOTONIC INTEGRATED CIRCUIT*. Published. Patent No.: *US 20260072212 A1*. Applicant Commissariat à l'Énergie Atomique et aux Énergies Alternatives, 2026-03-12.

[237] Sara Congia, Pierre Chausse and Sylvain Guerber. *Circuit intégré photonique*. Published. Patent No.: *FR 3166229 A1*. Applicant Commissariat à l'Énergie Atomique et aux Énergies Alternatives, 2026-03-13.

[238] Sara Congia, Pierre Chausse and Sylvain Guerber. *Circuit intégré photonique*. Published. Patent No.: *FR 3166228 A1*. Applicant Commissariat à l'Énergie Atomique et aux Énergies Alternatives, 2026-03-13.

[239] Francesco Garrisi. 'Nonclassical states of light: fundamental physics and CMOS devices'. Submitted to the Graduate School of Physics for the degree of Doctor of Philosophy in Physics at the University of Pavia. PhD thesis. 2019. URL: http://hdl.handle.net/11571/1317092.

[240] Rohde & Schwarz. *Understanding S-Parameters*. Accessed: 2026-02-26. URL: https://www.rohde-schwarz.com/tw/products/test-and-measurement/essentials-test-equipment/spectrum-analyzers/understanding-s-parameters_257831.html.